



HAL
open science

Intraseasonal descriptors and rainfall extremes in austral summer over South Africa: Observations and Meso-scale modelling

Asmat Ullah

► **To cite this version:**

Asmat Ullah. Intraseasonal descriptors and rainfall extremes in austral summer over South Africa: Observations and Meso-scale modelling. *Climatology*. Université Bourgogne Franche-Comté, 2022. English. NNT: 2022UBFCK110 . tel-04053512

HAL Id: tel-04053512

<https://theses.hal.science/tel-04053512v1>

Submitted on 31 Mar 2023

HAL is a multi-disciplinary open access archive for the deposit and dissemination of scientific research documents, whether they are published or not. The documents may come from teaching and research institutions in France or abroad, or from public or private research centers.

L'archive ouverte pluridisciplinaire **HAL**, est destinée au dépôt et à la diffusion de documents scientifiques de niveau recherche, publiés ou non, émanant des établissements d'enseignement et de recherche français ou étrangers, des laboratoires publics ou privés.



**THÈSE DE DOCTORAT DE L'UNIVERSITÉ BOURGOGNE FRANCHE-COMTÉ
PRÉPARÉE À L'UNIVERSITÉ DE BOURGOGNE DIJON**

École doctorale n°554 - Environnements-Santé

Doctorat de Climatologie

Par

Asmat ULLAH

**Intraseasonal descriptors and rainfall extremes in austral summer over
South Africa: Observations and Meso-scale modelling**

Composition du Jury:

Prof. Chris Reason	Professeur à l'université de Cape Town (Afrique du Sud)	Rapporteur
Prof. Willem Landman	Professeur à l'université de Pretoria (Afrique du Sud)	Rapporteur
Dr. Bastien Dieppois	Assistant professeur à l'université de Coventry (Royaume-Uni)	Examineur
Prof. Pierre Camberlin	Professeur à l'Université de Bourgogne	Président du jury
Dr. Benjamin Pohl	Directeur de recherches au CNRS (Laboratoire Biogéosciences)	Directeur de thèse
Dr. Julien Pergaud	Ingénieur d'études au CNRS (Laboratoire Biogéosciences)	C0-directeur de thèse

Abstract (English)

Rainfall extremes are of major and increasing importance in semi-arid countries and their variability has strong implications for water resource and climate impacts on the local societies and environment. Here, we examine intraseasonal descriptors (ISDs) and wet extremes in austral summer rainfall (November–February) over South Africa (SA). Using daily observations from 225 rain gauges and ERA5 reanalysis between 1979 and 2015, we propose a novel typology of wet extreme events based on their spatial fraction, thus differentiating large- and small-scale extremes. Long-term variability of both types of extreme rainfall events is then extensively discussed in the context of ISDs. Following the definition of a novel typology of rainfall extremes, disentangling large- and small-scale events we further examine the relationship between these two types of rainfall extremes and different modes of climate variability at different timescales. At low-frequencies, rainfall extremes are assessed at interannual (IV: 2–8 years) and quasi-decadal (QDV: 8–13 years) timescales, which are primarily associated with the El Niño Southern Oscillation (ENSO) and the Interdecadal Pacific Oscillation (IPO), respectively. At sub-seasonal timescales, the typology of rainfall extremes is analysed depending on the synoptic configurations, as inferred by seven convective regimes including Tropical Temperate Troughs (TTTs: 3–7 days), and the intraseasonal variability associated with the Madden-Julien Oscillation (MJO: 30–60 days). To identify potentially high-impact rainfall spells, we introduce duration into the definition of extreme rainfall typology. Large-scale longest-lived events are then considered as case studies of potentially high-impact rainfall spells and are selected for meso-scale modelling. To that end, we use state-of-the-art Weather Research and Forecasting (WRF version 4.2.1) model which is widely used for both atmospheric research and operational forecasting applications. ERA5 reanalysis is first used to drive WRF simulations with several experimental setups on different case studies to obtain the finest WRF configuration. The optimal experimental design is then used to drive WRF simulations using coarse resolution global forecast i.e., Re-forecast version 2 (RF2) developed by National Oceanic and Atmospheric Administration/Earth System Research Laboratory (NOAA/ESLR) having a resolution of 25 kms. Here, we attempt to investigate if the properties of such major events can be improved using convection-permitting downscaling of these global grids in terms on intensity and location.

The results demonstrate that using 7% of spatial fraction simultaneously exceeding the local threshold of the 90th percentile produces remarkable results in characterizing rainfall extremes into large- and small-scale extremes. Austral summer total rainfall is found to be primarily shaped by large-scale extremes which constitute more than half of the rainfall amount under observation, and nearly half in ERA5. Observation (ERA5) shows an average of 8 ± 5 (20 ± 7) days per season associated with large-scale extremes, which are comprised in 5 ± 3 (10 ± 3) spells with an average persistence of at least 2 days. Overall, we find a strong dependence of total rainfall on the number of wet days and wet spells that are associated with large-scale extremes. We also find that large- and small-scale extremes are well-organized and spatially coherent in nature yet extreme conditions during small-scale events are found sporadic over the region, contrasting with

large-scale events for which extreme conditions are found over a larger and coherent region. An added value of this work resides in the first presentation of a detailed mapping of rainfall variability over South Africa, including large- and small-scale extreme events, as well as non-extreme rainfall contribution. Such studies have immediate and considerable implications for theoretical and applied climate variability-based studies.

At the IV timescale, the occurrence of large-scale extremes is substantially higher during its wet seasons thereby suggesting a 400% rise in the occurrence large-scale extremes as compared to its dry seasons. QDV timescale found to be mostly related to modulate small-scale extremes during its wet seasons. Teleconnections with global sea surface temperature (SSTs) confirm that La Niña conditions favour overall wet conditions and extremes in South Africa. The numbers of large-scale extremes are consistently related to warmer SSTs in the North Atlantic, while their link with warmer Indian and tropical South Atlantic oceans is found to be statistically independent of the state of ENSO. At the sub-seasonal timescales, large-scale extremes largely occur during synoptic regimes #3 to #5 whereas small-scale extremes are nearly equiprobable during all regimes. The occurrence of large-scale extremes during continent rooted TTT is further enhanced during the locally wet phases of the MJO and is symmetrically weakened during its dry phases. The extensive characterization of rainfall extremes carried out in reference to low-frequency and sub-seasonal timescales of variability are crucial in promoting long-term multi-year seamless forecasts for the region on one hand, and sub-seasonal forecasts on the other hand.

For mesoscale modelling, three cases of large-scale longest-lived events that are identified during the period between 2000 to 2015, were taken as case studies to investigate their predictability by downscaling reforecasts using WRF model. We first downscale ERA5 reanalysis for all three case studies. We note that WRF was able to reproduce the observed characteristics of rainfall patterns, intensity and location for all three case studies when ERA5 was used as forcing. The WRF configuration setup was also found reliable to downscale such cases of heavy rainfall events as all three cases have different rain-bearing systems yet the performance of WRF was up to the mark. By analysing the preliminary results of downscaling of RF2 for case #1, we notice that raw RF2 forecasts have uncertainties in terms of total rainfall accumulation with different lead times as well as uncertainties between ensemble members. We note that WRF can remarkably reduce these uncertainties in simulating the total rainfall accumulation of the event. Overall, these potentially high-impact (large-scale long-lived) events are predictable in the raw RF2 grid, and their predictability can be improved by dynamical downscaling. These results will be extended to the other cases studies and also with other analyses which are important to further investigate the driving mechanisms of such events in terms of dynamics and probable causes of longer persistence of such events.

Resume (Français)

Les précipitations extrêmes sont d'une importance majeure et croissante dans les pays semi-arides et leur variabilité a de fortes implications pour les ressources en eau et les impacts climatiques sur les sociétés locales et l'environnement. Ici, nous examinons les descripteurs intrasaisonniers (ISD) et les extrêmes humides des précipitations d'été austral (novembre-février) sur l'Afrique du Sud (SA). En utilisant les observations quotidiennes de 225 pluviomètres et les réanalyses ERA5 entre 1979 et 2015, nous proposons une nouvelle typologie des événements extrêmes humides basée sur leur fraction spatiale, différenciant ainsi les extrêmes à grande et à petite échelle. La variabilité à long terme des deux types d'événements de précipitations extrêmes est ensuite discutée en détail dans le contexte des ISD. Suite à la définition d'une nouvelle typologie des extrêmes pluviométriques, distinguant les événements à grande et à petite échelle, nous examinons plus avant la relation entre ces deux types d'extrêmes pluviométriques et différents modes de variabilité climatique à différentes échelles de temps. Aux basses fréquences, les extrêmes pluviométriques sont évalués à des échelles de temps interannuelles (IV : 2 à 8 ans) et quasi décennales (QDV : 8 à 13 ans), qui sont principalement associées à l'oscillation australe El Niño (ENSO) et à l'Oscillation Pacifique inter-décennale (IPO), respectivement. Aux échelles de temps sub-saisonniers, la typologie des extrêmes pluviométriques est analysée en fonction des configurations synoptiques, déduites par sept régimes convectifs dont les thalwegs tropicaux tempérés (TTT : 3–7 jours), et la variabilité intrasaisonnaire associée à l'Oscillation de Madden-Julien (MJO : 30 à 60 jours). Afin d'identifier les épisodes de précipitations potentiellement à fort impact, nous introduisons la durée dans la définition de la typologie des précipitations extrêmes. Les événements à grande échelle et à durée de vie la plus longue sont ensuite considérés comme des études de cas de périodes de précipitations potentiellement à fort impact et sont sélectionnés pour la modélisation à méso-échelle. À cette fin, nous utilisons un modèle de recherche et de prévision météorologique de pointe (WRF version 4.2.1) qui est largement utilisé à la fois pour la recherche et les applications de prévision opérationnelle. Les réanalyses ERA5 sont d'abord utilisées pour forcer le modèle WRF avec plusieurs configurations expérimentales sur différents cas d'étude afin d'obtenir la configuration WRF la plus performante. La configuration optimale est ensuite utilisée pour piloter des simulations WRF à l'aide de prévisions globales à résolution grossière, la version 2 de retroprévision (RF2) développée par la National Oceanic and Atmospheric Administration/Earth System Research Laboratory (NOAA/ESLR) et à 25kms de résolution. Avec cette méthodologie, nous souhaitons déterminer si la prévisibilité de ces événements majeurs peut être améliorée en termes d'intensité et de localisation en utilisant un raffinement d'échelle permettant la résolution de la convection profonde.

Les résultats démontrent que l'utilisation de 7 % de la fraction spatiale dépassant simultanément le seuil local du 90e centile produit des résultats remarquables dans la caractérisation des extrêmes de précipitations en extrêmes à grande et à petite échelle. Les précipitations totales de l'été austral se révèlent principalement façonnées par des extrêmes à grande échelle qui constituent plus de la moitié de la quantité de précipitations observée, et près de la moitié dans

ERA5. L'observation (ERA5) montre une moyenne de 8 ± 5 (20 ± 7) jours par saison associés à des extrêmes à grande échelle, qui sont compris dans 5 ± 3 (10 ± 3) épisodes avec une persistance moyenne d'au moins 2 jours. Dans l'ensemble, nous constatons une forte dépendance des précipitations totales au nombre de jours et de périodes humides associés aux extrêmes à grande échelle. Nous constatons également que les extrêmes à grande et à petite échelle sont bien organisés et cohérents dans l'espace, mais que les conditions extrêmes lors d'événements à petite échelle ont une structure plutôt sporadique dans la région, contrairement aux événements à grande échelle pour lesquels des conditions extrêmes couvrent une plus grande région de manière cohérente. Une valeur ajoutée de ce travail réside dans la première présentation d'une cartographie détaillée de la variabilité des précipitations sur l'Afrique du Sud, y compris les événements extrêmes à grande et petite échelle, ainsi que la contribution des précipitations non extrêmes. De telles études ont des implications immédiates et considérables pour les études théoriques et appliquées basées sur la variabilité climatique.

À l'échelle de temps IV, l'occurrence d'extrêmes à grande échelle est considérablement plus élevée pendant les saisons humides, montrant ainsi une augmentation de 400 % de l'occurrence d'extrêmes à grande échelle par rapport aux saisons sèches. L'échelle de temps QDV s'est avérée principalement liée à la modulation des extrêmes à petite échelle pendant les saisons humides. Les téléconnexions avec la température globale de la surface de la mer (SST) confirment que les conditions La Niña favorisent les conditions humides et extrêmes en Afrique du Sud. Le nombre d'extrêmes à grande échelle est systématiquement lié à des SST plus chaudes dans l'Atlantique Nord, tandis que leur lien avec les océans indiens et tropicaux de l'Atlantique Sud plus chauds s'avère statistiquement indépendant de l'état de l'ENSO. Aux échelles de temps sous-saisonniers, les extrêmes à grande échelle se produisent principalement pendant les régimes synoptiques #3 à #5 alors que les extrêmes à petite échelle sont presque équiprobables pendant tous les régimes. L'apparition d'extrêmes à grande échelle pendant les TTT enracinés dans le continent est encore renforcée pendant les phases localement humides de la MJO et est symétriquement

Pour la modélisation à méso-échelle, trois cas d'événements à grande échelle de la plus longue durée de vie identifiés au cours de la période comprise entre 2000 et 2015 ont été pris comme études de cas pour étudier leur prévisibilité en réduisant les réprévisions à l'aide du modèle WRF. Nous avons d'abord réduit l'échelle de la réanalyse ERA5 pour les trois études de cas. Nous notons que WRF a pu reproduire les caractéristiques observées des régimes, de l'intensité et de l'emplacement des précipitations pour les trois études de cas lorsque ERA5 a été utilisé comme forçage. La configuration de la configuration WRF s'est également avérée fiable pour réduire ces cas d'événements de fortes pluies, car les trois cas ont des systèmes de pluie différents, mais les performances de WRF étaient à la hauteur. En analysant les résultats préliminaires de la réduction d'échelle de RF2 pour le cas #1, nous remarquons que les prévisions brutes de RF2 ont des incertitudes en termes d'accumulation totale de pluie avec des délais différents ainsi que des incertitudes entre les membres de l'ensemble. Nous notons que WRF peut réduire remarquablement ces incertitudes en simulant l'accumulation totale de précipitations de l'événement. Dans l'ensemble, ces événements potentiellement à fort impact (à grande échelle et à

longue durée de vie) sont prévisibles dans la grille RF2 brute, et leur prévisibilité peut être améliorée par une réduction d'échelle dynamique. Ces résultats seront étendus à d'autres études de cas ainsi qu'à d'autres analyses qui sont importantes pour approfondir les mécanismes moteurs de tels événements en termes de dynamique et de causes probables de persistance plus longue de tels événements.

This dissertation is dedicated to my parents

My father, who always wanted best for me in life and my mother, always full of prayers for me and encouragements.

Words can hardly describe my thanks and appreciation to you. You have been my source of inspiration, support, and guidance. You have taught me to be unique, determined, to believe in myself. I am truly thankful and honoured to have you as my parents.

Acknowledgements

First and foremost, I would like to praise and thank Allah, the Almighty, who has granted countless blessing, knowledge, and opportunity to me, so that I have been finally able to accomplish the thesis

∞

I want to thank my amazing advisers

Benjamin Pohl and Julien Pergaud

I truly mean it when I say that it would have been difficult for me to finish my PhD if they were not my advisers. I can probably write a whole book about the millions of ways both inspired me, made my life easier and helped me improve. I truly appreciate the confidence you both showed in me.

∞

I am also grateful to

Prof. Andrew Sturman and Dr. Hervé Quénot

for writing a strong recommendation for this PhD position

∞

I greatly appreciate the support from

Mathieu Rouault and Bastien Dieppois

for being an amazing collaborator and for providing useful datasets for this study

∞

I am also thankful to

Prof. Pierre Camberlin

Prof. Chris Reason

Prof. Willem Landman

(Members of the jury of dissertation)

for their time and insightful comments to improve the quality of the dissertation

∞

I am also grateful to the whole CRC team

Yves, Pierre, Pascal, Thierry, Olivier, Benjamin Bois, Albin, Nadège, Mario, Julien Crétat, Lea, Melissa, Sarah, Lola, Julita, Sebastien, Catinca and Maxime

for making my time in this lab so amazing and comfortable

∞

I am also thankful to

Pascal and Thierry

for being an amazing mentors and colleagues who always been ready to help me to understand lots of topics as well as thoughtful discussion on various aspects of life

∞

A special thanks to

Marie Charlotte

as she always been keen to know if I am facing any difficulties and always ready to help me.

I am also thankful to the **Administrative staff** of the University for handling my lots of complex administrative matters.

∞

I am also grateful to the **Housekeeping staff** of the University. I really appreciate the efforts they contributed in order to make the premises of university and labs clean and tidy so we could work in a healthy environment

∞

I also want to express my sincere thanks to my friends

Rana Amir Rasheed

Jameel Ahmed

Mohammad Rizwan Quddusi

Qaisar Ijaz

for their continuous encouragement

∞

I want to thank my entire family from the core of my heart

My father and mother

My brothers (Nasarullah and Zafarullah)

My sisters (Nasira, Shakira, Shahab, Asifa and Arifa)

My sister in laws (Lubna and Nazia)

My brother in laws (Latif, Naeem, Raheel, Rizawan and Ijaz)

My niece and nephews (Junaid, Jamshed, Rohma, Abdullah, Uswa, Bisma, Saif, Zubair, Iqra, Aqsa, Alyan, Nabera and Sulman)

Family support is the most important aspect in my success because they have been the first source of economic and emotional support. I am so fortunate that all of them always been ready to give what I needed at any stage of my life

∞

Last but not the least, my beloved wife

Arooj Zahid

Who sacrifice herself and supported me in every way possible so that I can achieve my goals and my **Son**

(Who was indeed the guest of honor in my defense ceremony)

∞

This work is part of the I-SITE Bourgogne Franche-Comté Junior Fellowship IMVULA (Grant N°: AAP2-JF-06). Calculations were performed using HPC resources from DNUM CCUB (Centre de Calcul de l'Université de Bourgogne)

∞ ∞ ∞ ∞ ∞ ∞ ∞ ∞ ∞ ∞ ∞

Table of Contents

General Introduction.....	1
Chapter 1	7
1.1. Climate of the region	7
1.1.1. Climate of the region during austral summer season	7
1.1.2. Major rain-bearing systems during austral summer season	8
1.1.3. Rainfall variability at low-frequency timescales during austral summer	10
1.1.4. Rainfall variability at sub-seasonal timescales during austral summer	12
1.1.5. Intraseasonal characteristics of austral summer season.....	12
1.2. Datasets to investigate summer climatology and statistical characteristics.....	13
1.2.1. In-situ observations	13
1.2.2. Re-analysis products	13
1.3. Datasets to investigate variability of extremes at low-frequency and sub-seasonal timescales	14
1.3.1. Intraseasonal descriptors	14
1.3.2. Summer Rainfall Index (SRI)	14
1.3.3. Sea surface temperature	15
1.3.4. Niño 3.4 index	15
1.3.5. Satellite based estimates for rainfall.....	15
1.3.6. Reanalysis data for validating physical mechanisms.....	15
1.3.7. Real-time Multivariate MJO (RMM) index.....	16
1.4. Datasets for meso-scale modelling.....	16
1.4.1. Weather Research and Forecasting Model (WRF-ARW)	16
1.4.2. Forcing datasets for WRF Model.....	16
1.5. Methodology to examining summer climatology and statistical characteristics	16
1.5.1. Seasonality test	17
1.5.2. Definition of intraseasonal descriptors at the regional scale.....	18
1.5.3. Local threshold for rainfall extremes	19
1.5.4. Regional threshold for rainfall extremes	22
1.5.6. Spatial characteristics of rainfall extremes.....	23
1.5.7. Spatial coherence of rainfall extremes.....	23
1.5.8. Definition of intraseasonal descriptors associated with rainfall extremes.....	23

1.6. Methodology to examine the relationship between rainfall extremes and low-frequency timescales of variability	25
1.6.1. Relationship of extremes with global SSTs.....	25
1.6.2. Quantification of risk of occurrence of extremes at low-frequency timescales.....	25
1.7. Examining the relationship between extremes and sub-seasonal timescales of climate variability	26
1.7.1. Seasonality and network-density tests	26
1.7.2. Defining three types of rainfall extremes based on duration and spatial extent	26
1.7.3. Characterizing the relationship between rainfall extremes and synoptic-scale variability	27
1.7.4. Characterizing the relationship between rainfall extremes and intraseasonal variability related to MJO	29
1.7.5. Characterizing the combined influence of synoptic and intraseasonal variability of MJO on rainfall extremes	31
1.7.6. Quantification of risk of occurrence of extremes during combined influence of sub-seasonal timescale of variability.....	31
1.8. WRF experimental design.....	32
1.8.1. WRF initialization setup for RF2.....	35
1.8.2. Validation of WRF simulations	35
Chapter 2	38
Summer climatology and statistical characteristics	38
Chapter 3	70
Summer teleconnections across multiple timescales	70
Chapter 4	146
Meso-scale modelling	146
General Conclusions.....	188
Future Perspectives	191
Bibliography.....	194

General Introduction

Climate change poses a serious threat to the ecosystem. According to the sixth assessment report (AR6) by the Intergovernmental Panel on Climate Change (IPCC), earth's climate is changing due to the human influence on the climate system thereby climate change is already affecting all regions on earth in several ways and these changes will increase with additional warming (IPCC, 2021). For 1.5°C of global warming, high frequency of heat wave, longer warm seasons and shorter cold seasons are expected while at 2°C of global warming, heat extremes would more often reach critical tolerance thresholds for agriculture and health (IPCC, 2021). Climate change is bringing several threats to different regions by altering the nature of physical processes. For instance, climate change is intensifying the water cycle, affecting rainfall patterns, sea level rise which causing coastal flooding in low-lying areas, amplification of permafrost thawing and numerous other impacts (McKittrick and Christy, 2018).

According to World Meteorological Organization (WMO), during the period of 1970 and 2019, there were more than 11,000 disasters attributed to climate and weather-related hazards which accounted for 2 million deaths and approximately US\$ 3.64 trillion in economic losses reported globally (WMO, 2021). **Africa is one of the most vulnerable regions in terms of climate change and global warming and shares significantly in global losses which accounts for 15% of weather and climate related disasters and 35% of associated deaths during the period of 1970 and 2019** (WMO, 2021). The 10 topmost disasters recorded during the period of 1970 and 2019 in Africa accounted for 95% (696,334 deaths) of deaths while 38% of economic losses (US\$ 14.37 billion). The tropical Cyclone *Idai* that hit Mozambique in 2019 and drought in South Africa during 1990 are the costliest events which were collectively estimated at US\$ 1.96 billion (WMO, 2021). **According to the global Climate Risk Index (CRI, 2021) developed by Germanwatch, for the period 2000–2019, with a CRI score of 32.50, Germanwatch ranked South Africa among the top 30 countries affected by climate change and extreme weather events.**

Over southern Africa, observation-based studies indicate decreasing precipitation trends since 1960s in winter rainfall regions and the eastern parts of South Africa (Engelbrecht *et al.*, 2009; Kruger and Nxumalo, 2017; Burls *et al.*, 2019; Lakhraj-Govender and Grab, 2019). The frequency of dry spells and agricultural droughts in the southern African region has increased

over the period 1961–2016 (Yuan *et al.*, 2018) while the frequency of meteorological drought increased by between 2.5–3 events per decade since 1961 (Spinoni *et al.*, 2021). Thoithi *et al.*, (2020) show decreasing trends of dry spells in the summer season over some parts of South African region. Over the southwestern cape of South Africa, the probability of the multi-year droughts increased by a factor of three in response to global warming (Otto *et al.*, 2018). The frequency and intensity of extreme rainfall events have increased over the last century (Kruger and Nxumalo, 2017; Ranasinghe, 2021; Sun *et al.*, 2021). Long-term station data shows that the Karoo region of southern South Africa is facing an increasing trend in annual rainfall of greater than 5 millimeter per decade over the period 1921–2015 (Kruger and Nxumalo, 2017).

Projection-based studies over southern Africa suggest that mean annual rainfall over summer rainfall regions is projected to decrease by 10–20%, accompanied by an increase in the frequency of consecutive dry days during the rainy season under Representative Concentration Pathways (RCPs) i.e., RCP8.5 (Kusangaya *et al.*, 2014; Engelbrecht *et al.*, 2015; Lazenby *et al.*, 2018; Maure *et al.*, 2018; Spinoni *et al.*, 2019). **Heavy rainfall events in the southwestern regions are also projected to decrease (Donat *et al.*, 2016) while frequency of such events over eastern parts of southern Africa is projected to increase at all global warming levels (Li *et al.*, 2021).** Dryness in the summer rainfall region is projected to increase at 1.5°C and above levels of global warming (Hoegh-Guldberg *et al.*, 2018) while increase in temperatures will enhance evaporation from the mega-dams and reduce soil-moisture content (Engelbrecht *et al.*, 2015). The western parts of the region are also projected to become drier with an increase in drought frequency, intensity and duration under RCP8.5 including multi-year droughts (Engelbrecht *et al.*, 2015; Dosio, 2017; Zhao and Dai, 2017; Liu *et al.*, 2018a, 2018b; Ukkola *et al.*, 2020). The frequency and duration of agricultural drought frequency are projected to increase over the large parts of southern Africa at 1.5°C global warming levels (Liu *et al.*, 2018a, 2018b) and unprecedented extreme droughts as compared to the 1981–2010 period are projected at 2°C global warming levels (Spinoni *et al.*, 2021). For instance, “Day-Zero” incident in 2018 is the most recent example of droughts in the region where in Cape Town a population of ~3.7 million was at grave risk due to a severe multi-year drought that led to the levels of supply dams falling to an unprecedented low (Burls *et al.*, 2019). The duration of meteorological droughts is also projected to increase from nearly 2 months during 1950–2014 to approximately 4 months in the mid to late 21st century under RCP8.5 (Ukkola *et al.*, 2020).

The Paris Agreement, however, now aims to constrain global warming to below 2°C, with efforts to further limit warming to 1.5°C (Russo *et al.*, 2016). **Given the significant impacts of extreme events, it is essential to understand how these events may change in the future under different warming scenarios** (Kruger, 2018). Nangombe *et al.*, (2018) addressed this question using the low-warming experiments of the Community Earth Systems Model (CESM), confirming that it can capture similar extreme events, the analysis is then followed by climate projections using RCP8.5 until stabilized 1.5°C and 2°C global mean temperature increases were reached. **This study suggests that limiting warming to 1.5°C offer considerable benefits in minimizing hydrometeorological extremes and their associated impacts across Africa** (Nangombe *et al.*, 2018).

Most of the regions in South Africa experiences a rainy season in the austral summer (November through February) and is characterised by sharp rainfall gradients from southwest to northeast, with a strong spatial and temporal climate variability (Reason and Jagadheesha, 2005; Hart *et al.*, 2013). Rainfall in the southwest region is dominated by mid-latitude cyclones, mostly in winter, while the north-eastern escarpment experience annual totals above 1,500 mm (Hart *et al.*, 2013). **Interannual variations in rainfall across South Africa have major consequences for human livelihoods and ecosystems through their impacts on water supply, drought, temperature, and agriculture. Thus, hydrometeorological extremes (either drought or floods) can have particularly detrimental effects on the economies and societies of the region.** Extreme weather events and how they are formed is complex. A recent study raises some uncomfortable possibilities that climate change is not only making the weather more severe but also harder to predict, potentially giving us less time to prepare for extreme floods, storms and heat waves in the coming years (Sheshadri *et al.*, 2021). **The severity and frequency of wet and dry extreme events are likely to increase at the global scale as a response to anthropogenic emissions of greenhouse gases** (Donat *et al.*, 2016). This statement is also true for South African rainfall (Mason and Joubert, 1997; Mason *et al.*, 1999; Shongwe *et al.*, 2009; Engelbrecht *et al.*, 2013; Pinto *et al.*, 2016). **Future scenarios include a combination of decreasing numbers of rainy days while increasing their intensity** (Pohl *et al.*, 2017), which are likely to modify the intrinsic characteristics of intraseasonal spells in the future. Numerous interrelated factors must be considered when seeking to explain the causes. For instance, Pohl *et al.*, (2017) suggest that this could be due to the so-called **Clausius–Clapeyron scaling which enhancing the atmospheric**

water cycle in terms of moisture convergence during unstable conditions and moisture divergence during stable phases, thereby increasing climate variability and rainfall extremes. However, science has been able to sufficiently demonstrate that climate change has a significant effect on extreme weather events in increasing their frequency, intensity, and duration. **A thorough understanding of these quantities at regional scale is essential for being able to mitigate the risks and prepare for extreme weather events on one hand and on the other hand such efforts will help to provide an up-to-date information to facilitate scientific community, policy makers and especially forecasters to ensure the reliable predictability of such extreme events in future.** Thus, in this work, we attempt to address these questions for South African austral summer rainfall i.e., (November through February).

In the light of issues raised above, this dissertation is aimed to provide a better understanding of intraseasonal variability of rainfall over South Africa where focus is given to extreme rainfall spells in various dimensions as study proceeds. To achieve this objective, we adopt a twofold methodology i.e., observation and meso-scale modelling. Concerning observations, this study aims to provide:

- an *overall assessment of intraseasonal descriptors* (hereafter ISDs), in which extremes are embedded using the latest available observation archive and a state-of-the-art reanalysis product (cf. chapter 2).
- a *novel typology of extreme rainfall events, based on the spatial fraction of these events as a base criterion, disentangling rainfall events into large-scale and small-scale extremes.* To our knowledge, there is hitherto no study that addresses the spatial dimension in the definition of rainfall extremes over the region, despite its importance for predictions over other regions (Lu *et al.*, 2017; Oueslati *et al.*, 2017). A novel typology may offer an ample framework to better understand and quantify the behavior of rainfall extremes (cf. chapter 2).
- an assessment of *large- and small-scale extremes in the context of ISDs in order to provide better understanding of their intrinsic characteristics.* Such a contribution may have a considerable importance for stakeholders in the environmental, agricultural, energy, water and economic sectors (cf. chapter 2).
- an investigation concerning *the relationship of large- and small-scale extremes with the leading modes of variability or atmospheric patterns that shape regional-scale climate at a wide range of timescales ranging from synoptic and intraseasonal on the one*

hand, to interannual and decadal on the other hand. Such quantifications are required to promote multi-year seamless forecast for the region on one hand and improve sub-seasonal forecasts for the region on the other hand (cf. chapter 3).

- *a framework to identify high-impact events by complementing the typology of extremes by considering their duration which is particularly important to differentiate short- and longest-lived large-scale events.* The latter may be considered as potentially high-impact rainfall events leading to the high environmental or societal impacts, a question of major and ever-increasing importance under climate change (cf. chapter 3).

Concerning meso-scale modelling, three large-scale longest-lived events (potentially high-impact spells) during 2000 to 2015 are selected to further investigate for dynamical downscaling using Weather Research and Forecasting (WRF-ARW) model which is first forced by latest available high-resolution state-of-the-art reanalysis (ERA5) and then by Re-forecast version 2 (RF2 hereinafter) developed by National Oceanic and Atmospheric Administration (NOAA) with lead time up to 9 days. The objective is to investigate:

- if the *dynamical downscaling of ERA5 and RF2 using WRF can improve the properties of such highly intense long-lived events in terms of intensity, rainfall accumulation and location.* These investigations are crucial to provide a better understanding of such events on one hand and to promote operational forecast of such high-impact rainfall events in the region on the other hand (cf. chapter 4).
- *how much accuracy in terms of predictability can be achieved by downscaling coarser resolution global forecasts of RF2 at different lead times.* In this study we attempt to analyze these global forecasts in a novel way and attempt to investigate if the atmospheric model can forecast them a few days in advance, using multi-year ensembles. Dynamical downscaling of global model outputs performed at higher spatial resolutions from cloud-resolving to convection-permitting may have/will have substantial improvements in their regionalization and provide relevant climate information for end users (cf. chapter 4).

This dissertation is organized as follows:

- ⇒ Chapter 1 presents *climate of the region, data and methodology* used for the study.
- ⇒ Chapter 2 specifically dedicated to *mean characteristics of rainfall extremes in South Africa where we provide an assessment of wet and dry ISDs and their summer climatology*.
- ⇒ Chapter 2 is also dedicated to *defining criteria to identify extreme rainfall events and to facilitate their categorization into large- and small-scale extreme events following an assessment of large- and small-scale rainfall extremes in the definition of ISDs*.
- ⇒ Chapter 3 investigates: 1) *the influence of large-scale modes (i.e., ENSO and IPO) of variability on rainfall extremes at their respective timescale i.e., interannual and quasi-decadal respectively*; 2) *variability of rainfall extremes at sub-seasonal (i.e., synoptic-scale and intraseasonal) timescales*.
- ⇒ Chapter 4 is dedicated to *meso-scale modelling where we attempt to downscale three large-scale long-lived rainfall spells to investigate their predictability and provide better understanding of such events*.

Chapter 1

1.1. Climate of the region

South Africa is a country characterised by sharp rainfall gradients while its subtropical location and complex topography produce substantial spatial heterogeneity in the seasonality and quantity of rainfall (Hart *et al.*, 2013). Winter rainfall is primarily associated with mid-latitude cyclones in the south-west region of South Africa. The north-eastern part on the other hand experience convective rainfall during austral summer. The interior of South Africa exhibits a strong east to west gradient where western boundary experience semi-arid conditions and eastern Highveld receive annual rainfall totals around 700 mm (Fig. 1.1b). A sharp escarpment that separates the interior from wetter south and east coast regions is quite distinguishable in Figure 1.1a. The region of north-eastern escarpment experience annual rainfall around 1100 mm as per in-situ observations (Fig. 1.1b).

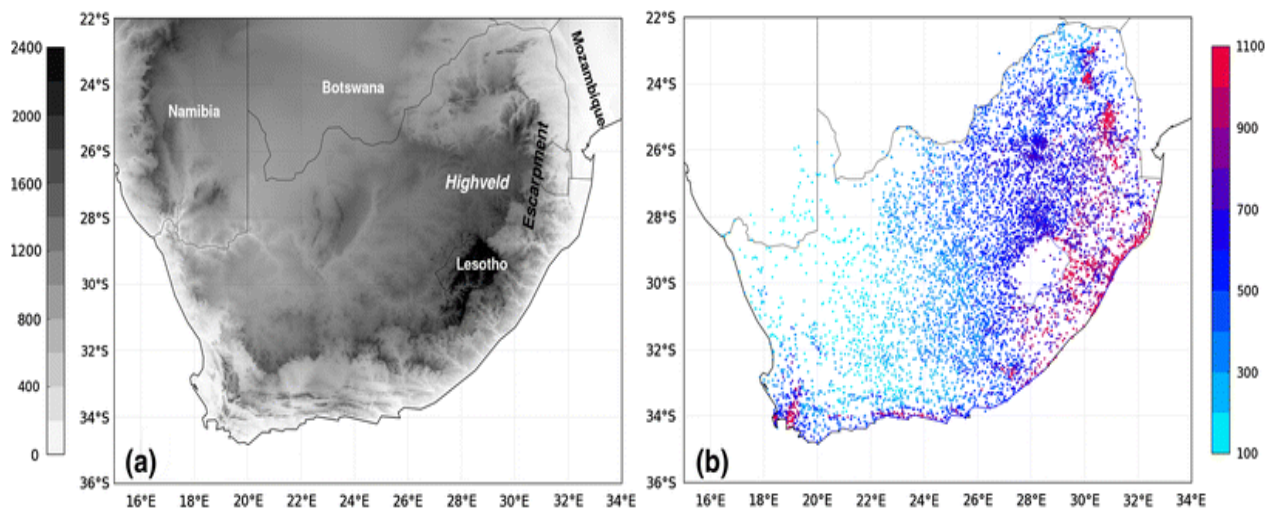


Figure. 1.1. South African topography in meters (a) and mean annual rainfall in millimetre (b) provided by Weather Research Commission (WRC) rainfall dataset (See, for instance, Hart *et al.*, 2013).

1.1.1. Climate of the region during austral summer season

Most of South Africa experience a rainy season in austral summer i.e., November through February (Pohl *et al.*, 2014; Favre *et al.*, 2016). Located at the interface between the tropics and the mid-latitudes of the Southern Hemisphere, while being surrounded by two thermally

contrasted oceans (Rouault *et al.*, 2003), South Africa is subject to both the influence of tropical convection and temperate dynamics (Washington and Todd, 1999; Hart *et al.*, 2010; Vigaud *et al.*, 2012). Together with highly heterogeneous vegetation and topography, these tropical and temperate influences form a mosaic of climates in association with contrasted surface atmospheric characteristics such as rainfall amount and temperature which strongly vary in time and space. Like many semi-arid regions in the subtropics, South Africa depends heavily on the quality of its rainy seasons (Masupha *et al.*, 2016). **Thus, rainfall variability and forecasting at fine spatial and temporal scales are a matter of crucial importance for South African agriculture and economy** (Conway *et al.*, 2015).

1.1.2. Major rain-bearing systems during austral summer season

In South Africa, **during the austral summer, precipitation events are generally associated with moist atmospheric convection, ranging in scale from single-cell storms to organized systems, such as Mesoscale Convective Complexes** (Blamey and Reason, 2013), **squall lines** (Rouault *et al.*, 2002) and tropical storms (Reason and Keibel, 2004; Reason, 2007; Malherbe *et al.*, 2012, 2014; Fitchett and Grab, 2014). **Cut-off lows (COLs) can also lead to extreme rainfall in South Africa, but they are rare during the summer season** (Favre *et al.*, 2013). In austral summer, three key regions (namely southwest Indian Ocean, tropical western Indian Ocean, and tropical southeast Atlantic Ocean) are known to inject moisture flux into the southern African continent (Desbiolles *et al.*, 2018; Rapolaki *et al.*, 2019, 2020). **The dominant rain-bearing systems over the region are synoptic-scale cloud bands, known locally as Tropical Temperate Troughs** (TTTs: Manhique *et al.*, 2011; Hart *et al.*, 2013; Macron *et al.*, 2014; James *et al.*, 2020). **TTTs correspond to synoptic-scale cloud bands that link tropical instability over the subcontinent with an upper-tropospheric frontal system embedded in the mid-latitude westerly circulation** (Washington and Todd, 1999; Todd *et al.*, 2004; Hart *et al.*, 2010) **and bring about 30–60% of summer rainfall over subtropical South Africa** (Hart *et al.*, 2013; Macron *et al.*, 2014). **The remaining 40–70% of the summer rainfall amounts are provided by rain-bearing mechanisms linked to tropical convection, such as regional thermal low-pressure** (Reason *et al.*, 2006) **or the Madden-Julian Oscillation** (MJO: Pohl *et al.*, 2007). The MJO is characterized as an eastward propagation of large-scale convective clusters in the tropics, which recur every 30 to 60 days (Madden and Julian, 1994; Zhang, 2005), and have overarching effects on rainfall patterns across the world (Zhang, 2005; Donald *et al.*,

2006). Rapolaki *et al.*, (2019) and Mpungose *et al.*, (2022) highlighted that, over the Limpopo River Basin, 48% of extreme events are associated with TTTs, 28% with tropical low-pressure systems, 14% with mesoscale convective systems, and 10% with COLs. The influence of blocking caused by ridging anticyclones or the Mascarene High over the southern tip of the continent is also known to influence the rainfall variability over southern Africa as such conditions are known to block the moisture over sub-continent causing extreme rainfall conditions (Xulu *et al.*, 2020; Ndarana *et al.*, 2022).

Figure 1.2 displays the summer rainfall region (SRR), winter rainfall region (WRR), and all-year rainfall region (ARR) respectively. These regions exist as a result of four vital synoptic features: 1) the presence of a semi-permanent high-pressure system inland; 2) baroclinic disturbances in the midlatitudes leading to Rossby waves over the southwestern and southern parts of the region; 3) a barotropic, quasi-stationary subtropical easterly wave of low pressure over the interior linking up with midlatitude westerlies; 4) ridging highs eastward from South Atlantic to the south Indian Oceans (Hart *et al.*, 2010; Quagraine *et al.*, 2019). TTTs have been identified as important driver of rainfall variability over the subcontinent. TTTs are related to moisture convergence supplied by a strong easterly flux from the Indian and westerly flux from the Atlantic Ocean (Todd and Washington, 1999). Reason *et al.*, (2006) and Hart *et al.*, (2010) suggest that the so-called Angola/Botswana low over the southern Angola/northern Namibia developing in summertime over the Kalahari altogether favour the penetration of moisture flux from the tropical south-eastern Atlantic and could thus be another key mechanism for TTT initiation and development.

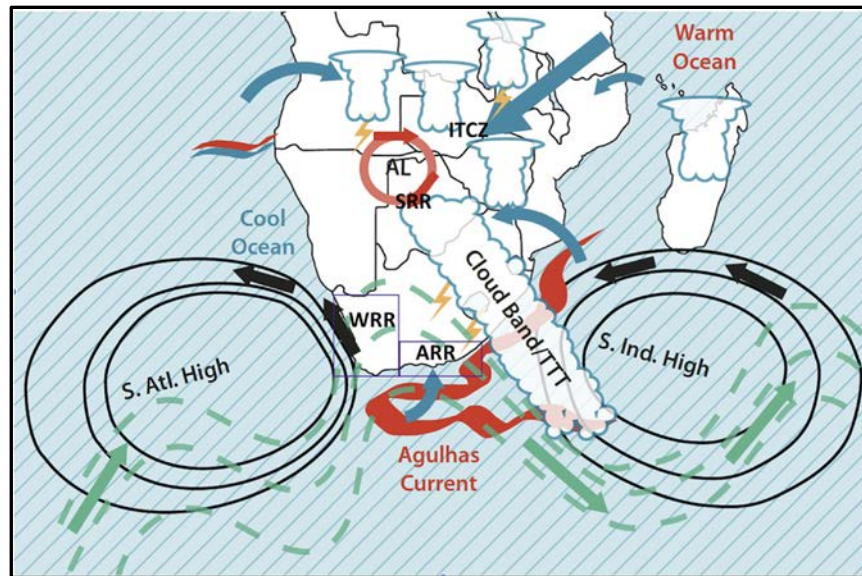


Figure 1.2. A schematic detailing key processes over southern Africa. AL 5 Angola low, ITCZ 5 intertropical convergence zone, and TTT 5 tropical temperate trough. Also shown here are three climatic regions: summer rainfall region (SRR), winter rainfall region (WRR), and all-year rainfall region (ARR) (modified after Hart *et al.*, 2010).

1.1.3. Rainfall variability at low-frequency timescales during austral summer

At lower-frequencies (i.e., below the annual cycle), **austral summer rainfall exhibits three significant timescales of variability over the twentieth century: interannual (IV: 2–8 years), quasi-decadal (QDV: 8–13 years) and interdecadal variations (IDV: 15–28 years: Dieppois *et al.*, 2016, 2019).** Decadal fluctuations in summer southern African rainfall are first proposed by Dyer and Tyson (1977) as the so-called interdecadal Dyer-Tyson cycle (18-20 years). The decadal variability is further explored in various studies. (Mason and Jury, 1997; Reason and Rouault, 2002; Malherbe *et al.*, 2012, 2014). By comparing synoptic maps, Tyson (1981) proposed that the northeastern regions of southern Africa are the core areas of the interdecadal cycle. This study suggests that the changes in the meridional circulations between the Indian Ocean and the South Atlantic Ocean are related to the changes in the subtropical ridge of the zonal wave over the Southern Hemisphere (Tyson, 1981). These findings found consisted of the atmospheric anomalies related to the southern annular mode (SAM) from January to March (Malherbe *et al.*, 2014, 2016). **Previous studies suggest that, at the interannual timescale, rainfall variability is strongly modulated by El Niño Southern Oscillation (ENSO: Nicholson and Kim, 1997; Reason *et al.*, 2000; Washington and Preston, 2006; Dieppois *et al.*, 2016; Pohl *et al.*, 2018).** Typically, El Niño conditions tend to favour dry summers while La

Nina tends to be associated with above normal rainfall in South Africa (Van Heerden *et al.*, 1988; Reason and Rouault, 2002; Blamey *et al.*, 2018). However, the relationship between ENSO and rainfall is not systematic, since not every El Niño event leads to dry conditions over the region (Rouault and Richard, 2004; Reason and Jagadheesha, 2005). This could be due to interferences with the Angola Low (Reason and Jagadheesha, 2005; Lyon and Mason, 2007; Pascale *et al.*, 2019) and/or the Subtropical Indian Ocean Dipole (SIOD: Hoell and Cheng, 2018). The SIOD is characterized as the oscillation of sea surface temperatures in Indian Ocean where its positive phase is characterized by warmer-than-normal SSTs in the southwestern part, south of Madagascar, and colder-than-normal SSTs off Australia, causing above-than-normal precipitation in many regions over south and central Africa (Hoell and Cheng, 2018). The southern annular mode (SAM) is the leading mode of atmospheric variability south of 20°S which basically consists of an atmospheric mass transfer from the Antarctic region to the southern midlatitudes, with these two regions experiencing out-of-phase surface pressure and geopotential height anomalies (Pohl and Fauchereau, 2012). A recent study also suggested that recent changes in the number of dry spells and wet days in Southern Africa could be related to ENSO, SAM, SIOD and the Botswana High (Thoithi *et al.*, 2020). During La Niña a low-pressure develop over southern Africa, which is related to anomalous upward motion and enhanced moisture fluxes into and over the region, thereby resulting in rainfall surplus. By contrast, El Niño is linked to high-pressure over southern Africa, which is associated with anomalous downward motion and reduced moisture fluxes into and over the region. This result in rainfall deficit during austral summer season (Ratnam *et al.*, 2014; Hoell *et al.*, 2015). **At the quasi-decadal and interdecadal timescales, rainfall variability mostly relates to the Interdecadal Pacific Oscillation (IPO) and Pacific Decadal Oscillation (PDO), respectively, previously shown to influence regional circulation patterns (Dieppois *et al.*, 2016, 2019), however, *how such low-frequency modes of climate variability affect the likelihood and the intensity of extreme rainfall events is yet to investigate.*** IPO and PDO exhibit ENSO-like sea surface temperature (SST) patterns, shifting the Walker-circulation zonally, and resulting in an eastward shift of South Indian Convergence Zone (SICZ), thus modifying the preferential location for TTTs (Pohl *et al.*, 2018).

1.1.4. Rainfall variability at sub-seasonal timescales during austral summer

At the sub-seasonal timescales, austral summer rainfall is strongly associated with synoptic-scale convective cloud bands conventionally termed as TTTs (Todd and Washington, 1999; Washington and Todd, 1999; Todd *et al.*, 2004; Pohl *et al.*, 2009; Hart *et al.*, 2010; Vigaud *et al.*, 2012; Macron *et al.*, 2014). **TTTs are responsible for 30%–60% of summer rainfall in southern Africa** (Reason *et al.*, 2006; Hart *et al.*, 2013; Macron *et al.*, 2014). TTTs are oriented from northwest to southeast and are the results of interactions between transient perturbations in the midlatitudes and tropical convection (Hart *et al.*, 2010; Macron *et al.*, 2014; James *et al.*, 2020), thereby linking the tropics to the temperate latitudes. Other notable rain-bearing systems of summer rainfall are Mesoscale Convective Complexes (MCCs: Blamey and Reason, 2013) squall lines (Rouault *et al.*, 2002), tropical storms (Reason and Keibel, 2004; Malherbe *et al.*, 2012, 2014; Fitchett and Grab, 2014) and Cut-off lows (Favre *et al.*, 2013). **At the slightly longer timescale of intraseasonal variability, the Madden-Julien Oscillation (MJO) is characterized as an eastward propagation of large-scale convective clusters along the equator which recur every 30 to 60 days** (Madden and Julian, 1994; Zhang, 2005). MJO appears to have overarching effects on rainfall patterns across the world (Zhang, 2005; Donald *et al.*, 2006). For South Africa some MJO phases favour increased moisture convergence, thus acting to enhance the regional convective activity (Pohl *et al.*, 2007; Oettli *et al.*, 2014). Hart *et al.*, (2013) **suggested a weak but significant decrease of TTT intensity during MJO phase 1 and an enhancement during MJO phase 6. However, no discernible relation could be found between the MJO and the likelihood, or occurrence, of TTTs** (Pohl *et al.*, 2009). *Yet, how the association of different MJO phases and TTTs modulate the frequency and intensity of extreme events, remains poorly understood.*

1.1.5. Intraseasonal characteristics of austral summer season

Intraseasonal descriptors (hereafter ISDs) are defined as wet and dry sequences of days during the rainy season (Ratan and Venugopal, 2013; Gitau *et al.*, 2015, 2018). **Examining ISDs provides information related to various intrinsic characteristics of a rainy season, such as the average number of wet and dry days, persistence of spells, intensity of wet spells and total rainfall.** Similar studies focused on other regions, such as equatorial East Africa (Camberlin *et al.*, 2009; Moron *et al.*, 2013; Gitau *et al.*, 2015, 2018; Philippon *et al.*, 2015), have already demonstrated their relevance and usefulness in climate diagnostics and prediction.

However, analyses devoted to ISDs remain quite rare in South Africa. Tennant and Hewitson (2002) found that anomalously wet rainy seasons tend to experience a larger number of heavy rainy days ($>20 \text{ mm.day}^{-1}$). Cook *et al.*, (2004) highlighted that moisture anomalies between wet and dry spells were strongly related to the Kalahari low. They also stated that wet years were characterized by longer and more intense wet spells, rather than by a greater number of wet spells (Cook *et al.*, 2004). Similarly, previous studies found a strong relationship between dry spells and El Niño Southern Oscillation (ENSO), suggesting potential predictability of ISDs using this relationship (Usman and Reason, 2004; Reason and Jagadheesha, 2005). Physically, El Niño conditions could act to shift TTTs eastwards over the Mozambique Channel (Nicholson and Kim, 1997; Cook, 2000, 2001; Misra, 2003; Nicholson, 2003; Dieppois *et al.*, 2015), thereby enhancing the number of dry spells over the continent. The relationship between TTTs and ENSO has been confirmed and further documented by (Fauchereau *et al.*, 2009; Pohl *et al.*, 2018). Thoithi *et al.*, (2020) investigated the wet and dry spells and suggested sharp gradients in dry spell frequency across southern Africa while the frequency of wet days significantly increased in several agricultural areas in southern Africa.

In this study we attempt to provide a profound knowledge of ISDs in a novel way by 1) assessing them at regional scale; 2) characterizing extremes and their further assessment in the context of ISDs; 3) variability of these ISDs at low-frequency and sub-seasonal timescale; 4) their meso-scale modelling.

1.2. Datasets to investigate summer climatology and statistical characteristics

1.2.1. In-situ observations

Observed daily rainfall data (OBS) from the Water Research Commission of South Africa (<http://www.wrc.org.za>; Fig. 1a) is used for 225 stations spanning 50 years (1965–2015). These 225 stations are selected based on two conditions: 1) stations with less than 1% of missing values; 2) seasonality test: i.e., stations for which 50% or more of the annual rainfall occurs during the austral summer season, in order to focus on the austral summer rainfall regions of South Africa (Crétat *et al.*, 2012a).

1.2.2. Re-analysis products

ERA5 reanalysis from Copernicus Climate Change Service (Hersbach *et al.*, 2020a) is the 5th generation reanalysis available from the European Centre for Medium-Range Weather Forecasts

(ECMWF). Here we use the daily rainfall field for the 1979–2015 period, taken from the deterministic member at $0.25^\circ \times 0.25^\circ$ global resolution (Fig. 1b). ERA5 has now been extended to 1950–1978 but the lack of assimilation of satellite data before 1979 raises the question of the homogeneity of the dataset, the detailed evaluation of which is mandatory before using it. However, it is not the scope of the present study, hence our choice to consider a common period of 36-years (1979–2015). For comparison purposes with the rain-gauge observational network, all grid-points (AGP) and those nearest to OBS (NN) are used in this study. The comparison of NN and AGP fields of ERA5 is particularly important to examine whether the network is dense enough to study rainfall extremes. The NN and AGP fields of ERA5 have here been named ERA5–NN and ERA5–AGP, respectively.

1.3. Datasets to investigate variability of extremes at low-frequency and sub-seasonal timescales

1.3.1. Intraseasonal descriptors

To investigate the variability of extremes during NDJF at low-frequency timescales, the time series of two extreme ISDs, i.e., wet days (WD_{EXT}) and total rainfall (TR_{EXT}) associated with large- and small-scale extremes are obtained from Chapter 2. WD_{EXT} (TR_{EXT}) is defined as the average number of wet days (total rainfall amount) associated with large- and small-scale extreme events in a season. These descriptors are computed using daily rainfall fields from the observational network of 225 stations (OBS) and deterministic members of ERA5 at a $0.25^\circ \times 0.25^\circ$ global resolution over the period of 1975–2015. The choice of two extreme ISDs i.e., wet days and total rainfall is made because of the strong dependence of total rainfall in NDJF on the number of wet days associated with large-scale extremes, suggesting their key role in shaping total rainfall variability.

1.3.2. Summer Rainfall Index (SRI)

To account for the timescale dependence of teleconnections, we use the Summer Rainfall Index (SRI), as introduced by Dieppois *et al.*, (2016) using the Climatic Research Unit (CRU TS 3.23) and the Global Precipitation Climatology Centre reanalysis version 7.0 (GPCC.v7). SRI is here decomposed into two significant timescales of variability using a fast Fourier transform: 2–8 years interannual variability (IV) and 8–13 years quasi-decadal variability (QDV). The filtered

SRI is linked to distinct modes of Pacific variability, namely, the ENSO for IV and Interdecadal Pacific Oscillation (IPO) for QDV.

1.3.3. Sea surface temperature

To examine the teleconnections between rainfall extremes and large-scale modes of climate variability, we use the latest version of the monthly SST field from the Extended Reconstructed Sea Surface Temperature (ERSST.v5) of the National Climatic Data Centre (NCDC). This ERSST.v5 gridded data set is generated using in-situ data from the International Comprehensive Ocean-Atmosphere Data Set (ICOADS) release 3.0. In this release several improvements are made, notably in quality control, bias adjustment, and interpolation techniques, allowing for an optimal reconstruction of sparse data over a $2^\circ \times 2^\circ$ resolution grid (Huang *et al.*, 2017).

1.3.4. Niño 3.4 index

Niño 3.4 index is calculated over the region of east-central equatorial Pacific between 5°N – 5°S , 170°W – 120°W , to monitor the state of ENSO and compute partial correlations of global SSTs, after linearly removing ENSO influence.

1.3.5. Satellite based estimates for rainfall

In addition to in-situ observations and ERA5 reanalysis, we also use Tropical Rainfall Measuring Mission (TRMM v.7) 3B42 product (Huffman *et al.*, 2007) as satellite-based estimation of extreme rainfall events specifically used in chapter 3. TRMM precipitation product covers an area from 50°S – 50°N and 180°W – 180°E , with a spatial resolution of $0.25^\circ \times 0.25^\circ$, from 1998 to the present on a 3-hourly basis. The daily accumulated precipitation (combined microwave and infrared) is used here from 1998 to 2015. This dataset allows for a gridded estimation of rainfall, and corresponding extreme spells, thereby forming a useful complement to rain-gauges and reanalysis.

1.3.6. Reanalysis data for validating physical mechanisms

Other variables from ERA5 also used to assess the physical processes concerning statistical quantifications of extremes include vertically integrated moisture divergence (VIMD) and low-tropospheric moisture fluxes which are derived from specific humidity, u-wind and v-wind at 850 hPa. Daily Outgoing Longwave Radiation (OLR) fields are also obtained from the ERA5 ensemble to redefine the recurrent synoptic-scale convective regimes, following the methodology of (Fauchereau *et al.*, 2009).

1.3.7. Real-time Multivariate MJO (RMM) index

The MJO signal extracted using two daily indices of the Real-time Multivariate MJO (RMM) index (Wheeler and Hendon, 2004), which uses 850 hPa and 200 hPa zonal winds from NCEP/NCAR reanalysis (Kalnay *et al.*, 1996) in addition to OLR daily fields.

1.4. Datasets for meso-scale modelling

1.4.1. Weather Research and Forecasting Model (WRF-ARW)

The Weather Research and Forecasting (WRF) model is one of a state-of-the-art mesoscale Numerical Weather Prediction (NWP) system designed for both atmospheric research and widely used for operational forecasting applications. For the downscaling of potentially high-impact rainfall events (i.e., large-scale and longest-lived events), we use state-of-the-art Weather Research and Forecasting model (WRF version 4.2.1; Skamarock *et al.*, 2021). WRF features two dynamical cores, a data assimilation system, and a software architecture supporting parallel computation and system extensibility (Skamarock *et al.*, 2021).

1.4.2. Forcing datasets for WRF Model

The ERA5 reanalysis data are widely analysed in climate science to assess changes in observation systems, to scale progress in model simulations and for forecast error evaluation (Hersbach *et al.*, 2020b). ERA5 reanalysis is the 5th generation dataset available from the European Centre for Medium-Range Weather Forecasts (ECMWF) providing $0.25^\circ \times 0.25^\circ$ global resolution of hourly gridded outputs of surface and atmospheric fields at the global scale, spanning 1979 to the present.

Reforecast version 2 (RF2) developed by National Oceanic and Atmospheric Administration/Physical Science Laboratory (NOAA/PSL: Hamill *et al.*, 2022) is also used to drive WRF simulations. The spatial resolution of the RF2 is 0.25° with 64 vertical hybrid levels and is provided every 3 hours for the first 10 days of the forecast; beyond 10 days 0.50° grid spacing is used with a temporal resolution of every 6 hours. The RF2 grid proceeds from 90°N to 90°S and from 0°E to 359.75°E . The skilful forecast lead time of midlatitude instantaneous weather is around 10 days, which serves as the practical predictability limit (Zhang *et al.*, 2019). Considering this, here we use the first 10 days of reforecast using five members of RF2 which includes a control run and four ensemble members where the small number of noises were added to the initial condition. The RF2 is one of several prediction systems maintained by the United

States' National Weather Service (NWS) and supports medium-range weather and sub-seasonal to seasonal forecasting. The role of reforecasts has been widely recognized in validating and calibrating climate models and weather forecasts (Hamill *et al.*, 2004, 2006, 2013, 2015, 2022) diagnosing model errors (Gascón *et al.*, 2019) and predicting rare extreme events (Li *et al.*, 2019). On 23 September 2020, the finite volume-based RF2 was implemented at the NOAA (Hamill *et al.*, 2022). In the newly implemented RF2, the integration time was extended from week 1 for weather forecasts, week 2 for extended forecasts and weeks 3–5 for sub-seasonal forecasts (Guan *et al.*, 2022). RF2 provides forecasts from 1989 through 2019 in which the Climate Forecast System (CFS) reanalysis served as initial conditions for the first phase (1989–1999) of reforecasts while Global Ensemble Forecast System Version 12 (GEFSv12) reanalysis was used for the second phase (cf. chapter 4: Guan *et al.*, 2022).

1.5. Methodology to examining summer climatology and statistical characteristics

1.5.1. Seasonality test

To focus on the summer rainfall regions, a seasonality test is then applied on OBS and ERA5 (Crétat *et al.*, 2012a). Using the seasonality test, only the stations and grid-points for which at least 50% of annual rainfall occurred during an extended austral summer (October to March) are retained. The spatial distribution of the percentage of summer rainfall in OBS and ERA5 is presented in Figure 1.3a-b.

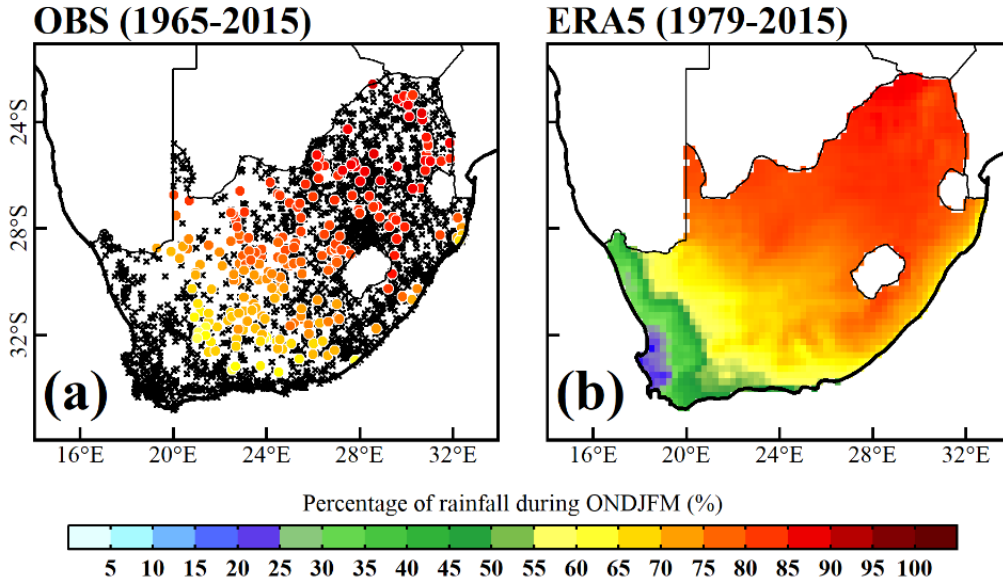


Figure 1.3. Spatial distribution of the percentage of rainfall during ONDJFM for OBS (a) for ERA5 (b). The unqualified stations are indicated by black “×” symbols based on the seasonality test and other quality control measures

To define new metrics accounting for the typology of rainfall extremes, we focused on the austral summer season (October–March), and we analysed two distinct baseline periods (1965–2015) for OBS and (1979–2015) for ERA5. By considering extended austral summer seasons and the two distinct baseline periods for the computation of 90th percentile values, we gained two advantages: 1) **a longer period for OBS ensures statistical robustness of low-frequency decadal variability**; 2) **longer seasons also include rainfall onset (October) and cessation (March) months (discussed later in chapter 3)**. For all remaining objectives, we **restricted the study to the period dating 1979–2015 and to the core of the rainy season (November–February)**.

1.5.2. Definition of intraseasonal descriptors at the regional scale

A threshold of $1.0 \text{ mm}\cdot\text{day}^{-1}$ is used to delineate wet from dry days (Gitau *et al.*, 2013, 2015). A unified definition for wet and dry spells is obtained as suggested in several previous studies (Ratan and Venugopal, 2013; Gitau *et al.*, 2015, 2018). A wet (dry) spell is defined as a duration of “*i*” wet (dry) days preceded and followed by a dry (wet) day. As summarized in Table 1.1a-b, various ISDs, which are associated with wet and dry spells, are computed for each station and

grid-point using OBS and ERA5. Multi-year variability of each ISD is then assessed using seasonal average computed at the regional scale (cf. chapter 2).

Table 1.1. The description of the wet ISDs (a) and dry ISDs (b).

a) Wet ISDs				
ISD Name	Acronym	Description	Unit	Scale
Wet Days	WD	Average number of wet days in a season	Days	Seasonal
Wet Days >90th Percentile	WD _{P90}	Average number of days exceeding the 90th percentile threshold	Days	Seasonal
Wet Spells	WS	Average number of wet spells in a season	Spells	Seasonal
Wet Spell Persistence	WSP	Average persistence of wet spells in a season	Days	Seasonal
Wet Spell Intensity	WSI	Average intensity of wet spells in a season	mm.day ⁻¹	Seasonal + Daily
Spatial Fraction	SF	Average spatial fraction associated with total rainfall amount in a season	Percent (%)	Seasonal + Daily
Total Rainfall	TR	Total rainfall amount in a season	mm.season ⁻¹	Seasonal + Daily
b) Dry ISDs				
Dry Spells	DS	Average number of dry spells in a season	Spells	Seasonal
Dry Days	DD	Average number of dry days in a season	Days	Seasonal
Dry Spell Persistence	DSP	Average persistence of dry spells	Days	Seasonal

Columns 1–5 represent the ISD name, acronym, description, unit and scale respectively.

To quantify and compare temporal variability of ISDs, commonly used statistical metrics are applied to each ISD: mean (μ), standard deviation (SD), root mean square error (RMSE) and coefficient of variation (CV: Asmat and Athar, 2017; Asmat *et al.*, 2018). The Mann Kendall (MK) non-parametric test is used to perform the trend analysis (Mann, 1945; Kendall, 1957). Pearson’s correlations are computed to quantify the dependence of total rainfall on ISDs.

1.5.3. Local threshold for rainfall extremes

We first compute the 90th percentile of daily rainfall amount of each station and grid-point, which are retrieved from the aforementioned seasonality test, over the two climatological baseline periods as described in Section 1.5.1. The 90th percentile values are calculated by removing all values below 1.0 mm.day⁻¹ for more robust identification of extreme rainfall events considering the semi-arid nature of the region like southern Africa where rainfall is rare in some places. The comparisons of the spatial distributions of the 90th percentile, as calculated before and after removing non-rainy and drizzle days (i.e., days with less than 1.0 mm), are presented in Figure 1.4a-b and Figure 1.4c-d respectively. This choice made the evaluation less sensitive to

measurement accuracy and to the tendency of some numerical models to produce an excessive number of drizzle events (Frei *et al.*, 2003; Gitau *et al.*, 2015; Maraun, 2016). A similar sensitivity to drizzle days is found to be more pronounced in ERA5; thus, not removing drizzle days would have led to underestimating the 90th percentiles.

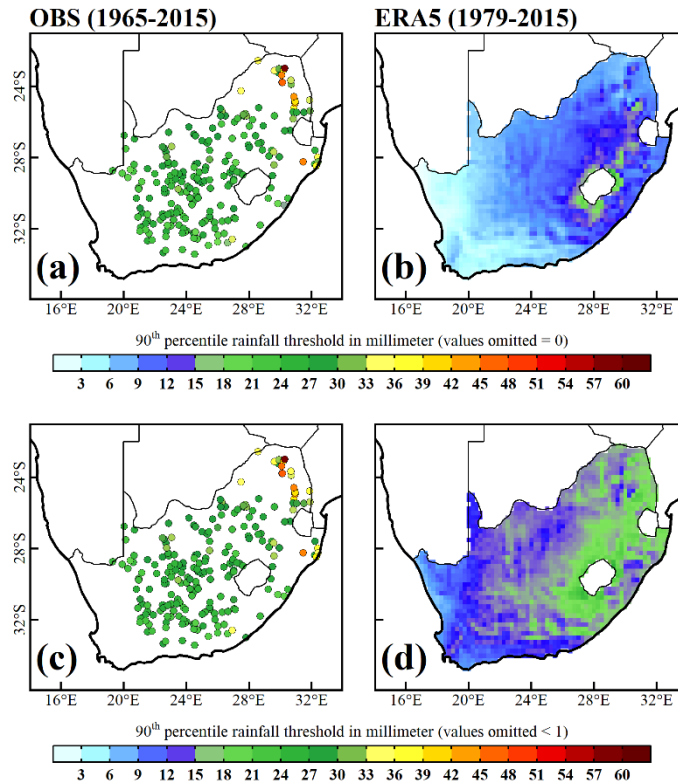


Figure 1.4. The 90th percentile threshold of rainfall computed after omitting the values = 0 for OBS (a) and for ERA5 (b). The 90th percentile threshold of rainfall after omitting the values <1 for OBS (c) and for ERA5 (d).

The local rainfall threshold is obtained as the 90th percentile for each station or grid-point. It is computed based on a normal distribution, and we note that it does not significantly differ from Gumbel and Gamma distribution (Fig. 1.5), thereby suggesting statistical robustness in the definition of the local rainfall thresholds.

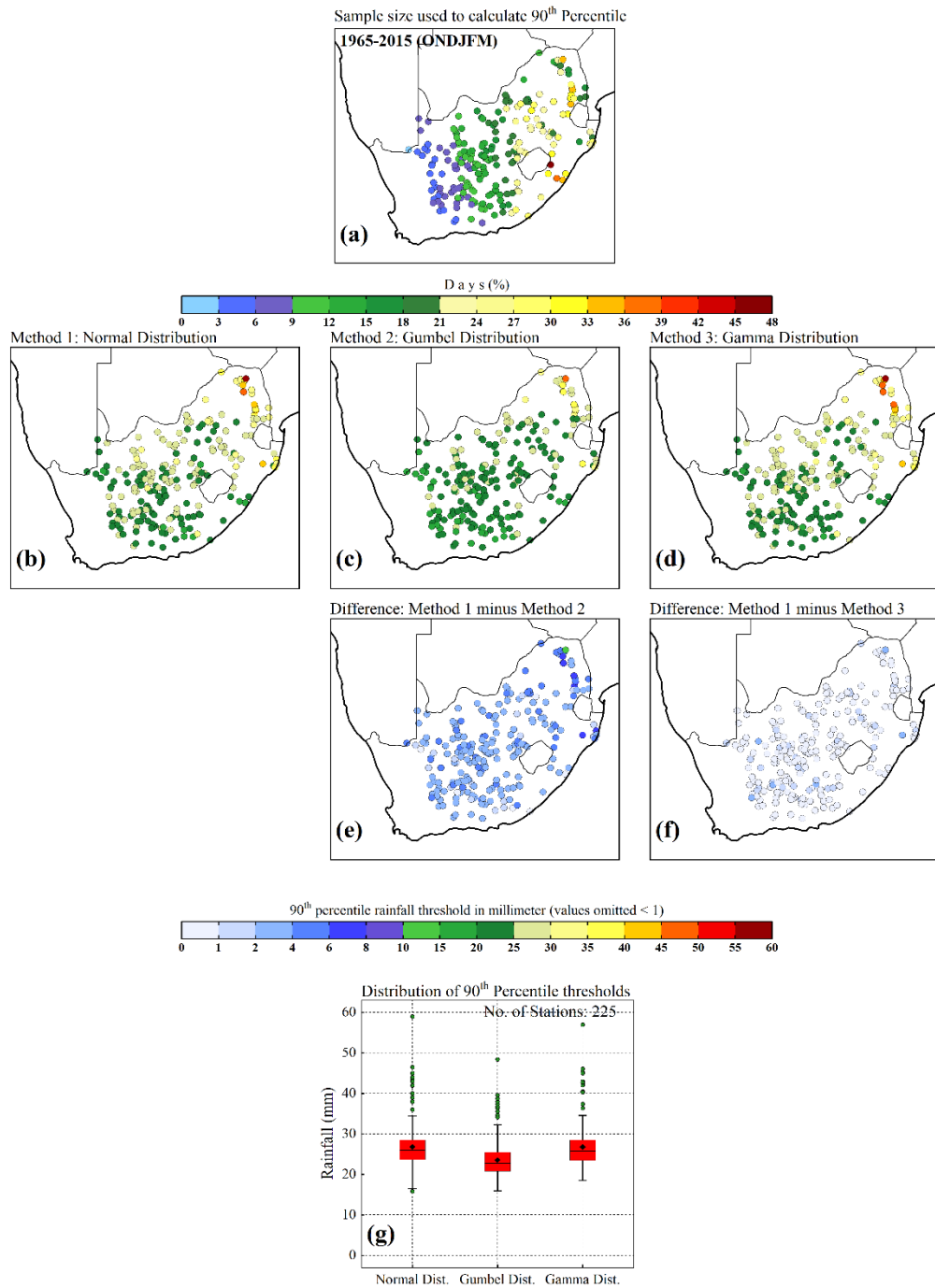


Figure 1.5. Sample size used to compute 90th percentile threshold (a), while 90th percentile threshold computed by considering Normal distribution (b), theoretical extreme value computed by Gumbel and Gamma distribution (c-d) and the difference of both methods with normal distribution (e-f). The overall distribution of 90th percentile thresholds using Normal, Gumbel and Gamma distribution is presented using Box and Whisker plots (g). The lower and upper end of red box show the lower and upper quartile respectively while the black line indicates the median of the distribution. The whiskers at the bottom and top indicate the lower and upper

extreme of the distribution. The black ◆” and green symbols “●” indicate mean and outliers of the distribution respectively.

1.5.4. Regional threshold for rainfall extremes

A novel typology of rainfall extremes based on the spatial fraction of rainfall events is then proposed. *“The spatial fraction of an extreme event is defined as the number of stations or grid-points that simultaneously reach their local 90th percentile threshold regardless of their location on the day of the event”*. A similar methodology has been successfully used for the identification of heat waves in West Africa (Oueslati *et al.*, 2017). The principal reason for using the spatial fraction as a base criterion is to differentiate localized, or small-scale extreme events from large-scale extreme events. On one hand, small-scale extreme events are related to isolated convective cells and therefore stochastic in nature, rendering them highly unpredictable. On the other hand, large-scale extreme events are embedded in large-scale modes of climate variability, hence potentially more predictable. **The spatial fraction of extreme events depends on the size of the rainfall event, but also on the density and anisotropy of the network, which is likely to cause some issues in the estimation of the spatial extension of the events because the stations are not uniformly distributed in space (cf. section 1.4.6). In reference to this assumption, the spatial fraction of events is here quantified using both the ERA5–NN and ERA5–AGP fields. The comparison between ERA5–NN and ERA5–AGP fields makes it possible to assess whether or not the network is dense enough to study rainfall extremes.** The density might not be sufficient if ERA5–NN exhibits substantially different properties than in ERA5–AGP. Thus, a caution is required to interpret the results related to large- and small-scale extremes as: 1) **the extremes are not characterized here based on environmental consequences but from an atmospheric point of view considering the characteristics of rainfall field itself;** 2) **considering the use of administrative boundaries, limitation in observation along with using NN and AGP fields of ERA5 yet there is a likelihood that some events that may have major environmental consequences, are not necessarily captured;** 3) **resolution of reanalysis is particularly important to capture small-scale extreme events.** Thus, a brief assessment is then conducted in order to define a robust and relevant threshold of spatial fraction to differentiate large- vs small-scale extremes (cf. chapter 2).

1.5.6. Spatial characteristics of rainfall extremes

Based on the defined threshold of spatial fraction, we first separate all days associated with large- and small-scale extreme events. *The average characteristics of both types of extremes are then assessed in terms of frequency and intensity for each station and grid point.* The frequency and intensity are computed based on two criteria: 1) average number of days exceeding the 1.0 mm threshold during large- and small-scale extreme events; 2) average number of days exceeding the 90th percentile threshold during large- and small-scale extreme events (cf. chapter 2).

1.5.7. Spatial coherence of rainfall extremes

An analysis addressing the spatial coherence of large- and small-scale extremes is also provided first time for the region. Here, we analyse the density of stations recording rainfall on the days of large- and small-scale extremes based on the same method used to address the spatial characteristics of extreme events i.e., 1) considering all stations recording rainfall >1.0 mm on the day of the event; 2) considering only those stations which exceeded their 90th percentile on the day of the event. The density of the stations is assessed using a narrow bin size of 0.5° , corresponding to the stations that are located within approximately 55 kilometres over latitudes and 43 kilometres over longitudes (cf. chapter 2).

1.5.8. Definition of intraseasonal descriptors associated with rainfall extremes

Large- and small-scale extreme rainy days are first obtained from the typology of rainfall extremes. Both types of events are then explicitly considered in the context of ISDs. *By placing these events in the framework of ISDs, we are able to further explore the climatology and intrinsic properties of such events on an interannual timescale.* Thus, several ISDs associated with large- and small-scale rainfall extremes are assessed using OBS and ERA5. A brief description of extreme ISDs is presented in Table 1.2. To quantify and compare temporal variability and trends, the same statistical metrics as introduced in section 1.5.2 are used (cf. chapter 2).

Table 1.2. The description of wet extreme ISDs.

Extreme ISDs				
ISD Name	Acronym	Description	Unit	Scale
Wet Days	WD _{EXT}	Average number of wet days associated with large- and small-scale extreme events in a season	Days	Seasonal
Wet Spells	WS _{EXT}	Average number of wet spells associated with large- and small-scale extreme events in a season	Spells	Seasonal
Wet Spell Persistence	WSP _{EXT}	Average persistence of wet spells associated with large- and small-scale extreme events in a season	Days	Seasonal
Wet Spell Intensity	WSI _{EXT}	Average intensity of wet spells associated with large- and small-scale extreme events in a season	mm.day ⁻¹	Seasonal + Daily
Spatial Fraction	SF _{EXT}	Average spatial fraction associated with total rainfall amount driven by large- and small-scale extreme events in a season	Percent (%)	Seasonal + Daily
Total Rainfall	TR _{EXT}	Total rainfall amount associated with large- and small-scale extreme events in a season	mm.season ⁻¹	Seasonal + Daily

Columns 1–5 represent the ISD name, acronym, description, unit and scale respectively.

1.6. Methodology to examine the relationship between rainfall extremes and low-frequency timescales of variability

1.6.1. Relationship of extremes with global SSTs

We first compute Pearson's correlation between global SST anomalies and the number of wet days and total rainfall associated with large- and small-scale extremes. The analysis is then followed by an assessment of the timescale dependence of the teleconnections at the interannual and quasi-decadal timescales (cf. chapter 3).

1.6.2. Quantification of risk of occurrence of extremes at low-frequency timescales

The behaviour of rainfall extremes during different phases of IV and QDV is quantified using the Risk Ratio (RR) metric, commonly used in climate attribution studies (Paciorek *et al.*, 2018). RR is defined as the ratio of the probability of an ISD under a factual scenario (P_F), to that probability under a counterfactual scenario (P_{CF}). Here, P_F (P_{CF}) corresponds to a period when a specific timescale of variability (i.e., SRI at IV or QDV timescale) is in the positive (negative) phase of the anomaly, and is given by:

$$RR = \frac{P_F}{P_{CF}} = \frac{\left[\frac{a}{(a+b)} \right]_{IV|QDV}}{\left[\frac{x}{(x+y)} \right]_{IV|QDV}} \quad \text{Eq.1}$$

where a (b) is the sum of a given ISD (i.e., number of wet days) when it lies in its positive (negative) phase of anomaly, when IV or QDV is in the positive phase, representing P_F scenario. Similarly, x (y) is the sum of a given ISD (i.e., number of wet days) when it lies in its positive (negative) phase of anomaly, when the IV or QDV is in the negative phase, representing P_{CF} scenario. In addition, we also consider two thresholds of SRI at IV and QDV timescales to better quantify the behaviour of extreme ISDs: 1) the RR of extreme events in the weaker positive phase of SRI (P_F : IV or QDV > 0 and $< +0.5$ SD), as calculated with respect to the weaker negative phase of SRI (P_{CF} : IV or QDV > -0.5 SD and < 0); 2) the risk of occurrence of extreme events in the strong positive phase of SRI (P_F : IV or QDV $> +0.5$ SD), calculated with respect to the strong negative phase of SRI (P_{CF} : IV or QDV < -0.5 SD). Physical mechanisms responsible for these changes in the RR metrics are assessed through composite anomalies of vertically

integrated moisture divergence (VIMD) and moisture fluxes in each P_F and P_{CF} scenarios (cf. chapter 3).

1.7. Examining the relationship between extremes and sub-seasonal timescales of climate variability

1.7.1. Seasonality and network-density tests

TRMM dataset is first submitted to the seasonality test following the methodology defined in section 1.5.1. Hence, only the grid-points or stations for which 50% or more of the annual rainfall occurs during austral summer season are retained (cf. chapter 3).

1.7.2. Defining three types of rainfall extremes based on duration and spatial extent

To investigate the variability of extremes at sub-seasonal timescales, we focus on the day-to-day variability of large- and small-scale extremes in NDJF. To that end, we first identify the days associated with large- and small-scale extremes using the daily values of spatial fraction (i.e., number of stations or grid-points exceeds simultaneously to the local 90th percentile) and complement this typology by introducing information related to the duration of the extreme rainy events. This allows us to differentiate between long-lived and short-lived large-scale extreme events.

Including duration in the definition of extreme events is important since synoptic and intraseasonal ranges of variability play a major role in shaping the persistence of extreme events. On the one hand, the average spatial fraction (cf. chapter 2) defines the spatial scale of the event and acts as a key to separate large-scale and small-scale extreme rainfall spells. On the other hand, their persistence acts as a parameter to distinguish between long-lived and short-lived events. Such characterization of rainfall extremes is not only novel for the region, but also essential to better understand the behaviour of rainfall extremes and their impacts, first in observations over recent years, and then under changing climate.

Large-scale long-lived events form a category of rainfall extremes that may potentially lead to high environmental or societal impacts. To date, the literature offers no clear statistical definition of such spells for the region. Chapter 2 depicts an average persistence of large-scale extreme events of 2 ± 1 days in observations. Based on the actual largest persistence values found over the study period and considering twice higher standard deviation, we retained a minimum threshold of at least 5 days as the best compromise to identify large-scale long-lived events. The

definition of large-scale long-lived events should be used with caution since: 1) such spells are not defined based on their consequences on the environment or societies, but from an atmospheric point of view, considering the characteristics of the rainfall field itself; 2) we hypothesize that an event with larger spatial extension and strong persistence, therefore bringing huge amounts of water, is more likely to have major consequences for the regional water budget than other types of rainfall events.

Large-scale short-lived events are the counterpart of the previous type, but with persistence of fewer than 5 days. Collectively, large-scale extreme rainfall events, regrouping short-lived and long-lived types, are important for the regional water balance since such events contribute to more than half of the total rainfall in the austral summer (cf. chapter 2). The remaining type of rainfall extremes corresponds to small-scale events, whose contribution to the total rainfall budget is much weaker (cf. chapter 2). The persistence of these localized extremes may not provide a meaningful metric because they are more rarely embedded in large-scale circulation patterns likely to last more than a few hours/days. Thus, we consider small-scale extremes as a single category.

Overall, the different types considered in this work may be summarized as follows:

Large-scale Long-lived events

Spatial fraction $\geq 7\%$ and Persistence ≥ 5 days

Large-scale Short-lived events

Spatial fraction $\geq 7\%$ and Persistence < 5 days

Small-scale events

Spatial fraction $< 7\%$

1.7.3. Characterizing the relationship between rainfall extremes and synoptic-scale variability

We first recalculate and update the work of Fauchereau *et al.* (2009) by applying the *k*-means algorithm on the latest available daily OLR fields from 10 ensemble members of ERA5 reanalysis between 1979 and 2015. OLR regimes are used as archetypes of the synoptic-scale convective variability over the region in NDJF. Figure 1.6 displays seven robust convective regimes based on ERA5 for NDJF, affecting southern Africa (Fauchereau *et al.*, 2009). Three regimes (#5, #6 and #7) correspond to the typical signatures of TTT systems. Regime #5 refers to

continental TTTs, which bring heavy convective rainfall over South Africa, while regimes #6 and #7 are shifted north-eastwards, thereby bringing rainfall over the Mozambique Channel, Madagascar and the southwest Indian Ocean (Macron *et al.*, 2014, 2016; Pohl *et al.*, 2018). Regimes #3 and #4 are generally associated with enhanced subtropical and extratropical convection, respectively while regimes #1 and #2 refer to the drier conditions over South Africa. OLR anomalies shown here tend to be of larger magnitude than in (Fauchereau *et al.*, 2009), possibly due to a higher time sampling of the diurnal cycle of atmospheric convection in ERA5, and/or a much-increased spatial resolution compared to NOAA's satellite estimates. By applying the methodology of Fauchereau *et al.* (2009) on the OLR fields from 10 ensemble members of ERA5, regime for each day of NDJF season from 1979 to 2015 is identified and then used for the comparative analysis with large- and small-scale extremes in this study (cf. chapter 3).

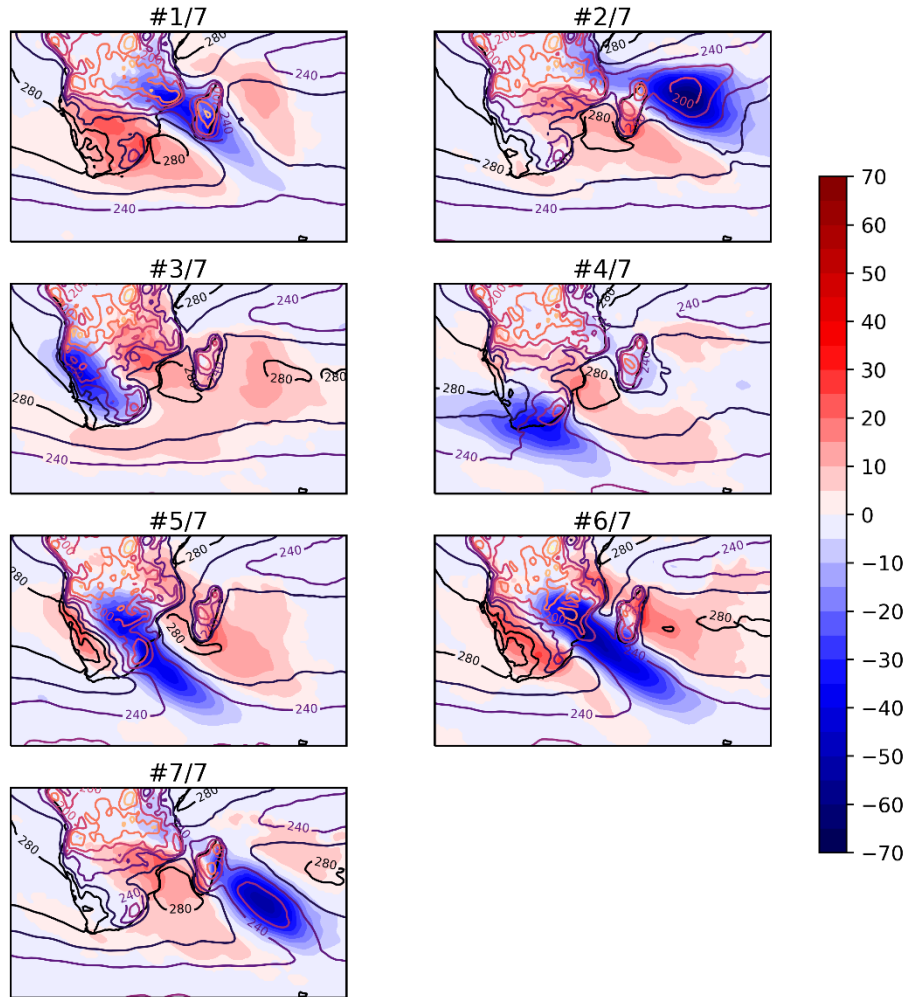


Figure 1.6. Mean daily OLR anomalies illustrating seven convective regimes during the austral summer season (NDJF) over the period 1979–2015. The color bar describes the composite anomalies (interval 5 W.m^{-2}), whereas the mean values are displayed by contours (interval 20 W.m^{-2}).

1.7.4. Characterizing the relationship between rainfall extremes and intraseasonal variability related to MJO

Large-scale atmospheric convective patterns associated with the eight phases of the MJO over southern Africa are first obtained (Fig. 1.7). The strongest wet and dry anomalies over South Africa are found during MJO phases #6–7 and #2–3, respectively, while moderate anomalies occur during other phases thereby corroborating Macron *et al.* (2016) and Grimm (2019). In NDJF, convective clusters associated with the MJO develop at phase #1 over the tropical Indian Ocean. The convective activity strengthens and propagates eastwards (phases #2–4) and reaches

the Maritime continent (phases #4–5), before shifting to the Pacific (#5–6), American, and eventually Atlantic sectors (phases #7–8–1). During these MJO phases, clear-sky conditions tend to prevail over equatorial Africa and the nearby Indian Ocean (Wheeler and Hendon, 2004) but in phase #8 this situation starts changing again (Grimm, 2019). *Two daily indices of MJO (phase and amplitude) of the RMM index are used to compare with rainfall extremes in this study* (cf. chapter 3).

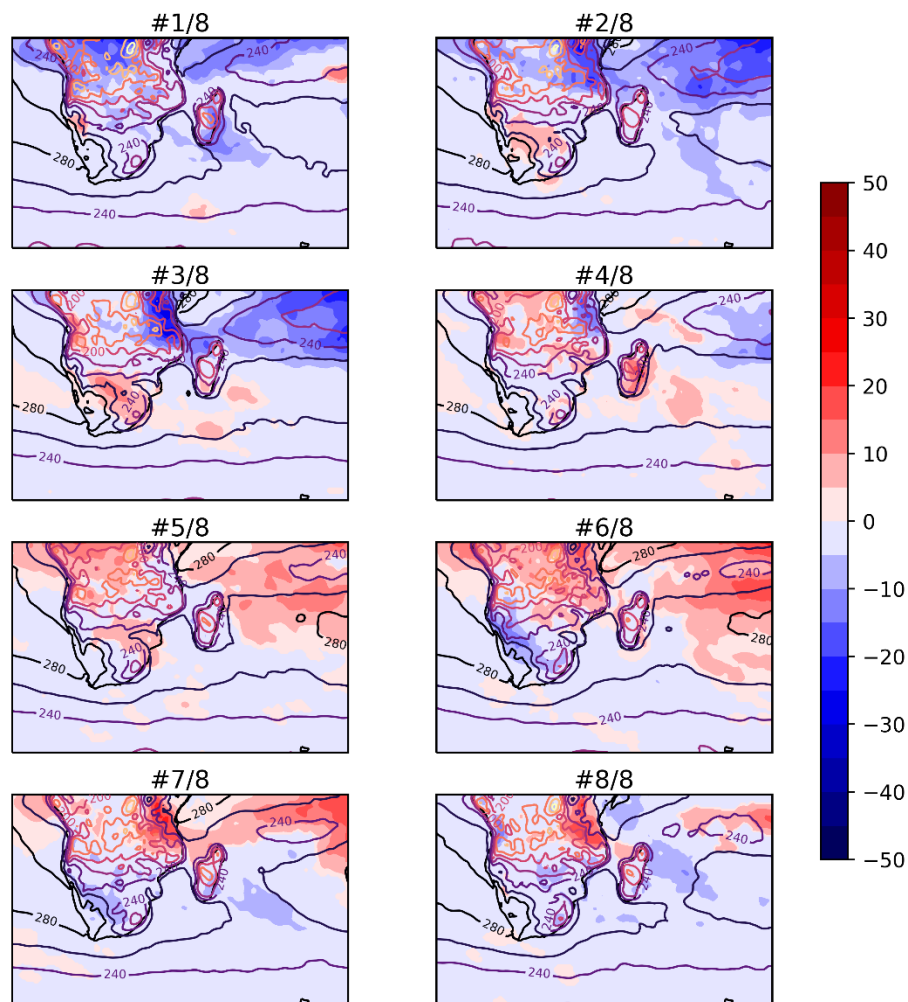


Figure 1.7. Mean daily OLR anomalies illustrating convective regimes related to eight MJO phases during the austral summer season (NDJF) over the period 1979–2015. The color bar describes the composite anomalies (interval $5 W.m^{-2}$), whereas the mean values are displayed by contours (interval $20 W.m^{-2}$).

1.7.5. Characterizing the combined influence of synoptic and intraseasonal variability of MJO on rainfall extremes

The combined influence of synoptic and intraseasonal variability on rainfall fields over Southern Africa has already been studied (Pohl *et al.*, 2009; Hart *et al.*, 2013; Macron *et al.*, 2016). *Here, we attempt to investigate how synoptic and intraseasonal variability influence different types of extremes and can combine their respective influence. Potential changes in the occurrence and intensity of rainfall extremes during different OLR regimes and MJO phases are explored using contingency analysis by considering all possible combinations between OLR regimes and MJO phases* (giving 56 different combinations). To quantify potential dampening and/or enhancement in the intensity of extremes, we first compute the average of all 56 classes. The behaviour of each ‘class’ is then presented in terms of anomaly against that mean value, and for each type of extreme (cf. chapter 3).

1.7.6. Quantification of risk of occurrence of extremes during combined influence of sub-seasonal timescale of variability

Risk Ratio assessment is also used here to further explore the combined influence of MJO and synoptic-scale convective regimes on the number of large- and small-scale extremes and is given by:

$$RR = \frac{P_F}{P_{CF}} = \frac{\left[\frac{a}{(a+b)} \right]_{OLR \text{ Regime and MJO Phase of interest (MJO} > 1.0RMM)}}{\left[\frac{x}{(x+y)} \right]_{OLR \text{ Regime and MJO Phase of interest (MJO} < 1.0RMM)}} \quad \text{Eq.2}$$

where a (b) is the sum of extreme (non-extreme) days when $MJO > 1.0$ RMM, representing the P_F scenario. Similarly, the x (y) is the sum of extreme (non-extreme) days when $MJO < 1.0$ RMM, representing the P_{CF} scenario. Following section 2.2.1, the composite anomalies of VIMD and moisture fluxes in each P_F and P_{CF} scenarios is also provided (cf. chapter 3).

1.8. WRF experimental design

Large-scale long-lived rainfall events are considered for the meso-scale modelling in order to investigate if dynamical downscaling using a higher resolution regional model i.e., WRF can improve the predictability of such highly intense longest-lived events in terms of intensity, rainfall accumulation and location. To that end, we first choose a few case studies from a list of large-scale long-lived rainfall spells during the period between 2000–2015 (see Table 1.3). Thus, three cases are selected for downscaling using ERA5 and RF2 as forcing datasets for WRF simulations to investigate the predictability of such events.

Table 1.3. List of large-scale long-lived rainfall spells between 2000–2015 identified by 225 in-situ observations and co-identified by NN and AGP fields of ERA5 and TRMM.

Date	Season	OLR Regime	MJO Phase	MJO Amplitude	Average Intensity (Millimetre)					Average spatial fraction > 90th Percentile (%)				
					OBS	ERA5-NN	ERA5-AGP	TRMM-NN	TRMM-AGP	OBS	ERA5-NN	ERA5-AGP	TRMM-NN	TRMM-AGP
a) Case #1 (05Feb2000-0600-UTC to 10Feb2000-0600-UTC)														
02/06/2000	1999-00	5	NA	0.79	134.72	44.99	33.27	82.04	68.34	12.00	13.33	17.91	12.44	14.13
02/07/2000	1999-00	5	NA	0.96	65.43	41.41	37.42	62.12	51.95	13.78	18.22	19.57	21.33	16.56
02/08/2000	1999-00	5	NA	0.96	56.31	46.05	42.42	60.58	52.96	7.56	14.22	15.51	15.11	19.65
02/09/2000	1999-00	5	NA	0.70	48.70	48.60	48.19	33.05	34.22	11.56	16.00	15.45	15.11	14.39
02/10/2000	1999-00	5	NA	0.56	50.44	43.05	40.32	49.04	40.85	10.67	15.11	15.75	10.22	13.86
b) Case #2 (29Dec2010-0600-UTC to 04Jan2011-0600-UTC)														
12/30/2010	2010-11	3	NA	0.43	50.41	25.49	27.26	34.57	34.32	12.89	10.67	12.49	4.89	5.58
12/31/2010	2010-11	3	NA	0.62	42.69	23.79	22.59	32.02	27.09	16.44	39.56	30.09	22.22	15.70
01/01/2011	2010-11	4	NA	0.71	44.64	30.49	27.76	31.41	29.27	14.22	49.78	37.85	7.56	7.16
01/02/2011	2010-11	3	NA	0.91	52.09	20.69	20.70	31.96	40.13	10.22	25.33	24.49	5.78	8.28
01/03/2011	2010-11	3	NA	0.88	43.23	20.86	20.36	31.58	34.74	9.33	29.33	26.22	8.00	8.28
01/04/2011	2010-11	3	NA	0.64	38.52	21.53	20.32	30.51	25.38	8.44	20.44	18.52	3.11	7.29
c) Case #3 (19Jan2011-0600-UTC to 24Jan2011-0600-UTC)														
01/20/2011	2010-11	3	7	2.43	51.26	18.45	19.29	38.92	40.13	8.44	3.56	3.82	14.22	11.17
01/21/2011	2010-11	3	7	2.59	53.78	24.50	23.02	31.43	31.46	18.22	23.11	14.58	20.00	11.43
01/22/2011	2010-11	4	7	2.54	43.55	26.86	26.33	33.15	35.13	17.78	48.00	38.09	22.22	17.15
01/23/2011	2010-11	2	7	2.49	59.16	22.88	24.34	41.39	38.81	10.22	23.11	27.14	12.00	14.59
01/24/2011	2010-11	2	8	2.17	44.58	24.82	24.92	27.09	23.16	8.44	27.11	20.68	1.33	1.05

The first two columns represent the date (mm/dd/yyyy) and season of the spell. Columns 3–5 represent the OLR regime, phase, and amplitude of MJO. Columns 6–10 (11–15) show the average intensity (spatial fraction) corresponding to each day of the event by NN and AGP fields of OBS, ERA5 and TRMM.

WRF simulations over South Africa are performed using two one-way nested domains with 60 sigma levels (Fig. 1.8). The parent domain with 9 km horizontal resolution covers southern Africa (1.32°E–46.01°E; 44.32°S–14.22°S) with 371 grid-points in the east–west and 327 grid-points in north–south directions. The nested inner domain with a 3 km horizontal resolution covers South Africa and a few neighbouring countries (12.06°E–37.17°E; 37.96°S–19.41°S) with 1130 grid-points in the east–west and 1010 grid-points in the north–south directions.

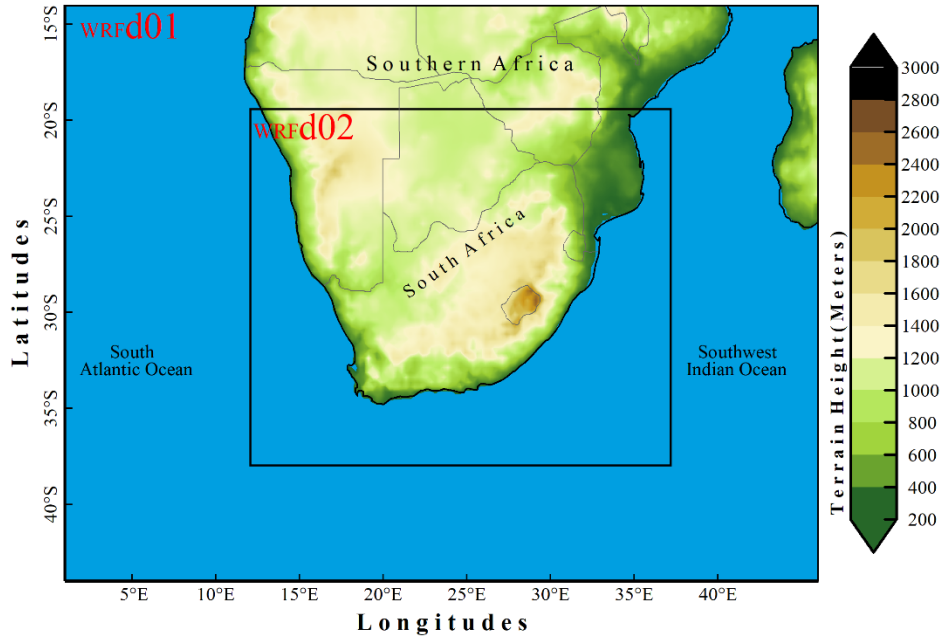


Figure 1.8. Model nested domains with resolutions of 9 km (d01) and 3 km (d02) in the WRF with topography in the background.

It is to note that the WRF domain 01 at its eastern boundary cuts through the mountainous island of Madagascar. It was done in order to eliminate the impact of mountains on the simulations. During the process of assessing WRF experimental design (various runs on three cases), we note no issues in the results which could be related to the sensitivity of boundary placement of WRF domain 01.

Three-stage evaluations are then applied on three case studies in order to obtain the finest experimental setup for WRF as follows:

- 1) Nudging and frequency of forcing
- 2) Cumulus parameterization schemes and spin-up time
- 3) Microphysics parameterization schemes

Nudging modifies the model's skill for capturing the spatial and temporal variability of the simulated convection. For nudging (Stauffer and Seaman, 1994) and forcing frequency testing, we run four experiments on three different case studies with 1-hour and 6-hour time steps with and without nudging at the parent domain. Kain–Fritsch scheme with moisture advection-based trigger function (KFtr: Ma and Tan, 2009) is used for cumulus parameterization, while WRF Single–Moment 6–class scheme (WSM6: Hong and Lim, 2006) is used for microphysics parameterization. For cumulus parameterization schemes and spin-up time, we consider three schemes namely Betts–Miller–Janjic scheme (BMJ: Betts and Miller, 1986; Janjic, 1994), Kain–Fritsch scheme (Kain, 2004) and KFtr as all the experiments are repeated up to 4 days spin up time. For the physical parameterization, we consider two microphysics schemes namely WSM6 and Morrison 2–moment scheme (MOR: Morrison *et al.*, 2009). In all three validation stages, we consider Yonsei University (YSU) scheme for the Planetary Boundary Layer (PBL: Hong *et al.*, 2006) and the Rapid Radiative Transfer Model (RRTM) scheme for long and short waves (Iacono *et al.*, 2008). Surface Elevation Data (GMTED2010) are taken from the United States Geological Survey database, which has replaced GTOPO30 as the elevation dataset of choice for global and continental scale applications. The MODIS Combined Land Cover product is used for land use which incorporates five different land cover classification schemes, derived through a supervised decision-tree classification method. The primary land cover scheme identifies 17 classes including 11 natural vegetation classes, three human-altered classes, and three non-vegetated classes. The sensitivity tests conducted on three case studies are summarized in Table 1.4.

Table 1.4. Three stage verification for WRF experimental design.

Stage 1 <i>Nudging and time steps</i>			
Without nudging		With nudging*	
1-hour	6-hour	1-hour	6-hour*
Stage 2 <i>Cumulus parameterization schemes and spin up time</i>			
Betts-Miller-Janjic scheme* (BMJ)	Kain-Fritsch scheme (KF)	Kain-Fritsch scheme with trigger function (KFtr)	
1 day spin up*	1 day spin up	1 day spin up	
2 days spin up	2 days spin up	2 days spin up	
3 days spin up	3 days spin up	3 days spin up	
4 days spin up	4 days spin up	4 days spin up	
Stage 3 <i>Microphysics parameterization schemes</i>			
WRF Single-moment 6-class scheme* (WSM6)		Morrison 2-moment scheme (MOR)	

Selected parameters in each stage are shown with bold and asterisk

The skill of the WRF experimental design is evaluated on three case studies using OBS, ERA5 and TRMM with various analysis. By carefully examining the results on three case studies we find that, nudging with 6-hour forcing frequency produces good results in simulating such high intensity long-lived events. BMJ scheme for cumulus parameterization with 24h spin up time and WSM6 for microphysics parameterization outperform other options which is also in line with previous studies over southern/South Africa (Crétat *et al.*, 2011, 2012b; Ratna *et al.*, 2014). The finest WRF experimental setup is summarized in Table 1.5.

1.8.1. WRF initialization setup for RF2

The finest WRF experimental setup is then used to obtain simulations by using one control run and 4 ensemble members of RF2 as forcing. The WRF model is initialized at 0600 UTC up to 9 days of lead time starting from the first day of the event. The initialization setup for each case study is summarized in Table 1.6.

1.8.2. Evaluation of WRF simulations

Several model validation techniques are applied on each run to evaluate the simulations and uncertainties between ensemble members by comparing with a dense network of observations (1832 in-situ observations), reanalysis and satellite estimates i.e., ERA5 and TRMM respectively. Further, we also assess the raw fields of ERA5 and RF2 (cf. Chapter 4).

Table 1.5. Summary of major parameterization schemes used to run WRF simulations for the study.

Parameterization	Scheme	Usage	Acronym	Reference
Cumulus parameterization	Betts Miller and Janjic scheme	Domain 01	BMJ	(Betts and Miller, 1986)
Microphysics parameterization	WRF Single-moment 6-class scheme	Domain 01 and 02	WSM6	(Hong and Lim, 2006)
Radiation (Long and short wave)	Rapid Radiative Transfer Model	Domain 01 and 02	RRTM	(Iacono <i>et al.</i> , 2008)
Planetary boundary layer	Yonsei University scheme	Domain 01 and 02	YSU	(Hong <i>et al.</i> , 2006)

Table 1.6. WRF initialization setup for RF2 for each case study.

Case #1 (05Feb-0600-UTC to 10Feb-0600-UTC)																
Lead Time		Days of the Event														
Model Initialization Date	1st day of event								<i>Init. On</i>	05 Feb	06 Feb	07 Feb	08 Feb	09 Feb	10 Feb	
	1 day before							<i>Init. On</i>	04 Feb	05 Feb	06 Feb	07 Feb	08 Feb	09 Feb	10 Feb	
	2 days before						<i>Init. On</i>	03 Feb	04 Feb	05 Feb	06 Feb	07 Feb	08 Feb	09 Feb	10 Feb	
	3 days before					<i>Init. On</i>	02 Feb	03 Feb	04 Feb	05 Feb	06 Feb	07 Feb	08 Feb	09 Feb	10 Feb	
	4 days before				<i>Init. On</i>	01 Feb	02 Feb	03 Feb	04 Feb	05 Feb	06 Feb	07 Feb	08 Feb	09 Feb	10 Feb	
	5 days before			<i>Init. On</i>	31 Jan	01 Feb	02 Feb	03 Feb	04 Feb	05 Feb	06 Feb	07 Feb	08 Feb	09 Feb		
	6 days before		<i>Init. On</i>	30 Jan	31 Jan	01 Feb	02 Feb	03 Feb	04 Feb	05 Feb	06 Feb	07 Feb	08 Feb			
	7 days before	<i>Init. On</i>	29 Jan	30 Jan	31 Jan	01 Feb	02 Feb	03 Feb	04 Feb	05 Feb	06 Feb	07 Feb				
8 days before	<i>Init. On</i>	28 Jan	29 Jan	30 Jan	31 Jan	01 Feb	02 Feb	03 Feb	04 Feb	05 Feb	06 Feb					
Case #2 (29Dec2010-0600-UTC to 04Jan2011-0600-UTC)																
Model Initialization Date	1st day of event								<i>Init. On</i>	29 Dec	30 Dec	31 Dec	01 Jan	02 Jan	03 Jan	04 Jan
	1 day before							<i>Init. On</i>	28 Dec	29 Dec	30 Dec	31 Dec	01 Jan	02 Jan	03 Jan	04 Jan
	2 days before						<i>Init. On</i>	27 Dec	28 Dec	29 Dec	30 Dec	31 Dec	01 Jan	02 Jan	03 Jan	04 Jan
	3 days before					<i>Init. On</i>	26 Dec	27 Dec	28 Dec	29 Dec	30 Dec	31 Dec	01 Jan	02 Jan	03 Jan	04 Jan
	4 days before				<i>Init. On</i>	25 Dec	26 Dec	27 Dec	28 Dec	29 Dec	30 Dec	31 Dec	01 Jan	02 Jan	03 Jan	
	5 days before			<i>Init. On</i>	24 Dec	25 Dec	26 Dec	27 Dec	28 Dec	29 Dec	30 Dec	31 Dec	01 Jan	02 Jan		
	6 days before		<i>Init. On</i>	23 Dec	24 Dec	25 Dec	26 Dec	27 Dec	28 Dec	29 Dec	30 Dec	31 Dec	01 Jan			
	7 days before	<i>Init. On</i>	22 Dec	23 Dec	24 Dec	25 Dec	26 Dec	27 Dec	28 Dec	29 Dec	30 Dec	31 Dec				
8 days before	<i>Init. On</i>	21 Dec	22 Dec	23 Dec	24 Dec	25 Dec	26 Dec	27 Dec	28 Dec	29 Dec	30 Dec					
Case #3 (18Jan2011-0600-UTC to 23Jan2011-0600-UTC)																
Model Initialization Date	1st day of event								<i>Init. On</i>	18 Jan	19 Jan	20 Jan	21 Jan	22 Jan	23 Jan	
	1 day before							<i>Init. On</i>	19 Jan	18 Jan	19 Jan	20 Jan	21 Jan	22 Jan	23 Jan	
	2 days before						<i>Init. On</i>	18 Jan	19 Jan	18 Jan	19 Jan	20 Jan	21 Jan	22 Jan	23 Jan	
	3 days before					<i>Init. On</i>	17 Jan	18 Jan	19 Jan	18 Jan	19 Jan	20 Jan	21 Jan	22 Jan	23 Jan	
	4 days before				<i>Init. On</i>	16 Jan	17 Jan	18 Jan	19 Jan	18 Jan	19 Jan	20 Jan	21 Jan	22 Jan	23 Jan	
	5 days before			<i>Init. On</i>	15 Jan	16 Jan	17 Jan	18 Jan	19 Jan	18 Jan	19 Jan	20 Jan	21 Jan	22 Jan		
	6 days before		<i>Init. On</i>	14 Jan	15 Jan	16 Jan	17 Jan	18 Jan	19 Jan	18 Jan	19 Jan	20 Jan	21 Jan			
	7 days before	<i>Init. On</i>	13 Jan	14 Jan	15 Jan	16 Jan	17 Jan	18 Jan	19 Jan	18 Jan	19 Jan	20 Jan				
8 days before	<i>Init. On</i>	12 Jan	13 Jan	14 Jan	15 Jan	16 Jan	17 Jan	18 Jan	19 Jan	18 Jan	19 Jan					

The model is initialized at 0600-UTC. The days of the event assessed in the study are shown in bold and italic

Chapter 2


Summer climatology and statistical characteristics

Abstract

Rainfall extremes are of major and increasing importance in semi-arid countries and their variability has strong implications for water resource and climate impacts on the local societies and environment. Here, we examine intraseasonal descriptors (ISDs) and wet extremes in austral summer rainfall (November–February) over South Africa (SA). Using daily observations from 225 rain gauges and ERA5 reanalysis between 1979 and 2015, we propose a novel typology of wet extreme events based on their spatial fraction, thus differentiating large- and small-scale extremes. Long-term variability of both types of extreme rainfall events is then extensively discussed in the context of ISDs.

The results demonstrate that using 7% of spatial fraction simultaneously exceeding the local threshold of the 90th percentile produces remarkable results in characterizing rainfall extremes into large- and small-scale extremes. Austral summer total rainfall is found to be primarily shaped by large-scale extremes which constitute more than half of the rainfall amount under observation, and nearly half in ERA5. Observation (ERA5) shows an average of 8 ± 5 (20 ± 7) days per season associated with large-scale extremes, which are comprised in 5 ± 3 (10 ± 3) spells with an average persistence of at least 2 days. Overall, we find a strong dependence of total rainfall on the number of wet days and wet spells that are associated with large-scale extremes. We also find that large- and small-scale extremes are well-organized and spatially coherent in nature yet extreme conditions during small-scale events are found sporadic over the region, contrasting with large-scale events for which extreme conditions are found over a larger and coherent region.

Intraseasonal descriptors and extremes in South African rainfall. Part I: Summer climatology and statistical characteristics

Asmat Ullah¹  | Benjamin Pohl¹ | Julien Pergaud¹ | Bastien Dieppois² | Mathieu Rouault³

¹Centre de Recherches de Climatologie, UMR 6282 Biogéosciences, CNRS/ Université de Bourgogne Franche-Comté, Dijon, France

²Centre for Agroecology, Water and Resilience, Coventry University, Coventry, UK

³Nansen Tutu Center for Marine Environmental Research, Department of Oceanography, University of Cape Town, Cape Town, South Africa

Correspondence

Asmat Ullah, Centre de Recherches de Climatologie, UMR 6282 Biogéosciences, Université de Bourgogne, 6 Boulevard Gabriel, 21000 Dijon, France.
Email: asmat-786@hotmail.com

Funding information

I-SITE Bourgogne Franche-Comté, Grant/Award Number: AAP2-JF-06

Abstract

Rainfall extremes are of major and increasing importance in semi-arid countries and their variability has strong implications for water resource and climate impacts on the local societies and environment. Here, we examine intraseasonal descriptors (ISDs) and wet extremes in austral summer rainfall (November–February) over South Africa (SA). Using daily observations from 225 rain gauges and ERA5 reanalysis between 1979 and 2015, we propose a novel typology of wet extreme events based on their spatial fraction, thus differentiating large- and small-scale extremes. Long-term variability of both types of extreme rainfall events is then extensively discussed in the context of ISDs. The results demonstrate that using 7% of spatial fraction simultaneously exceeding the local threshold of the 90th percentile produces remarkable results in characterizing rainfall extremes into large- and small-scale extremes. Austral summer total rainfall is found to be primarily shaped by large-scale extremes which constitute more than half of the rainfall amount under observation, and nearly half in ERA5. Observation (ERA5) shows an average of 8 ± 5 (20 ± 7) days per season associated with large-scale extremes, which are comprised in 5 ± 3 (10 ± 3) spells with an average persistence of at least 2 days. Overall, we find a strong dependence of total rainfall on the number of wet days and wet spells that are associated with large-scale extremes. We also find that large- and small-scale extremes are well-organized and spatially coherent in nature yet extreme conditions during small-scale events are found sporadic over the region, contrasting with large-scale events for which extreme conditions are found over a larger and coherent region.

KEYWORDS

climate variability, intraseasonal descriptors, rainfall extremes, South Africa, spatial coherence

1 | INTRODUCTION

Most of South Africa (SA hereafter) experiences a rainy season in austral summer (November–February; Pohl *et al.*, 2014; Favre *et al.*, 2016). Located at the interface between the Tropics and the midlatitudes of the Southern Hemisphere, while being surrounded by two thermally contrasted oceans (Rouault *et al.*, 2003), SA is subject to both the influence of tropical convection and temperate dynamics (Washington and Todd, 1999; Hart *et al.*, 2010; Vigaud *et al.*, 2012). Together with highly heterogeneous vegetation and topography, these tropical and temperate influences form a mosaic of climates in association with contrasted surface atmospheric characteristics such as rainfall amount and temperature which strongly vary in time and space. Like many semi-arid regions in the Tropics, SA depends heavily on the quality of its rainy seasons, as irrigation remains rather rare in this region (Crétat *et al.*, 2012; Masupha *et al.*, 2016). Thus, rainfall variability and forecasting at fine spatial and temporal scales are a matter of crucial importance for SA agriculture and economy (Conway *et al.*, 2015).

In SA, during the austral summer, precipitation events are generally associated with moist atmospheric convection, ranging in scale from single-cell storms to organized systems, such as Mesoscale Convective Complexes (MCCs; Blamey and Reason, 2013), squall lines (Rouault *et al.*, 2002) and tropical storms (Reason and Keibel, 2004; Reason, 2007; Malherbe *et al.*, 2012; 2014; Fitchett and Grab, 2014). Cut-off lows (CoLs) can also lead to extreme rainfall in SA, but they are rare during the summer season (Favre *et al.*, 2013). In austral summer, three key regions (namely southwest Indian Ocean, tropical western Indian Ocean, and tropical southeast Atlantic Ocean) are known to inject moisture flux into the southern African continent (Desbiolles *et al.*, 2018; Rapolaki *et al.*, 2019; 2020). The dominant rain-bearing systems over the region are synoptic-scale cloud bands, known locally as Tropical Temperate Troughs (TTTs; Manhique *et al.*, 2011; Hart *et al.*, 2013; Macron *et al.*, 2014; James *et al.*, 2020). TTTs correspond to synoptic-scale cloud bands that link tropical instability over the subcontinent with an upper-tropospheric frontal system embedded in the mid-latitude westerly circulation (Todd and Washington, 1999; Todd *et al.*, 2004; Hart *et al.*, 2010) and bring about 30–60% of summer rainfall over subtropical SA (Hart *et al.*, 2013; Macron *et al.*, 2014). The remaining 40–70% of the summer rainfall amounts are provided by rain-bearing mechanisms linked to tropical convection, such as regional thermal low pressure (Reason *et al.*, 2006) or the Madden–Julian Oscillation (MJO; Pohl *et al.*, 2007). Rapolaki *et al.* (2019) highlighted that, over the Limpopo River basin, 48% of

extreme events are associated with TTTs, 28% with tropical low-pressure systems, 14% with mesoscale convective systems, and 10% with CoLs.

Intraseasonal descriptors (hereafter ISDs) are defined as wet and dry sequences of days during the rainy season (Ratan and Venugopal, 2013; Gitau *et al.*, 2015; 2018). Examining ISDs provides various intrinsic characteristics of a rainy season, such as the average number of wet and dry days, persistence of spells, intensity of wet spells, and total rainfall. Similar studies focused on other regions, such as equatorial East Africa (Camberlin *et al.*, 2009; Moron *et al.*, 2013; Gitau *et al.*, 2015; 2018; Philippon *et al.*, 2015), have already demonstrated their relevance and usefulness in climate diagnostics and prediction. However, analyses devoted to ISDs remain quite rare in SA. Tennant and Hewitson (2002) found that anomalously wet rainy seasons tend to experience a larger number of heavy rainy days ($>20 \text{ mm}\cdot\text{day}^{-1}$). Cook *et al.* (2004) highlighted that moisture anomalies between wet and dry spells were strongly related to the Kalahari low. They also stated that wet years were characterized by longer and more intense wet spells, rather than by a greater number of wet spells (Cook *et al.*, 2004). Similarly, previous studies found a strong relationship between dry spells and El Niño–Southern Oscillation (ENSO), suggesting potential predictability of ISDs using this relationship (Usman and Reason, 2004; Reason *et al.*, 2005; Crétat *et al.*, 2012). Physically, El Niño conditions could act to shift TTTs eastwards over the Mozambique Channel (Nicholson and Kim, 1997; Cook, 2000; 2001; Misra, 2003; Nicholson, 2003; Dieppois *et al.*, 2015; 2016; 2019), thereby enhancing the number of dry spells over the continent. The relationship between TTTs and ENSO has been confirmed and further documented by Fauchereau *et al.* (2009) and Pohl *et al.* (2018). During La Niña a low pressure develop over southern Africa, which is related to anomalous upwards motion and enhanced moisture fluxes into and over the region which results in rainfall surplus while El Niño is linked with high pressure over southern Africa, which is associated with anomalous downwards motion and reduced moisture fluxes into and over the region which result in rainfall deficit during austral summer season (Ratnam *et al.*, 2014; Hoell *et al.*, 2015).

The severity and frequency of wet and dry extreme events are likely to increase at the global scale as a response to anthropogenic emissions of greenhouse gases (Donat *et al.*, 2016). This statement is also true for SA rainfall (Mason and Joubert, 1997; Mason *et al.*, 1999; Shongwe *et al.*, 2009; Engelbrecht *et al.*, 2013; Pinto *et al.*, 2016). Future scenarios include a combination of decreasing numbers of rainy days and increasing intensity of extreme rainy days (Pohl *et al.*, 2017), which are

likely to modify the intrinsic characteristics of intra-seasonal spells in the future.

This study aims to provide fundamental and up-to-date knowledge about the intrinsic characteristics of wet and dry ISDs. First, we provide an overall assessment of ISDs, in which extremes are embedded using the latest available observation archive and a state-of-the-art reanalysis product. This study then proposes a novel typology of extreme rainfall events, based on their spatial fraction as a base criterion, disentangling rainfall events into large-scale and small-scale extremes. To our knowledge, there is hitherto no study that addresses the spatial dimension in the definition of rainfall extremes over the region, despite its importance for predictions over other regions (Lu *et al.*, 2017; Oueslati *et al.*, 2017). In this paper, we calculate and discuss the intrinsic characteristics of large- and small-scale extremes in the context of ISDs over SA. The contribution made should be of interest for a wide range of the scientific community working on seasonal forecasts. Such results also have considerable importance for stakeholders in the environmental, agricultural, energy, water, and economic sectors. A companion paper will further assess how these different types of extreme events vary in time, and/or are modulated by modes of large-scale variability at different timescales ranging from the synoptic scale to decadal variability.

This paper (Part I), more specifically dedicated to the mean characteristics of rainfall extremes in SA, is organized as follows. Section 2 presents datasets and methodology. Section 3 provides an assessment of wet and dry ISDs and their summer climatology over SA. Section 4 is dedicated to defining criteria to identify extreme rainfall events and to facilitate their categorization into large- and small-scale extreme events. Section 5 addresses an assessment of large- and small-scale rainfall extremes in the definition of ISDs. Section 6 summarizes the results and establishes the main conclusions.

2 | DATA AND METHODOLOGY

2.1 | In situ and reanalysis data

Observed daily rainfall data from 225 stations (hereafter OBS), spanning 50 years between 1965 and 2015, in which missing values represent less than 1%, were retrieved from the archives of the Water Research Commission of South Africa, which constitutes a dense network of 2,625 stations (<http://www.wrc.org.za>) (Figure 1a).

In addition, we used state-of-the-art ERA5 reanalysis to compare and cross-validate our results. ERA5 reanalysis (Copernicus Climate Change Service, 2017;

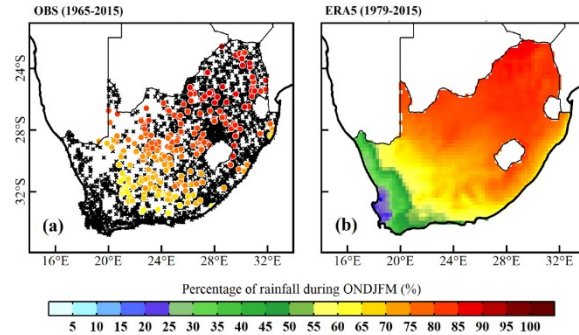


FIGURE 1 Spatial distribution of the percentage of rainfall during ONDJFM for OBS (a) for ERA5 (b). The unqualified stations are indicated by black “x” symbols based on the seasonality test and other quality control measures [Colour figure can be viewed at wileyonlinelibrary.com]

Hersbach *et al.*, 2020) is the 5th generation reanalysis available from the European Center for Medium-Range Weather Forecasts (ECMWF), providing $0.25^\circ \times 0.25^\circ$ resolution of hourly gridded outputs of surface and atmospheric fields at the global scale, spanning 1979 to the present. ERA5 has now been extended to 1950–1978 but the lack of assimilation of satellite data before 1979 raises the question of the homogeneity of the dataset, the detailed evaluation of which is mandatory before using it. However, it is not the scope of the present study, hence our choice to consider a common period of 36 years (1979–2015).

To focus on the summer rainfall regions, a seasonality test was then applied on OBS and ERA5 (Crétat *et al.*, 2012). Using the seasonality test, only the stations and grid-points for which at least 50% of annual rainfall occurred during an extended austral summer (October–March) were retained. The spatial distribution of the percentage of summer rainfall in OBS and ERA5 is presented in Figure 1a,b. Regarding ERA5, all grid-points (AGP) and those nearest to OBS (NN) were used in this study. The Comparing the NN and AGP fields of ERA5 is particularly important in order to examine whether the network is dense enough to study rainfall extremes. The NN and AGP fields of ERA5 have here been named ERA5–NN and ERA5–AGP, respectively.

To define new metrics accounting for the typology of rainfall extremes, we focused on the austral summer season (October–March), and we analysed two distinct baseline periods (1965–2015) for OBS and (1979–2015) for ERA5. By considering extended austral summer seasons and the two distinct baseline periods for the computation of 90th percentile values, we gained two advantages: (a) a longer period for OBS ensures statistical robustness of low-frequency decadal variability; (b) longer seasons also include rainfall onset (October) and cessation (March)

months (discussed later in the companion paper). For all remaining objectives, we restricted the study to the period dating 1979–2015 and to the core of the rainy season (November–February).

2.2 | Methods

2.2.1 | Definition of intraseasonal descriptors at the regional scale

A threshold of $1.0 \text{ mm}\cdot\text{day}^{-1}$ was used to delineate wet from dry days (Gitau *et al.*, 2013; 2015). A unified definition for wet and dry spells was obtained as suggested in several previous studies (Ratan and Venugopal, 2013; Gitau *et al.*, 2015; 2018). A wet (dry) spell is defined as a duration of “i” wet (dry) days preceded and followed by a dry (wet) day. As summarized in Table 1(a), (b), various ISDs, which are associated with wet and dry spells, are computed for each station and grid-point using OBS and ERA5. Multi-year variability of each ISD is then assessed using seasonal average computed at the regional scale (cf. section 3).

To quantify and compare temporal variability, commonly used statistical metrics were applied to each ISD: mean (μ), standard deviation (SD), root-mean-square error (RMSE), and coefficient of variation (CV; Asmat and Athar, 2017; Asmat *et al.*, 2018). The Mann–Kendall (MK) nonparametric test was used to perform the trend analysis (Mann, 1945; Kendall, 1957). Pearson’s correlations were computed to quantify the dependence of total rainfall on ISDs.

2.2.2 | Assessment of rainfall extremes

Local threshold for rainfall extremes

We first computed the 90th percentile of daily rainfall amount of each station and grid-point, which were retrieved from the aforementioned seasonality test, over the two climatological baseline periods as described in section 2.1. The 90th percentile values were calculated by removing all values below $1.0 \text{ mm}\cdot\text{day}^{-1}$ for more robust identification of extreme rainfall events. The comparisons of the spatial distributions of the 90th percentile, as calculated before and after removing nonrainy and drizzle days (i.e., days with less than 1.0 mm), are presented in Figure 2a,b and Figure 2c,d, respectively. This choice made the evaluation less sensitive to measurement accuracy and to the tendency of some numerical models to produce an excessive number of drizzle events (Frei *et al.*, 2003; Gitau *et al.*, 2015; Maraun, 2016). A similar sensitivity to drizzle days was found to be more pronounced in ERA5; thus, not removing drizzle days would have led to underestimating the 90th percentiles. The 90th percentile threshold is calculated based on a normal distribution, and we note that it did not significantly differ from one calculated based on a theoretical extreme value distribution (Gumbel distribution, cf. Figure S1c,d, Supporting Information). This suggests the statistical robustness of the approach used to calculate the extreme thresholds in this study.

Regional threshold for rainfall extremes

A novel typology of rainfall extremes based on the spatial fraction of rainfall events is then proposed. The spatial

TABLE 1 The description of the wet ISDs (a) and dry ISDs (b)

(a) Wet ISDs				
ISD name	Acronym	Description	Unit	Scale
Wet days	WD	Average number of wet days in a season	Days	Seasonal
Wet days >90th percentile	WD _{P90}	Average number of days exceeding the 90th percentile threshold	Days	Seasonal
Wet spells	WS	Average number of wet spells in a season	Spells	Seasonal
Wet spell persistence	WSP	Average persistence of wet spells in a season	Days	Seasonal
Wet spell intensity	WSI	Average intensity of wet spells in a season	$\text{mm}\cdot\text{day}^{-1}$	Seasonal + daily
Spatial fraction	SF	Average spatial fraction associated with total rainfall amount in a season	%	Seasonal + daily
Total rainfall	TR	Total rainfall amount in a season	$\text{mm}\cdot\text{season}^{-1}$	Seasonal + daily
(b) Dry ISDs				
ISD name	Acronym	Description	Unit	Scale
Dry spells	DS	Average number of dry spells in a season	Spells	Seasonal
Dry days	DD	Average number of dry days in a season	Days	Seasonal
Dry spell persistence	DSP	Average persistence of wet spells	Days	Seasonal

Note: Columns 1–5 represent the ISD name, acronym, description, unit, and scale respectively.

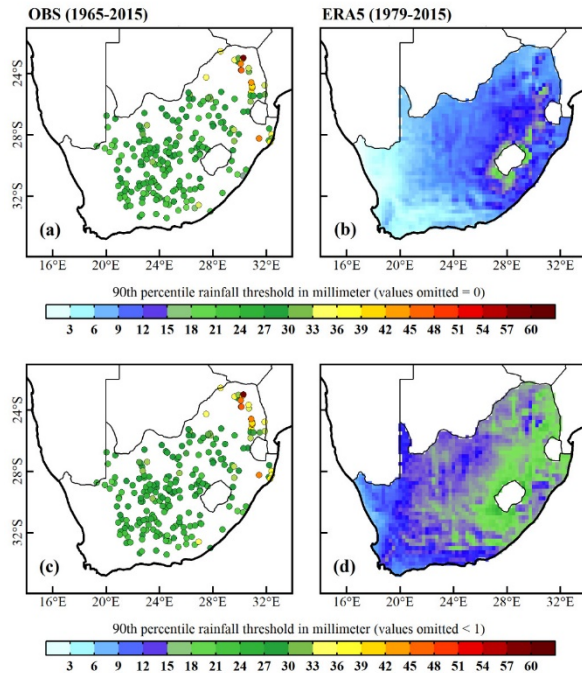


FIGURE 2 The 90th percentile threshold of rainfall computed after omitting the values = 0 for OBS (a) and for ERA5 (b). The 90th percentile threshold of rainfall after omitting the values < 1 for OBS (c) and for ERA5 (d) [Colour figure can be viewed at wileyonlinelibrary.com]

fraction of an extreme event is defined as the number of stations or grid-points that simultaneously reach the 90th percentile regardless of their location on the day of the event. A similar methodology has been successfully used for the identification of heat waves in West Africa (Oueslati *et al.*, 2017). The principal reason for using the spatial fraction as a base criterion is to differentiate localized, or small-scale extreme events from large-scale extreme events. On one hand, small-scale extreme events are related to isolated convective cells and therefore stochastic in nature, rendering them highly unpredictable. On the other hand, large-scale extreme events are embedded in large-scale modes of climate variability, hence potentially more predictable. The spatial fraction of extreme events depends on the density of the network, but also on its anisotropy, which is likely to cause some issues in the estimation of the spatial extension of the events because the stations are not uniformly distributed in space. In reference to this assumption, the spatial fraction of events is here quantified using both the ERA5–NN and ERA5–AGP fields. The comparison between ERA5–NN and ERA5–AGP fields makes it possible to assess whether or not the network is dense enough to study rainfall extremes. The density might not be sufficient if ERA5–NN exhibits substantially different

properties than in ERA5–AGP. Thus, a caution is required to interpret the results related to large- and small-scale extremes as (a) the extremes are not characterized here based on environmental consequences but from an atmospheric point of view considering the characteristics of rainfall field itself; (b) considering the use of administrative boundaries, limitation in observation along with using NN and AGP fields of ERA5 yet there is a likelihood that some events that may have major environmental consequences, are not necessarily captured; (c) resolution of reanalysis is particularly important to capture small-scale extreme events. Section 4.1 addresses a brief assessment conducted in defining a robust and relevant threshold of spatial fraction.

Spatial characteristics of rainfall extremes

Based on the defined threshold of spatial fraction, we first separated all days associated with large- and small-scale extreme events (cf. section 4.1). The average characteristics of both types of extremes were then assessed in terms of frequency and intensity for each station and grid point. The frequency and intensity were computed based on two criteria: (a) average number of days exceeding the 1.0 mm threshold during large- and small-scale extreme events; (b) average number of days exceeding the 90th percentile threshold during large- and small-scale extreme events. For the sake of clarity, in this paper, this analysis is only provided for OBS (cf. section 4.2).

Spatial coherence of rainfall extremes

An analysis addressing the spatial coherence of large- and small-scale extremes is also provided. Here, we analyse the density of stations recording rainfall on the days of large- and small-scale extremes based on the same method used to address the spatial characteristics of extreme events: (a) considering all stations recording rainfall >1.0 mm on the day of the event; (b) considering only those stations which exceeded their 90th percentile on the day of the event. The density of the stations was assessed using a narrow bin size of 0.5°, corresponding to the stations that are located within approximately 55 km over latitudes and 43 km over longitudes (cf. section 4.3).

2.2.3 | Definition of intraseasonal descriptors associated with rainfall extremes

Large- and small-scale extreme rainy days were first obtained from the typology of rainfall extremes (cf. section 4). Both types of events were then explicitly considered in the context of ISDs. By placing these events in the framework of ISDs, we were able to further explore

the climatology and intrinsic properties of such events on an interannual timescale. Thus, several ISDs associated with large- and small-scale rainfall extremes were assessed using OBS and ERA5. A brief description of extreme ISDs is presented in Table 2. To quantify and compare temporal variability and trends, the same statistical metrics as introduced in section 2.2.1 are used in section 5.

3 | ISDs AT THE REGIONAL SCALE

3.1 | Multiyear variability of ISDs

The average spatial distribution of each ISD is presented in Figure 3. A spatial gradient from southwest to northeast clearly prevails in all ISDs, as northeastern regions are much wetter than southern regions in all wet ISDs (Figure 3a). Meanwhile, dry ISDs show larger values over the southwestern regions denoting drier conditions (Figure 3b), in agreement with Cr  tat *et al.* (2012). When compared with OBS, ERA5 displays nearly realistic responses for all ISDs in terms of spatial distribution but shows some biases when spatial average is assessed (cf. Figure S2). Notably, ERA5 overestimates the values in all wet ISDs, except for the intensity of wet spells (Figure S2a). Such overestimations of seasonal rainfall in ERA5 could be related to a higher number of wet spells with weaker intensity (WS and WSI panels in Figures 3 and 4). In addition, looking at the spatial distribution of biases in ISDs, we note that the intensity of wet spells is underestimated throughout the region (WSI panel in Figure S3b). Meanwhile, the overestimation of the number of wet days is more pronounced from the northeast to the

southwest (WD panel in Figure S3b). ERA5 also largely underestimates the number of wet spells, especially in regions of higher altitude (>1,400 m above sea level), such as the Drakensberg region (WS panel in Figure S3b). This suggests that ERA5 struggles to break the continuity of rainy days within a spell, which results in fewer but more prolonged spells (WS and WSP panels in Figure S3b).

Reanalysis bias over the African continent across three generations of ECMWF reanalysis is extensively discussed in Gleixner *et al.* (2020). This study highlights substantial improvements in ERA5 achieved by improved model physics and data assimilation schemes. In this study, we still note significant discrepancies between ERA5 and observations in ISDs as discussed above. The foremost problem in ERA5 is its ability to produce a realistic response for those regions characterized by a complex terrain (Wang *et al.*, 2019), given the fact that such regions tend to have a lower number of observations. In SA, the average biases that we find in intraseasonal characteristics could also result from similar constraints, since the northeastern part of SA is characterized by a complex topography that often enhances the biases present in numerical models (Favre *et al.*, 2016; Koseki *et al.*, 2018).

Figure 4 presents the statistical distribution and multi-year variability of ISDs. Both ERA5–NN and ERA5–AGP fields show consistent results in all wet and dry ISDs (see violin plots in Figure 4), suggesting that the density of observational archives used for OBS (i.e., 225 stations) is sufficient to monitor the spatial and temporal variability of ISDs throughout SA. Regarding wet ISDs, OBS and ERA5 display an average of 20 ± 4 and 44 ± 6 days over a season, respectively (WD panel in Figure 4a). These wet days are driven by 13 ± 2 spells for

TABLE 2 The description of extreme ISDs

Extreme ISDs				
ISD name	Acronym	Description	Unit	Scale
Wet days	WD _{EXT}	Average number of wet days associated with large- and small-scale extreme events in a season	Days	Seasonal
Wet spells	WS _{EXT}	Average number of wet spells associated with large- and small-scale extreme events in a season	Spells	Seasonal
Wet spell persistence	WSP _{EXT}	Average persistence of wet spells associated with large- and small-scale extreme events in a season	Days	Seasonal
Wet spell intensity	WSI _{EXT}	Average intensity of wet spells associated with large- and small-scale extreme events in a season	mm-day ⁻¹	Seasonal + daily
Spatial fraction	SF _{EXT}	Average spatial fraction associated with total rainfall amount driven by large- and small-scale extreme events in a season	%	Seasonal + daily
Total rainfall	TR _{EXT}	Total rainfall amount associated with large- and small-scale extreme events in a season	mm-season ⁻¹	Seasonal + daily

Note: Columns 1–5 represent the ISD name, acronym, description, unit, and scale, respectively.

(a) Wet ISDs

(b) Dry ISDs

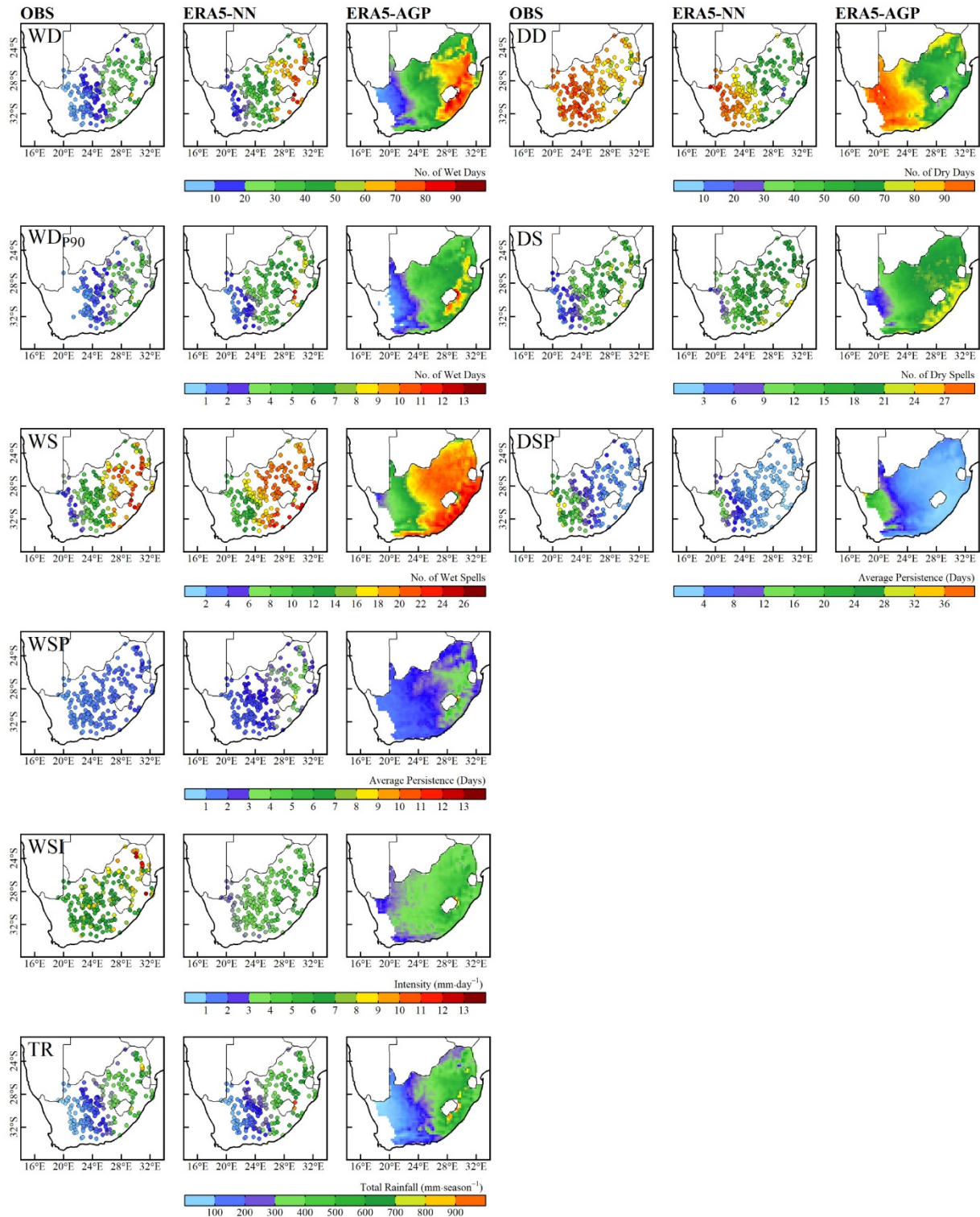
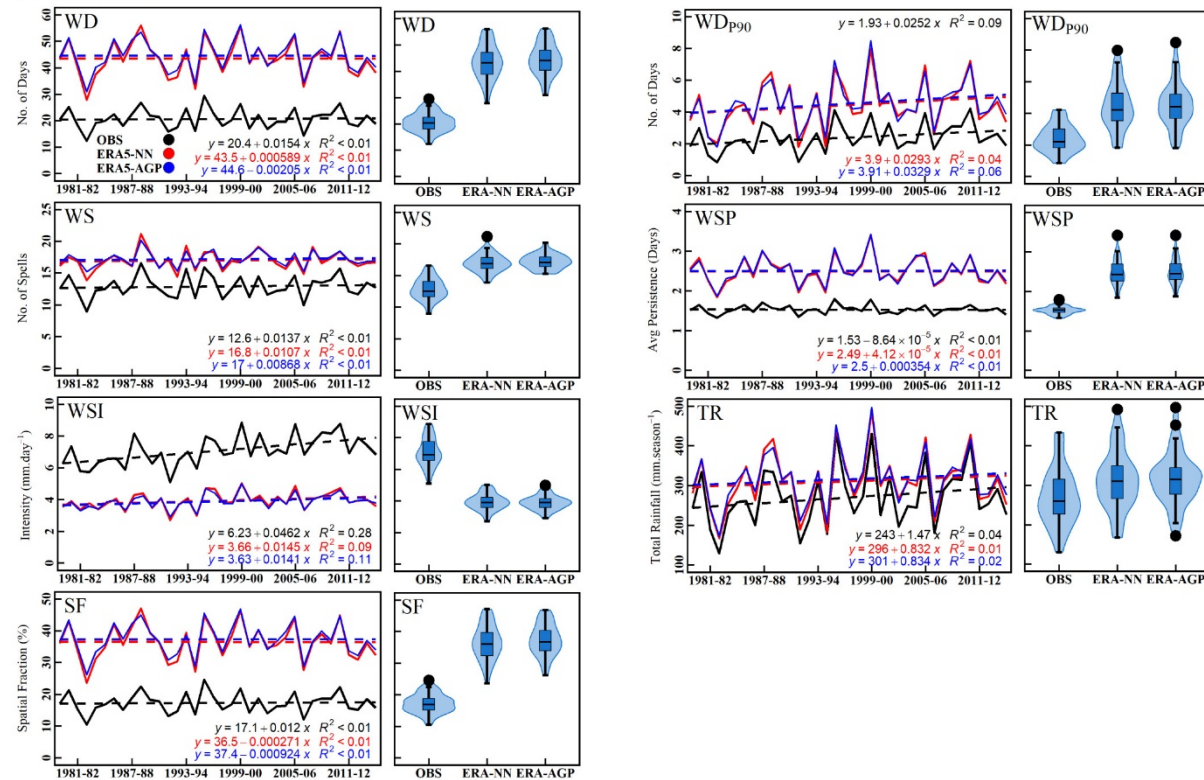


FIGURE 3 The average spatial distribution of ISDs, set of three column panels on the left (right) refers to the wet ISDs (dry ISDs) for OBS, ERA5-NN and ERA5-AGP. The statistics are averaged over the period of 1979–2015 for the austral summer season NDJF [Colour figure can be viewed at wileyonlinelibrary.com]

(a) Wet ISDs



(b) Dry ISDs

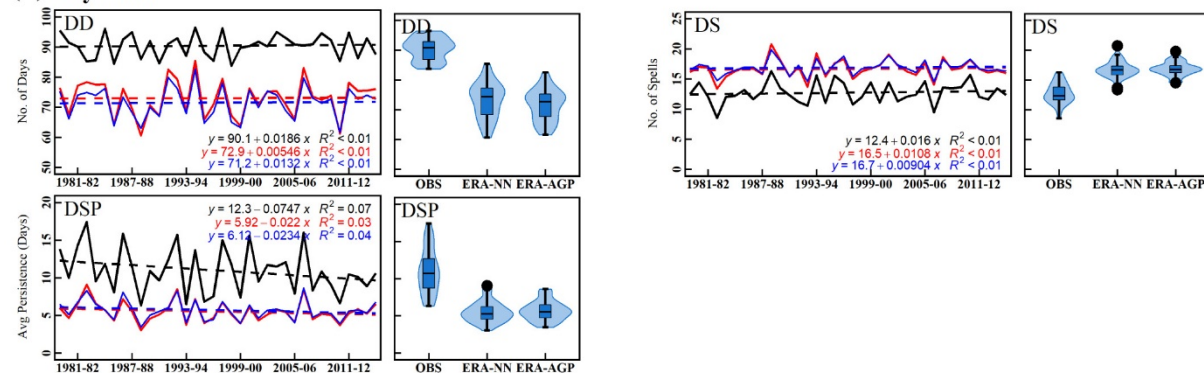


FIGURE 4 The average time series (line plots) and overall statistical distribution (violin plots) for wet ISDs (a) and for dry ISDs (b). The black line in each time series panel refers to the OBS, the red line is used to indicate ERA5-NN and the blue line for ERA5-AGP [Colour figure can be viewed at wileyonlinelibrary.com]

OBS and 17 ± 2 spells for ERA5 (WS panel in Figure 4a). For OBS (ERA5), the austral summer season is composed of 90 (70) dry days and 12 (16) dry spells (DD and DS panels in Figure 4b). Although biases exist in ERA5, multiyear variability appears realistic with a statistically significant correlation (>0.8) to OBS for most of the wet and dry ISDs (Table 3).

The average number of wet days exceeding the 90th percentiles is 2 and 4 in OBS and ERA5, respectively

(WD_{P90} panel in Figure 4a). As discussed above, ERA5 also overestimates the number of wet days, including the number of wet days exceeding the 90th percentiles. The temporal patterns of extreme wet days and total rainfall show coherent peaks in both ISDs between 1993–1994 and 1999–2000 (WD_{P90} and TR panels in Figure 4a), which clearly indicates that the wettest years tend to correspond to the largest seasonal occurrences of extremes. Overall, the CV remains higher OBS in most

TABLE 3 Average statistics of ISDs in the austral summer season computed over the period 1979–2015 using OBS, ERA5–NN and ERA5–AGP

ISD	Mean	±SD	CV %	RMSE w.r.t OBS	R ²	CC w.r.t OBS	CC w.r.t TR	Trend
OBS								
WD	20.66	3.68	17.83		0.00		0.94*	0.03
WD _{P90}	2.39	0.86	35.76		0.09		0.98*	1.74
WS	12.90	1.70	13.14		0.01		0.86*	0.29
WSP	1.53	0.11	7.05		0.00		0.87*	0.00
WSI	7.09	0.90	12.76		0.28		0.86*	3.23*
SF	17.30	3.07	17.75		0.00		0.94*	0.07
TR	270.12	72.17	26.72		0.04			0.99
DD	90.40	3.79	4.19		0.00		−0.14	0.40
DS	12.71	1.73	13.61		0.01		0.87*	0.53
DSP	10.96	3.01	27.46		0.07		−0.79*	−1.40
ERA5–NN								
WD	43.53	6.65	15.28	23.13	0.00	0.93*	0.95*	−0.23
WD _{P90}	4.44	1.48	33.41	2.17	0.04	0.95*	0.97*	1.19
WS	17.00	1.45	8.55	4.22	0.01	0.80*	0.56*	0.35
WSP	2.49	0.33	13.40	0.99	0.00	0.90*	0.91*	−0.26
WSI	3.93	0.51	13.04	3.20	0.09	0.88*	0.88*	1.65
SF	36.51	5.55	15.20	19.43	0.00	0.93*	0.95*	−0.16
TR	311.01	73.15	23.52	45.49	0.01	0.96*		0.64
DD	73.00	6.03	8.25	18.18	0.00	0.49*	−0.89*	0.07
DS	16.66	1.50	9.00	4.08	0.01	0.81*	0.56*	0.38
DSP	5.51	1.37	24.87	5.77	0.03	0.89*	−0.82*	−0.86
ERA5–AGP								
WD	44.55	5.98	13.42	24.07	0.00	0.92*	0.95*	−0.10
WD _{P90}	4.52	1.42	31.29	2.23	0.06	0.94*	0.97*	1.19
WS	17.19	1.14	6.65	4.43	0.01	0.77*	0.49*	0.45
WSP	2.51	0.32	12.94	1.00	0.00	0.90*	0.91*	0.00
WSI	3.89	0.45	11.47	3.25	0.11	0.88*	0.88*	2.06*
SF	37.36	4.98	13.33	20.21	0.00	0.92*	0.95*	−0.01
TR	316.05	66.96	21.19	49.65	0.02	0.97*		0.56
DD	71.49	5.21	7.29	19.43	0.00	0.55*	−0.84*	−0.01
DS	16.86	1.19	7.06	4.29	0.01	0.79*	0.50*	0.20
DSP	5.69	1.30	22.85	5.60	0.04	0.92*	−0.79*	−1.05

Note: Column 1 refers to the acronym of ISD. Columns 2–9 refer to the mean, SD, CV, RMSE w.r.t OBS, R², correlation of ISDs w.r.t OBS, correlation of ISDs w.r.t total rainfall and trend, respectively.

*Significant at $p = .05$ according to Pearson's correlation and Mann–Kendall nonparametric trend test.

of wet and dry ISDs as compared to ERA5, whereas ERA5–NN exhibits slightly lower RMSE as compared to ERA5–AGP (Table 3). No significant trends appear in any ISD, except in the intensity of wet spells, which increases in OBS (ERA5–AGP) at a rate of +3.23 (+2.06) mm·day^{−1}, based on the Mann–Kendall trend test at $p = .05$ (Table 3).

3.2 | Contribution of ISDs to total seasonal rainfall

The relationship between total rainfall and ISDs was assessed using point-wise correlation (Figure 5). Overall, all wet ISDs exhibit a positive correlation with total rainfall, but the wet spells show a negative correlation over the northeastern

regions in ERA5 (WS panels in Figure 5a). Such negative correlations between wet spells and total rainfall over the northeastern regions, where the elevation is the highest, may once again highlight the limitation of ERA5 over complex terrains (cf. Figure S3). Regarding the relationship between dry ISDs (Thoithi *et al.*, 2020) and total rainfall, a significant negative relationship logically prevails (Figure 5b).

The correlation of two ISDs, WD and WD_{p90}, with total rainfall is particularly strong, exceeding 0.8 (significant at $p = .05$) in almost all grid-points (WD and WD_{p90} panels in Figure 5a). This indicates that the anomalously wet seasons primarily correspond to a higher number of wet and extreme wet days, thereby confirming the results of Tennant and Hewitson (2002). In addition to point-wise correlations, we also estimated the contributions of

ISDs to austral summer rainfall at the regional scale, using spatially averaged time series (lower right corner of each panel in Figure 5). The highest correlations are >0.94 and significant at $p = .05$ and are found for WD and WD_{p90}, consistently with the point-wise correlations. This highlights the critical importance of the two ISDs in shaping the rainfall variability over SA.

4 | RAINFALL EXTREMES

4.1 | Typology of extreme rainfall events

Here, we use the average spatial fraction of extreme rainfall events as a base criterion to differentiate large- and

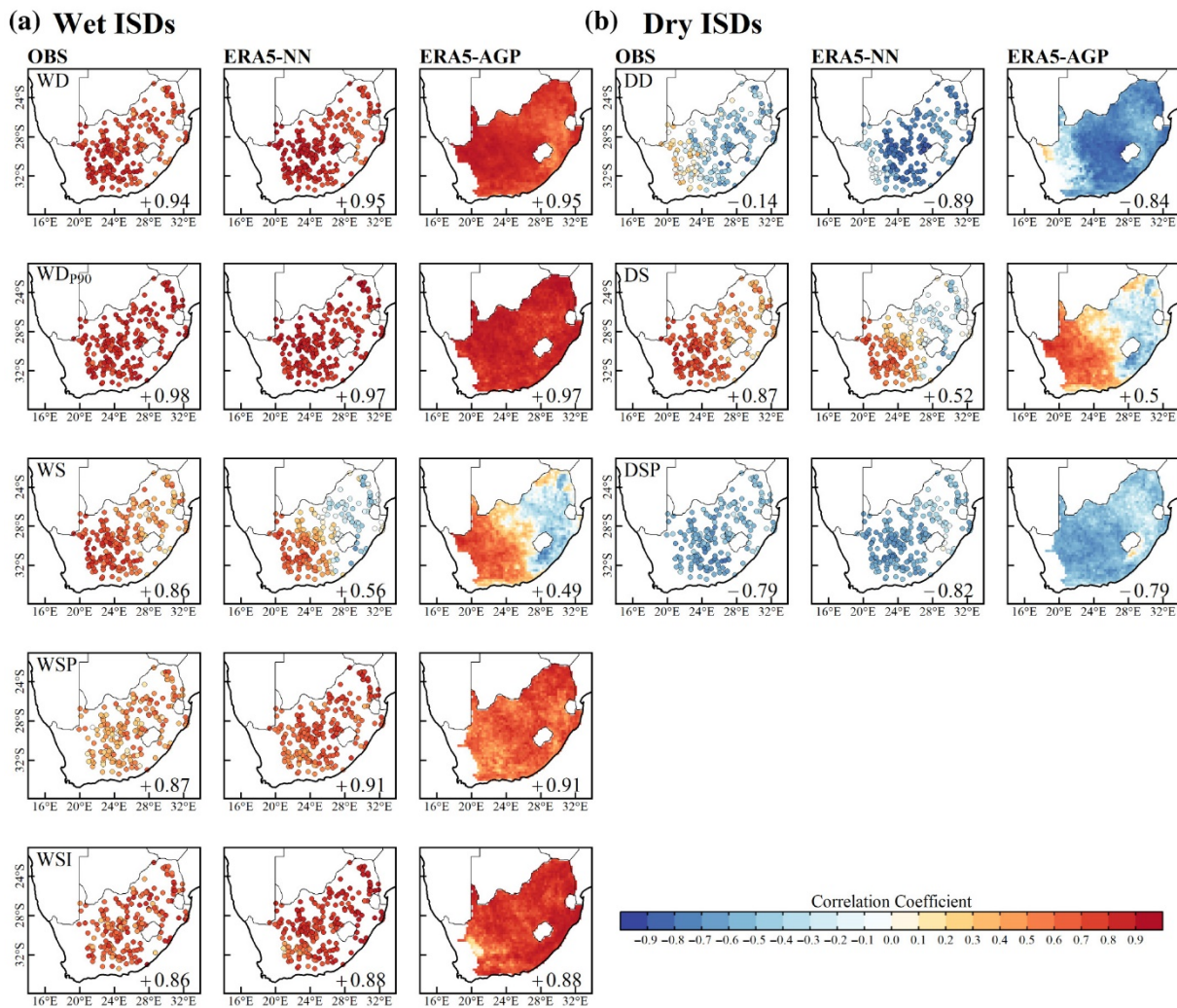


FIGURE 5 The spatial distribution of point-wise correlation of ISDs with total rainfall. The first set of three column panels on the left refers to the wet ISDs (a) and the set of three columns of panels on the right refers to the dry ISDs (b). The statistics are averaged over the period of 1979–2015 for NDJF using OBS, ERA5–NN and ERA5–AGP. The temporal correlations are presented in the lower right corner of each panel [Colour figure can be viewed at wileyonlinelibrary.com]

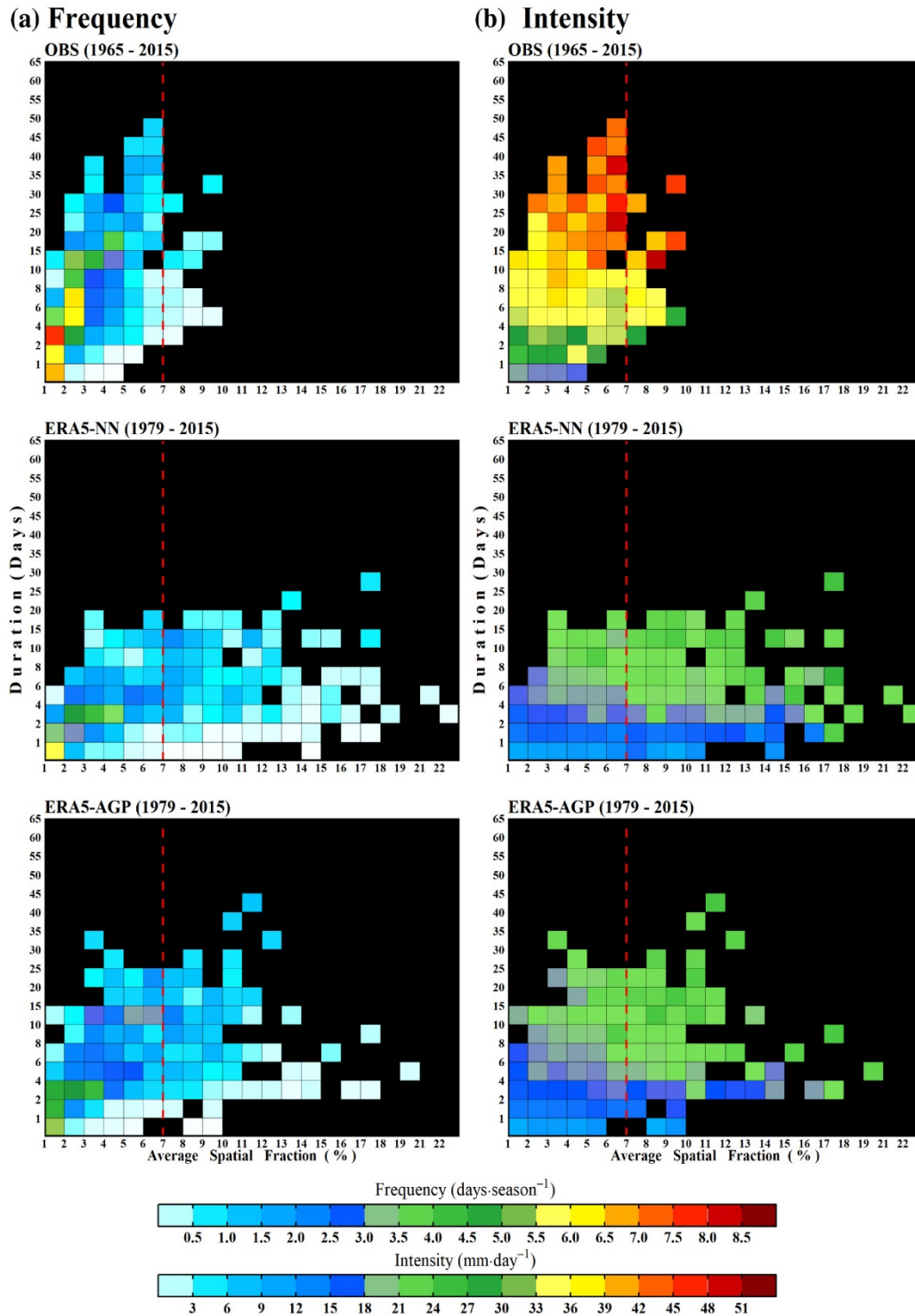


FIGURE 6 The frequency and intensity of extreme rainfall events as a function of average spatial fraction and duration. The set of three panels in the left column refers to frequency (a) and the set of three panels in the right column refers to intensity (b), distributed row-wise from top to bottom for OBS, ERA5-NN and ERA5-AGP, respectively. The vertical red line at 7% spatial fraction separates each panel in two quadrants which distinguishes the typology of rainfall extremes. The right (left) quadrant is associated with large-scale (small-scale) extreme rainfall events [Colour figure can be viewed at wileyonlinelibrary.com]

small-scale extreme events. Theoretically, large-scale extreme events should be embedded in large-scale modes of climate variability, and therefore show greater potential predictability. Meanwhile, small-scale extreme events are more likely related to isolated or organized convective cells, such as MCCs, which are stochastic in nature, and thus less predictable (Blamey and Reason, 2013). Thus, large-scale extreme events must exhibit a higher fraction of stations or grid-points simultaneously reaching the extreme threshold as compared to small-scale extremes. Moreover, it is also reasonable to speculate that large-scale extreme events are less frequent as compared to small-scale extremes in the austral summer season. To differentiate the characteristics of these two contrasting types of extremes, we assess here their multivariate distributions in terms of duration, spatial fraction, frequency, and intensity (Figure 6).

Defining a robust and relevant threshold for the spatial fraction of events was critically important. Given the aforementioned biases in the reanalysis, we rely solely on OBS to develop a relevant definition for the typology of extreme rainfall events (upper two panels in Figure 6). In OBS, the higher event intensity ($>27 \text{ mm}\cdot\text{day}^{-1}$) and lower frequency lies above a spatial fraction of 7% (Figure 6). A threshold of 7% for the spatial fraction therefore appears to be a good compromise to differentiate large- and small-scale extreme events. In order to assess the sensitivity to this threshold, we also considered 5 and 6% thresholds, and quantified the differences in the average characteristics of small- and large-scale extremes by assessing them in the context of ISDs. We found that, using other thresholds, large-scale extremes resulted in high frequency, thus obscuring distinct characteristics as compared to small-scale extremes (results not shown). The physical properties and the variability of the extreme rainfall events retrieved from the typology are further discussed in the context of ISDs in section 5.

4.2 | Spatial characteristics of rainfall extremes

Figure 7a (left panel) displays the average frequency of days exceeding the 1.0 mm threshold during large-scale extreme events for each station. Stations located along the preferable location of continental TTTs (bringing rainfall over SA: Fauchereau *et al.*, 2009; Macron *et al.*, 2014) tend to exhibit the highest frequency, which accounts for 4–7 days $\cdot\text{season}^{-1}$ (left panel in Figure 7a). This suggests that synoptic-scale rain-bearing systems could be responsible for large-scale extremes. When considering the 90th percentile threshold, an average frequency of 1–4 days $\cdot\text{season}^{-1}$ was shown by all stations

during large-scale extreme events (right panel in Figure 7a). It is interesting to note that each station exhibits extreme conditions from 1 to 4 times in a season. However, for each event, in order to qualify as a large-scale extreme event, at least 7% of the stations should attain their 90th percentile threshold on the same day. This suggests that during each event, a distinct set of stations responds with extreme conditions which depend exclusively on the synoptic features of the rain-bearing system and storm track. When analysing the intensity of large-scale extreme events by considering either the 1.0 mm or 90th percentile threshold, we note that the intensity of large-scale events is spatially uniform. This finding thus suggests that such extreme events bring sustained extreme conditions over the entire region (Figure 7c).

Different patterns of event frequency emerge when examining small-scale extremes (Figure 7b). Here, a SW–NE gradient prevails, especially when event frequency is computed by considering the 90th percentile threshold (right panel in Figure 7b). In particular, northeastern parts of SA show a higher frequency of small-scale extremes. These results are consistent with the findings of Blamey and Reason (2013) who demonstrated that the northeastern region of SA is the preferable location of MCCs. A SW–NE gradient is also quite visible for event intensity when computed by considering the 1.0 mm threshold (left panel in Figure 7d). No remarkable differences appear over the region when the intensity is computed by considering the 90th percentile threshold (right panel in Figure 7d). This result may be explained by the fact that the 90th percentile threshold of each station remains the same for large- and small-scale extremes.

In summary, a uniform distribution of frequency and intensity, computed either by considering the 1.0 mm or the 90th percentile threshold, indicates that large-scale extremes result from coherent rain-bearing systems with uniform extreme conditions throughout the spatial extension of the events. Meanwhile, during small-scale extreme events the extreme conditions largely prevail over the northeastern parts of SA.

4.3 | Spatial coherence of rainfall extremes

In this section, we assess the spatial coherence of large- and small-scale extremes. This analysis is particularly important in the context of large-scale extremes as it indicates whether extreme conditions during events are (a) uniformly distributed over the spatial extension of the events, suggesting that large-scale extremes are spatially coherent; (b) sporadically located, suggesting there could

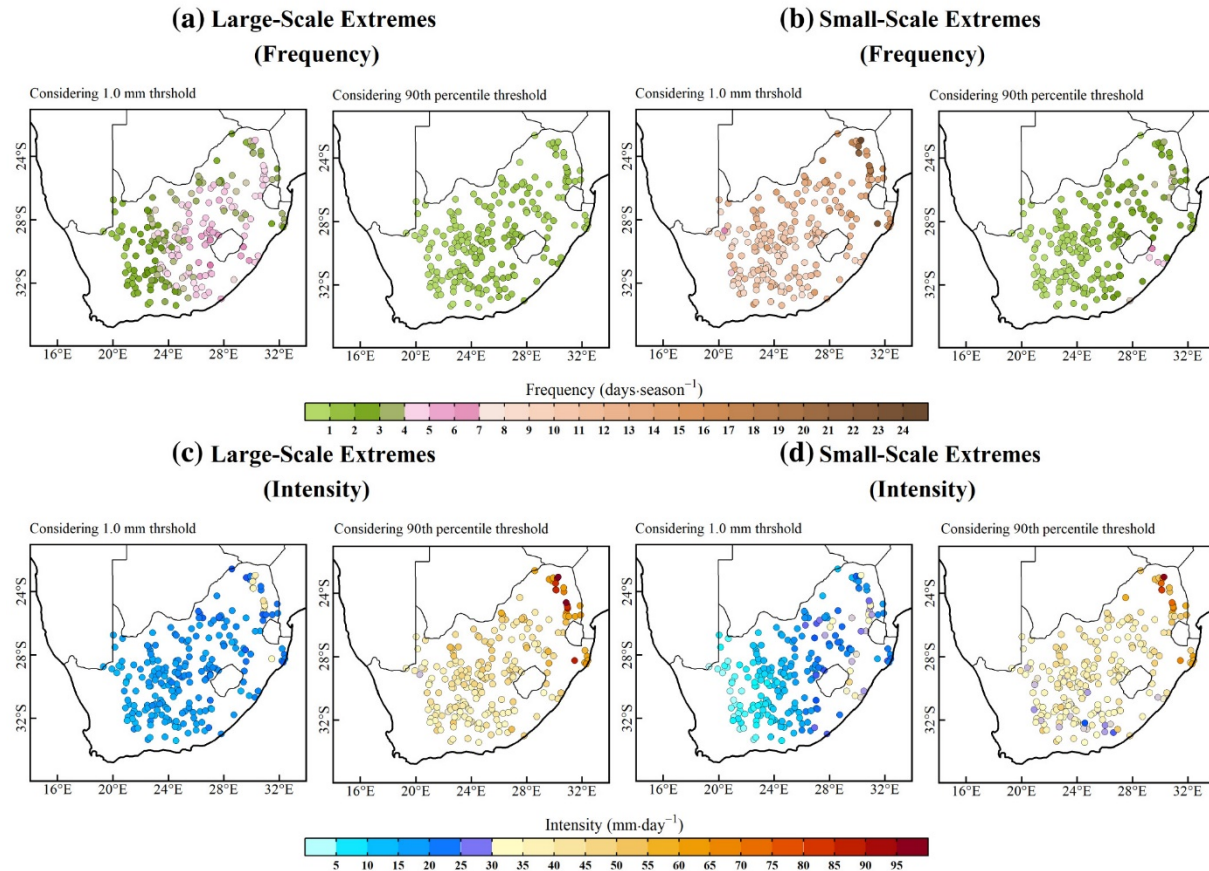


FIGURE 7 Average frequency computed over each station during large-scale extremes (a) and small-scale extremes (b) by considering the number of days exceeding 1.0 mm during events (left panel) and the 90th percentile during events (right panel). Same presentation for intensity in (c) and (d) [Colour figure can be viewed at wileyonlinelibrary.com]

be an aggregation of small-scale events occurring at the same time.

Figure 8 presents the density of the stations exceeding 1.0 mm-day^{-1} during the large-scale extreme events according to their latitude and longitude. A well-organized, nearly unimodal distribution of station density clearly prevails during all large-scale extreme events, fitting well with the distribution of the stations in the observational network. This suggests that the latter are spatially coherent in nature. Figure 9 duplicates this analysis for the core of the large-scale extreme events, where rainfall intensity causes the extreme threshold excess (i.e., only the stations exceeding their local 90th percentile of daily rainfall amounts). These stations also display organized and spatially coherent patterns, with unimodal distributions clearly prevailing. This suggests that during these events, the extreme wet conditions also show strong spatial coherence, most events being characterized by one single large-scale core rather than many smaller ones. Taken together, the results displayed in Figures 8

and 9 lead us to discard the hypothesis of several smaller and/or scattered events occurring at the same time. They also increase our confidence in the method used here to track large-scale rainfall extremes in SA.

The same analysis was then replicated for small-scale extreme events. As small-scale events are higher in number, for the sake of clarity we show the results for the month of January only (similar results were obtained for the other months and are not shown). Figure S4 shows the collective response of stations recording $>1.0 \text{ mm-day}^{-1}$ of rainfall during small-scale extreme events. Small-scale extreme events also exhibit an organized extension of rain-bearing systems over latitudes and longitudes, but with slightly fewer stations in each bin (Figure S4). Figure S5 displays the number of stations exceeded their 90th percentile in each 0.5° bin during the small-scale extreme events. Interestingly, we notice that extreme conditions occur only sporadically and locally over the region during small-scale events (Figure S5). Over longitudes, the over-representation of events located

between 28°E and 33°E could denote the influence of MCCs over eastern SA (Figure S5b), confirming the results reported by Blamey and Reason (2013). Taken together, these results suggest that the spatial extension of the rain-bearing system remains quite similar between small- and large-scale events, suggesting that they have the same physical nature (except for a larger proportion of MCCs in the case of small-scale extremes). However, the core regions associated with heavy rainfall dramatically change, showing that the rain-bearing systems mostly differ in the size of their core, bringing the largest rainfall amounts and thereby causing the climatic wet extreme.

In summary, analysing the spatial coherence of rainfall extremes provides a remarkable advantage in monitoring the collective behaviour of all stations during extreme events. The results demonstrate that using a 7% threshold of spatial extension as a base criterion to differentiate large- and small-scale extremes is robust and leads to separate events that drastically differ in terms of spatial coherence. Although both types of extremes can be considered as spatially coherent, as rainfall events occur over a large region at the same time, extreme conditions only occur sporadically over the region during small-scale events, contrasting with large-scale events for which extreme conditions are found over a larger and coherent region. This suggests that the nature of corresponding rain-bearing systems is the same, but that their intensity changes, an issue that will be further discussed and explored in Part II.

5 | INTRASEASONAL CHARACTERISTICS OF RAINFALL EXTREMES

In this section, large- and small-scale extreme rainfall events are examined in the context of ISDs.

5.1 | Multiyear variability of large-scale rainfall extremes

The average characteristics and multiyear variability of ISDs associated with large-scale extremes are displayed in Figure 10a. OBS (ERA5) shows an average of 8 ± 5 (20 ± 7) days associated with large-scale extremes, which are included in 5 ± 3 (10 ± 3) spells-season⁻¹, with an average persistence of 2 days (WD_{EXT} , WS_{EXT} and WSP_{EXT} panels in Figure 10a). In OBS (ERA5) total rainfall of about 167 ± 36 (129 ± 30) mm-season⁻¹ is driven by wet spells associated with large-scale extreme events (TR_{EXT} panels in Figure 10a). The multiyear variability of

ISDs is well captured by ERA5-NN and ERA5-AGP fields, with statistically significant correlations to OBS at $p < .05$ (Table 4(a)). Nevertheless, the intensity of wet spells remains highly underestimated by ERA5-NN and ERA5-AGP which shows average wet spell intensity of about 25.49 and 25.21 mm-day⁻¹, respectively (WSI_{EXT} panels in Figure 10a). In addition, in OBS, larger seasonal rainfall variability seems related to the smaller number of wet spells and wet days, as well as more intense events, but this is not identified in ERA5. Importantly, the observational network is found to be dense enough to study the variability of extreme ISDs associated with large-scale rainfall extremes, since there are no major differences in the results obtained with ERA5-NN and ERA5-AGP (Figure 10a). In all ISDs associated with large-scale extreme events, the CV remains higher in OBS than in ERA5 (Table 4(a)). Meanwhile, ERA5-NN exhibits lower RMSE as compared to ERA5-AGP, when computed with respect to OBS (Table 4(a)). No significant trend appears in most ISDs, except a significant increase of 2.30 spells-season⁻¹ identified in the observed number of wet spells, based on the Mann-Kendall trend test at $p = .05$ (Table 4(a)).

Relationships between seasonal total rainfall and ISDs associated with large-scale extremes are presented in Figure 11a. In all datasets, large-scale extreme ISDs exhibit strong positive correlations with total rainfall (significant at $p < .05$), except for the intensity of wet spells (Figure 11a). Overall, we find a strong association between seasonal total rainfall and the number of wet days and wet spells associated with large-scale extremes, as identified in OBS. The performance of ERA5 is still weaker, especially in the relationship between wet spells and total rainfall. This leads to conclusions similar to those presented in section 3 above, regarding the limitations of ERA5 in producing realistic wet spells and intensity.

5.2 | Multiyear variability of small-scale rainfall extremes

Analysis of ISDs associated with small-scale extremes is presented in Figure 10b. In OBS (ERA5), the frequency of days associated with small-scale extremes is 80 ± 9 (48 ± 7 for NN and 64 ± 7 for AGP), with an average frequency of 19 ± 3 (24 ± 3) spells-season⁻¹ (WD_{EXT} and WS_{EXT} panels in Figure 10b). These spells are, by construction, highly localized in space, with an average spatial extension of 1.5–2.5% over the SA domain, but they do exhibit a persistence of 2–4 days on average (WSP_{EXT} and ME_{EXT} panels in Figure 10b). OBS and ERA5 fields show average wet spells intensity of about 41.86 and

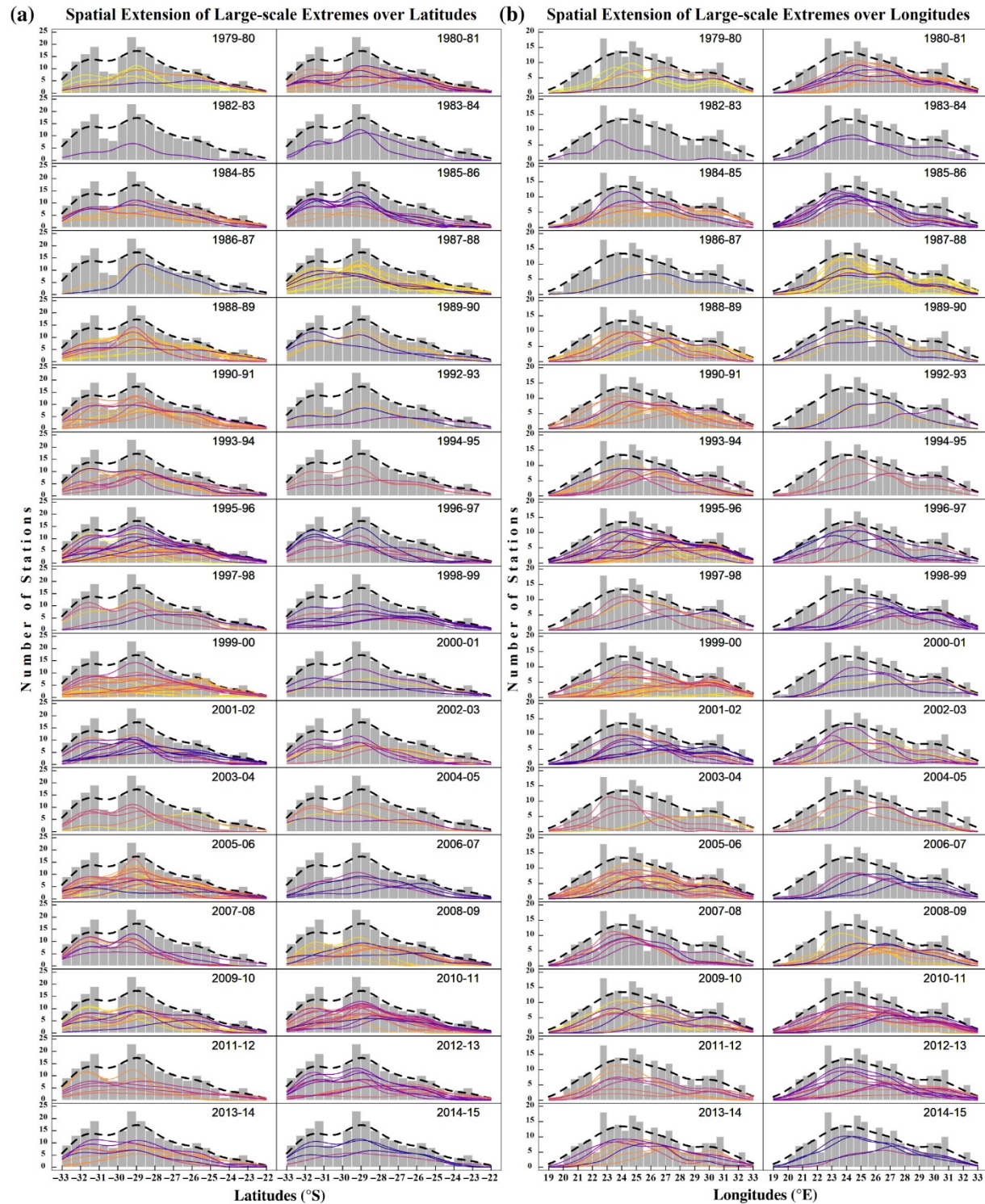


FIGURE 8 Spatial extension of large-scale extremes over latitudes (a) and over longitudes (b) computed by considering only those stations which exceeded 1.0 mm during large-scale extreme rainfall events with bin size = 0.5° . The histogram in each panel shows the frequency of the stations in each bin, whereas the black-dashed line in each panel represents the density of the stations provided as reference over latitudes and longitudes. Lines in distinct colours represent the density of the stations associated with each day of rainfall event in the respective seasons [Colour figure can be viewed at wileyonlinelibrary.com]

TABLE 4 Average statistics of extreme ISDs associated with large-scale extreme events (a) and small-scale extreme (b) in the austral summer season computed over the period 1979–2015 using OBS, ERA5–NN and ERA5–AGP

(a) Large-scale extremes								
ISD	Mean	±SD	CV%	RMSE w.r.t OBS	R ²	CC w.r.t OBS	CC w.r.t TR	Trend
OBS								
WD _{EXT}	8.03	5.35	66.66		0.06		0.93*	1.53
WS _{EXT}	4.88	2.55	52.28		0.08		0.82*	2.30*
WSP _{EXT}	1.70	0.57	33.21		0.01		0.49*	0.34
WSI _{EXT}	43.86	5.08	11.58		0.00		0.49*	0.74
SF _{EXT}	10.61	1.71	16.13		0.00		0.43*	1.02
TR _{EXT}	166.68	36.55	21.93		0.05			1.69
ERA5–NN								
WD _{EXT}	20.14	7.12	35.37	12.67	0.04	0.86*	0.92*	1.37
WS _{EXT}	10.47	3.20	30.57	6.50	0.06	0.56*	0.61*	1.28
WSP _{EXT}	1.95	0.55	28.31	0.74	0.00	0.43*	0.53*	0.00
WSI _{EXT}	25.49	1.60	6.27	19.19	0.01	0.38*	0.14	0.23
SF _{EXT}	16.14	2.45	15.19	6.70	0.02	0.51*	0.50*	0.26
TR _{EXT}	136.95	29.96	21.88	42.28	0.05	0.72*		0.94
ERA5–AGP								
WD _{EXT}	20.61	6.93	33.60	13.18	0.05	0.83*	0.90*	1.23
WS _{EXT}	10.39	3.22	30.97	6.39	0.02	0.59*	0.65*	0.66
WSP _{EXT}	2.02	0.49	24.37	0.76	0.02	0.43*	0.43*	1.50
WSI _{EXT}	25.21	1.18	4.69	19.49	0.02	0.36*	0.21	1.10
SF _{EXT}	15.33	2.30	15.02	5.91	0.03	0.53*	0.53*	0.86
TR _{EXT}	129.50	28.01	21.63	46.65	0.06	0.72*		1.10
(b) Small-scale extremes								
ISD	Mean	±SD	CV%	RMSE w.r.t OBS	R ²	CC w.r.t OBS	CC w.r.t TR	Trend
OBS								
WD _{EXT}	79.33	8.84	66.66		0.11		0.48*	1.75
WS _{EXT}	19.83	3.21	52.28		0.01		−0.20	0.76
WSP _{EXT}	4.16	1.09	33.21		0.01		0.31	0.16
WSI _{EXT}	41.86	2.28	11.58		0.08		0.38*	1.81
SF _{EXT}	1.89	0.29	16.13		0.11		0.82*	1.73
TR _{EXT}	29.57	7.44	21.93		0.16			2.17*
ERA5–NN								
WD _{EXT}	48.25	7.18	35.37	31.89	0.00	0.62*	0.54*	−0.12
WS _{EXT}	24.42	2.90	30.57	6.29	0.00	0.01	0.29	0.49
WSP _{EXT}	1.99	0.33	28.31	2.37	0.00	0.55*	0.30	−0.20
WSI _{EXT}	22.14	0.91	6.27	19.87	0.16	−0.02	−0.38*	2.00*
SF _{EXT}	2.37	0.34	15.19	0.58	0.02	0.43*	0.24	0.86
TR _{EXT}	20.02	4.01	21.88	10.87	0.05	0.74*		1.40
ERA5–AGP								
WD _{EXT}	64.28	6.93	33.60	16.65	0.01	0.62*	0.40*	−0.59
WS _{EXT}	24.14	2.95	30.97	5.43	0.00	0.42*	−0.14	0.67
WSP _{EXT}	2.72	0.54	24.37	1.70	0.01	0.59*	0.32	−0.99

(Continues)

TABLE 4 (Continued)

(b) Small-scale extremes								
ISD	Mean	$\pm SD$	CV%	RMSE w.r.t OBS	R^2	CC w.r.t OBS	CC w.r.t TR	Trend
WSI _{EXT}	21.49	0.70	4.69	20.48	0.13	0.27	-0.04	2.22*
SF _{EXT}	2.04	0.28	15.02	0.32	0.07	0.51*	0.60*	1.43
TR _{EXT}	17.22	3.55	21.63	13.36	0.10	0.79*		1.89

Note: Column 1 refers to the acronym of ISDs. Columns 2–9 refer to the mean, SD , CV, RMSE w.r.t OBS, R^2 , correlation of ISDs w.r.t OBS, correlation of ISDs w.r.t total rainfall and trend, respectively.

*Significant at $p = .05$ according to Pearson's correlation and Mann–Kendall nonparametric trend test.

21.49–22.14 mm·day⁻¹ (WSI_{EXT} panels in Figure 10b) which is quite like the average wet spell intensities noted for large-scale extremes. The plausible explanation of this similar behaviour is that both types of extremes are first tracked by using local 90th percentile threshold which is indeed same for each station or grid-point. These extremes are recognized differently in terms of spatial fraction (number of stations or grid-points which exceed the 90th percentile threshold simultaneously during a spell; cf. section 4.1).

In ERA5 (especially ERA–NN) and OBS, a significant trend appears in the intensity of wet spells associated with small-scale extreme events indicating a +2.0 mm·day⁻¹ average increase in the spell's intensity (Table 4). Although the contribution of small-scale extremes to total rainfall is quite low as compared to that of large-scale extremes, the increasing trend in the intensity of such highly localized storms could nonetheless have crucial importance, especially for the agricultural sector, among others. Such intensification of rainfall extremes could be a consequence of ongoing climate change (Kendon *et al.*, 2017, 2019; Pohl *et al.*, 2017) and could be due to the so-called Clausius–Clapeyron scaling, linking air warming trends to rainfall intensity increase through hygrometry (Betts and Harshvardhan, 1987; Trenberth *et al.*, 2003; Pall *et al.*, 2006; Kharin *et al.*, 2007; O'Gorman and Schneider, 2009; Muller *et al.*, 2011; Westra *et al.*, 2014). The relationship between the ISDs associated with small-scale extremes and the seasonal total rainfall amount is presented in Figure 11b. Except for the relationship between wet days associated with small-scale extremes and total rainfall, we note weak or negative relationships between ISDs and total rainfall (Figure 11b). Table 4b summarizes the relevant statistics for small-scale extreme ISDs.

The role of small-scale extremes in shaping total rainfall variability is moderate in austral summer. One plausible explanation for this is that the small-scale extremes are highly localized and are embedded in spatially coherent rain-bearing systems, which are mostly associated with nonextreme rainfall conditions over the region, as

already discussed in section 4. ERA5 fields show contrasting behaviours in small-scale extremes, as opposed to the results reported for large-scale extreme in section 5.1. In addition, the long-term variability of a few small-scale extreme ISDs (i.e., wet spells and wet spell intensity) is not fully realistic in ERA5, as demonstrated by weaker and nonsignificant correlations between both ERA5 fields and OBS (Table 4(b)). On the other hand, weaker yet significant correlations between ERA5 fields and OBS ranging from 0.42 to 0.79 are noted in other small-scale extreme ISDs (Table 4(b)). This implies that the density of the observational network might not be sufficient to detect most of these highly localized small-scale events, and/or that higher resolution reanalysis is required to skilfully capture these events.

5.3 | Respective contribution of large- and small-scale extremes to seasonal rainfall amount

Figure 12 displays the contribution of large-scale, small-scale and nonextreme rainfall to seasonal total rainfall amount. In OBS (ERA5), total rainfall associated with large-scale extremes shows an average contribution of about 58% (41–45%), against 11% (6%) for small-scale extremes (see, pie plots in Figure 12). This shows how dependent the region is on a small number of events that concentrate most of the rainfall. Although ERA5 overestimates austral summer rainfall amounts (section 3.1), it underestimates the contribution of rainfall extremes to total amounts. In ERA5, summer rainfall is mainly driven by nonextreme events, as opposed to OBS, where more than half of the summer rains seem to be associated with large-scale extreme events. The biases in ERA5 may result from an overestimation of the spatial extension of rain-bearing systems over the region, due to: (a) perfectible model physics and/or strong internal variability, for example, to simulate the small-scale atmospheric convection, and/or; (b) a limited amount of available radiosonde data to constrain the reanalysis, or

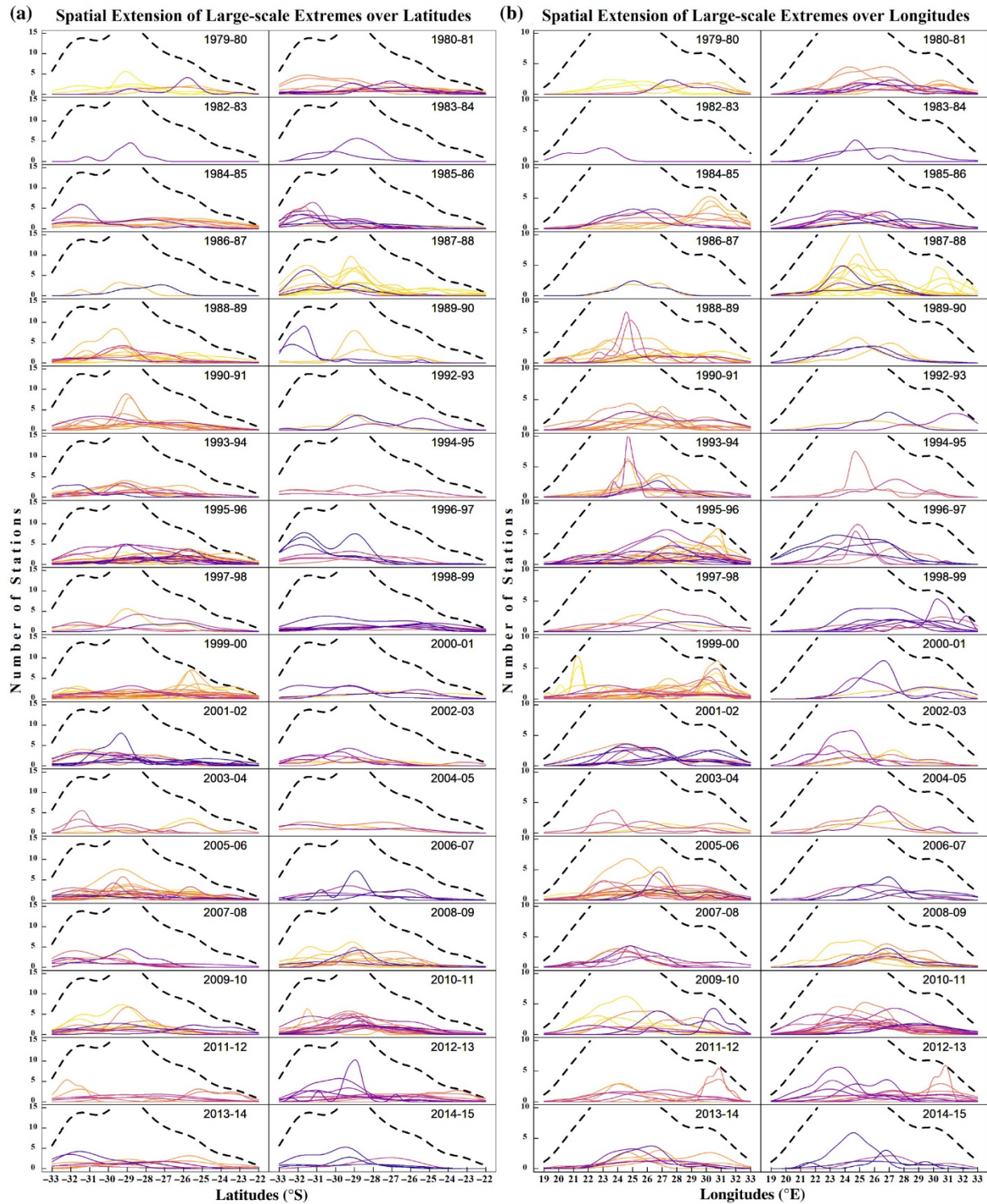
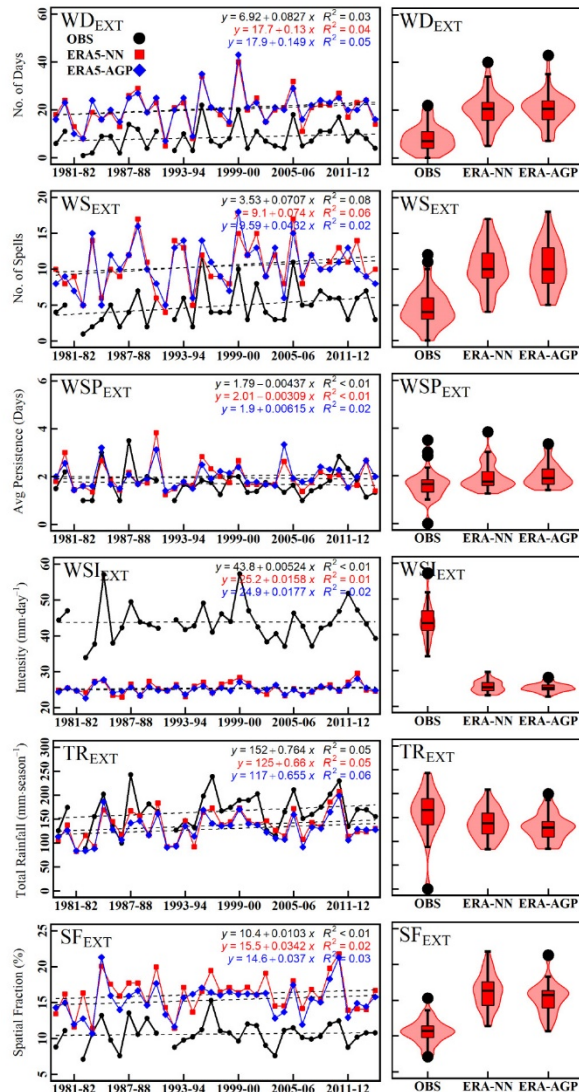


FIGURE 9 Spatial extension of large-scale extremes over latitudes (a) and over longitudes (b) computed by considering only those stations which exceeded the 90th percentile during large-scale extreme rainfall events with bin size = 0.5°. The black-dashed line in each panel represents the density of the stations provided as reference over latitudes and longitudes. Lines in distinct colours represent the density of the stations associated with each day of rainfall event in the respective seasons. For better visualization of density patterns, the y-axis has been reduced, and the histogram removed [Colour figure can be viewed at wileyonlinelibrary.com]

(a) ISDs (Large-scale Extremes)



(b) ISDs (Small-scale Extremes)

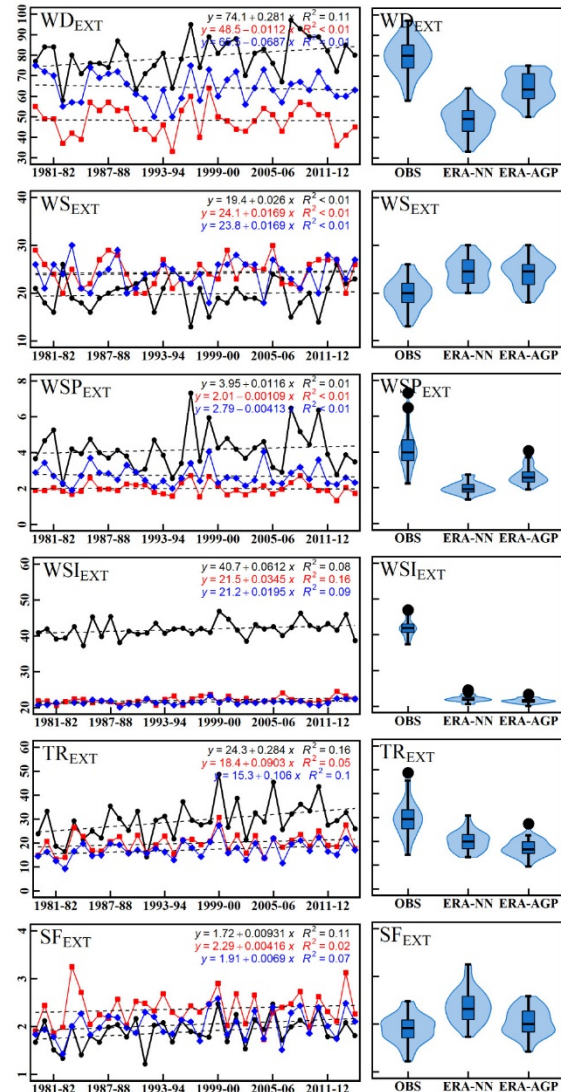


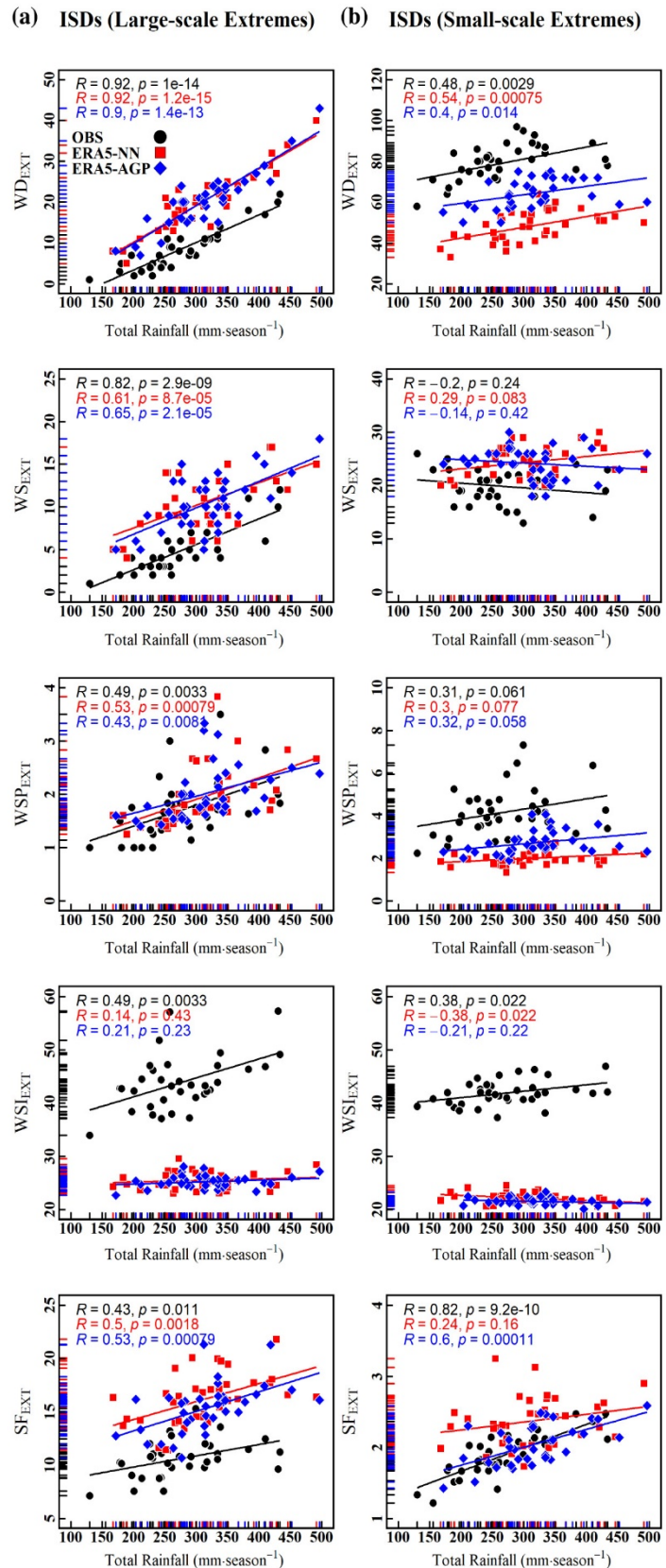
FIGURE 10 The average time series and overall statistical distribution (violin plots) of the ISDs associated with large-scale extremes (a) and for ISDs associated with small-scale extremes (b). The black line in each panel refers to the OBS, the red line indicates ERA5-NN and the blue line represents ERA5-AGP [Colour figure can be viewed at wileyonlinelibrary.com]

an assimilation technique that could extend atmospheric instability over too large regions.

Interestingly, during the 1981–1982 and 1991–1992 seasons, large-scale extremes do not contribute to rainfall amount, as rainfall is mostly driven by nonextreme rainfall in OBS (contributing to >90%; Figure 12). These two seasons are, however, extremely dry, with seasonal rainfall amounts 30–42% lower than normal, as noted in OBS (Figure 12). Such results are not found in ERA5, although a closer examination of these two seasons reveals that: (a) total rainfall deficit also exist

in ERA5 which accounts up to 22–40%, which is quite close to the OBS (see, TR panel in Figure 3); (b) ERA5 overestimates total rainfall and spatial fraction, which is why ERA5 could capture the few large-scale extreme events during these seasons (see, TR_{EXT} and SF_{EXT} panels in Figure 10a). In addition, these two seasons correspond to strong El Niño episodes, and it is well-understood that El Niño episodes can favour dry conditions over SA, and particularly large rainfall deficits (see, for instance, Dieppois *et al.*, 2015; 2016; 2019; Pascale *et al.*, 2019).

FIGURE 11 The scatter plot represents the statistical relationship between seasonal total rainfall and the extreme ISDs distributed row-wise from top to bottom for each descriptor. The set of five panels in the left column refers to large-scale extremes (a) and the set of five panels in the right column refers to small-scale extremes (b). In each panel OBS is indicated by the black symbol ●, ERA5–NN by the red symbols ■ and ERA5–AGP is presented in blue ◆ symbols [Colour figure can be viewed at wileyonlinelibrary.com]



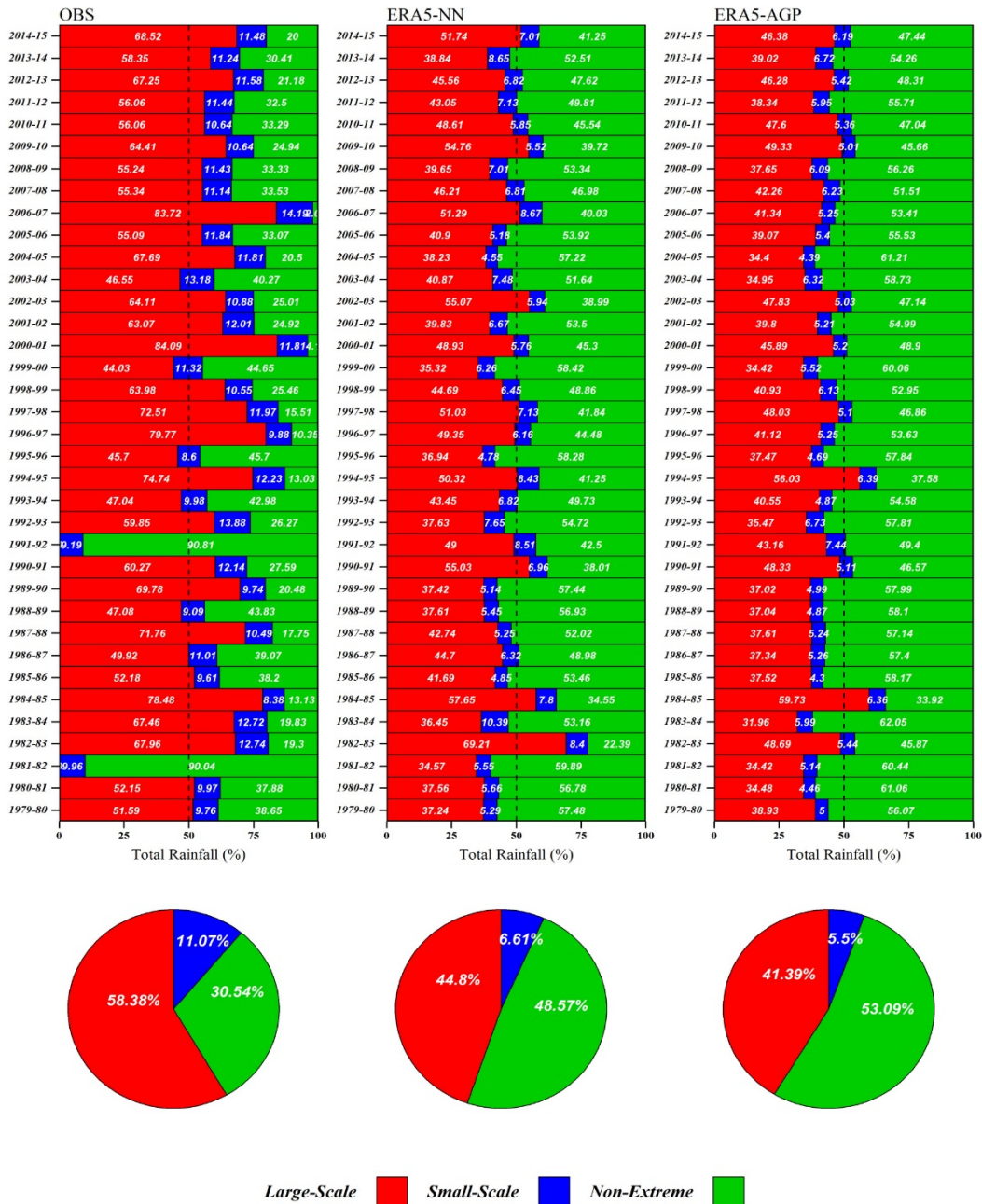


FIGURE 12 The stacked bar plot represents the overall contribution to the total rainfall in a season associated with large-scale extremes in red, small-scale extremes in blue and nonextreme contribution in green for OBS in the left panel, for ERA5-NN in the middle panel and ERA5-AGP in the right panel. Three pie plots at the bottom of each panel represent the overall distribution of total rainfall based on large-, small-scale and nonextreme rainfall variability averaged over the period of 1979–2015 [Colour figure can be viewed at wileyonlinelibrary.com]

On the contrary, in 1996–1997 and 2000–2001, the contribution of large-scale extremes to total rainfall amount exceeds 79%. Results from these wettest seasons

tie in well with previous studies (Hoell and Cheng, 2018), highlighting a synchronous influence of La Niña, active Angola Low and SIOD phasing, bringing together a

substantial surplus of rainfall over SA over those specific seasons. It is therefore likely that such connections do exist between rainfall extremes and different modes of variability. Thus, in the companion paper, we attempt to provide a comprehensive assessment of how rainfall extremes respond under low (interannual and decadal) and high (intraseasonal and synoptic) frequency modes of climate variability.

6 | CONCLUSIONS AND DISCUSSION

This study first examines the average characteristics of wet and dry intraseasonal descriptors in South Africa during the austral summer season from 1979 to 2015. A focus is then placed on extreme daily rainfall events. Using OBS and ERA5 reanalysis, extreme rainfall events are grouped into two types, according to their spatial fraction, separating large- and small-scale extremes. An investigation is then carried out to examine the spatial characteristics and coherence of such extremes. Finally, for the first time in a region-wide study, large- and small-scale extremes are explicitly assessed in the definition of intraseasonal descriptors.

The observational network of 225 stations provides an adequate spatial resolution to examine general rainfall characteristics and large-scale extremes in terms of intraseasonal descriptors. This is also true for ERA5, as the reanalysis performs remarkably well in the analysis of large-scale extremes, when analysed using its nearest neighbour and all-grid-point fields. Nevertheless, compared to OBS, ERA5 shows larger biases in reproducing small-scale extremes, thereby confirming that such reanalysis is primarily suited to analysis of large-scale climate processes and mechanisms.

Strong correlations between wet days (including extreme wet days) and total rainfall indicates that anomalously wet seasons generally correspond to higher numbers of extreme events. Summer SA rainfall is found to be primarily associated with large-scale extremes, which account for more than half of the seasonal amount in OBS, and nearly half of it in ERA5. The contribution and variability of small-scale extremes are not consistent across datasets and remain quite low. Moreover, the density of the observational network and the spatial resolution of current global reanalysis might not be sufficient to skilfully capture these events.

This study is a first step towards a more profound understanding of rainfall extremes in the region. The results demonstrate that using a threshold of 7% network density as base criterion and as a metric for the spatial

fraction produces good quality results in characterizing rainfall extremes over the region. The 7% threshold used to differentiate large- versus small-scale events is found not only relevant for the observational network, but also for ERA5-NN and ERA5-AGP. Based on our results, we find that large-scale extremes are well-organized and spatially coherent and might be embedded in TTTs of particularly stronger intensities. Meanwhile, small-scale extreme events, which might be related to mesoscale convective complexes and/or embedded in TTTs of weaker intensities, are highly localized in space and prevail largely over the northeastern parts of SA.

An added value of this work resides in the first presentation of a detailed mapping of rainfall variability over South Africa, including large- and small-scale extreme events, as well as nonextreme rainfall contribution. Such studies have immediate and considerable implications for theoretical and applied climate variability-based studies. These include, but are not limited to, societal sectors related to environment and energy, hydrology modelling and water resource management, and more specifically to agriculture, especially given the fact that South Africa is highly dependent on rain-fed agriculture.

In the companion paper (Part II) of this study, we attempt to assess the relationships of large- and small-scale extremes with low-frequency (interannual- and decadal-scale) and high-frequency (intraseasonal- and synoptic-scale) modes of variability. Such a typology of extremes will also be completed by considering their duration which is particularly important to differentiate short- and long-lived large-scale events. The latter may be considered as potentially high-impact rainfall events leading to high environmental or societal impacts, a question of major and ever-increasing importance under climate change.

ACKNOWLEDGEMENTS

This work is part of the I-SITE Bourgogne Franche-Comté Junior Fellowship IMVULA (AAP2-JF-06). It was also supported by the NRF SARCHI chair on “modeling ocean-atmosphere-land interactions” and the Nansen Tutu Centre for Marine studies. Calculations were performed using HPC resources from DNUM CCUB (Centre de Calcul de l’Université de Bourgogne).

AUTHOR CONTRIBUTIONS

Asmat Ullah: Conceptualization; formal analysis; investigation; methodology; validation; visualization; writing – original draft. **Benjamin Pohl:** Conceptualization; funding acquisition; resources; supervision; writing – review and editing. **Julien Pergaud:** Data curation; resources; software; supervision. **Bastien Dieppois:**

Conceptualization; data curation; writing – review and editing. **Mathieu Rouault:** Conceptualization; data curation; writing – review and editing.

ORCID

Asmat Ullah  <https://orcid.org/0000-0002-3453-0347>

REFERENCES

- Asmat, U. and Athar, H. (2017) Run-based multi-model interannual variability assessment of precipitation and temperature over Pakistan using two IPCC AR4-based AOGCMs. *Theoretical and Applied Climatology*, 127(1–2), 1–16. <https://doi.org/10.1007/s00704-015-1616-6>.
- Asmat, U., Athar, H., Nabeel, A. and Latif, M. (2018) An AOGCM based assessment of interseasonal variability in Pakistan. *Climate Dynamics*, 50(1–2), 349–373. <https://doi.org/10.1007/s00382-017-3614-0>.
- Betts, A.K. and Harshvardhan. (1987) Thermodynamic constraint on the cloud liquid water feedback in climate models. *Journal of Geophysical Research: Atmospheres*, 92(D7), 8483–8485. <https://doi.org/10.1029/JD092ID07P08483>.
- Blamey, R.C. and Reason, C.J.C. (2013) The role of mesoscale convective complexes in southern Africa summer rainfall. *Journal of Climate*, 26(5), 1654–1668. <https://doi.org/10.1175/JCLI-D-12-00239.1>.
- Camberlin, P., Moron, V., Okoola, R., Philippon, N. and Gitau, W. (2009) Components of rainy seasons' variability in equatorial East Africa: onset, cessation, rainfall frequency and intensity. *Theoretical and Applied Climatology*, 98(3–4), 237–249. <https://doi.org/10.1007/s00704-009-0113-1>.
- Conway, D., Van Garderen, E.A., Deryng, D., Dorling, S., Krueger, T., Landman, W., Lankford, B., Lebek, K., Osborn, T., Ringler, C., Thurlow, J., Zhu, T. and Dalin, C. (2015) Climate and southern Africa's water-energy-food nexus. *Nature Climate Change*, 5(9), 837–846. <https://doi.org/10.1038/nclimate2735>.
- Cook, C., Reason, C.J.C. and Hewitson, B.C. (2004) Wet and dry spells within particularly wet and dry summers in the South African summer rainfall region. *Climate Research*, 26(1), 17–31. <https://doi.org/10.3354/cr026017>.
- Cook, K.H. (2000) The south Indian convergence zone and interannual rainfall variability over southern Africa. *Journal of Climate*, 13(21), 3789–3804. [https://doi.org/10.1175/1520-0442\(2000\)013<3789:TSICZA>2.0.CO;2](https://doi.org/10.1175/1520-0442(2000)013<3789:TSICZA>2.0.CO;2).
- Cook, K.H. (2001) A southern hemisphere wave response to ENSO with implications for southern Africa precipitation. *Journal of the Atmospheric Sciences*, 58(15), 2146–2162. [https://doi.org/10.1175/1520-0469\(2001\)058<2146:ASHWRT>2.0.CO;2](https://doi.org/10.1175/1520-0469(2001)058<2146:ASHWRT>2.0.CO;2).
- Copernicus Climate Change Service (C3S). (2017) *ERA5: fifth generation of ECMWF atmospheric reanalyses of the global climate*. Copernicus Climate Change Service Climate Data Store (CDS). <https://doi.org/10.1002/joc.7310>
- Crétat, J., Richard, Y., Pohl, B., Rouault, M., Reason, C. and Fauchereau, N. (2012) Recurrent daily rainfall patterns over South Africa and associated dynamics during the core of the austral summer. *International Journal of Climatology*, 32(2), 261–273. <https://doi.org/10.1002/joc.2266>.
- Desbiolles, F., Blamey, R., Illig, S., James, R., Barimalala, R., Renault, L. and Reason, C. (2018) Upscaling impact of wind/sea surface temperature mesoscale interactions on southern Africa austral summer climate. *International Journal of Climatology*, 38(12), 4651–4660. <https://doi.org/10.1002/joc.5726>.
- Dieppois, B., Pohl, B., Crétat, J., Eden, J., Sidibe, M., New, M., Rouault, M. and Lawler, D. (2019) Southern African summer-rainfall variability, and its teleconnections, on interannual to interdecadal timescales in CMIP5 models. *Climate Dynamics*, 53(5–6), 3505–3527. <https://doi.org/10.1007/s00382-019-04720-5>.
- Dieppois, B., Pohl, B., Rouault, M., New, M., Lawler, D. and Keenlyside, N. (2016) Interannual to interdecadal variability of winter and summer southern African rainfall, and their teleconnections. *Journal of Geophysical Research*, 121, 6215–6239. <https://doi.org/10.1002/2015JD024576>.
- Dieppois, B., Rouault, M. and New, M. (2015) The impact of ENSO on southern African rainfall in CMIP5 ocean atmosphere coupled climate models. *Climate Dynamics*, 45(9–10), 2425–2442. <https://doi.org/10.1007/s00382-015-2480-x>.
- Donat, M.G., Lowry, A.L., Alexander, L.V., O'Gorman, P.A. and Maher, N. (2016) More extreme precipitation in the world's dry and wet regions. *Nature Climate Change*, 6, 508–513. <https://doi.org/10.1038/nclimate2941>.
- Engelbrecht, C.J., Engelbrecht, F.A. and Dyson, L.L. (2013) High-resolution model-projected changes in mid-tropospheric closed-lows and extreme rainfall events over southern Africa. *International Journal of Climatology*, 33(1), 173–187. <https://doi.org/10.1002/joc.3420>.
- Fauchereau, N., Pohl, B., Reason, C.J.C., Rouault, M. and Richard, Y. (2009) Recurrent daily OLR patterns in the southern Africa/southwest Indian ocean region, implications for South African rainfall and teleconnections. *Climate Dynamics*, 32(4), 575–591. <https://doi.org/10.1007/s00382-008-0426-2>.
- Favre, A., Hewitson, B., Lennard, C., Cerezo-Mota, R. and Tadross, M. (2013) Cut-off lows in the South Africa region and their contribution to precipitation. *Climate Dynamics*, 41(9–10), 2331–2351. <https://doi.org/10.1007/s00382-012-1579-6>.
- Favre, A., Philippon, N., Pohl, B., Kalognomou, E.A., Lennard, C., Hewitson, B., Nikulin, G., Dosio, A., Panitz, H.J. and Cerezo-Mota, R. (2016) Spatial distribution of precipitation annual cycles over South Africa in 10 CORDEX regional climate model present-day simulations. *Climate Dynamics*, 46(5–6), 1799–1818. <https://doi.org/10.1007/s00382-015-2677-z>.
- Fitchett, J.M. and Grab, S.W. (2014) A 66-year tropical cyclone record for south-east Africa: temporal trends in a global context. *International Journal of Climatology*, 34(13), 3604–3615. <https://doi.org/10.1002/joc.3932>.
- Frei, C., Christensen, J.H., Déqué, M., Jacob, D., Jones, R.G. and Vidale, P.L. (2003) Daily precipitation statistics in regional climate models: evaluation and intercomparison for the European Alps. *Journal of Geophysical Research: Atmospheres*, 108(3), 1–19. <https://doi.org/10.1029/2002jd002287>.
- Gitau, W., Camberlin, P., Ogallo, L. and Bosire, E. (2018) Trends of intraseasonal descriptors of wet and dry spells over equatorial eastern Africa. *International Journal of Climatology*, 38(3), 1189–1200. <https://doi.org/10.1002/joc.5234>.
- Gitau, W., Camberlin, P., Ogallo, L. and Okoola, R. (2015) Oceanic and atmospheric linkages with short rainfall season intraseasonal statistics over equatorial eastern Africa and their predictive potential. *International Journal of Climatology*, 35(9), 2382–2399. <https://doi.org/10.1002/joc.4131>.

- Gitau, W., Ogallo, L., Camberlin, P. and Okoola, R. (2013) Spatial coherence and potential predictability assessment of intra-seasonal statistics of wet and dry spells over equatorial eastern Africa. *International Journal of Climatology*, 33(12), 2690–2705. <https://doi.org/10.1002/joc.3620>.
- Gleixner, S., Demissie, T. and Diro, G.T. (2020) Did ERA5 improve temperature and precipitation reanalysis over East Africa? *Atmosphere*, 11(9), 1–19. <https://doi.org/10.3390/atmos11090996>.
- Hart, N.C.G., Reason, C.J.C. and Fauchereau, N. (2010) Tropical-extratropical interactions over southern Africa: three cases of heavy summer season rainfall. *Monthly Weather Review*, 138(7), 2608–2623. <https://doi.org/10.1175/2010MWR3070.1>.
- Hart, N.C.G., Reason, C.J.C. and Fauchereau, N. (2013) Cloud bands over southern Africa: seasonality, contribution to rainfall variability and modulation by the MJO. *Climate Dynamics*, 41(5–6), 1199–1212. <https://doi.org/10.1007/s00382-012-1589-4>.
- Hersbach, H., Bell, B., Berrisford, P., Hirahara, S., Horányi, A., Muñoz-Sabater, J., Nicolas, J., Peubey, C., Radu, R., Schepers, D., Simmons, A., Soci, C., Abdalla, S., Abellan, X., Balsamo, G., Bechtold, P., Biavati, G., Bidlot, J., Bonavita, M., De Chiara, G., Dahlgren, P., Dee, D., Diamantakis, M., Dragani, R., Flemming, J., Forbes, R., Fuentes, M., Geer, A., Haimberger, L., Healy, S., Hogan, R.J., Hólm, E., Janisková, M., Keeley, S., Laloyaux, P., Lopez, P., Lupu, C., Radnoti, G., de Rosnay, P., Rozum, I., Vamborg, F., Villaume, S. and Thépaut, J.N. (2020) The ERA5 global reanalysis. *Quarterly Journal of the Royal Meteorological Society*, 146(730), 1999–2049. <https://doi.org/10.1002/qj.3803>.
- Hoell, A. and Cheng, L. (2018) Austral summer southern Africa precipitation extremes forced by the El Niño–Southern Oscillation and the subtropical Indian Ocean Dipole. *Climate Dynamics*, 50(9–10), 3219–3236. <https://doi.org/10.1007/s00382-017-3801-z>.
- Hoell, A., Funk, C., Magadzire, T., Zinke, J. and Husak, G. (2015) El Niño–Southern Oscillation diversity and southern Africa teleconnections during austral summer. *Climate Dynamics*, 45(5–6), 1583–1599. <https://doi.org/10.1007/s00382-014-2414-z>.
- James, R., Hart, N.C.G., Munday, C., Reason, C.J.C. and Washington, R. (2020) Coupled climate model simulation of tropical–extratropical cloud bands over southern Africa. *Journal of Climate*, 33(19), 8579–8602. <https://doi.org/10.1175/JCLI-D-19-0731.1>.
- Kendall, M.G. (1957) *Rank Correlation Methods*, 4th edition. London: Charles Griffin.
- Kendon, E.J., Ban, N., Roberts, N.M., Fowler, H.J., Roberts, M.J., Chan, S.C., Evans, J.P., Fosser, G. and Wilkinson, J.M. (2017) Do convection-permitting regional climate models improve projections of future precipitation change? *Bulletin of the American Meteorological Society*, 98(1), 79–93. <https://doi.org/10.1175/BAMS-D-15-0004.1>.
- Kendon, E.J., Stratton, R.A., Tucker, S., Marsham, J.H., Berthou, S., Rowell, D.P. and Senior, C.A. (2019) Enhanced future changes in wet and dry extremes over Africa at convection-permitting scale. *Nature Communications*, 10(1), 1794. <https://doi.org/10.1038/s41467-019-09776-9>.
- Kharin, V.V., Zwiers, F.W., Zhang, X. and Hegerl, G.C. (2007) Changes in temperature and precipitation extremes in the IPCC Ensemble of Global Coupled Model Simulations. *Journal of Climate*, 20(8), 1419–1444. <https://doi.org/10.1175/JCLI4066.1>.
- Koseki, S., Pohl, B., Bhatt, B.C., Keenlyside, N. and Njoudo, A.S.N. (2018) Insights into the summer diurnal cycle over eastern South Africa. *Monthly Weather Review*, 146(12), 4339–4356. <https://doi.org/10.1175/MWR-D-18-0184.1>.
- Lu, E., Zhao, W., Zou, X., Ye, D., Zhao, C. and Zhang, Q. (2017) Temporal-spatial monitoring of an extreme precipitation event: determining simultaneously the time period it lasts and the geographic region it affects. *Journal of Climate*, 30(16), 6123–6132. <https://doi.org/10.1175/JCLI-D-17-0105.1>.
- Macron, C., Pohl, B., Richard, Y. and Bessafi, M. (2014) How do tropical temperate troughs form and develop over southern Africa? *Journal of Climate*, 27(4), 1633–1647. <https://doi.org/10.1175/JCLI-D-13-00175.1>.
- Malherbe, J., Engelbrecht, F.A., Landman, W.A. and Engelbrecht, C.J. (2012) Tropical systems from the Southwest Indian Ocean making landfall over the Limpopo River Bassouthern Africa: a historical perspective. *International Journal of Climatology*, 32(7), 1018–1032. <https://doi.org/10.1002/joc.2320>.
- Malherbe, J., Landman, W.A. and Engelbrecht, F.A. (2014) The bi-decadal rainfall cycle, Southern Annular Mode and tropical cyclones over the Limpopo River basin, southern Africa. *Climate Dynamics*, 42(11–12), 3121–3138. <https://doi.org/10.1007/s00382-013-2027-y>.
- Manhique, A.J., Reason, C.J.C., Rydberg, L. and Fauchereau, N. (2011) ENSO and Indian Ocean Sea surface temperatures and their relationships with tropical temperate troughs over Mozambique and the Southwest Indian Ocean. *International Journal of Climatology*, 31(1), 1–13. <https://doi.org/10.1002/joc.2050>.
- Mann, H. (1945) Mann nonparametric test against trend. *Econometrica*, 13, 245.
- Maraun, D. (2016) Bias correcting climate change simulations—a critical review. *Current Climate Change Reports*, 2(4), 211–220. <https://doi.org/10.1007/s40641-016-0050-x>.
- Mason, S.J., Goddard, L., Graham, N.E., Yulaeva, E., Sun, L. and Arkin, P.A. (1999) The IRI seasonal climate prediction system. WRPMD 1999: Preparing for the 21st Century. [https://doi.org/10.1061/40430\(1999\)4](https://doi.org/10.1061/40430(1999)4).
- Mason, S.J. and Joubert, A.M. (1997) Simulated changes in extreme rainfall over southern Africa. *International Journal of Climatology*, 17(3), 291–301. [https://doi.org/10.1002/\(sici\)1097-0088\(19970315\)17:3<291::aid-joc120>3.3.co;2-t](https://doi.org/10.1002/(sici)1097-0088(19970315)17:3<291::aid-joc120>3.3.co;2-t).
- Masupha, T.E., Moeletsi, M.E. and Tsubo, M. (2016) Dry spells assessment with reference to the maize crop in the Luvuvhu River catchment of South Africa. *Physics and Chemistry of the Earth*, 92, 99–111. <https://doi.org/10.1016/j.pce.2015.10.014>.
- Misra, V. (2003) The influence of Pacific SST variability on the precipitation over southern Africa. *Journal of Climate*, 16(14), 2408–2418. <https://doi.org/10.1175/2785.1>.
- Moron, V., Camberlin, P. and Robertson, A.W. (2013) Extracting subseasonal scenarios: an alternative method to analyze seasonal predictability of regional-scale tropical rainfall. *Journal of Climate*, 26(8), 2580–2600. <https://doi.org/10.1175/JCLI-D-12-00357.1>.
- Muller, C.J., O’Gorman, P.A. and Back, L.E. (2011) Intensification of precipitation extremes with warming in a cloud-resolving model. *Journal of Climate*, 24(11), 2784–2800. <https://doi.org/10.1175/2011JCLI3876.1>.

- Nicholson, S. (2003) Comments on "The south Indian convergence zone and interannual rainfall variability over southern Africa" and the question of ENSO's influence on southern Africa. *Journal of Climate*, 16(3), 555–562. [https://doi.org/10.1175/1520-0442\(2003\)016<0555:COTSIC>2.0.CO;2](https://doi.org/10.1175/1520-0442(2003)016<0555:COTSIC>2.0.CO;2).
- Nicholson, S.E. and Kim, J. (1997) The relationship of the el MNO–Southern Oscillation to African rainfall. *International Journal of Climatology*, 17(2), 117–135. [https://doi.org/10.1002/\(SICI\)1097-0088\(199702\)17:2<117::AID-JOC84>3.0.CO;2-O](https://doi.org/10.1002/(SICI)1097-0088(199702)17:2<117::AID-JOC84>3.0.CO;2-O).
- O'Gorman, P.A. and Schneider, T. (2009) Scaling of precipitation extremes over a wide range of climates simulated with an idealized GCM. *Journal of Climate*, 22(21), 5676–5685. <https://doi.org/10.1175/2009JCLI2701.1>.
- Oueslati, B., Pohl, B., Moron, V., Rome, S. and Janicot, S. (2017) Characterization of heat waves in the Sahel and associated physical mechanisms. *Journal of Climate*, 30(9), 3095–3115. <https://doi.org/10.1175/JCLI-D-16-0432.1>.
- Pall, P., Allen, M.R. and Stone, D.A. (2006) Testing the Clausius–Clapeyron constraint on changes in extreme precipitation under CO₂ warming. *Climate Dynamics*, 28(4), 351–363. <https://doi.org/10.1007/S00382-006-0180-2>.
- Pascale, S., Pohl, B., Kapnick, S.B. and Zhang, H. (2019) On the Angola low interannual variability and its role in modulating ENSO effects in southern Africa. *Journal of Climate*, 32(15), 4783–4803. <https://doi.org/10.1175/JCLI-D-18-0745.1>.
- Philippon, N., Camberlin, P., Moron, V. and Boyard-Micheau, J. (2015) Anomalously wet and dry rainy seasons in equatorial East Africa and associated differences in intra-seasonal characteristics. *Climate Dynamics*, 45(7–8), 2101–2121. <https://doi.org/10.1007/s00382-014-2460-6>.
- Pinto, I., Lennard, C., Tadross, M., Hewitson, B., Dosio, A., Nikulin, G., Panitz, H.J. and Shongwe, M.E. (2016) Evaluation and projections of extreme precipitation over southern Africa from two CORDEX models. *Climatic Change*, 135(3–4), 655–668. <https://doi.org/10.1007/s10584-015-1573-1>.
- Pohl, B., Dieppois, B., Crétat, J., Lawler, D. and Rouault, M. (2018) From synoptic to interdecadal variability in southern African rainfall: toward a unified view across time scales. *Journal of Climate*, 31(15), 5845–5872. <https://doi.org/10.1175/JCLI-D-17-0405.1>.
- Pohl, B., MacRon, C. and Monerie, P.A. (2017) Fewer rainy days and more extreme rainfall by the end of the century in southern Africa. *Scientific Reports*, 7, 6–12. <https://doi.org/10.1038/srep46466>.
- Pohl, B., Richard, Y. and Fauchereau, N. (2007) Influence of the Madden–Julian oscillation on southern African summer rainfall. *Journal of Climate*, 20(16), 4227–4242. <https://doi.org/10.1175/JCLI4231.1>.
- Pohl, B., Rouault, M. and Sen, R.S. (2014) Simulation of the annual and diurnal cycles of rainfall over South Africa by a regional climate model. *Climate Dynamics*, 43(7–8), 2207–2226. <https://doi.org/10.1007/s00382-013-2046-8>.
- Rapolaki, R.S., Blamey, R.C., Hermes, J.C. and Reason, C.J.C. (2019) A classification of synoptic weather patterns linked to extreme rainfall over the Limpopo River basin in southern Africa. *Climate Dynamics*, 53(3–4), 2265–2279. <https://doi.org/10.1007/s00382-019-04829-7>.
- Rapolaki, R.S., Blamey, R.C., Hermes, J.C. and Reason, C.J.C. (2020) Moisture sources associated with heavy rainfall over the Limpopo River basin, southern Africa. *Climate Dynamics*, 55(5–6), 1473–1487. <https://doi.org/10.1007/s00382-020-05336-w>.
- Ratan, R. and Venugopal, V. (2013) Wet and dry spell characteristics of global tropical rainfall. *Water Resources Research*, 49(6), 3830–3841. <https://doi.org/10.1002/wrcr.20275>.
- Ratnam, J.V., Behera, S.K., Masumoto, Y. and Yamagata, T. (2014) Remote effects of El Niño and Modoki events on the austral summer precipitation of southern Africa. *Journal of Climate*, 27(10), 3802–3815. <https://doi.org/10.1175/JCLI-D-13-00431.1>.
- Reason, C.J.C. (2007) Tropical cyclone Dera, the unusual 2000/01 tropical cyclone season in the south West Indian Ocean and associated rainfall anomalies over southern Africa. *Meteorology and Atmospheric Physics*, 97(1–4), 181–188. <https://doi.org/10.1007/s00703-006-0251-2>.
- Reason, C.J.C., Hachigonta, S. and Phaladi, R.F. (2005) Interannual variability in rainy season characteristics over the Limpopo region of southern Africa. *International Journal of Climatology*, 25(14), 1835–1853. <https://doi.org/10.1002/joc.1228>.
- Reason, C.J.C. and Keibel, A. (2004) Tropical cyclone Eline and its unusual penetration and impacts over the southern Africa mainland. *Weather and Forecasting*, 19(5), 789–805. [https://doi.org/10.1175/1520-0434\(2004\)019<0789:TCEAIU>2.0.CO;2](https://doi.org/10.1175/1520-0434(2004)019<0789:TCEAIU>2.0.CO;2).
- Reason, C.J.C., Landman, W. and Tennant, W. (2006) Seasonal to decadal prediction of southern African climate and its links with variability of the Atlantic Ocean. *Bulletin of the American Meteorological Society*, 87(7), 941–955. <https://doi.org/10.1175/BAMS-87-7-941>.
- Rouault, M., Florenchie, P., Fauchereau, N. and Reason, C.J.C. (2003) South east tropical Atlantic warm events and southern African rainfall. *Geophysical Research Letters*, 30(5), 1–4. <https://doi.org/10.1029/2002GL014840>.
- Rouault, M., White, S.A., Reason, C.J.C., Lutjeharms, J.R.E. and Jobard, I. (2002) Ocean–atmosphere interaction in the Agulhas current region and a South African extreme weather event. *Weather and Forecasting*, 17, 655–669. [https://doi.org/10.1175/1520-0434\(2002\)017<0655:OAITA>2.0.CO;2](https://doi.org/10.1175/1520-0434(2002)017<0655:OAITA>2.0.CO;2).
- Shongwe, M.E., Van Oldenborgh, G.J., Van Den Hurk, B.J.J.M., De Boer, B., Coelho, C.A.S. and Van Aalst, M.K. (2009) Projected changes in mean and extreme precipitation in Africa under global warming. Part I: southern Africa. *Journal of Climate*, 22(13), 3819–3837. <https://doi.org/10.1175/2009JCLI2317.1>.
- Tennant, W.J. and Hewitson, B.C. (2002) Intra-seasonal rainfall characteristics and their importance to the seasonal prediction problem. *International Journal of Climatology*, 22(9), 1033–1048. <https://doi.org/10.1002/joc.778>.
- Thoithi, W., Blamey, R.C. and Reason, C.J.C. (2020) Dry spell frequencies, wet day counts and their trends across southern Africa during the summer rainy season. *Geophysical Research Letters*, 48, e91041. <https://doi.org/10.1029/2020GL091041>.
- Todd, M. and Washington, R. (1999) Circulation anomalies associated with tropical-temperate troughs in southern Africa and the south west Indian Ocean. *Climate Dynamics*, 15(12), 937–951. <https://doi.org/10.1007/s003820050323>.
- Todd, M.C., Washington, R. and Palmer, P.I. (2004) Water vapour transport associated with tropical-temperate trough systems over southern Africa and the southwest Indian Ocean. *International Journal of Climatology*, 24(5), 555–568. <https://doi.org/10.1002/joc.1023>.

- Trenberth, K.E., Dai, A., Rasmussen, R.M. and Parsons, D.B. (2003) The changing character of precipitation. *Bulletin of the American Meteorological Society*, 84(9), 1205–1218. <https://doi.org/10.1175/BAMS-84-9-1205>.
- Usman, M.T. and Reason, C.J.C. (2004) Dry spell frequencies and their variability over southern Africa. *Climate Research*, 26(3), 199–211. <https://doi.org/10.3354/cr026199>.
- Vigaud, N., Pohl, B. and Crétat, J. (2012) Tropical-temperate interactions over southern Africa simulated by a regional climate model. *Climate Dynamics*, 39(12), 2895–2916. <https://doi.org/10.1007/s00382-012-1314-3>.
- Wang, G., Zhang, X. and Zhang, S. (2019) Performance of three reanalysis precipitation datasets over the qinling-daba mountains, eastern fringe of tibetan plateau, China. *Advances in Meteorology*, 2019, 1–16. <https://doi.org/10.1155/2019/7698171>.
- Washington, R. and Todd, M. (1999) Tropical-temperate links in southern African and Southwest Indian Ocean satellite-derived daily rainfall. *International Journal of Climatology*, 19, 1601–1616. [https://doi.org/10.1002/\(SICI\)1097-0088\(19991130\)19:14<1601::AID-JOC407>3.0.CO;2-0](https://doi.org/10.1002/(SICI)1097-0088(19991130)19:14<1601::AID-JOC407>3.0.CO;2-0).
- Westra, S., Fowler, H.J., Evans, J.P., Alexander, L.V., Berg, P., Johnson, F., Kendon, E.J., Lenderink, G. and Roberts, N.M. (2014) Future changes to the intensity and frequency of short-duration extreme rainfall. *Reviews of Geophysics*, 52(3), 522–555. <https://doi.org/10.1002/2014RG000464>.

SUPPORTING INFORMATION

Additional supporting information may be found in the online version of the article at the publisher's website.

How to cite this article: Ullah, A., Pohl, B., Pergaud, J., Dieppois, B., & Rouault, M. (2022). Intraseasonal descriptors and extremes in South African rainfall. Part I: Summer climatology and statistical characteristics. *International Journal of Climatology*, 42(9), 4538–4563. <https://doi.org/10.1002/joc.7489>

Supplementary Figures: Chapter 2

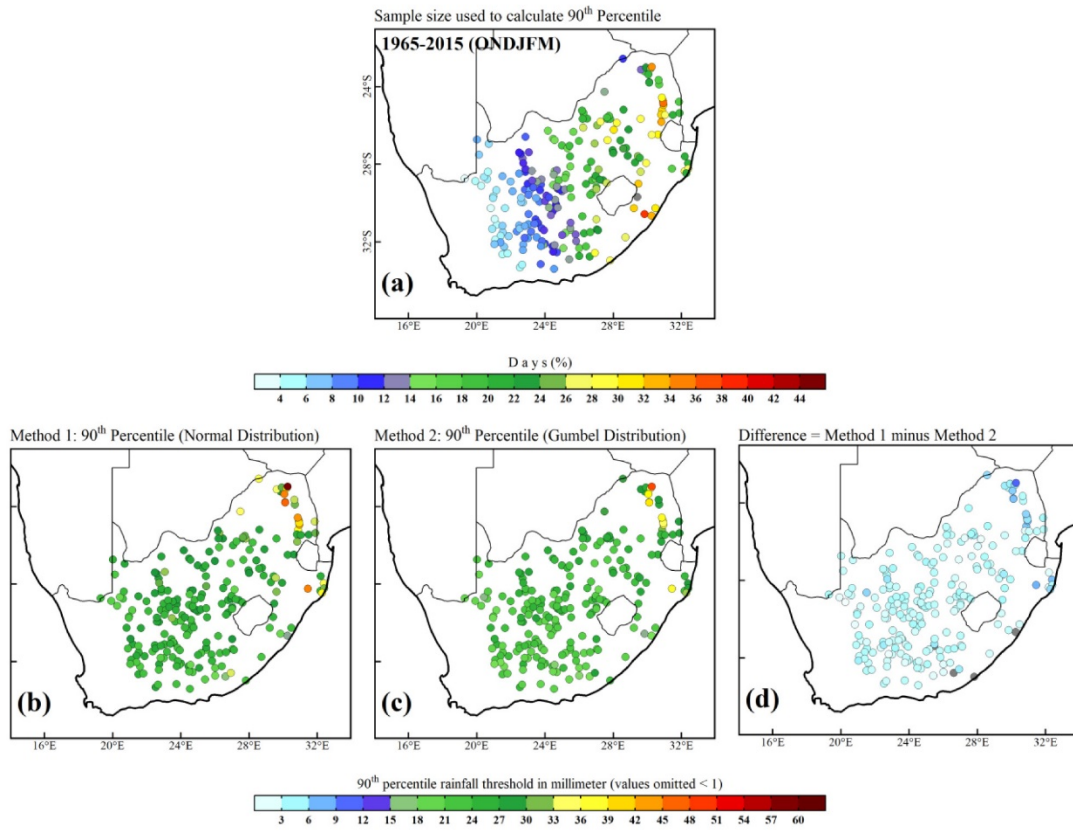


Figure S1 Sample size used to compute 90th percentile (a), 90th percentile threshold computed by considering normal distribution (b), theoretical extreme value computed by Gumbel distribution (c) and the difference of both methods (d).

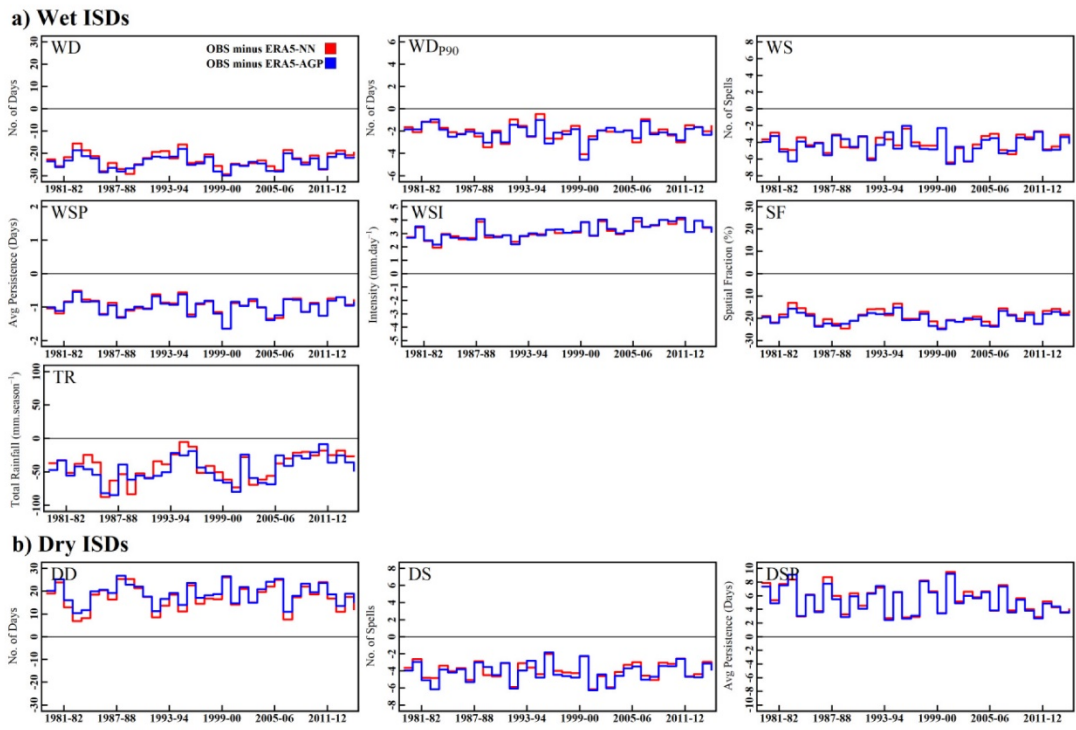


Figure S2 The average seasonal bias of ISDs, set of first three rows containing seven panels from top refers to the wet ISDs (a) and set of three panels in bottom refers to the dry ISDs (b). OBS minus ERA5-NN is displayed by a red line and OBS minus ERA5-AGP is presented with a blue line.

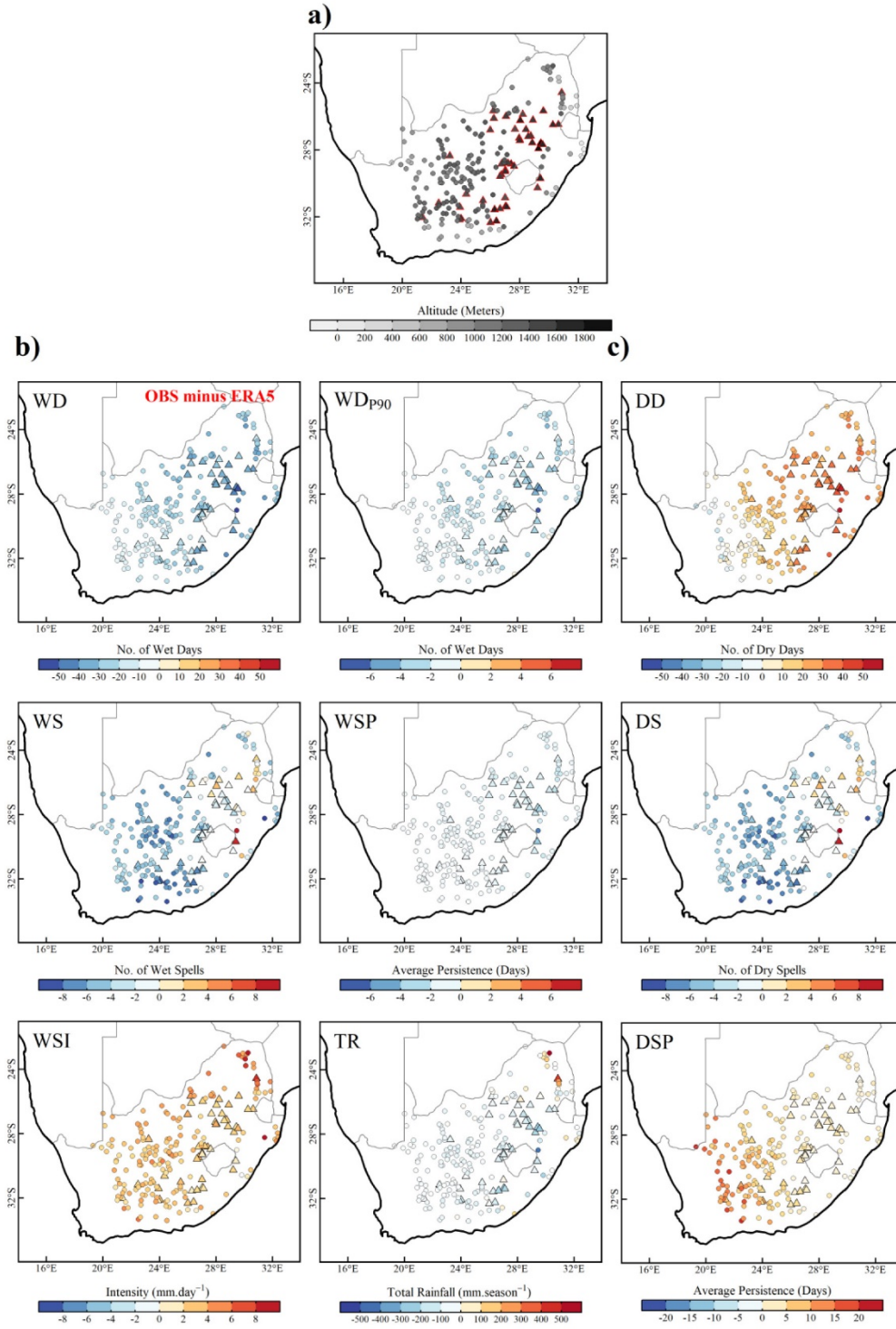


Figure S3 Altitude of stations in meters (a). The two columns from left are associated with spatial bias in the wet ISDs (b). The third column from left is associated with spatial bias in the dry ISDs (c). The stations located at $>1,400$ m are indicated by triangle symbols in each panel.

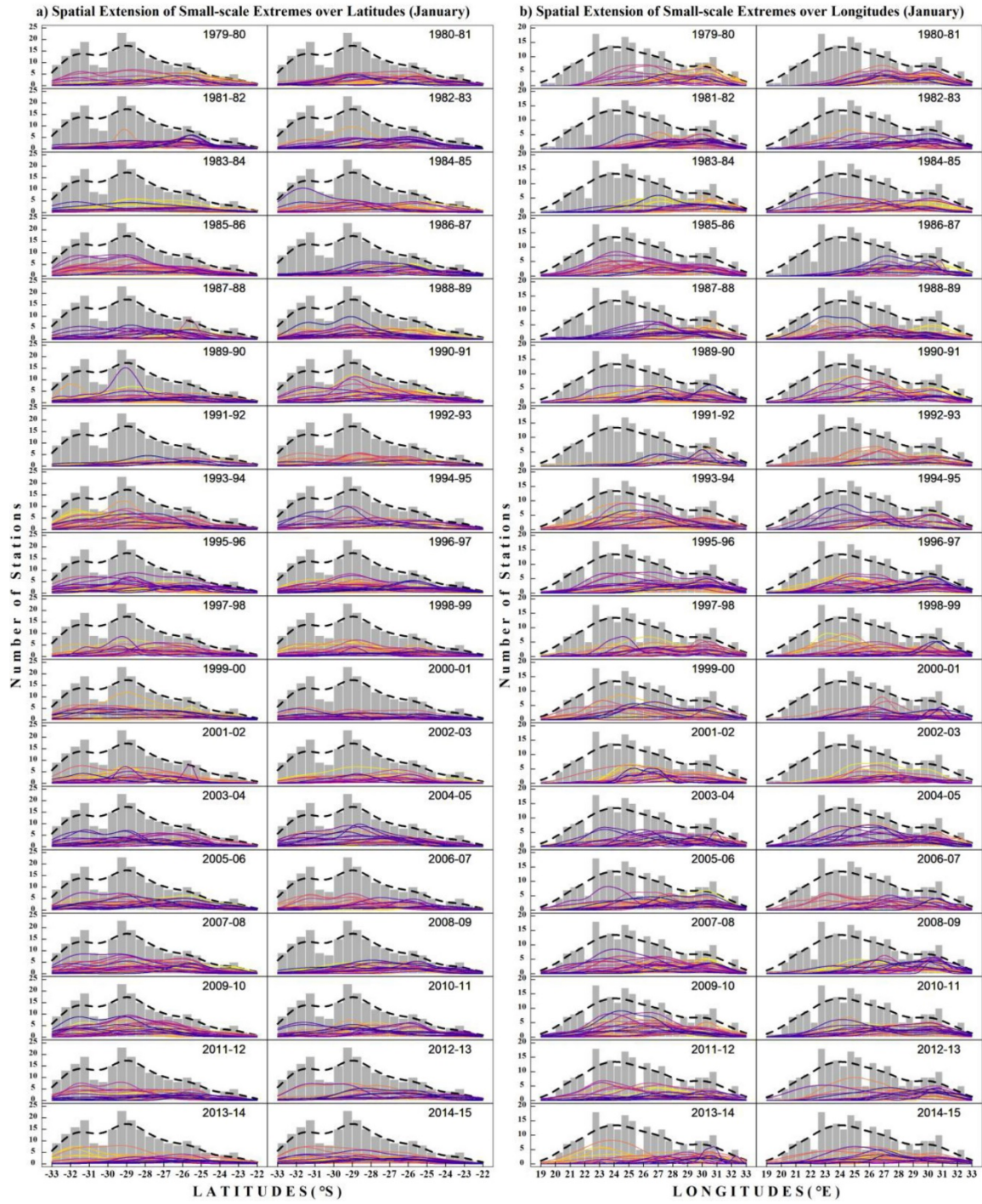


Figure S4 Same as Figure 8 but for small-scale extremes.

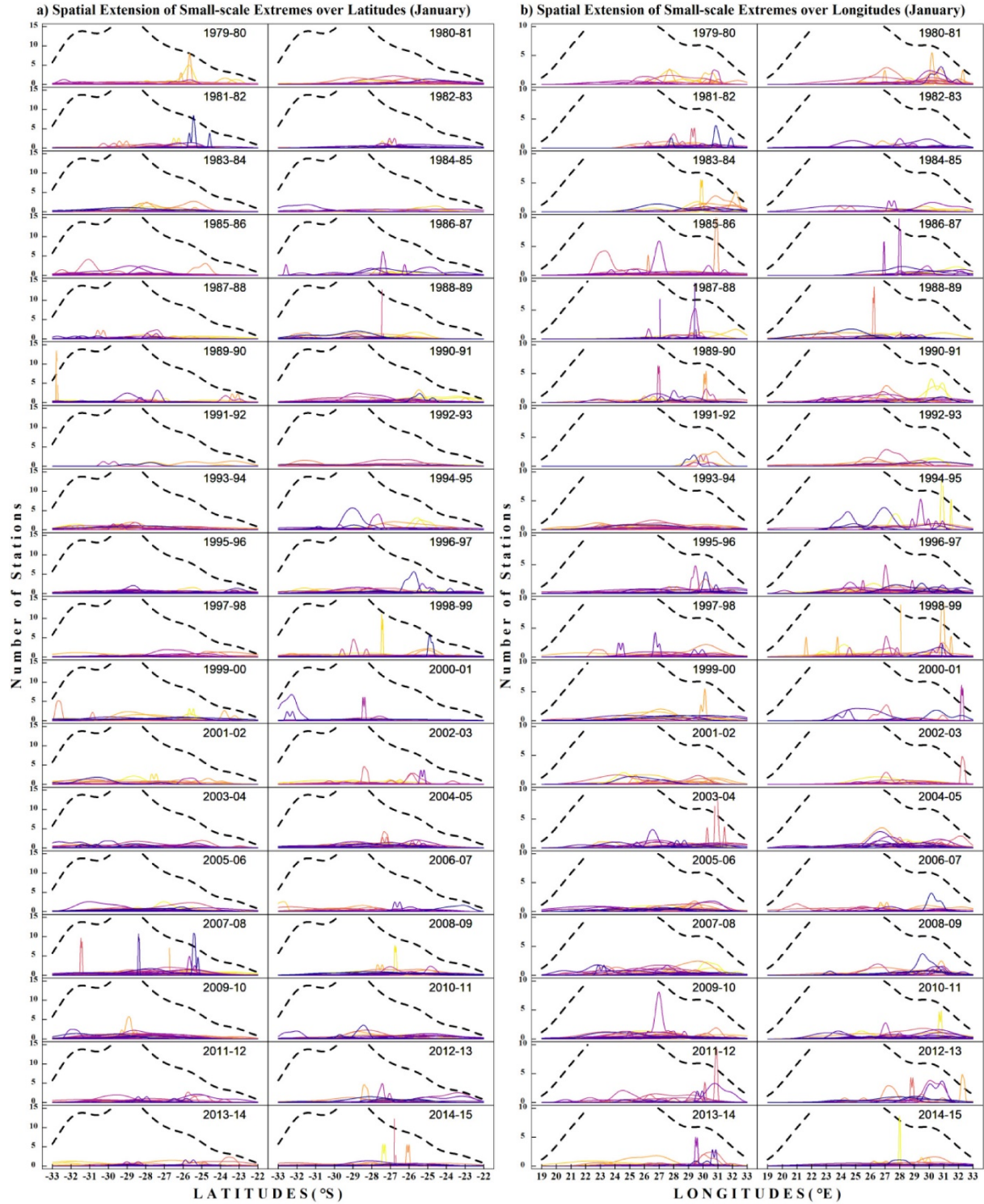


Figure S5 Same as Figure 9 but for small-scale extremes.

Chapter 3

Summer teleconnections across multiple timescales

Abstract

Extreme events contribute significantly to rainfall variability in semi-arid regions like South Africa. Here, following the definition of a novel typology of rainfall extremes, disentangling large- and small-scale events in Part I, we use quality-controlled observational databases in South Africa, the ERA5 reanalysis and satellite estimates TRMM-3B42 to examine the relationship between these two types of rainfall extremes and different modes of climate variability at various timescales. At low-frequencies, rainfall extremes are assessed at interannual (IV: 2–8 years) and quasi-decadal (QDV: 8–13 years) timescales, which are primarily associated with the El Niño Southern Oscillation (ENSO) and the Interdecadal Pacific Oscillation (IPO), respectively. At sub-seasonal timescales, the typology of rainfall extremes is analysed depending on the synoptic configurations, as inferred by seven convective regimes including Tropical Temperate Troughs (TTTs: 3–7 days), and the intraseasonal variability associated with the Madden-Julien Oscillation (MJO: 30–60 days).

At the IV timescale, the occurrence of large-scale extremes is substantially higher during its wet phases thereby suggesting a 400% rise in the occurrence of large-scale extremes as compared to its dry phases. At the QDV timescale, variability mostly relates to the modulation of small-scale extremes during its wet phases. Teleconnections with global Sea Surface Temperature (SST) confirm that La Niña conditions favour overall wet conditions and extremes in South Africa. The numbers of large-scale extremes are consistently related to warmer SSTs in the North Atlantic, while their link with warmer Indian and tropical South Atlantic oceans is found to be statistically independent of the state of ENSO. At the sub-seasonal timescales, large-scale extremes largely occur during 3 out of the 7 convective regimes identified in the southern African region whereas small-scale extremes are nearly equiprobable during all convective regimes. The occurrence of large-scale extremes during continent-rooted TTT is further enhanced during the locally wet phases of the MJO and is symmetrically weakened during its dry phases.

Intraseasonal descriptors and extremes in South African rainfall.

Part II: Summer teleconnections accros multiple timescales

Asmat Ullah^{1*} ; Benjamin Pohl¹ ; Julien Pergaud¹ ; Bastien Dieppois² ; Mathieu Rouault³

¹ Centre de Recherches de Climatologie, UMR 6282 Biogéosciences, CNRS/ Université de Bourgogne Franche-Comté, Dijon, France

² Centre for Agroecology, Water and Resilience, Coventry University, Coventry, UK

³ Nansen Tutu Center for Marine Environmental Research, Department of Oceanography, University of Cape Town, South Africa

International Journal of Climatology

Accepted 03 March 2023

*** Corresponding Author's Address**

Asmat ullah: asmat-786@hotmail.com

Laboratoire Biogéosciences
Université de Bourgogne
6 Boulevard Gabriel
21000 DIJON – FRANCE

Abstract

Extreme events contribute significantly to rainfall variability in semi-arid regions like South Africa. Here, following the definition of a novel typology of rainfall extremes, disentangling large- and small-scale events in Part I, we use quality-controlled observational databases in South Africa, the ERA5 reanalysis and satellite estimates TRMM-3B42 to examine the relationship between these two types of rainfall extremes and different modes of climate variability at various timescales. At low-frequencies, rainfall extremes are assessed at interannual (IV: 2–8 years) and quasi-decadal (QDV: 8–13 years) timescales, which are primarily associated with the El Niño Southern Oscillation (ENSO) and the Interdecadal Pacific Oscillation (IPO), respectively. At sub-seasonal timescales, the typology of rainfall extremes is analysed depending on the synoptic configurations, as inferred by seven convective regimes including Tropical Temperate Troughs (TTTs: 3–7 days), and the intraseasonal variability associated with the Madden-Julien Oscillation (MJO: 30–60 days).

At the IV timescale, the occurrence of large-scale extremes is substantially higher during its wet phases thereby suggesting a 400% rise in the occurrence of large-scale extremes as compared to its dry phases. At the QDV timescale, variability mostly relates to the modulation of small-scale extremes during its wet phases. Teleconnections with global Sea Surface Temperature (SST) confirm that La Niña conditions favour overall wet conditions and extremes in South Africa. The numbers of large-scale extremes are consistently related to warmer SSTs in the North Atlantic, while their link with warmer Indian and tropical South Atlantic oceans is found to be statistically independent of the state of ENSO. At the sub-seasonal timescales, large-scale extremes largely occur during 3 out of the 7 convective regimes identified in the southern African region whereas small-scale extremes are nearly equiprobable during all convective regimes. The occurrence of large-scale extremes during continent-rooted TTT is further enhanced during the locally wet phases of the MJO and is symmetrically weakened during its dry phases.

Key-Words

Rainfall — Large-scale and small-scale extremes — South Africa — El Niño Southern Oscillation — Interdecadal Pacific Oscillation — Tropical–temperate troughs — Atmospheric convection — Madden–Julien oscillation

1. Introduction

Hydrometeorological extremes such as droughts and floods are of crucial importance for human society. Such extremes are likely to be more frequent and intense at and above 1.5°C global warming levels (Donat *et al.*, 2016). Several studies have explored the response of rainfall extremes to climate change in South Africa (Mason and Joubert, 1997; Mason *et al.*, 1999; Shongwe *et al.*, 2009; Engelbrecht *et al.*, 2013; Pinto *et al.*, 2016). Pohl *et al.* (2017) pointed out a significant decrease in the number of rainy days and an increase in their intensity, in line with the Clausius-Clapeyron relation linking air moisture to temperature. Similar results are drawn using convection-permitting models at the regional scales (Kendon *et al.*, 2017, 2019; Jackson *et al.*, 2020; Senior *et al.*, 2021). However, despite its primary importance in predicting potential climate risks in sectors such as agriculture and hydropower (Conway *et al.*, 2015, 2017), we currently know very little about how these extreme rainfall events are distributed during the austral summer season at the synoptic, intraseasonal, interannual and decadal timescale.

During the main rainy season from November to February (hereinafter NDJF), rainfall exhibits three significant timescales of variability related to the distinct modes of Pacific variability over the twentieth century: interannual (IV: 2–8 years), quasi-decadal (QDV: 8–13 years) and interdecadal variations (IDV: 15–28 years; Dieppois *et al.*, 2016, 2019). Hereafter, the IV, QDV and IDV timescales are referred to as low-frequency timescales of variability.

At the IV timescale, rainfall variability is strongly modulated by El Niño Southern Oscillation (Nicholson and Kim, 1997; Washington and Preston, 2006; Dieppois *et al.*, 2015). Typically, El Niño conditions tend to favour dry summers while La Niña led to above-normal rainfall in South Africa. However, the relationship between ENSO and rainfall is not systematic, since not every El Niño event leads to dry conditions over the region (Rouault and Richard, 2004; Reason and Jagadheesha, 2005). This could be due to interferences with the Angola Low (Lyon and Mason, 2007; Pascale *et al.*, 2019) or the Subtropical Indian Ocean Dipole (SIOD: Hoell and Cheng, 2018). Moreover, recent changes in the number of dry spells and wet days in southern Africa could relate to a combined influence of ENSO, the Southern Annular Mode (SAM), SIOD and the Botswana High (Thoithi *et al.*, 2020).

At the quasi-decadal timescale, rainfall variability mostly relates to the Interdecadal Pacific Oscillation (IPO: Dieppois *et al.*, 2016, 2019). IPO exhibits ENSO-like Sea Surface Temperature

(SST) patterns, shifting the Walker-circulation zonally and resulting in an eastward shift of the South Indian Convergence Zone (SICZ), thus modifying the preferential location and intensity of Tropical Temperate Troughs (TTTs: Pohl *et al.*, 2018). However, how much interannual and decadal timescales of climate variability affect the likelihood and the total rainfall variability associated with extreme rainfall events is not known.

At the sub-seasonal timescales, austral summer rainfall variability is strongly associated with synoptic-scale (i.e., 1–7 days), notably the convective cloud bands widely known as TTTs (Todd and Washington, 1999; Washington and Todd, 1999; Todd *et al.*, 2004; Fauchereau *et al.*, 2009; Hart *et al.*, 2010; Vigaud *et al.*, 2012; Macron *et al.*, 2014). TTTs are responsible for 30–60% of summer rainfall in southern Africa (Reason *et al.*, 2006; Hart *et al.*, 2013; Macron *et al.*, 2014). TTTs are oriented from northwest to southeast and are the results of interactions between transient perturbations in the midlatitudes and tropical convection (Hart *et al.*, 2010; Macron *et al.*, 2014; James *et al.*, 2020), thereby linking the tropics to the temperate latitudes. Other notable rain-bearing systems of summer rainfall are Mesoscale Convective Complexes (MCCs: Blamey and Reason, 2013), squall lines (Rouault *et al.*, 2002), tropical storms (Reason and Keibel, 2004; Malherbe *et al.*, 2012, 2014; Fitchett and Grab, 2014) and Cut-off lows (Favre *et al.*, 2013).

Austral summer rainfall also varies at intraseasonal timescales (i.e., 30–60 days), where the Madden-Julien Oscillation (MJO) is the dominant mode of variability (Madden and Julian, 1994; Zhang, 2005). The MJO is characterized as an eastward propagation of large-scale convective clusters in the tropics, which recur every 30 to 60 days (Madden and Julian, 1994; Zhang, 2005), and have overarching effects on rainfall patterns across the world (Zhang, 2005; Donald *et al.*, 2006). Several cohort studies investigated the connection between MJO and precipitation over South Africa in various dimensions. Pohl *et al.* (2007) were the first to point out the influence of the MJO on summer rainfall variability across southern Africa. Their results were further completed and confirmed by Oettli *et al.* (2014). Grimm and Reason (2015) assessed the intraseasonal teleconnections between South America and South African rainfall and show that these teleconnections are caused by eastward propagating wave trains, which are modulated by the convective activity of MJO over tropical South America. Puaud *et al.* (2017) confirmed and further investigated these teleconnections and suggest that at the intraseasonal timescale, the co-variability is related to the modulations of large-scale atmospheric convection over South

America, and then over tropical southern Africa after around 10 days. Grimm (2019) suggested the strongest convective activity over South Africa relate to MJO phase #7 and noted positive anomalies in MJO phase #6. This study highlighted that the connection between MJO and regional convective activity is not very strong (although significant), thereby confirming the conclusions of Pohl *et al.* (2009) for southern Africa. This is probably because at least part of the MJO influence is indirect, exerted through the MJO-related anomalies over South America (Grimm, 2019) or through modulation of moisture fluxes and moisture convergence over Africa (Pohl *et al.*, 2007). Silvério and Grimm (2022) proposed a precipitation index for southern Africa and suggest that the enhancement of precipitation in Mozambique is preceded by enhanced precipitation over South Africa.

In terms of the combined influence of synoptic-scale convective regimes and intraseasonal variability associated with MJO, no discernible relation could be found between MJO and the occurrence of TTTs (Pohl *et al.*, 2009) but Hart *et al.* (2013) did find a weak but significant weakening of TTT intensity during MJO phase #1, and an enhancement during phase #6. Yet, how the association of different MJO phases and synoptic-scale convective regimes modulate the numbers and the daily intensity of extreme events, remains to be shown. Thus, in this study, we attempt to assess such combined influence on a newly developed typology of rainfall extreme (Ullah *et al.*, 2022: Part I hereafter). Due to the rapidly changing patterns of these synoptic-scale convective regimes and intraseasonal variability related to MJO, these timescales are referred to as sub-seasonal timescales in the following sections.

In Part I, a novel typology of extreme rainfall events was proposed for NDJF season based on their spatial fraction as a base criterion, disentangling rainfall events into large-scale (Spatial fraction $\geq 7\%$) and small-scale extremes (Spatial fraction $< 7\%$). The spatial fraction of an extreme event was defined as the proportion of South African rain-gauge stations or grid-points that simultaneously exceed their local 90th percentile threshold, regardless of their location, on the day of the event. These thresholds were found to be a good compromise to categorize extreme events according to their spatial extension. Intrinsic properties of both types of events were then explicitly assessed in the context of intraseasonal descriptors of rainfall variability (ISDs), characterizing the duration, spatial extension, and intensity of wet spells. NDJF total rainfall was found to be primarily shaped by large-scale extremes, which constitute, despite their rareness,

more than half of the rainfall amount according to observation, and nearly half of it in ERA5. Observation (ERA5) shows an average of 8 ± 5 (20 ± 7) days per season associated with large-scale extremes, which are composed of 5 ± 3 (10 ± 3) spells with an average persistence of at least 2 days.

Here, we aim to investigate the variability of large- and small-scale extremes during NDJF at both 1) low-frequency (interannual and quasi-decadal) and 2) sub-seasonal (synoptic-scale and intraseasonal) timescales of variability. Such analyses are required to better identify the drivers of rainfall extremes in the region, to eventually promote multi-year seamless forecasts of extremes on one hand and improve sub-seasonal operational forecasts on the other hand.

This paper is organized as follows. Section 2 presents the data and methods. Section 3 investigates the influence of variability at low-frequency (interannual and quasi-decadal) timescales on rainfall extremes. Section 4 is dedicated to investigating the influence of variability at sub-seasonal (synoptic-scale and intraseasonal) timescales on rainfall extremes. The results are then summarized and discussed in section 5.

2. Data and Methodology

2.1. Investigating the variability of extremes at low-frequency timescales

To investigate the variability of extremes during NDJF at low-frequency timescales, the time series of two extreme ISDs, i.e., wet days (WD_{EXT}) and total rainfall (TR_{EXT}) associated with large- and small-scale extremes are obtained from Part I. WD_{EXT} (TR_{EXT}) is defined as the average number of wet days (total rainfall amount) associated with large- and small-scale extreme events in a season. These descriptors are computed using daily rainfall fields from the observational network of 225 stations (OBS) and deterministic members of ERA5 at a $0.25^\circ \times 0.25^\circ$ global resolution over the period of 1975–2015. The choice of two extreme ISDs, i.e., wet days and total rainfall is made because of the strong dependence of total rainfall in NDJF on the number of wet days associated with large-scale extremes, suggesting their key role in shaping total rainfall variability.

To account for the timescale dependence of teleconnections, we use the Summer Rainfall Index (SRI), as introduced by Dieppois *et al.* (2016) using the Climatic Research Unit (CRU TS 3.23) and the Global Precipitation Climatology Centre reanalysis version 7.0 (GPCC.v7). SRI is here

decomposed into two significant timescales of variability using a fast Fourier transform: 2–8 years interannual variability (IV) and 8–13 years quasi-decadal variability (QDV). The filtered SRI is linked to distinct modes of Pacific variability, namely, the ENSO for IV and Interdecadal Pacific Oscillation (IPO) for QDV.

Monthly SST fields from the Extended Reconstructed Sea Surface Temperature, version 5 (Huang *et al.*, 2017) of the National Climatic Data Centre are used for describing the large-scale climate background conditions modulating South African rainfall extremes and analysing teleconnections. This gridded data set is generated using in-situ data from the International Comprehensive Ocean-Atmosphere Data Set release 3.0. In this release, several improvements are made, notably in quality control, bias adjustment, and interpolation techniques, allowing for optimal reconstruction of sparse data over a $2^\circ \times 2^\circ$ resolution grid (Huang *et al.*, 2017). In addition, a Niño 3.4 index is calculated over the region of east-central equatorial Pacific between 5°N – 5°S , 170°W – 120°W , to monitor the state of ENSO and compute partial correlations of global SSTs, after linearly removing ENSO influence.

2.2. Investigating the variability of extremes at sub-seasonal timescales

Observed daily rainfall data (OBS) from the Water Research Commission of South Africa (<http://www.wrc.org.za>; Fig. 1a) is used for 225 stations spanning 50 years (1965–2015). As in Part I, these 225 stations are selected based on two conditions: 1) stations with less than 1% of missing values; 2) seasonality test, i.e., stations for which 50% or more of the annual rainfall occurs during the austral summer season (Crétat *et al.*, 2012b).

ERA5 reanalysis Copernicus Climate Change Service (Hersbach *et al.*, 2020a) is the 5th generation reanalysis available from the European Centre for Medium-Range Weather Forecasts (ECMWF). Here we use the daily rainfall field for the 1979–2015 period, taken from the deterministic member at $0.25^\circ \times 0.25^\circ$ global resolution (Fig. 1b). Other variables used to assess the physical processes concerning statistical quantifications of extremes include vertically integrated moisture divergence (VIMD) and low-tropospheric moisture fluxes, which are derived from specific humidity, u-wind and v-wind at 850 hPa. Daily Outgoing Longwave Radiation (OLR) fields are also obtained from the ERA5 ensemble to redefine the recurrent synoptic-scale convective regimes, following the methodology of Fauchereau *et al.* (2009).

Tropical Rainfall Measuring Mission (TRMM v.7) 3B42 product (Huffman *et al.*, 2007) is used for satellite-based estimation of extreme rainfall events. TRMM precipitation product covers an area from 50°S–50°N and 180°W–180°E, with a spatial resolution of $0.25^\circ \times 0.25^\circ$, from 1998 to the present on a 3-hourly basis. The daily accumulated precipitation (combined microwave and infrared) is used here from 1998 to 2015 (Fig. 1c). This dataset allows for a gridded estimation of rainfall, and corresponding extreme spells, thereby forming a useful complement to rain-gauges and reanalysis.

The MJO signal was extracted using two daily indices of the Real-time Multivariate MJO (RMM) index (Wheeler and Hendon, 2004), which uses 850 hPa and 200 hPa zonal winds from NCEP/NCAR reanalysis (Kalnay *et al.*, 1996) in addition to OLR daily fields.

2.3. Examining the relationship between rainfall extremes and low-frequency timescales of variability

We first compute Pearson’s correlation between global SST anomalies and the number of wet days and total rainfall associated with large- and small-scale extremes (cf. section 3.1). The analysis is then followed by an assessment of the timescale dependence of the teleconnections at the interannual and quasi-decadal timescales (cf. section 3.2).

The behaviour of rainfall extremes during different phases of IV and QDV is quantified using the Risk Ratio (RR) metric, commonly used in climate attribution studies (Paciorek *et al.*, 2018). RR is defined as the ratio of the probability of an ISD under a factual scenario (P_F), to that probability under a counterfactual scenario (P_{CF}). Here, P_F (P_{CF}) corresponds to a period when a specific timescale of variability (i.e., SRI at IV or QDV timescale) is in the positive (negative) phase of the anomaly, and is given by:

$$RR = \frac{P_F}{P_{CF}} = \frac{\left[\frac{a}{(a+b)}\right]_{IV|QDV}}{\left[\frac{x}{(x+y)}\right]_{IV|QDV}} \quad \text{Eq.1}$$

where a (b) is the sum of a given ISD (i.e., number of wet days) when it lies in its positive (negative) phase of anomaly, when IV or QDV is in a positive phase, representing the P_F scenario. Similarly, x (y) is the sum of a given ISD (i.e., number of wet days) when it lies in its positive (negative) phase of anomaly, when the IV or QDV is in the negative phase, representing the P_{CF} scenario. In addition, we also consider two thresholds obtained by using Standard

Deviations (SD) of SRI at IV and QDV timescales to better quantify the behaviour of extreme ISDs: 1) the RR of extreme events in the weaker positive phase of SRI (P_F : IV or QDV > 0 and $< +0.5$ SD), as calculated concerning the weaker negative phase of SRI (P_{CF} : IV or QDV > -0.5 SD and < 0); 2) the risk of occurrence of extreme events in the strongly positive phase of SRI (P_F : IV or QDV $> +0.5$ SD), calculated concerning the strong negative phase of SRI (P_{CF} : IV or QDV < -0.5 SD). Physical mechanisms responsible for these changes in the RR metrics are assessed through composite anomalies of vertically integrated moisture divergence (VIMD) and moisture fluxes in each P_F and P_{CF} scenarios (cf. section 3.3).

2.4. Examining the relationship between extremes and sub-seasonal timescales of climate variability

2.4.1. Seasonality and network-density tests

Rainfall fields from OBS, ERA5 and TRMM are first submitted to the seasonality test. Hence, only the grid-points or stations for which 50% or more of the annual rainfall occurs during the austral summer season are retained (Fig. 1a-c). Comparison with OBS may be biased by the weaker density and anisotropy of the rain-gauge network. Similarly, one can question whether the OBS network is dense enough to detect all extreme events, and more particularly small-scale events. To address these questions, for gridded ERA5 and TRMM fields, we alternatively consider all-grid-points (AGP), or only those nearest to OBS (NN). The NN and AGP fields of ERA5 (TRMM) have been named ERA5–NN and ERA5–AGP (TRMM–NN and TRMM–AGP), respectively. For conciseness, the results related to the NN fields of ERA5 and TRMM are shown in the supplementary material.

2.4.2. Defining three types of rainfall extremes based on duration and spatial extension

To investigate the variability of extremes at sub-seasonal timescales, we focus on the day-to-day variability of large- and small-scale extremes in NDJF. We thus first identify the days associated with large- and small-scale extremes using the daily values of spatial fraction (i.e., the number of stations or grid-points exceeds simultaneously the local 90th percentile) and complement this typology by introducing information related to the duration of the extreme rainy events. This allows us to differentiate between long-lived and short-lived large-scale extreme events. The local rainfall threshold is obtained as the 90th percentile for each station or grid-point. It is computed based on a normal distribution, and we note that it does not significantly differ from

Gumbel and Gamma distribution (cf. Supp. Fig. S1), thereby suggesting statistical robustness in the definition of the local rainfall thresholds.

Including duration in the definition of extreme events is important since synoptic and intraseasonal ranges of variability play a major role in shaping the persistence of extreme events. On the one hand, the average spatial fraction defines the spatial scale or extent of the event and acts as a key to separate large-scale and small-scale extreme rainfall spells (Part I). On the other hand, their persistence acts as a parameter to distinguish between long-lived and short-lived events. Such characterization of rainfall extremes is not only novel for the region, but also essential to better understand the behaviour of rainfall extremes and their impacts, first in observations over recent years, and then under changing climate.

Large-scale long-lived events form a category of rainfall extremes that may potentially lead to high environmental and societal impacts. To date, the literature offers no clear statistical definition of such spells for the region. Part I depicts an average persistence of large-scale extreme events of 2 ± 1 days in observations. Based on the actual largest persistence values found over the study period and considering twice higher standard deviation, we retained a minimum threshold of at least 5 days as the best compromise to identify large-scale long-lived events. The definition of large-scale long-lived events should be used with caution since: 1) such spells are not defined based on their consequences on the environment and societies, but from an atmospheric point of view, considering the characteristics of the rainfall field itself; 2) we hypothesize that an event with larger spatial extension and longer persistence, therefore bringing huge amounts of water, is more likely to have major consequences for the regional water budget than other types of rainfall events.

Large-scale short-lived events are the counterpart of the previous type, but with a persistence of fewer than 5 days. Collectively, large-scale extreme rainfall events, regrouping short-lived and long-lived types, are important for the regional water balance since such events contribute to more than half of the total rainfall in the austral summer (Part I). The remaining type of rainfall extremes corresponds to small-scale events, whose contribution to the total rainfall budget is much weaker (Part I). The persistence of these localized extremes may not provide a meaningful metric because they are more rarely embedded in large-scale circulation patterns likely to last more than a few hours/days. Thus, we consider small-scale extremes as a single category.

Overall, the different types considered in this work may be summarized as follows:

Large-scale Long-lived events

Spatial fraction $\geq 7\%$ and Persistence ≥ 5 days

Large-scale Short-lived events

Spatial fraction $\geq 7\%$ and Persistence < 5 days

Small-scale events

Spatial fraction $< 7\%$

2.4.3. Characterising the relationship between rainfall extremes and synoptic-scale variability

We first recalculate and update the work of Fauchereau *et al.* (2009) by applying the *k*-means algorithm on the latest available daily OLR fields from 10 ensemble members of ERA5 reanalysis between 1979 and 2015. OLR regimes are used as archetypes of the synoptic-scale convective variability over the region in NDJF. Figure S2 displays seven robust convective regimes based on ERA5 for NDJF, affecting southern Africa (Fauchereau *et al.*, 2009). Three regimes (#5, #6 and #7) correspond to the typical signatures of TTT systems. Regime #5 refers to continental TTTs, which bring heavy convective rainfall over South Africa, while regimes #6 and #7 are shifted north-eastwards, thereby bringing rainfall over the Mozambique Channel, Madagascar, and the southwest Indian Ocean (Macron *et al.*, 2014, 2016; Pohl *et al.*, 2018). Regimes #3 and #4 are generally associated with enhanced subtropical and extratropical convection, respectively while regimes #1 and #2 refer to the drier conditions over South Africa (Fig. S2). OLR anomalies shown here tend to be of larger magnitude than in Fauchereau *et al.* (2009), possibly due to a higher time sampling of the diurnal cycle of atmospheric convection in ERA5, and/or a much-increased spatial resolution compared to NOAA's satellite estimates. By applying the methodology proposed by Fauchereau *et al.* (2009) on the OLR fields from 10 ensemble members of ERA5, the regime for each day of NDJF season from 1979 to 2015 is identified and used for the comparative analysis with large- and small-scale extremes in this study (cf. section 4.1).

2.4.4. *Characterising the relationship between rainfall extremes and intraseasonal variability related to MJO*

Large-scale atmospheric convective patterns associated with the eight phases of the MJO over southern Africa are first obtained (Fig. S3). The strongest wet and dry anomalies over South Africa are found during MJO phases #6–7 and #2–3, respectively, while moderate anomalies occur during other phases thereby corroborating Macron *et al.* (2016) and Grimm (2019). In NDJF, convective clusters associated with the MJO develop at phase #1 over the tropical Indian Ocean. The convective activity strengthens and propagates eastwards (phases #2–4) and reaches the Maritime continent (phases #4–5), before shifting to the Pacific (#5–6), American, and eventually Atlantic sectors (phases #7–8–1). During these MJO phases, clear-sky conditions tend to prevail over equatorial Africa and the nearby Indian Ocean (Wheeler and Hendon, 2004) but in phase #8 this situation starts changing again (Grimm, 2019). Two daily indices of MJO (phase and amplitude) of the RMM index are used to compare with rainfall extremes in this study (cf. section 4.2).

2.4.5. *Characterising the combined influence of synoptic and intraseasonal variability of MJO on rainfall extremes*

The combined influence of synoptic and intraseasonal variability on rainfall fields over southern Africa has already been studied (Pohl *et al.*, 2009; Hart *et al.*, 2013; Macron *et al.*, 2016). Here, we attempt to investigate how synoptic and intraseasonal variability influence different types of extremes and can combine their respective influence. Potential changes in the occurrence and intensity of rainfall extremes during different OLR regimes and MJO phases are explored using contingency analysis by considering all possible combinations between OLR regimes and MJO phases (giving 56 different combinations; cf. section 4.3). To quantify potential dampening and/or enhancement in the intensity of extremes, we first compute the average of all 56 classes. The behaviour of each ‘class’ is then presented in terms of anomaly against that mean value, and for each type of extreme (cf. section 4.3). Risk Ratio assessment is also used here to further explore the combined influence of MJO and synoptic-scale convective regimes on the number of large- and small-scale extremes and is given by:

$$RR = \frac{P_F}{P_{CF}} = \frac{\left[\frac{a}{(a+b)} \right]_{OLR \text{ Regime and MJO Phase of interest (MJO} > 1.0RMM)}}{\left[\frac{x}{(x+y)} \right]_{OLR \text{ Regime and MJO Phase of interest (MJO} < 1.0RMM)}} \quad \text{Eq.2}$$

where a (b) is the sum of extreme (non-extreme) days when $MJO > 1.0$ RMM, representing the P_F scenario. Similarly, the x (y) is the sum of extreme (non-extreme) days when $MJO < 1.0$ RMM, representing the P_{CF} scenario. Following section 2.3, the composite anomalies of VIMD and moisture fluxes in each P_F and P_{CF} scenarios is also provided (cf. section 4.4).

3. Rainfall extremes at low-frequency timescales variability

3.1. Teleconnections of extremes with global SSTs

We first analyse the seasonal rainfall amounts due to daily extremes, and their contribution to seasonal rainfall totals. For each austral summer season between 1979 and 2015, Figure 2 presents the respective contribution of small-scale and large-scale extremes to total rainfall, as a function of the seasonal amounts. Rainfall extremes are responsible for a larger proportion of total rainfall when the austral summer rainfall amounts are low. This negative relationship is significant at 95% for both large-scale and small-scale extremes, and according to OBS and ERA5 reanalysis (Fig. 2a-b; Supp. Fig. S4a). It denotes a weaker interannual variability of the rainfall amounts due to daily extremes than those caused by non-extreme rainy days. These same time series are also represented as a function of the seasonal mean Niño 3.4 index during the same austral summer seasons (Fig. 2c-d; Supp. Fig. S4b). The negative relationship between total austral summer rainfall and Niño3.4 is confirmed and is here extended to the seasonal amounts resulting from both small-scale and large-scale extremes. However, the ENSO dependency of the latter appears weaker than seasonal amounts. In the following, we further explore the driving mechanisms responsible for such changes, from one year or group of years to another, in seasonal extreme occurrence, and corresponding rainfall amounts.

Correlations between global SST fields and the seasonal occurrence of large- and small-scale extremes in NDJF are shown in Figure 3a, and the correlations between global SST fields and total rainfall associated with large-scale, small-scale, and non-extreme rainfall totals are in Figure 4a. The contributions of these different rainfall types (in terms of percentage) to seasonal rainfall totals are also assessed with global SSTs (Fig. 4b). To better identify potential sources of variability in the Atlantic, Southern and Indian Oceans, always strongly cross-correlated to ENSO these analyses have all been replicated after removing linearly the influence of ENSO (Fig. 3b and 4c-d).

La Niña conditions have been identified in many previous studies as favourable to anomalously wet rainy seasons in southern Africa in austral summer. Figure 3a shows that they also favour the occurrence of large- and small-scale extreme events. Moreover, a warmer north Atlantic Ocean and west tropical Atlantic significantly favour the occurrence of extremes, especially large-scale ones (Fig. 3a-b). Similarly, a colder Indian Ocean, tropical east Atlantic Ocean and subtropical south Atlantic Ocean seem to favour the occurrence of small-scale extremes (Fig. 3a). After linearly removing the influence of ENSO, we note that the correlation between large-scale extremes and SSTs in the north tropical Atlantic and subtropical south Atlantic is higher (Fig. 3b). Interestingly, large-scale extremes are more strongly related to warmer SSTs in the northwest Indian Ocean, after removing the ENSO influence (Fig. 3b), as observed during the anomalously wet summer following the 1997/98 El Niño event (Lyon and Mason, 2007).

After removing ENSO influence, teleconnections with small-scale extremes become weaker (Fig. 3b). ERA5 data suggest a significant relationship with the sub-tropical Indian Ocean dipole (Reason, 2001; Washington and Preston, 2006; Dieppois *et al.*, 2016, 2019; Pohl *et al.*, 2018), but these results are not confirmed by OBS. By contrast, our results suggest that the variations in SSTs over the tropical southeast Atlantic mainly affect small-scale extremes in South Africa. Interestingly, organized correlation patterns of SSTs for large- and small-scale extremes are remarkably consistent using OBS and ERA5. The potential role of the tropical southeast Atlantic and associated Angola Current has been notably documented in previous studies (Rouault *et al.*, 2003; Grimm and Reason, 2011; Desbiolles *et al.*, 2020).

Figure 4 displays the correlation between global SSTs and total rainfall fields. Here, once again, La Niña conditions appear to favour wet conditions, including rainfall totals associated with large- and small-scale extremes, and non-extreme rainfall over South Africa. These results are consistent in all datasets (Fig. 4a), confirming the results of Figure 2. Warmer conditions over the north Atlantic and west tropical Atlantic are also linked to rainfall caused by large- and small-scale extremes, especially in OBS (left and middle column panels in Fig. 4a). Warm SST anomalies around the southern tip of the African continent (southeast Atlantic and southwest Indian Oceans) and cold SST anomalies in the Southern Ocean also tend to relate to total rainfall associated with large- and small-scale extremes (left and middle column panels in Fig. 4a). However, these correlations are not significant with non-extreme rainfall (right column panel in

Fig. 4a). The latter appears better correlated with the south Atlantic Ocean and equatorial Indian Ocean (right column panel in Fig. 4a), besides the equatorial central-east Pacific Ocean.

As illustrated in Figure 4b, the contribution of large- and small-scale extremes to total rainfall is positively correlated with the equatorial Pacific SSTs, suggesting that the contribution of extreme events to total rainfall is greater during El Niño and lower during La Niña. This may appear contradictory because drier conditions tend to prevail during El Niño (Crétat *et al.*, 2012b). Pohl *et al.* (2007) also suggested a larger influence of the MJO on South African rainfall during El Niño events, despite seasonal droughts. Here, this result is due to the stronger influence of ENSO on non-extreme days, while extreme-related rainfall is more constant interannually (Fig. 2).

To better identify potential sources of variability in the Atlantic, Southern and Indian Oceans, this analysis is replicated after removing linearly the influence of ENSO on global SSTs (Fig. 4c-d). When the ENSO influence is removed, correlations with the tropical Atlantic are stronger, for both large- and small-scale extremes (left and middle column panels in Fig. 4c). In OBS, the relationship between the eastern and tropical Indian Ocean and small-scale extremes also strengthens, but this is not the case for ERA5 (middle column panels in Fig. 4c). The relationship between extreme conditions and SST anomalies in the Southern Ocean tend to weaken (Malherbe *et al.*, 2016), which may be due to the inter-dependency between ENSO and the phase of the SAM in austral summer (Pohl *et al.*, 2010). The influence of SIOD on large-scale extremes (left column panels in Fig. 4d) is also clearer, in OBS, after removing ENSO influence, thereby suggesting a potential, yet secondary, influence on rainfall extremes in South Africa.

These results are consistent with previous studies that identified significant associations between southern African rainfall and SST changes in the Pacific (Dieppois *et al.*, 2016, 2019), the southern Indian Ocean (Hoell and Cheng, 2018) and the Atlantic Ocean (Pomposi *et al.*, 2018; Rapolaki *et al.*, 2019, 2020). We complement these studies by assessing how these teleconnections also modify the occurrence of rainfall extremes, with a distinction made between small-scale and large-scale events as such analyses are meant to better identify their large-scale drivers.

3.2. Timescale dependence of rainfall extremes

Figure 5 displays the linear correlation of the number of wet days and total rainfall associated with large- and small-scale extremes with the SRI filtered at interannual (IV) and quasi-decadal (QDV) timescales (Fig. 5a-b), as in Pohl *et al.* (2018). A strong relationship between IV and the number of wet days associated with large-scale extremes is found using all datasets with a correlation between 0.70 and 0.72 (Fig. 5a). The number of small-scale extremes seems weakly influenced at the IV timescale with correlations between 0.30 and 0.32 (Fig. 5b). At the IV timescale, we note a consistent response of total rainfall associated with large- and small-scale extremes where all datasets show statistically significant correlations between 0.51 and 0.69 (Fig. 5c-d). It is interesting to note that the number of small-scale extremes is weakly modulated at the IV timescale while the total rainfall at that timescale is strongly modulated. This could be due to the regional- to local-scale perturbations such as weaker TTTs and/or mesoscale convective complexes (MCCs) may have a larger influence on the number of small-scale extremes. In Part I, we note that small-scale extremes were largely embedded in non-extreme but spatially coherent rainfall events while extreme conditions were mostly located over the north-eastern parts of South Africa (cf. Fig. S4-S5; Part I), a region known to be affected by MCCs (Blamey and Reason, 2013).

At the QDV timescale, all datasets show correlations between SRI and the number of both types of extremes of about 0.20 and 0.35 (Fig. 5a-b). In contrast, the relationship of total rainfall associated with large-scale extremes is stronger at the QDV timescale, with correlations of about 0.48 and 0.50 (Fig. 5c-d). However, the linear correlations at the QDV timescale are not significant according to the Bravais-Pearson test at $p=0.05$ accounting for the autocorrelation in the time series. The latter dramatically decreases the actual number of degrees of freedom, thereby leading to a biased significance assessment.

3.3. Risk assessment at low-frequency timescales

To better assess the potential variations in ISDs at IV and QDV timescales, we estimate these variations through changes in the risk ratio RR. Figure 6a displays the RR metric for the number of wet days associated with large- and small-scale extremes computed for the weaker positive phase (P_F : $IV > 0$ and $IV < +0.5$ SD) with respect to the weaker negative phase (P_{CF} : $IV > -0.5$ SD and $IV < 0$) of IV timescale using OBS and ERA5-AGP. For large-scale extremes, OBS and

ERA5–AGP show RR of about 1.32 and 1.41 respectively with a narrow bin of confidence interval between 1–2 (Fig. 6a). This suggests that the number of large-scale extremes at the weaker positive phase of IV timescale could be 32–41% higher as compared to the weaker negative phase of IV timescale. Figures 6b–c show the composite anomalies of VIMD and moisture flux at 850 hPa corresponding to P_F and P_{CF} scenario respectively. Weaker anomalies prevail during both scenarios yet during P_F scenario, slightly higher convergence over the north-eastern and some central domains of South Africa are quite notable which are leading to a 32–41% rise in the risk of occurrence of large-scale extremes as compared to P_{CF} scenario.

Figure 6d shows a similar analysis but RR is computed for the number of days associated with extreme events occurring during the stronger positive phase (P_F : $IV > +0.5$ SD) with respect to the number of days associated with the extreme events occurring during the stronger negative phase (P_{CF} : $IV < -0.5$ SD) of the IV timescale. OBS and ERA5–AGP indicate a RR of nearly 5 with a confidence interval of about 3–7 suggesting; 1) a 400% higher risk on the numbers of large-scale extreme wet days when IV lies in a strong positive phase, as compared to its stronger negative phase; 2) larger confidence interval suggests anomalously wet conditions with a higher number of large-scale extremes (Fig. 6d). In OBS, small-scale extremes are more frequent during the P_F scenario of IV timescale with a RR of about 1.89 with a narrow bin of confidence interval suggesting that the number of such extremes is less variable (Fig. 6d). Extended to Madagascar, wet and dry dipole conditions clearly prevail over 20°S during P_F and P_{CF} scenarios of IV timescale (Fig. 6e–f). Figure 6e clearly represents the moisture flux convergence over South Africa during strong La Niña conditions. Another notable signal is the location of Angola low, which is known as a tropical source of convergent moisture that can next be embedded in TTTs (Reason and Jagadheesha, 2005). This could result in increased occurrence of large-scale extremes during the seasons when $IV > +0.5$ SD. Such moisture flux anomalies as shown in Figure 6e are also well discussed by Hoell and Cheng (2018) as they identified such anomalies because of La Niña and positive SIOD phasing. In such cases, cyclonic circulation prevails over southern Africa and anticyclonic circulations over Madagascar and the adjacent Indian Ocean. Nearly opposite features of VIMD and moisture fluxes appear during the composites of the seasons when $IV < -0.5$ SD. Here, strong divergent anomalies represent departure of moisture from southern Africa thus enhancing dry conditions (Fig. 6f).

Figure 7a displays the risk ratio assessment for the number of large- and small-scale extremes computed for the weaker positive phase (P_F : $QDV > 0$ and $QDV < +0.5$ SD) with respect to the weaker negative phase (P_{CF} : $QDV > -0.5$ SD and $QDV < 0$) of SRI at QDV timescale. OBS data show a RR of 1.32 with a confidence interval between 0.94–1.85, suggesting that the numbers of large-scale extremes are typically 32% higher in the P_F scenario of QDV timescale as compared to P_{CF} (Fig. 7a). The convergence signals found over southern Africa during P_F scenario of QDV timescale may be related to the moisture transport patterns associated with SICZ, which is formed by the convergence between the South Atlantic westerlies and the South Indian easterlies (Fig. 7b). However, during P_{CF} scenario of the QDV timescale, we note a strong cyclonic circulation over Madagascar and southeast Indian Ocean, with moisture convergence over Madagascar and divergence from eastern parts of southern Africa (Fig. 7c). Such anomalies indicate: 1) strong equatorial moisture anomalies over Indian Ocean and southerly anomalies over southern Africa; 2) strong influence of the Indian Ocean warming on low level circulation and moisture, all together bringing dry conditions over the regions (at least for the large-scale extreme events).

No substantial change in the RR metric emerges in the number of large-scale extremes when QDV lies in its strong positive phase (P_F : $QDV > +0.5$ SD), with respect to its strong negative phase (P_{CF} : $QDV < -0.5$ SD: Fig. 7d). However, OBS and ERA5–AGP show a RR of about 1.29–1.35 for large-scale extremes with a confidence interval varies in between 1.06–1.58, suggesting that such extremes could be 29–35% higher, and can be increased by up to 58%, during P_F scenario of QDV timescale as compared to its P_{CF} scenario. For small-scale extremes, both datasets show a RR of about 1.49–1.91 with a confidence interval between 1.38–2.1 (Fig. 7d). Notably, the RR for small-scale extremes is slightly higher as compared to the RR of large-scale extremes, this suggests that variability at the QDV timescale has a larger influence on the numbers of small-scale extremes (Fig. 7d). The RR value is lesser in OBS for small-scale extremes as compared to ERA5–AGP suggesting: 1) a critical deficiency of network density in OBS particularly for small-scale extremes; 2) the viability of using ERA5–AGP to deal with the network density issue in OBS.

Figures 7e-f display the composite anomalies of VIMD and moisture flux for P_F and P_{CF} scenarios related to strong opposite phases of the QDV timescale. During P_F scenario, an easterly moisture flux from the South Indian Ocean is quite notable over tropical southern Africa (above

15°S), the moisture flux then propagates toward the south-western regions before converging over the north-eastern parts of South Africa (Fig. 7e). Dieppois *et al.* (2016) suggest that the moisture fluxes from the Indian Ocean converge with south-easterly moisture fluxes from the South Atlantic High, thereby strengthening the SICZ and this relates to a northward shift of the Intertropical Convergence Zone (ITCZ), north of Madagascar from the western Indian Ocean to central Africa.

The results of RR for small-scale extremes shown by OBS and ERA5–AGP are in line with the previous section, where we note that the total rainfall associated with small-scale extremes is well correlated with the SRI at QDV timescale (cf. Fig. 5c). Secondly, shallow convergence and weaker moisture flux over South Africa indicate why the risk of large-scale extremes is comparatively lesser than the risk of small-scale extremes.

In this section, we attempt to quantify changes in the occurrence of extreme events using the varying magnitude of SRI on IV and QDV timescales. The SRI is a rainfall index, selected over a homogeneous region and partially shaped by extremes itself. This suggests that the SRI and daily extremes are not independent of each other, due to the major contribution of large-scale extremes to rainfall totals (Part I). The quantifications made using RR are in line with the physical mechanism shown via changes in the moisture fluxes and divergence. We note that the effect of the SRI at IV timescale on the RR is particularly stronger for the large-scale extremes. The analysis presented in section 3 is also provided for NN fields of ERA5 in supplementary Figures S4–S7.

4. Rainfall extremes at sub-seasonal timescales

In this section, we attempt to quantify the changes in daily rainfall extremes at sub-seasonal (synoptic-scale and intraseasonal) timescales. To that end, we first complement the typology of rainfall extremes with duration statistics (section 2.4.2) prior to investigating the characteristics of extremes. Figure 8 shows an intraseasonal calendar of complemented typology of rainfall extremes. All days associated with large-scale long-lived events in OBS are also identified using the all-grid-points fields of ERA5 and TRMM. A similar analysis is then applied to the nearest neighbour fields of ERA5 and TRMM where both datasets generally show remarkable efficiency in monitoring large-scale long-lived extremes (Fig. S8). This allows us to conclude that the

density of the observational network (i.e., 225 stations) seems sufficient to detect most large-scale long-lived rainfall spells. Figure 8 also shows that the occurrence of large-scale long-lived extremes in the onset and cessation months of the austral summer is substantially fewer than during the core of the rainy season. No event is detected by OBS during October and only one in March of 1975/1976 summer, except a few spells detected by ERA5 and TRMM in March (Figs. 8 and S8). A list of large-scale long-lived rainfall spells identified by OBS is provided in Table S1.

4.1. Characteristics of rainfall extremes in synoptic-scale convective regimes

Figure 9 displays the co-occurrence of different types of rainfall extremes identified by OBS, ERA5 and TRMM in each synoptic-scale convective regime. About 45–50% of days associated with large-scale long-lived events occur during regime #5, corresponding to the continental TTT events whereas about 20–30% of these days occur during regimes #3 and #4, respectively (cf. Fig. S2). The days associated with large-scale short-lived events, which are more frequent than large-scale long-lived ones, mostly occur during the same regimes (#3, #4 and #5: Fig. 9b). These results are consistent in OBS, ERA5 and TRMM, albeit a slightly lower contribution for the two latter (Fig. 9b). Small-scale extremes are more likely during regimes #3 and #5 with a contribution of 25% and 20%, respectively (Fig. 9c). The days associated with large-scale events occur largely during synoptic regimes #3 to #5 describing the precursors and then the mature phases of continental TTT systems (Fauchereau *et al.*, 2009). However, according to the lead-lag composites of circulation and convection anomalies associated with different bands of intraseasonal variability in southern African monsoon, presented by Silv erio and Grimm (2022), the TTT pattern (here identified as the regime #5) is part of the evolution of these anomalies and is preceded and followed by anomaly patterns like regimes #3 and #6.

Regarding the daily average intensity of each type of extreme event during different OLR regimes, we note that large-scale long-lived events appear slightly more intense during regime #5, with an average intensity exceeding 60 mm.day^{-1} in OBS and TRMM (Fig. 10a). This is consistent with previous studies (Hart *et al.*, 2013; Macron *et al.*, 2014), showing that TTTs produce heavier and more extreme rainfall than normal. In OBS, the overall average intensity of large-scale short-lived events is $44.33 \text{ mm.day}^{-1}$ but regime-to-regime differences are substantially larger (OBS panel in Fig. 10b). Large-scale short-lived events tend to be 8–23%

more intense in regimes #5 and #6 even though they are less likely during regime #6 (Fig. 10b). Such higher intensity during regimes #5 and #6 is also found in ERA5 and TRMM, but they underestimate the average intensity of large-scale short-lived events (Fig. 10b).

Small-scale extremes also display slightly higher intensity during regimes #5 and #6 where OBS shows an average intensity of about 48 mm.day^{-1} as compared to $40\text{--}44 \text{ mm.day}^{-1}$ during other regimes (Fig. 10c). In ERA5, no remarkable differences appear in the intensity of small-scale events across different regimes and ensemble members (ERA5 panels in Fig. 10c). Overall, inter-member differences are lower for small-scale extremes, while, for other types of extremes, the behaviour of ensemble members is slightly more variable.

4.2. Characteristics of rainfall extremes in different MJO phases

As illustrated in Figure 11, between 1979 and 2015, 63% of austral summer days are associated with active MJO variability (Amplitude > 1). To assess the regional response of MJO phases on different types of rainfall extremes, we assess how the numbers of extremes, and their corresponding intensities, vary according to the MJO phases (Fig. 12).

Around 9–27% of days associated with large-scale long-lived events occur in MJO phases #7 and #8 as shown by OBS and ERA5–AGP, while in phase #4 these datasets indicate 11% to 12% of days associated with such events (left panel in Fig. 12a). TRMM shows different results and yields higher numbers of days associated with large-scale long-lived events during MJO phases #2 and #3, questioning the robustness of this dataset (left panel in Fig. 12a). Particularly in OBS, we note that days of large-scale long-lived events are more intense during MJO phases #7 and #8, with an average intensity exceeding 50 mm.day^{-1} (right panel in Fig. 12a).

The number of wet days associated with large-scale short-lived extremes are higher in austral summer during MJO phases #6–8 (28–37%), moderately frequent in phases #3–5 (21–24%) and less frequent in phases #1–2 (7–11%), and these results are consistent for all datasets (Fig. 12b). The intensity of large-scale short-lived extremes appear slightly lower during phases #1–2, while an extremely high-intensity signal in OBS is notable during phases #3–8 with an average intensity of about $41.05\text{--}47.86 \text{ mm.day}^{-1}$ (right panel in Fig. 12b). Similar results emerge for the number of days associated with small-scale extreme events, where MJO phases #1–2, #3–5 and #6–8 show frequencies of about 8–12.5%, 21.5–26.5% and 26.5–30.5% respectively (left panel

in Fig. 12c). No remarkable inter-phase differences appear for the intensity of small-scale extreme events (right panel in Fig. 12c). Overall, regardless of the type of extreme events, we note therefore that the numbers of extremes are lesser in MJO phase #1–2, moderate in #3–5 and higher in #6–8. These coherent and successive groups of MJO phases are referred to hereafter as dry, moderate, and wet MJO phases, in the context of South African rainfall extremes.

4.3. Characteristics of rainfall extremes during the combined influence of synoptic-scale (OLR regimes) and intraseasonal variability (MJO)

We assess here the combined influence of synoptic-scale convective regimes and MJO phases on the different types of extremes. Contingency analysis is provided for the number of days associated with different types of extremes and their corresponding intensity in Figures 13 and 14, respectively.

In Figure 13a, OBS and ERA5 suggest that the days associated with large-scale long-lived events are largely occurring in regimes #3 to #5 during moderate and wet MJO phases. Large-scale short-lived events also exhibit few notable and robust associations: 1) regime #5 with phase #6 with a contribution of 6–8% of days according to all datasets (Fig. 13b); 2) regime #3 with phase #3 in OBS and TRMM for 6% of days, although this signal is not identified in ERA5 (Fig. 13b). ERA5 shows difficulties in reproducing such localized events, while OBS and TRMM tend to lead to convergent results. Finally, days associated with small-scale extreme events are nearly equiprobable in almost all 56 concomitance classes. They appear slightly more frequently in regime #3 under moderate and wet MJO phases (Fig. 13c).

Figure 14 displays the intensity of rainfall extremes during the combined influence of OLR regimes and MJO phases. In OBS, days associated with large-scale long-lived events are more intense in regime #5 occurring with MJO phases #4 and #8, with an average intensity of 56.8 mm.day⁻¹ (above one standard deviation: see, OBS panel in Fig. 14a). For the days of large-scale short-lived events, all datasets show increased intensity when regime #5 is associated with all moderate and wet MJO phases (Fig.14b). Similar patterns appear in the intensity of small-scale extremes (see regimes #5–6 and their associations with most MJO phases in Fig. 14c). This association seems coherent, as the MJO is known as a tropical mode of variability and regime #6 materializes strong tropical-temperate connections, favoured by sustained convective activity in the tropics that help convection extend southwards over South Africa (Macron et al. 2014; Fig.

S2). Our results show that 11–16% of days associated with small-scale events occur in regime #6. Thus, small-scale extreme events with extremely high intensity can be anticipated when regime #6 coincides with strong MJO activity. The analysis presented in sections 4.1–4.3 is also provided for NN fields of ERA5 and TRMM in supplementary Figures S8–S13.

4.4. Risk assessment at combined influence of synoptic and intraseasonal variability

To assess the risks of occurrence of extremes under different combinations of OLR regimes and MJO phases, we use a RR assessment (cf. section 2.3; Fig. 15). Only regimes #3, #4 and #5 are presented here since the highest number of extremes occur in these regimes (section 4.1). The RR is then provided for each regime for dry (#1–2), moderate (#3–5) and wet phases (#6–8) of the MJO, as these groups of contiguous phases are also found to be coherent and homogeneous in terms of rainfall extremes (section 4.2). RR is computed for each set of combinations when MJO is active (P_F : Amplitude > 1.0 RMM) with respect to all days when MJO does not represent any phase (P_{CF} : Amplitude < 1.0 RMM) and is provided here only for OBS.

Regime #3 is associated with a RR of about 1.35 for the days associated with large-scale extremes when MJO is active, regardless of the phase with respect to the days when MJO is not present in this regime (Fig. 15a). These differences are coherent with slightly weaker negative anomalies of VIMD and easterly moisture flux (Fig 16a-b). Further, in regime #3, the RR for large-scale extremes was found nearly 1.0 with wet and dry phases of MJO indicating that the occurrence of such extremes is equiprobable either with or without MJO. In regime #3, we note a RR of 1.36 with a confidence interval of 1.02–1.82 suggesting a 36% increase in the risk of occurrence of large-scale extremes with moderate phases of MJO as compared to when MJO is not active (Fig. 15a). It may seem contradictory because the wet phases are known to favour convection over southern Africa. It is because RR is sensitive to the sample size. For instance, OBS data identified 70 days associated with large-scale extremes in regime #3 where 49 days were found when MJO show a phase with amplitude above 1.0 RMM and only 21 days when MJO does not show any phase. Among these 49 days, 25 days were associated with moderate phases of the MJO in a sample size of 219 days while 21 days occur during a substantially higher sample size of 315 days when MJO was not active with any phase. It is also worth noting that during regime #3 and moderate phases of the MJO, the occurrence of small-scale extremes was

also higher as compared to other combinations as this signal is not only identified by AGP fields of ERA5 and TRMM but also with their NN fields as well (Fig. 13 and S12). Figures 16c-e indicate that the differences in terms of convergence over South Africa are higher when MJO is active with the respective set of phases. For further clarification, we provide the composite anomalies of VIMD and moisture fluxes during regime #3 with moderate phases of the MJO (see, Figure S14). Figures 16a-b show that the moisture is diverging towards the northwest and over western parts of South Africa creating a regime structure while if we consider only those days when MJO is active with moderate phases (as shown in Figure S14), convergence extends on a larger region with higher strength while the moisture flux is more inward toward South Africa thus resulting in a higher number of large-scale extremes thereby confirming the RR result.

Figure 15b indicates the risk of occurrence of large-scale extremes is higher when MJO is inactive during regime #4 (i.e., P_{CF} scenario). However, this is not the case with wet phases of the MJO during regime #4, here we note a risk ratio of about 1.10 suggesting a 10% higher risk of occurrence of large-scale extremes (Fig. 15b). Indo-Pacific composites of MJO circulation reveal that moisture flux anomalies are directed away from Africa during phases #2–4, and towards Africa during phases #6–8 (Wheeler and Hendon, 2004). Our results confirm this as the differences in terms of divergence (convergence) are higher in regime #4 with dry and moderate (wet) phases of the MJO and these synoptic behaviours in terms of VIMD and moisture flux anomalies over South Africa are accurately mimicked by the risk ratio assessment (Fig. 16h-j).

Like regime #4, the risk of occurrence of large-scale extremes in regime #5 is also higher without the influence of MJO (during P_{CF} scenario) when computed for the active MJO days of dry phases with respect to all days when MJO does not show any phase in regime #5 (Fig. 15c). The differences in composite anomalies also suggest dry conditions during dry phases of the MJO over South Africa (Fig. 16m). However, during regime #5 and wet phases of MJO, we note a RR of about 1.15 with a confidence interval between 0.85–1.55 suggesting a risk of occurrence of large-scale extremes is 15% higher with the MJO influence and even more if we consider the upper bound of the confidence interval. Moisture flux anomalies also suggest the difference is higher in terms of convergence over South Africa (Fig. 16o). During all three regimes with different set of MJO phases, the risk of occurrence of small-scale extremes remains equiprobable

either with or without the MJO activity. This suggests that MJO plays an important role in modulating the number of days associated with large-scale extremes.

The association between MJO phases and synoptic regimes works well mostly for regime #5 this confirms the results of Hart et al. (2013) according to which TTTs tend to be more intense, that is, bring more rainfall, when they occur during the wet phase of the MJO. The dry phases act to weaken them and decrease associated rainfall amounts. This translates into a different probability to exceed the local 90th percentile thresholds, hence a change in the RR metric. The results obtained from RR metric are quantitative and statistically significant but physical mechanisms studied here result in weak statistical significance (but not insignificant), confirming the results of RR by showing some interesting signals. The uncertainties in the physical mechanisms studied here may be due to the biases in the reanalysis and shorter sample size. Here we propose further aspects to extend this study by 1) considering a larger sample size; 2) using different reanalysis products to be sure if the signals are like ERA5; 3) exploring dynamical perspective using the strength of MJO amplitude; 4) investigating teleconnections with other regions in the perspective of the combined influence of synoptic regimes and MJO phases. Characterization of extremes for the region was never done before; this study fills this gap and by characterizing extremes according to their properties thus opening new dimensions for further research.

5. Conclusions and Discussion

In Part I, we introduced a novel typology of rainfall extremes, accounting for their spatial extensions and disentangling large- and small-scale extreme events. Here, we attempt to investigate the variability of two types of rainfall extremes, first at interannual (IV: 2–8 years) and quasi-decadal (QDV: 8–13 years) timescales of variability, which are associated with ENSO and IPO, respectively (Dieppois *et al.*, 2016, 2019; Pohl *et al.*, 2018). Changes in the occurrence of rainfall extremes are next analysed at sub-seasonal (synoptic and intraseasonal) timescales. They are respectively related to short-lived disturbances either related to tropical convection, mid-latitude dynamics or interactions between both (Fauchereau *et al.*, 2009; Hart *et al.*, 2013; Macron *et al.*, 2014, 2016) and to the regional influence of the MJO (Pohl *et al.*, 2007; Oettli *et al.*, 2014). For all timescales, risk ratio assessments are provided, to quantify the change in the probability for either small-scale or large-scale extremes to occur. To our knowledge, such quantifications of rainfall extremes have never been carried out for the region.

We first explore the link between extremes, either large- or small-scales, and global SSTs. The different ocean basins have substantially contrasted results with large- and small-scale extremes. This suggests the adequacy of the method used in Part I to characterize South African rainfall extremes as we speculated that large-scale circulations or modes of variability have a greater influence on the occurrence of large-scale extremes. We note that: 1) La Niña conditions favour overall wet conditions in South Africa, including an increased occurrence of rainfall extremes; 2) the number of days associated with large-scale extremes and contribution of total rainfall is related to warmer SSTs in the North Atlantic, while the relationship with warmer Indian Ocean and tropical South Atlantic appears as statistically independent of the state of ENSO; 3) the contribution of large- and small-scale extremes to total rainfall is greater during El Niño, despite generally drier conditions during these years.

At low frequencies (IV and QDV), a risk ratio assessment suggests that the probability of extremes varies with the changing magnitude of IV and QDV timescales, primarily associated with ENSO and IPO respectively. At the IV timescale, the number of large-scale extremes and the total rainfall associated with small-scale extremes is much more frequent when this timescale lies in a strong positive phase, i.e., $> +0.5$ standard deviation. During these strong positive IV phases, we note a 400% rise in the probability of large-scale extremes as compared to the strong negative IV phases. This is consistent with the strong La Niña episodes in the Pacific SSTs, where interannual variations play a primary role in shaping rainfall variability in South Africa. No substantial increment in the risk ratio is noted when computed for strong positive phases of the QDV timescale compared to strong negative phases. Considering these results, it is conceivable that the whole statistical distribution of daily rainfall extremes is strongly related to rainfall variations at the IV timescale and weak but significant on QDV timescale. These findings may play an important role in promoting multi-year seamless forecasts of rainfall extremes since they identify the modes of climate variability that drive part of their variability at both the IV and QDV timescales.

At the sub-seasonal timescales, days associated with large-scale events occur largely during synoptic regimes #3 to #5 (describing the precursors and then the mature phases of continental TTT systems), whereas small-scale extremes are nearly equiprobable during all regimes, except for regime #3, which shows slightly higher numbers of such extremes. In terms of intraseasonal

variability, MJO phases #1–2, #3–5 and #6–8 are three coherent and homogeneous groups which are respectively associated with weak, moderate, and high numbers of both types of extremes for South African rainfall. Previous studies suggested that the intensity of TTT events (that is, their corresponding rainfall amounts) is increased during phase #6 and decreased in phase #1, even though TTT occurrence is not statistically modified by MJO phases (Hart *et al.*, 2013). Our results related to regime #5 corroborate the results found in the literature and extend them to rainfall extremes.

In Part I, we noted that the large-scale extremes are spatially coherent and organized events, bringing more than half of total seasonal rainfall during just 8 ± 5 days.season⁻¹. In this study, we find that around 75% of days associated with large-scale extreme events occur in regimes #3–5 which are characterized as early to mature TTT regimes. Thus, our results support the argument made by Hart *et al.* (2013) “*that a single extreme event has the potential to drastically alter the seasonal rainfall total*”. The extensive characterization of rainfall extremes carried out in this study is crucial in promoting long-term multi-year seamless forecasts for the region on one hand, and sub-seasonal operational forecasts on the other hand.

We investigate here the intraseasonal variability of rainfall extremes separately at low-frequency and sub-seasonal timescales. It would be ideal to consider these timescales together, to analyse climate variability according to a real continuum of scales. This would include climate change, with expected changes in the rainfall extremes due to the Clausius-Clapeyron scaling relating air temperature to its humidity (Betts and Harshvardhan, 1987; Kharin *et al.*, 2007; Muller *et al.*, 2011; Pohl *et al.*, 2017). The interdecadal timescale could also modify the changes in the intensity and occurrence of rainfall extremes, from one decade to another, thereby influencing the changes that the region will experience in the coming decades. Observational datasets may be too short to perform such analyses of slowly changing modes of variability or mechanisms, hence the need for long model simulations. However, current climate models are mostly based on parameterized atmospheric convection, and convection-permitting simulations may be needed to better ascertain the influence of interdecadal variability on rainfall extremes (Kendon *et al.*, 2017, 2019; Jackson *et al.*, 2020; Senior *et al.*, 2021). The question of their seamless predictability is also important because these events may be considered as those more likely to lead to strong

impacts. Hence the need to develop a seamless prediction tool for rainfall extremes, and more generally, high-impact events over southern Africa and even Africa as a whole.

Acknowledgements

This work is part of the I-SITE Bourgogne Franche-Comté Junior Fellowship IMVULA (Grant N°: AAP2-JF-06), and the Alliance Programme 2020 (Grant N°: 608081922), co-funded by the British Council and Campus-France. It was also supported by the NRF SARCHI chair on “modeling ocean-atmosphere-land interactions” and the Nansen Tutu Centre for Marine studies. Two anonymous reviewers are thanked for their constructive comments that helped us to improve the quality of the manuscript. Calculations were performed using HPC resources from DNUM CCUB (Centre de Calcul de l’Université de Bourgogne).

References

- Asmat U, Athar H. 2017. Run-based multi-model interannual variability assessment of precipitation and temperature over Pakistan using two IPCC AR4-based AOGCMs. *Theoretical and Applied Climatology*, 127(1–2). <https://doi.org/10.1007/s00704-015-1616-6>.
- Asmat U, Athar H, Nabeel A, Latif M. 2018. An AOGCM based assessment of interseasonal variability in Pakistan. *Climate Dynamics*. Springer Berlin Heidelberg, 50(1–2): 349–373. <https://doi.org/10.1007/s00382-017-3614-0>.
- Betts AK, Harshvardhan. 1987. Thermodynamic constraint on the cloud liquid water feedback in climate models. *Journal of Geophysical Research: Atmospheres*. John Wiley & Sons, Ltd, 92(D7): 8483–8485. <https://doi.org/10.1029/JD092ID07P08483>.
- Betts AK, Miller MJ. 1986. A new convective adjustment scheme. Part II: Single column tests using GATE wave, BOMEX, ATEX and arctic air-mass data sets. *Quarterly Journal of the Royal Meteorological Society*. John Wiley & Sons, Ltd, 112(473): 693–709. <https://doi.org/10.1002/QJ.49711247308>.
- Blamey RC, Kolusu SR, Mahlalela P, Todd MC, Reason CJC. 2018. The role of regional circulation features in regulating El Niño climate impacts over southern Africa: A comparison of the 2015/2016 drought with previous events. *International Journal of Climatology*, 38(11): 4276–4295. <https://doi.org/10.1002/joc.5668>.
- Blamey RC, Reason CJC. 2013. The role of mesoscale convective complexes in southern Africa summer rainfall. *Journal of Climate*, 26(5): 1654–1668. <https://doi.org/10.1175/JCLI-D-12-00239.1>.
- Burls NJ, Blamey RC, Cash BA, Swenson ET, Fahad A al, Bopape MJM, Straus DM, Reason CJC. 2019. The Cape Town “Day Zero” drought and Hadley cell expansion. *npj Climate and Atmospheric Science 2019 2:1*. Nature Publishing Group, 2(1): 1–8. <https://doi.org/10.1038/s41612-019-0084-6>.
- Camberlin P, Moron V, Okoola R, Philippon N, Gitau W. 2009. Components of rainy seasons’ variability in Equatorial East Africa: Onset, cessation, rainfall frequency and intensity. *Theoretical and Applied Climatology*, 98(3–4): 237–249. <https://doi.org/10.1007/s00704-009-0113-1>.
- Conway D, Dalin C, Landman WA, Osborn TJ. 2017. Hydropower plans in eastern and southern Africa increase risk of concurrent climate-related electricity supply disruption. *Nature Energy 2017 2:12*. Nature Publishing Group, 2(12): 946–953. <https://doi.org/10.1038/s41560-017-0037-4>.
- Conway D, Van Garderen EA, Deryng D, Dorling S, Krueger T, Landman W, Lankford B, Lebek K, Osborn T, Ringler C, Thurlow J, Zhu T, Dalin C. 2015. Climate and southern Africa’s water-energy-food nexus. *Nature Climate Change*. Nature Publishing Group, 5(9): 837–846. <https://doi.org/10.1038/nclimate2735>.
- Cook C, Reason CJC, Hewitson BC. 2004. Wet and dry spells within particularly wet and dry summers in the South African summer rainfall region. *Climate Research*, 26(1): 17–31. <https://doi.org/10.3354/cr026017>.

- Cook KH. 2000. The South Indian convergence zone and interannual rainfall variability over Southern Africa. *Journal of Climate*, 13(21): 3789–3804. [https://doi.org/10.1175/1520-0442\(2000\)013<3789:TSICZA>2.0.CO;2](https://doi.org/10.1175/1520-0442(2000)013<3789:TSICZA>2.0.CO;2).
- Cook KH. 2001. A southern hemisphere wave response to ENSO with implications for Southern Africa precipitation. *Journal of the Atmospheric Sciences*, 58(15): 2146–2162. [https://doi.org/10.1175/1520-0469\(2001\)058<2146:ASHWRT>2.0.CO;2](https://doi.org/10.1175/1520-0469(2001)058<2146:ASHWRT>2.0.CO;2).
- Crétat J, Macron C, Pohl B, Richard Y. 2011. Quantifying internal variability in a regional climate model: A case study for Southern Africa. *Climate Dynamics*, 37(7–8): 1335–1356. <https://doi.org/10.1007/s00382-011-1021-5>.
- Crétat J, Pohl B, Dieppois B, Berthou S, Pergaud J. 2019. The Angola Low: relationship with southern African rainfall and ENSO. *Climate Dynamics*. Springer Berlin Heidelberg, 52(3–4): 1783–1803. <https://doi.org/10.1007/s00382-018-4222-3>.
- Crétat J, Pohl B, Richard Y, Drobinski P. 2012a. Uncertainties in simulating regional climate of Southern Africa: Sensitivity to physical parameterizations using WRF. *Climate Dynamics*, 38(3–4): 613–634. <https://doi.org/10.1007/s00382-011-1055-8>.
- Crétat J, Richard Y, Pohl B, Rouault M, Reason C, Fauchereau N. 2012b. Recurrent daily rainfall patterns over South Africa and associated dynamics during the core of the austral summer. *International Journal of Climatology*, 32(2): 261–273. <https://doi.org/10.1002/joc.2266>.
- CRI. 2021. *Global Climate Risk Index 2021: Who suffers most from extreme weather events? weather-related loss events in 2019 and 2000-2019*. .
- Desbiolles F, Blamey R, Illig S, James R, Barimalala R, Renault L, Reason C. 2018. Upscaling impact of wind/sea surface temperature mesoscale interactions on southern Africa austral summer climate. *International Journal of Climatology*, 38(12): 4651–4660. <https://doi.org/10.1002/joc.5726>.
- Desbiolles F, Howard E, Blamey RC, Barimalala R, Hart NCG, Reason CJC. 2020. Role of ocean mesoscale structures in shaping the Angola-Low pressure system and the southern Africa rainfall. *Climate Dynamics*. Springer Berlin Heidelberg, 54(7–8): 3685–3704. <https://doi.org/10.1007/s00382-020-05199-1>.
- Dieppois B, Pohl B, Crétat J, Eden J, Sidibe M, New M, Rouault M, Lawler D. 2019. Southern African summer-rainfall variability, and its teleconnections, on interannual to interdecadal timescales in CMIP5 models. *Climate Dynamics*. Springer Berlin Heidelberg, 53(5–6): 3505–3527. <https://doi.org/10.1007/s00382-019-04720-5>.
- Dieppois B, Pohl B, Rouault M, New M, Lawler D, Keenlyside N. 2016. Interannual to interdecadal variability of winter and summer southern African rainfall, and their teleconnections. *Journal of Geophysical Research*. <https://doi.org/10.1002/2015JD024576>.
- Dieppois B, Rouault M, New M. 2015. The impact of ENSO on Southern African rainfall in CMIP5 ocean atmosphere coupled climate models. *Climate Dynamics*, 45(9–10): 2425–2442. <https://doi.org/10.1007/s00382-015-2480-x>.
- Donald A, Meinke H, Power B, Maia A de HN, Wheeler MC, White N, Stone RC, Ribbe J. 2006. Near-global impact of the Madden-Julian Oscillation on rainfall. *Geophysical Research Letters*,

33(9): 6–9. <https://doi.org/10.1029/2005GL025155>.

Donat MG, Lowry AL, Alexander L V., O’Gorman PA, Maher N. 2016. More extreme precipitation in the world’s dry and wet regions. *Nature Climate Change*. <https://doi.org/10.1038/nclimate2941>.

Dosio A. 2017. Projection of temperature and heat waves for Africa with an ensemble of CORDEX Regional Climate Models. *Climate Dynamics*. Springer Verlag, 49(1–2): 493–519. <https://doi.org/10.1007/S00382-016-3355-5/FIGURES/15>.

Dyer TGJ, Tyson PD. 1977. Estimating Above and Below Normal Rainfall Periods over South Africa, 1972–2000. *Journal of Applied Meteorology*, 16(2): 145–147. [https://doi.org/10.1175/1520-0450\(1977\)016<0145:EAABNR>2.0.CO;2](https://doi.org/10.1175/1520-0450(1977)016<0145:EAABNR>2.0.CO;2).

Engelbrecht CJ, Engelbrecht FA, Dyson LL. 2013. High-resolution model-projected changes in mid-tropospheric closed-lows and extreme rainfall events over southern Africa. *International Journal of Climatology*, 33(1): 173–187. <https://doi.org/10.1002/joc.3420>.

Engelbrecht F, Adegoke J, Bopape MJ, Naidoo M, Garland R, Thatcher M, McGregor J, Katzfey J, Werner M, Ichoku C, Gatebe C. 2015. Projections of rapidly rising surface temperatures over Africa under low mitigation. *Environmental Research Letters*. IOP Publishing, 10(8): 085004. <https://doi.org/10.1088/1748-9326/10/8/085004>.

Engelbrecht FA, McGregor JL, Engelbrecht CJ. 2009. Dynamics of the Conformal-Cubic Atmospheric Model projected climate-change signal over southern Africa. *International Journal of Climatology*. John Wiley & Sons, Ltd, 29(7): 1013–1033. <https://doi.org/10.1002/JOC.1742>.

Fauchereau N, Pohl B, Reason CJC, Rouault M, Richard Y. 2009. Recurrent daily OLR patterns in the Southern Africa/Southwest Indian ocean region, implications for South African rainfall and teleconnections. *Climate Dynamics*, 32(4): 575–591. <https://doi.org/10.1007/s00382-008-0426-2>.

Favre A, Hewitson B, Lennard C, Cerezo-Mota R, Tadross M. 2013. Cut-off Lows in the South Africa region and their contribution to precipitation. *Climate Dynamics*, 41(9–10): 2331–2351. <https://doi.org/10.1007/s00382-012-1579-6>.

Favre A, Philippon N, Pohl B, Kalognomou EA, Lennard C, Hewitson B, Nikulin G, Dosio A, Panitz HJ, Cerezo-Mota R. 2016. Spatial distribution of precipitation annual cycles over South Africa in 10 CORDEX regional climate model present-day simulations. *Climate Dynamics*. Springer Berlin Heidelberg, 46(5–6): 1799–1818. <https://doi.org/10.1007/s00382-015-2677-z>.

Fitchett JM, Grab SW. 2014. A 66-year tropical cyclone record for south-east Africa: Temporal trends in a global context. *International Journal of Climatology*, 34(13): 3604–3615. <https://doi.org/10.1002/joc.3932>.

Frei C, Christensen JH, Déqué M, Jacob D, Jones RG, Vidale PL. 2003. Daily precipitation statistics in regional climate models: Evaluation and intercomparison for the European Alps. *Journal of Geophysical Research: Atmospheres*, 108(3): 1–19. <https://doi.org/10.1029/2002jd002287>.

Gascón E, Lavers D, Hamill TM, Richardson DS, Bouallègue ZB, Leutbecher M, Pappenberger F. 2019. Statistical postprocessing of dual-resolution ensemble precipitation forecasts across Europe. *Quarterly Journal of the Royal Meteorological Society*, 145(724): 3218–3235.

<https://doi.org/10.1002/qj.3615>.

Gitau W, Camberlin P, Ogallo L, Bosire E. 2018. Trends of intraseasonal descriptors of wet and dry spells over equatorial eastern africa. *International Journal of Climatology*, 38(3): 1189–1200. <https://doi.org/10.1002/joc.5234>.

Gitau W, Camberlin P, Ogallo L, Okoola R. 2015. Oceanic and atmospheric linkages with short rainfall season intraseasonal statistics over Equatorial Eastern Africa and their predictive potential. *International Journal of Climatology*, 35(9): 2382–2399. <https://doi.org/10.1002/joc.4131>.

Gitau W, Ogallo L, Camberlin P, Okoola R. 2013. Spatial coherence and potential predictability assessment of intraseasonal statistics of wet and dry spells over Equatorial Eastern Africa. *International Journal of Climatology*, 33(12): 2690–2705. <https://doi.org/10.1002/joc.3620>.

Goddard L, Baethgen WE, Bhojwani H, Robertson AW. 2014. The International Research Institute for Climate. *Earth Perspectives*, 1–14. <https://doi.org/https://doi.org/10.1186/2194-6434-1-10>.

Grimm AM. 2019. Madden–Julian Oscillation impacts on South American summer monsoon season: precipitation anomalies, extreme events, teleconnections, and role in the MJO cycle. *Climate Dynamics*. Springer Berlin Heidelberg, 53(1–2): 907–932. <https://doi.org/10.1007/s00382-019-04622-6>.

Grimm AM, Reason CJC. 2011. Does the South American Monsoon Influence African Rainfall? *Journal of Climate*. American Meteorological Society, 24(4): 1226–1238. <https://doi.org/10.1175/2010JCLI3722.1>.

Grimm AM, Reason CJC. 2015. Intraseasonal teleconnections between South America and South Africa. *Journal of Climate*, 28(23): 9489–9497. <https://doi.org/10.1175/JCLI-D-15-0116.1>.

Guan H, Zhu Y, Sinsky E, Fu B, Li W, Zhou X, Xue X, Hou D, Peng J, Nageswararao MM, Tallapragada V, Hamill TM, Whitaker JS, Bates G, Pegion P, Frederick S, Rosencrans M, Kumar A. 2022. GEFSv12 Reforecast Dataset for Supporting Subseasonal and Hydrometeorological Applications. *Monthly Weather Review*, 150(3): 647–665. <https://doi.org/10.1175/mwr-d-21-0245.1>.

Hamill TM, Bates GT, Whitaker JS, Murray DR, Fiorino M, Galarneau TJ, Zhu Y, Lapenta W. 2013. NOAA’s second-generation global medium-range ensemble reforecast dataset. *Bulletin of the American Meteorological Society*, 94(10): 1553–1565. <https://doi.org/10.1175/BAMS-D-12-00014.1>.

Hamill TM, Scheuerer M, Bates GT. 2015. Analog probabilistic precipitation forecasts using GEFS reforecasts and climatology-calibrated precipitation analyses. *Monthly Weather Review*, 143(8): 3300–3309. <https://doi.org/10.1175/MWR-D-15-0004.1>.

Hamill TM, Whitaker JS, Mullen SL. 2006. Reforecasts: An Important Dataset for Improving Weather Predictions. *Bulletin of the American Meteorological Society*. American Meteorological Society, 87(1): 33–46. <https://doi.org/10.1175/BAMS-87-1-33>.

Hamill TM, Whitaker JS, Shlyayeva A, Bates G, Fredrick S, Pegion P, Sinsky E, Zhu Y, Tallapragada V, Guan H, Zhou X, Woollen J. 2022. The Reanalysis for the Global Ensemble

Forecast System, Version 12. *Monthly Weather Review*. American Meteorological Society, 150(1): 59–79. <https://doi.org/10.1175/MWR-D-21-0023.1>.

Hamill TM, Whitaker JS, Wei X. 2004. Ensemble re-forecasting: Improving medium-range forecast skill using retrospective forecasts. *Bulletin of the American Meteorological Society*, 132(6): 1434–1447. [https://doi.org/https://doi.org/10.1175/1520-0493\(2004\)132<1434:ERIMFS>2.0.CO;2](https://doi.org/https://doi.org/10.1175/1520-0493(2004)132<1434:ERIMFS>2.0.CO;2).

Hart NCG, Reason CJC, Fauchereau N. 2010. Tropical-extratropical interactions over southern Africa: Three cases of heavy summer season rainfall. *Monthly Weather Review*, 138(7): 2608–2623. <https://doi.org/10.1175/2010MWR3070.1>.

Hart NCG, Reason CJC, Fauchereau N. 2013. Cloud bands over southern Africa: Seasonality, contribution to rainfall variability and modulation by the MJO. *Climate Dynamics*, 41(5–6): 1199–1212. <https://doi.org/10.1007/s00382-012-1589-4>.

Hersbach H, Bell B, Berrisford P, Hirahara S, Horányi A, Muñoz-Sabater J, Nicolas J, Peubey C, Radu R, Schepers D, Simmons A, Soci C, Abdalla S, Abellan X, Balsamo G, Bechtold P, Biavati G, Bidlot J, Bonavita M, De Chiara G, Dahlgren P, Dee D, Diamantakis M, Dragani R, Flemming J, Forbes R, Fuentes M, Geer A, Haimberger L, Healy S, Hogan RJ, Hólm E, Janisková M, Keeley S, Laloyaux P, Lopez P, Lupu C, Radnoti G, de Rosnay P, Rozum I, Vamborg F, Villaume S, Thépaut JN. 2020a. The ERA5 global reanalysis. *Quarterly Journal of the Royal Meteorological Society*, 146(730): 1999–2049. <https://doi.org/10.1002/qj.3803>.

Hersbach H, Bell B, Berrisford P, Hirahara S, Horányi A, Muñoz-Sabater J, Nicolas J, Peubey C, Radu R, Schepers D, Simmons A, Soci C, Abdalla S, Abellan X, Balsamo G, Bechtold P, Biavati G, Bidlot J, Bonavita M, De Chiara G, Dahlgren P, Dee D, Diamantakis M, Dragani R, Flemming J, Forbes R, Fuentes M, Geer A, Haimberger L, Healy S, Hogan RJ, Hólm E, Janisková M, Keeley S, Laloyaux P, Lopez P, Lupu C, Radnoti G, de Rosnay P, Rozum I, Vamborg F, Villaume S, Thépaut JN. 2020b. The ERA5 global reanalysis. *Quarterly Journal of the Royal Meteorological Society*. John Wiley & Sons, Ltd, 146(730): 1999–2049. <https://doi.org/10.1002/QJ.3803>.

Hoegh-Guldberg O, Jacob D, Taylor M, Bindi M, Abdul Halim S, Achlatis Australia M, Alexander L V, Allen MR, Berry P, Boyer C, Brilli L, Buckeridge M, Byers Austria E, Antonio Marengo Brazil J, Pereira J, Sherstyukov B, Jacob D, Taylor M, Bindi M, Brown S, Camilloni I, Diedhiou A, Djalante R, Ebi K, Engelbrecht F, Guiot J, Hijioka Y, Mehrotra S, Payne A, Seneviratne S, Thomas A, Warren R, Zhou G, Zhai P, Pörtner H, Roberts D, Skeea J, Shukla P, Pirani A, Moufouma-Okia W, Péan C, Pidcock R, Connors S, Matthews J, Chen Y, Zhou X, Gomis M, Lonnoy E, Maycock T, Tignor M, Waterfield T. 2018. *Impacts of 1.5°C global warming on natural and human systems*. .

Hoell A, Cheng L. 2018. Austral summer Southern Africa precipitation extremes forced by the El Niño–Southern oscillation and the subtropical Indian Ocean dipole. *Climate Dynamics*. Springer Berlin Heidelberg, 50(9–10): 3219–3236. <https://doi.org/10.1007/s00382-017-3801-z>.

Hoell A, Funk C, Magadzire T, Zinke J, Husak G. 2015. El Niño–Southern Oscillation diversity and Southern Africa teleconnections during Austral Summer. *Climate Dynamics*. Springer Berlin Heidelberg, 45(5–6): 1583–1599. <https://doi.org/10.1007/s00382-014-2414-z>.

- Hong S, Lim J. 2006. The WRF single-moment 6-class microphysics scheme (WSM6). *Journal of the Korean Meteorological Society*, 42(2): 129–151.
- Hong SY, Noh Y, Dudhia J. 2006. A New Vertical Diffusion Package with an Explicit Treatment of Entrainment Processes. *Monthly Weather Review*. American Meteorological Society, 134(9): 2318–2341. <https://doi.org/10.1175/MWR3199.1>.
- Huang B, Thorne PW, Banzon VF, Boyer T, Chepurin G, Lawrimore JH, Menne MJ, Smith TM, Vose RS, Zhang HM. 2017. Extended reconstructed Sea surface temperature, Version 5 (ERSSTv5): Upgrades, validations, and intercomparisons. *Journal of Climate*, 30(20): 8179–8205. <https://doi.org/10.1175/JCLI-D-16-0836.1>.
- Huffman GJ, Adler RF, Bolvin DT, Gu G, Nelkin EJ, Bowman KP, Hong Y, Stocker EF, Wolff DB. 2007. The TRMM Multisatellite Precipitation Analysis (TMPA): Quasi-global, multiyear, combined-sensor precipitation estimates at fine scales. *Journal of Hydrometeorology*, 8(1): 38–55. <https://doi.org/10.1175/JHM560.1>.
- Iacono MJ, Delamere JS, Mlawer EJ, Shephard MW, Clough SA, Collins WD. 2008. Radiative forcing by long-lived greenhouse gases: Calculations with the AER radiative transfer models. *Journal of Geophysical Research: Atmospheres*. John Wiley & Sons, Ltd, 113(D13): 13103. <https://doi.org/10.1029/2008JD009944>.
- IPCC. 2021. *Climate Change 2021: The Physical Science Basis. Contribution of Working Group I to the Sixth Assessment Report of the Intergovernmental Panel on Climate Change*. Cambridge University Press: Cambridge, United Kingdom and New York, NY, USA.
- Jackson LS, Finney DL, Kendon EJ, Marsham JH, Parker DJ, Stratton RA, Tomassini L, Tucker S. 2020. The effect of explicit convection on couplings between rainfall, humidity, and ascent over Africa under climate change. *Journal of Climate*, 33(19): 8315–8337. <https://doi.org/10.1175/JCLI-D-19-0322.1>.
- James R, Hart NCG, Munday C, Reason CJC, Washington R. 2020. Coupled climate model simulation of tropical–extratropical cloud bands over Southern Africa. *Journal of Climate*, 33(19): 8579–8602. <https://doi.org/10.1175/JCLI-D-19-0731.1>.
- Janjic ZI. 1994. The step-mountain eta coordinate model: further developments of the convection, viscous sublayer, and turbulence closure schemes. *Monthly Weather Review*, 122(5): 927–945. [https://doi.org/10.1175/1520-0493\(1994\)122<0927:TSMECM>2.0.CO;2](https://doi.org/10.1175/1520-0493(1994)122<0927:TSMECM>2.0.CO;2).
- Kain JS. 2004. The Kain–Fritsch Convective Parameterization: An Update. *Journal of Applied Meteorology and Climatology*, 43(1): 170–181. [https://doi.org/https://doi.org/10.1175/1520-0450\(2004\)043<0170:TKCPAU>2.0.CO;2](https://doi.org/https://doi.org/10.1175/1520-0450(2004)043<0170:TKCPAU>2.0.CO;2).
- Kalnay E, Kanamitsu M, Kistler R, Collins W, Deaven D, Gandin L, Iredell M, Saha S, White G, Woollen J, Zhu Y, Chelliah M, Ebisuzaki W, Higgins W, Janowiak J, Mo KC, Ropelewski C, Wang J, Leetmaa A, Reynolds R, Jenne R, Joseph D. 1996. The NCEP/NCAR 40-Year Reanalysis Project in: *Bulletin of the American Meteorological Society* Volume 77 Issue 3 (1996). *American Meteorological Society*, 77(3): 437–472.
- Kendall MG. 1957. *Rank Correlation Methods. 4th Edition*. Charles Griffin, London.
- Kendon EJ, Ban N, Roberts NM, Fowler HJ, Roberts MJ, Chan SC, Evans JP, Fosser G,

Wilkinson JM. 2017. Do convection-permitting regional climate models improve projections of future precipitation change? *Bulletin of the American Meteorological Society*, 98(1): 79–93. <https://doi.org/10.1175/BAMS-D-15-0004.1>.

Kendon EJ, Stratton RA, Tucker S, Marsham JH, Berthou S, Rowell DP, Senior CA. 2019. Enhanced future changes in wet and dry extremes over Africa at convection-permitting scale. *Nature Communications*. Springer US, 10(1). <https://doi.org/10.1038/s41467-019-09776-9>.

Kharin V V., Zwiers FW, Zhang X, Hegerl GC. 2007. Changes in Temperature and Precipitation Extremes in the IPCC Ensemble of Global Coupled Model Simulations. *Journal of Climate*. American Meteorological Society, 20(8): 1419–1444. <https://doi.org/10.1175/JCLI4066.1>.

Kruger AC. 2018. Africa and the Paris Agreement. *Nature Climate Change*. Springer US, 8(5): 365–366. <https://doi.org/10.1038/s41558-018-0146-5>.

Kruger AC, Nxumalo MP. 2017. Historical rainfall trends in South Africa: 1921–2015. *Water SA*, 43(2): 285–297. <https://doi.org/10.4314/wsa.v43i2.12>.

Kusangaya S, Warburton ML, Archer van Garderen E, Jewitt GPW. 2014. Impacts of climate change on water resources in southern Africa: A review. *Physics and Chemistry of the Earth, Parts A/B/C*. Pergamon, 67–69: 47–54. <https://doi.org/10.1016/J.PCE.2013.09.014>.

Lakhraj-Govender R, Grab SW. 2019. Rainfall and river flow trends for the Western Cape Province, South Africa. *South African Journal of Science*, 115(9–10): 1–6. <https://doi.org/10.17159/sajs.2019/6028>.

Lazenby MJ, Todd MC, Chadwick R, Wang Y. 2018. Future Precipitation Projections over Central and Southern Africa and the Adjacent Indian Ocean: What Causes the Changes and the Uncertainty? *Journal of Climate*. American Meteorological Society, 31(12): 4807–4826. <https://doi.org/10.1175/JCLI-D-17-0311.1>.

Li C, Zwiers F, Zhang X, Li G, Sun Y, Wehner M. 2021. Changes in Annual Extremes of Daily Temperature and Precipitation in CMIP6 Models. *Journal of Climate*. American Meteorological Society, 34(9): 3441–3460. <https://doi.org/10.1175/JCLI-D-19-1013.1>.

Li W, Zhu Y, Zhou X, Hou D, Sinsky E, Melhauser C, Peña M, Guan H, Wobus R. 2019. Evaluating the MJO prediction skill from different configurations of NCEP GEFS extended forecast. *Climate Dynamics*. Springer Verlag, 52(7–8): 4923–4936. <https://doi.org/10.1007/S00382-018-4423-9/FIGURES/12>.

Liu W, Lim WH, Sun F, Mitchell D, Wang H, Chen D, Bethke I, Shiogama H, Fischer E. 2018a. Global Freshwater Availability Below Normal Conditions and Population Impact Under 1.5 and 2 °C Stabilization Scenarios. *Geophysical Research Letters*. John Wiley & Sons, Ltd, 45(18): 9803–9813. <https://doi.org/10.1029/2018GL078789>.

Liu W, Sun F, Ho Lim W, Zhang J, Wang H, Shiogama H, Zhang Y. 2018b. Global drought and severe drought-Affected populations in 1.5 and 2 °C warmer worlds. *Earth System Dynamics*. Copernicus GmbH, 9(1): 267–283. <https://doi.org/10.5194/ESD-9-267-2018>.

Lu E, Zhao W, Zou X, Ye D, Zhao C, Zhang Q. 2017. Temporal-spatial monitoring of an extreme precipitation event: Determining simultaneously the time period it lasts and the geographic region it affects. *Journal of Climate*, 30(16): 6123–6132.

<https://doi.org/10.1175/JCLI-D-17-0105.1>.

Lyon B, Mason SJ. 2007. The 1997-98 summer rainfall season in Southern Africa. Part I: Observations. *Journal of Climate*, 20(20): 5134–5148. <https://doi.org/10.1175/JCLI4225.1>.

Ma LM, Tan ZM. 2009. Improving the behavior of the cumulus parameterization for tropical cyclone prediction: Convection trigger. *Atmospheric Research*. Elsevier B.V., 92(2): 190–211. <https://doi.org/10.1016/j.atmosres.2008.09.022>.

Macron C, Pohl B, Richard Y, Bessafi M. 2014. How do tropical temperate troughs form and develop over Southern Africa? *Journal of Climate*, 27(4): 1633–1647. <https://doi.org/10.1175/JCLI-D-13-00175.1>.

Macron C, Richard Y, Garot T, Bessafi M, Pohl B, Ratiarison A, Razafindrabe A. 2016. Intraseasonal rainfall variability over Madagascar. *Monthly Weather Review*, 144(5): 1877–1885. <https://doi.org/10.1175/MWR-D-15-0077.1>.

Madden RA, Julian PR. 1994. Observations of the 40-50-day tropical oscillation - a review. *Monthly Weather Review*. [https://doi.org/10.1175/1520-0493\(1994\)122<0814:OOTDTP>2.0.CO;2](https://doi.org/10.1175/1520-0493(1994)122<0814:OOTDTP>2.0.CO;2).

Malherbe J, Dieppois B, Maluleke P, Van Staden M, Pillay DL. 2016. South African droughts and decadal variability. *Natural Hazards*. Springer Netherlands, 80(1): 657–681. <https://doi.org/10.1007/s11069-015-1989-y>.

Malherbe J, Engelbrecht FA, Landman WA, Engelbrecht CJ. 2012. Tropical systems from the southwest Indian Ocean making landfall over the Limpopo River Basin southern Africa: A historical perspective. *International Journal of Climatology*, 32(7): 1018–1032. <https://doi.org/10.1002/joc.2320>.

Malherbe J, Landman WA, Engelbrecht FA. 2014. The bi-decadal rainfall cycle, Southern Annular Mode and tropical cyclones over the Limpopo River Basin, southern Africa. *Climate Dynamics*, 42(11–12): 3121–3138. <https://doi.org/10.1007/s00382-013-2027-y>.

Manhique AJ, Reason CJC, Rydberg L, Fauchereau N. 2011. ENSO and Indian Ocean sea surface temperatures and their relationships with tropical temperate troughs over Mozambique and the Southwest Indian Ocean. *International Journal of Climatology*, 31(1): 1–13. <https://doi.org/10.1002/joc.2050>.

Mann H. 1945. Mann Nonparametric test against trend. *Econometrica*.

Maraun D. 2016. Bias Correcting Climate Change Simulations - a Critical Review. *Current Climate Change Reports*. Current Climate Change Reports, 2(4): 211–220. <https://doi.org/10.1007/s40641-016-0050-x>.

Mason SJ, Goddard L, Graham NE, Yulaeva E, Sun L, Arkin PA. 1999. The IRI seasonal climate prediction system. *WRPMD 1999: Preparing for the 21st Century*. [https://doi.org/10.1061/40430\(1999\)4](https://doi.org/10.1061/40430(1999)4).

Mason SJ, Joubert AM. 1997. Simulated changes in extreme rainfall over southern Africa. *International Journal of Climatology*, 17(3): 291–301. [https://doi.org/10.1002/\(sici\)1097-0088\(19970315\)17:3<291::aid-joc120>3.3.co;2-t](https://doi.org/10.1002/(sici)1097-0088(19970315)17:3<291::aid-joc120>3.3.co;2-t).

- Mason SJ, Jury MR. 1997. Climatic variability and change over southern Africa: a reflection on underlying processes. *Progress in Physical Geography: Earth and Environment*, 21(1): 23–50. <https://doi.org/10.1177/030913339702100103>.
- Masupha TE, Moeletsi ME, Tsubo M. 2016. Dry spells assessment with reference to the maize crop in the Luvuvhu River catchment of South Africa. *Physics and Chemistry of the Earth*. <https://doi.org/10.1016/j.pce.2015.10.014>.
- Maure G, Pinto I, Ndebele-Murisa M, Muthige M, Lennard C, Nikulin G, Dosio A, Meque A. 2018. The southern African climate under 1.5 °C and 2 °C of global warming as simulated by CORDEX regional climate models. *Environmental Research Letters*. IOP Publishing, 13(6): 065002. <https://doi.org/10.1088/1748-9326/AAB190>.
- McKittrick R, Christy J. 2018. A Test of the Tropical 200- to 300-hPa Warming Rate in Climate Models. *Earth and Space Science*. Wiley-Blackwell Publishing Ltd, 5(9): 529–536. <https://doi.org/10.1029/2018EA000401>.
- Misra V. 2003. The influence of Pacific SST variability on the precipitation over southern Africa. *Journal of Climate*, 16(14): 2408–2418. <https://doi.org/10.1175/2785.1>.
- Moron V, Camberlin P, Robertson AW. 2013. Extracting subseasonal scenarios: An alternative method to analyze seasonal predictability of regional-scale tropical rainfall. *Journal of Climate*, 26(8): 2580–2600. <https://doi.org/10.1175/JCLI-D-12-00357.1>.
- Morrison H, Thompson G, Tatarskii V. 2009. Impact of Cloud Microphysics on the Development of Trailing Stratiform Precipitation in a Simulated Squall Line: Comparison of One- and Two-Moment Schemes. *Monthly Weather Review*. American Meteorological Society, 137(3): 991–1007. <https://doi.org/10.1175/2008MWR2556.1>.
- Mpungose N, Thoithi W, Blamey RC, Reason CJC. 2022. Extreme rainfall events in southeastern Africa during the summer. *Theoretical and Applied Climatology*. Springer Vienna, 150(1–2): 185–201. <https://doi.org/10.1007/s00704-022-04162-w>.
- Muller CJ, O’Gorman PA, Back LE. 2011. Intensification of Precipitation Extremes with Warming in a Cloud-Resolving Model. *Journal of Climate*. American Meteorological Society, 24(11): 2784–2800. <https://doi.org/10.1175/2011JCLI3876.1>.
- Nangombe S, Zhou T, Zhang W, Wu B, Hu S, Zou L, Li D. 2018. Record-breaking climate extremes in Africa under stabilized 1.5 °c and 2 °c global warming scenarios. *Nature Climate Change*, 8(5): 375–380. <https://doi.org/10.1038/s41558-018-0145-6>.
- Ndarana T, Lekoloane LE, Rammopo TS, Reason CJC, Bopape M-JM, Chikoore H, Engelbrecht FA. 2022. *Downstream development associated with two types of ridging South Atlantic Ocean anticyclones over South Africa. Weather and Climate Dynamics Discussions*.
- Nicholson S. 2003. Comments on “The South Indian convergence zone and interannual rainfall variability over southern Africa” and the question of ENSO’s influence on southern Africa. *Journal of Climate*, 16(3): 555–562. [https://doi.org/10.1175/1520-0442\(2003\)016<0555:COTSIC>2.0.CO;2](https://doi.org/10.1175/1520-0442(2003)016<0555:COTSIC>2.0.CO;2).
- Nicholson SE, Kim J. 1997. THE RELATIONSHIP OF THE EL NIÑO–SOUTHERN OSCILLATION TO AFRICAN RAINFALL. *International Journal of Climatology*, 17(2): 117–

135. [https://doi.org/10.1002/\(SICI\)1097-0088\(199702\)17:2<117::AID-JOC84>3.0.CO;2-O](https://doi.org/10.1002/(SICI)1097-0088(199702)17:2<117::AID-JOC84>3.0.CO;2-O).

Oettli P, Tozuka T, Izumo T, Engelbrecht FA, Yamagata T. 2014. The self-organizing map, a new approach to apprehend the Madden-Julian Oscillation influence on the intraseasonal variability of rainfall in the southern African region. *Climate Dynamics*, 43(5–6): 1557–1573. <https://doi.org/10.1007/s00382-013-1985-4>.

Otto FEL, Wolski P, Lehner F, Tebaldi C, Van Oldenborgh GJ, Hogesteegeer S, Singh R, Holden P, Fučkar NS, Odoulami RC, New M. 2018. Anthropogenic influence on the drivers of the Western Cape drought 2015-2017. *Environmental Research Letters*, 13(12). <https://doi.org/10.1088/1748-9326/aae9f9>.

Oueslati B, Pohl B, Moron V, Rome S, Janicot S. 2017. Characterization of heat waves in the Sahel and associated physical mechanisms. *Journal of Climate*, 30(9): 3095–3115. <https://doi.org/10.1175/JCLI-D-16-0432.1>.

Paciorek CJ, Stone DA, Wehner MF. 2018. Quantifying statistical uncertainty in the attribution of human influence on severe weather. *Weather and Climate Extremes*, 20(June 2017): 69–80. <https://doi.org/10.1016/j.wace.2018.01.002>.

Pascale S, Pohl B, Kapnick SB, Zhang H. 2019. On the Angola low interannual variability and its role in modulating ENSO effects in southern Africa. *Journal of Climate*, 32(15): 4783–4803. <https://doi.org/10.1175/JCLI-D-18-0745.1>.

Philippon N, Camberlin P, Moron V, Boyard-Micheau J. 2015. Anomalously wet and dry rainy seasons in Equatorial East Africa and associated differences in intra-seasonal characteristics. *Climate Dynamics*. Springer Berlin Heidelberg, 45(7–8): 2101–2121. <https://doi.org/10.1007/s00382-014-2460-6>.

Pinto I, Lennard C, Tadross M, Hewitson B, Dosio A, Nikulin G, Panitz HJ, Shongwe ME. 2016. Evaluation and projections of extreme precipitation over southern Africa from two CORDEX models. *Climatic Change*, 135(3–4): 655–668. <https://doi.org/10.1007/s10584-015-1573-1>.

Pohl B, Crétat J, Camberlin P. 2011. Testing WRF capability in simulating the atmospheric water cycle over Equatorial East Africa. *Climate Dynamics*, 37(7–8): 1357–1379. <https://doi.org/10.1007/s00382-011-1024-2>.

Pohl B, Dieppois B, Crétat J, Lawler D, Rouault M. 2018. From synoptic to interdecadal variability in southern African rainfall: Toward a unified view across time scales. *Journal of Climate*, 31(15): 5845–5872. <https://doi.org/10.1175/JCLI-D-17-0405.1>.

Pohl B, Fauchereau N. 2012. The southern annular mode seen through weather regimes. *Journal of Climate*, 25(9): 3336–3354. <https://doi.org/10.1175/JCLI-D-11-00160.1>.

Pohl B, Fauchereau N, Reason CJC, Rouault M. 2010. Relationships between the Antarctic oscillation, the Madden-Julian oscillation, and ENSO, and consequences for rainfall analysis. *Journal of Climate*, 23(2): 238–254. <https://doi.org/10.1175/2009JCLI2443.1>.

Pohl B, Fauchereau N, Richard Y, Rouault M, Reason CJC. 2009. Interactions between synoptic, intraseasonal and interannual convective variability over Southern Africa. *Climate Dynamics*, 33(7–8): 1033–1050. <https://doi.org/10.1007/s00382-008-0485-4>.

- Pohl B, MacRon C, Monerie PA. 2017. Fewer rainy days and more extreme rainfall by the end of the century in Southern Africa. *Scientific Reports*. Nature Publishing Group, 7(April): 6–12. <https://doi.org/10.1038/srep46466>.
- Pohl B, Richard Y, Fauchereau N. 2007. Influence of the Madden-Julian oscillation on southern African summer rainfall. *Journal of Climate*, 20(16): 4227–4242. <https://doi.org/10.1175/JCLI4231.1>.
- Pohl B, Rouault M, Roy S Sen. 2014. Simulation of the annual and diurnal cycles of rainfall over South Africa by a regional climate model. *Climate Dynamics*, 43(7–8): 2207–2226. <https://doi.org/10.1007/s00382-013-2046-8>.
- Pomposi C, Funk C, Shukla S, Harrison L, Magadzire T. 2018. Distinguishing southern Africa precipitation response by strength of El Niño events and implications for decision-making. *Environmental Research Letters*, 13(7). <https://doi.org/10.1088/1748-9326/aacc4c>.
- Puaud Y, Pohl B, Fauchereau N, Macron C, Beltrando G. 2017. Climate co-variability between South America and Southern Africa at interannual, intraseasonal and synoptic scales. *Climate Dynamics*. Springer Verlag, 48(11–12): 4029–4050. <https://doi.org/10.1007/S00382-016-3318-X/FIGURES/13>.
- Quagraine KA, Hewitson B, Jack C, Pinto I, Lennard C. 2019. A methodological approach to assess the co-behavior of climate processes over Southern Africa. *Journal of Climate*, 32(9): 2483–2495. <https://doi.org/10.1175/JCLI-D-18-0689.1>.
- Ranasinghe. 2021. Chapter 12: Climate change information for regional impact and for risk assessment. *Climate Change 2021: The Physical Science Basis. Contribution of Working Group I to the Sixth Assessment Report of the Intergovernmental Panel on Climate Change*, (August 2021): 351–364.
- Rapolaki RS, Blamey RC, Hermes JC, Reason CJC. 2019. A classification of synoptic weather patterns linked to extreme rainfall over the Limpopo River Basin in southern Africa. *Climate Dynamics*. Springer Berlin Heidelberg, 53(3–4): 2265–2279. <https://doi.org/10.1007/s00382-019-04829-7>.
- Rapolaki RS, Blamey RC, Hermes JC, Reason CJC. 2020. Moisture sources associated with heavy rainfall over the Limpopo River Basin, southern Africa. *Climate Dynamics*. Springer Berlin Heidelberg, 55(5–6): 1473–1487. <https://doi.org/10.1007/s00382-020-05336-w>.
- Ratan R, Venugopal V. 2013. Wet and dry spell characteristics of global tropical rainfall. *Water Resources Research*, 49(6): 3830–3841. <https://doi.org/10.1002/wrcr.20275>.
- Ratna SB, Ratnam J V., Behera SK, Rautenbach CJ d. W, Ndarana T, Takahashi K, Yamagata T. 2014. Performance assessment of three convective parameterization schemes in WRF for downscaling summer rainfall over South Africa. *Climate Dynamics*, 42(11–12): 2931–2953. <https://doi.org/10.1007/s00382-013-1918-2>.
- Ratnam J V., Behera SK, Masumoto Y, Yamagata T. 2014. Remote effects of El Niño and Modoki events on the austral summer precipitation of Southern Africa. *Journal of Climate*, 27(10): 3802–3815. <https://doi.org/10.1175/JCLI-D-13-00431.1>.
- Ratnam J V., Behera SK, Ratna SB, De Rautenbach CJW, Lennard C, Luo JJ, Masumoto Y,

Takahashi K, Yamagata T. 2013. Dynamical Downscaling of Austral Summer Climate Forecasts over Southern Africa Using a Regional Coupled Model. *Journal of Climate*, 26(16): 6015–6032. <https://doi.org/10.1175/JCLI-D-12-00645.1>.

Reason CJC. 2001. Subtropical Indian Ocean SST dipole events and southern African rainfall. *Geophysical Research Letters*. <https://doi.org/10.1029/2000GL012735>.

Reason CJC. 2007. Tropical cyclone Dera, the unusual 2000/01 tropical cyclone season in the South West Indian Ocean and associated rainfall anomalies over Southern Africa. *Meteorology and Atmospheric Physics*, 97(1–4): 181–188. <https://doi.org/10.1007/s00703-006-0251-2>.

Reason CJC, Allan RJ, Lindesay JA, Ansell TJ. 2000. Enso and climatic signals across the Indian Ocean basin in the global context: Part I, Interannual composite patterns. *International Journal of Climatology*, 20(11): 1285–1327. [https://doi.org/10.1002/1097-0088\(200009\)20:11<1285::AID-JOC536>3.0.CO;2-R](https://doi.org/10.1002/1097-0088(200009)20:11<1285::AID-JOC536>3.0.CO;2-R).

Reason CJC, Jagadheesha D. 2005. A model investigation of recent ENSO impacts over southern Africa. *Meteorology and Atmospheric Physics*, 89(1–4): 181–205. <https://doi.org/10.1007/s00703-005-0128-9>.

Reason CJC, Keibel A. 2004. Tropical Cyclone Eline and its unusual penetration and impacts over the Southern Africa mainland. *Weather and Forecasting*, 19(5): 789–805. [https://doi.org/10.1175/1520-0434\(2004\)019<0789:TCEAIU>2.0.CO;2](https://doi.org/10.1175/1520-0434(2004)019<0789:TCEAIU>2.0.CO;2).

Reason CJC, Landman W, Tennant W. 2006. Seasonal to decadal prediction of southern African climate and its links with variability of the Atlantic ocean. *Bulletin of the American Meteorological Society*, 87(7): 941–955. <https://doi.org/10.1175/BAMS-87-7-941>.

Reason CJC, Rouault M. 2002. ENSO-like decadal variability and South African rainfall. *Geophysical Research Letters*, 29(13): 1638. <https://doi.org/10.1029/2002GL014663>.

Rouault M, Florenchie P, Fauchereau N, Reason CJC. 2003. South East tropical Atlantic warm events and southern African rainfall. *Geophysical Research Letters*, 30(5): 1–4. <https://doi.org/10.1029/2002GL014840>.

Rouault M, Richard Y. 2004. Intensity and spatial extension of drought in South Africa at different time scales. *Water SA*, 29(4): 489–500. <https://doi.org/10.4314/wsa.v29i4.5057>.

Rouault M, White SA, Reason CJC, Lutjeharms JRE, Jobard I. 2002. Ocean-atmosphere interaction in the Agulhas Current region and a South African extreme weather event. *Weather and Forecasting*. [https://doi.org/10.1175/1520-0434\(2002\)017<0655:OAIITA>2.0.CO;2](https://doi.org/10.1175/1520-0434(2002)017<0655:OAIITA>2.0.CO;2).

Russo S, Marchese AF, Sillmann J, Immé G. 2016. When will unusual heat waves become normal in a warming Africa? *Environmental Research Letters*. IOP Publishing, 11(5). <https://doi.org/10.1088/1748-9326/11/5/054016>.

Scaife AA, Camp J, Comer R, Davis P, Dunstone N, Gordon M, MacLachlan C, Martin N, Nie Y, Ren HL, Roberts M, Robinson W, Smith D, Vidale PL. 2019. Does increased atmospheric resolution improve seasonal climate predictions? *Atmospheric Science Letters*, 20(8): 1–10. <https://doi.org/10.1002/asl.922>.

Senior CA, Marsham JH, Berthou S, Burgin LE, Folwell SS, Kendon EJ, Klein CM, Jones RG,

Mittal N, Rowell DP, Tomassini L, Vischel T, Becker B, Birch CE, Crook J, Dougill AJ, Finney DL, Graham RJ, Hart NCG, Jack CD, Jackson LS, James R, Koelle B, Misiani H, Mwalukanga B, Parker DJ, Stratton RA, Taylor CM, Tucker SO, Wainwright CM, Washington R, Willet MR. 2021. Convection-permitting regional climate change simulations for understanding future climate and informing decision-making in Africa. *Bulletin of the American Meteorological Society*, 102(6): E1206–E1223. <https://doi.org/10.1175/BAMS-D-20-0020.1>.

Sheshadri A, Borrus M, Yoder M, Robinson T. 2021. Midlatitude Error Growth in Atmospheric GCMs: The Role of Eddy Growth Rate. *Geophysical Research Letters*, 48(23): 1–7. <https://doi.org/10.1029/2021GL096126>.

Shongwe ME, Van Oldenborgh GJ, Van Den Hurk BJM, De Boer B, Coelho CAS, Van Aalst MK. 2009. Projected changes in mean and extreme precipitation in Africa under global warming. Part I: Southern Africa. *Journal of Climate*, 22(13): 3819–3837. <https://doi.org/10.1175/2009JCLI2317.1>.

Silvério KC, Grimm AM. 2022. Southern African monsoon: intraseasonal variability and monsoon indices. *Climate Dynamics*. Springer Berlin Heidelberg, 58(3–4): 1193–1220. <https://doi.org/10.1007/s00382-021-05954-y>.

Skamarock WC., Klemp JB, Dudhia JB, Gill DO, Barker DM, Duda MG, Huang X-Y., Wang W, Powers JG. 2021. A Description of the Advanced Research WRF Model Version 4.3. *NCAR Technical Note*, (July): 1–165. <https://doi.org/http://dx.doi.org/10.5065/1dfh-6p97>.

Spinoni J, Barbosa P, Bucchignani E, Cassano J, Cavazos T, Cescatti A, Christensen JH, Christensen OB, Coppola E, Evans JP, Forzieri G, Geyer B, Giorgi F, Jacob D, Katzfey J, Koenigk T, Laprise R, Lennard CJ, Kurnaz ML, Li D, Llopart M, McCormick N, Naumann G, Nikulin G, Ozturk T, Panitz HJ, da Rocha RP, Solman SA, Syktus J, Tangang F, Teichmann C, Vautard R, Vogt J V., Winger K, Zittis G, Dosio A. 2021. Global exposure of population and land-use to meteorological droughts under different warming levels and SSPs: A CORDEX-based study. *International Journal of Climatology*, 41(15): 6825–6853. <https://doi.org/10.1002/joc.7302>.

Spinoni J, Barbosa P, De Jager A, McCormick N, Naumann G, Vogt J V., Magni D, Masante D, Mazzeschi M. 2019. A new global database of meteorological drought events from 1951 to 2016. *Journal of Hydrology: Regional Studies*. Elsevier, 22: 100593. <https://doi.org/10.1016/J.EJRH.2019.100593>.

Stauffer DR, Seaman NL. 1994. Multiscale four-dimensional data assimilation. *Journal of Applied Meteorology*, 33(3): 416–434. [https://doi.org/10.1175/1520-0450\(1994\)033<0416:MFDDA>2.0.CO;2](https://doi.org/10.1175/1520-0450(1994)033<0416:MFDDA>2.0.CO;2).

Sun Q, Zhang X, Zwiers F, Westra S, Alexander L V. 2021. A global, continental, and regional analysis of changes in extreme precipitation. *Journal of Climate*, 34(1): 243–258. <https://doi.org/10.1175/JCLI-D-19-0892.1>.

Tennant WJ, Hewitson BC. 2002. Intra-seasonal rainfall characteristics and their importance to the seasonal prediction problem. *International Journal of Climatology*, 22(9): 1033–1048. <https://doi.org/10.1002/joc.778>.

Thoithi W, Blamey RC, Reason CJC. 2020. Dry spell frequencies, wet day counts and their

trends across southern Africa during the summer rainy season. *Geophysical Research Letters*, 48(5): 1–22. <https://doi.org/10.1029/2020GL091041>.

Todd M, Washington R. 1999. Circulation anomalies associated with tropical-temperate troughs in southern Africa and the south west Indian Ocean. *Climate Dynamics*, 15(12): 937–951. <https://doi.org/10.1007/s003820050323>.

Todd MC, Washington R, Palmer PI. 2004. Water vapour transport associated with tropical-temperate trough systems over southern Africa and the southwest Indian Ocean. *International Journal of Climatology*, 24(5): 555–568. <https://doi.org/10.1002/joc.1023>.

Tyson PD. 1981. Atmospheric circulation variations and the occurrence of extended wet and dry spells over Southern Africa. *Journal of Climatology*, 1(2): 115–130. <https://doi.org/10.1002/joc.3370010203>.

Ukkola AM, De Kauwe MG, Roderick ML, Abramowitz G, Pitman AJ. 2020. Robust Future Changes in Meteorological Drought in CMIP6 Projections Despite Uncertainty in Precipitation. *Geophysical Research Letters*. John Wiley & Sons, Ltd, 47(11): e2020GL087820. <https://doi.org/10.1029/2020GL087820>.

Ullah A, Pohl B, Pergaud J, Dieppois B, Rouault M. 2022. Intraseasonal descriptors and extremes in South African rainfall. Part I: Summer climatology and statistical characteristics. *International Journal of Climatology*. John Wiley & Sons, Ltd, 42(9): 4538–4563. <https://doi.org/10.1002/JOC.7489>.

Usman MT, Reason CJC. 2004. Dry spell frequencies and their variability over southern Africa. *Climate Research*, 26(3): 199–211. <https://doi.org/10.3354/cr026199>.

Van Heerden J, Terblanche DE, Schulze GC. 1988. The southern oscillation and South African summer rainfall. *Journal of Climatology*, 8(6): 577–597. <https://doi.org/10.1002/joc.3370080603>.

Vigaud N, Pohl B, Cr  tat J. 2012. Tropical-temperate interactions over southern Africa simulated by a regional climate model. *Climate Dynamics*, 39(12): 2895–2916. <https://doi.org/10.1007/s00382-012-1314-3>.

Washington R, Preston A. 2006. Extreme wet years over southern Africa: Role of Indian Ocean sea surface temperatures. *Journal of Geophysical Research: Atmospheres*. John Wiley & Sons, Ltd, 111(D15): 15104. <https://doi.org/10.1029/2005JD006724>.

Washington R, Todd M. 1999. Tropical-temperate links in southern African and Southwest Indian Ocean satellite-derived daily rainfall. *International Journal of Climatology*. [https://doi.org/10.1002/\(SICI\)1097-0088\(19991130\)19:14<1601::AID-JOC407>3.0.CO;2-0](https://doi.org/10.1002/(SICI)1097-0088(19991130)19:14<1601::AID-JOC407>3.0.CO;2-0).

Wheeler MC, Hendon HH. 2004. An all-season real-time multivariate MJO index: Development of an index for monitoring and prediction. *Monthly Weather Review*, 132(8): 1917–1932. [https://doi.org/10.1175/1520-0493\(2004\)132<1917:AARMMI>2.0.CO;2](https://doi.org/10.1175/1520-0493(2004)132<1917:AARMMI>2.0.CO;2).

WMO. 2021. *WMO Atlas of Mortality and Economic Losses from Weather, Climate and Water Extremes (1970–2019)* (WMO-No. 1267). WMO: Geneva.

Xulu NG, Chikoore H, Bopape MJM, Nethengwe NS. 2020. Climatology of the Mascarene High and Its Influence on Weather and Climate over Southern Africa. *Climate 2020, Vol. 8, Page 86*.

Multidisciplinary Digital Publishing Institute, 8(7): 86. <https://doi.org/10.3390/CLI8070086>.

Yuan X, Wang L, Wood EF. 2018. Anthropogenic Intensification of Southern African Flash Droughts as Exemplified by the 2015/16 Season. *Bulletin of the American Meteorological Society*. American Meteorological Society, 99(1): S86–S90. <https://doi.org/10.1175/BAMS-D-17-0077.1>.

Zhang C. 2005. Madden-Julian Oscillation. *Reviews of Geophysics*. John Wiley & Sons, Ltd, 43(2): 1–36. <https://doi.org/10.1029/2004RG000158>.

Zhang F, Qiang Sun Y, Magnusson L, Buizza R, Lin SJ, Chen JH, Emanuel K. 2019. What is the predictability limit of midlatitude weather? *Journal of the Atmospheric Sciences*, 76(4): 1077–1091. <https://doi.org/10.1175/JAS-D-18-0269.1>.

Zhao T, Dai A. 2017. Uncertainties in historical changes and future projections of drought. Part II: model-simulated historical and future drought changes. *Climatic Change*. Springer Netherlands, 144(3): 535–548. <https://doi.org/10.1007/S10584-016-1742-X/FIGURES/6>.

Figures: Chapter 3

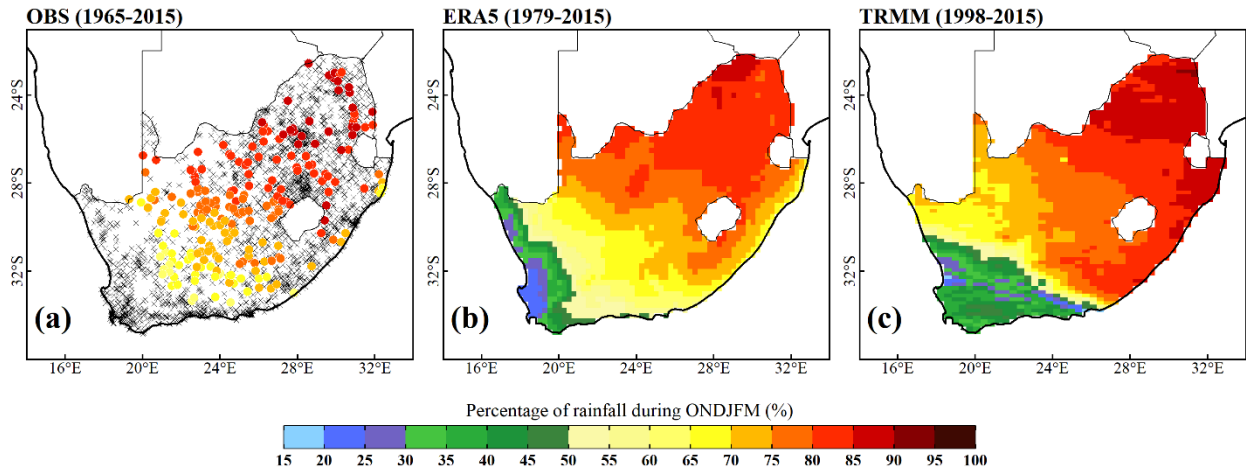


Figure. 1: Spatial distribution of the percentage of rainfall during ONDJFM for OBS (a) for ERA5 (b) and for TRMM (c). The unqualified stations in (a) are indicated by black “x” symbols based on the seasonality test and/or other quality control measures.

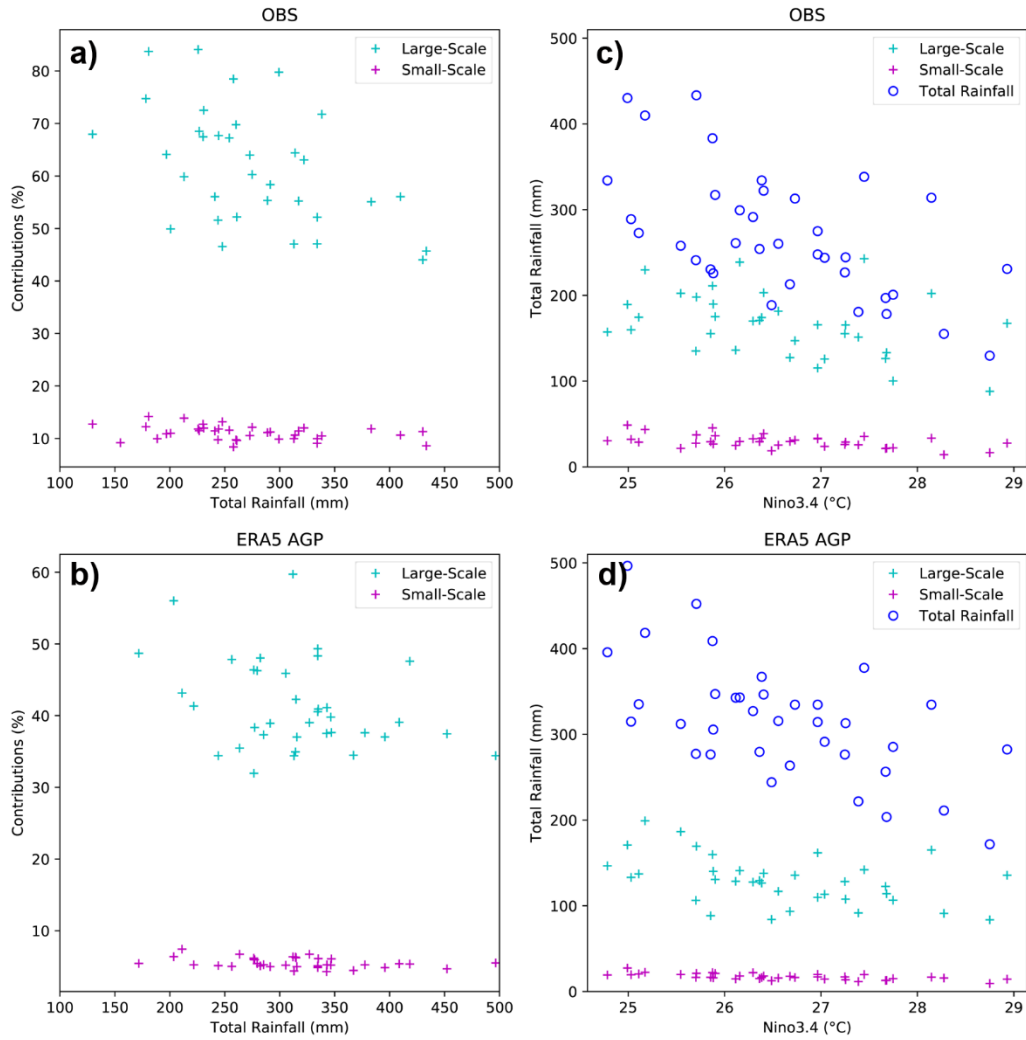


Figure. 2: The contribution of large- and small-scale extremes (in percentage) to total rainfall during NDJF for OBS (a) and for ERA5–AGP (b). Seasonal total rainfall, total rainfall associated with large- and small-scale extremes as a function of Niño 3.4 index presented in (c) and (d) for OBS and ERA5–AGP respectively.

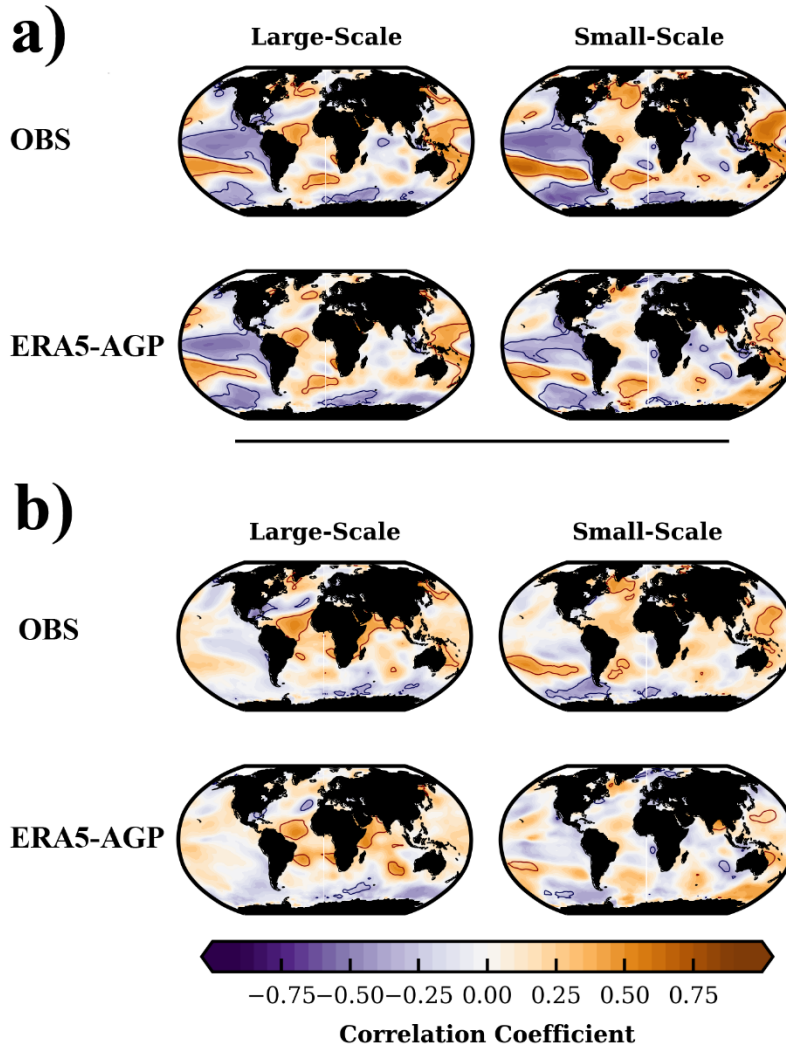


Figure. 3: The correlation to global SST fields with the number of large- and small-scale extremes in the austral summer over the period of 1979–2015. The set of four panels in (a) refers to the correlation to global SSTs with the number of large-scale extremes (left panels) and for small-scale extremes (right panels) for OBS and ERA5–AGP. The same figure distribution is applied in (b), but the correlations are computed after removing the influence of ENSO. Niño 3.4 index is used to compute partial correlations of global SSTs. Regions with solid contours indicate the correlations are significant at the 95% confidence level according to a student's *t*-test.

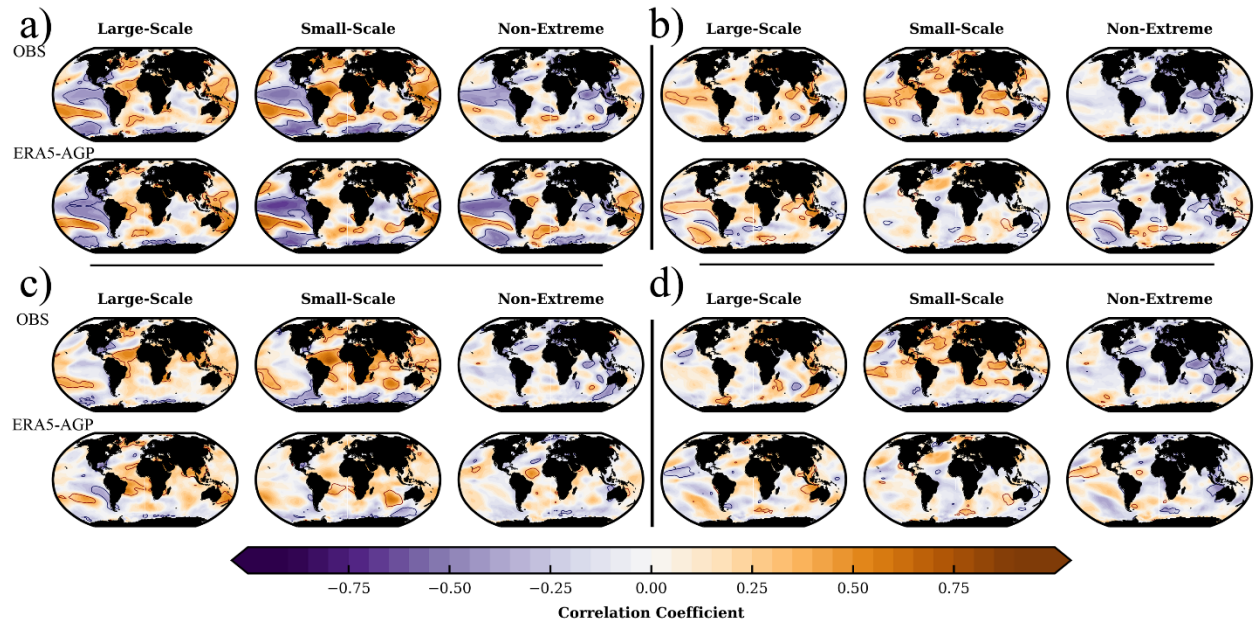


Figure. 4: The correlation to global SST fields with total rainfall in the austral summer over the period of 1979–2015. The set of six panels in (a) refers to the correlation to global SSTs with total rainfall associated with large-scale extremes, small-scale extremes, and non-extreme rainfall (distributed column-wise from left to right respectively) for OBS and ERA5–AGP. The set of six panels in (b) refers to the contributions of total rainfall associated with large-scale extremes, small-scale extremes, and non-extreme rainfall to total rainfall (distributed column-wise from left to right respectively) for OBS and ERA5–AGP. The same figure distribution is applied in (c) and (d) but the correlations are computed after removing the influence of ENSO. Niño 3.4 index is used to compute partial correlations of global SSTs. Regions with solid contours indicate the correlations are significant at the 95% confidence level according to a students’ *t*-test.

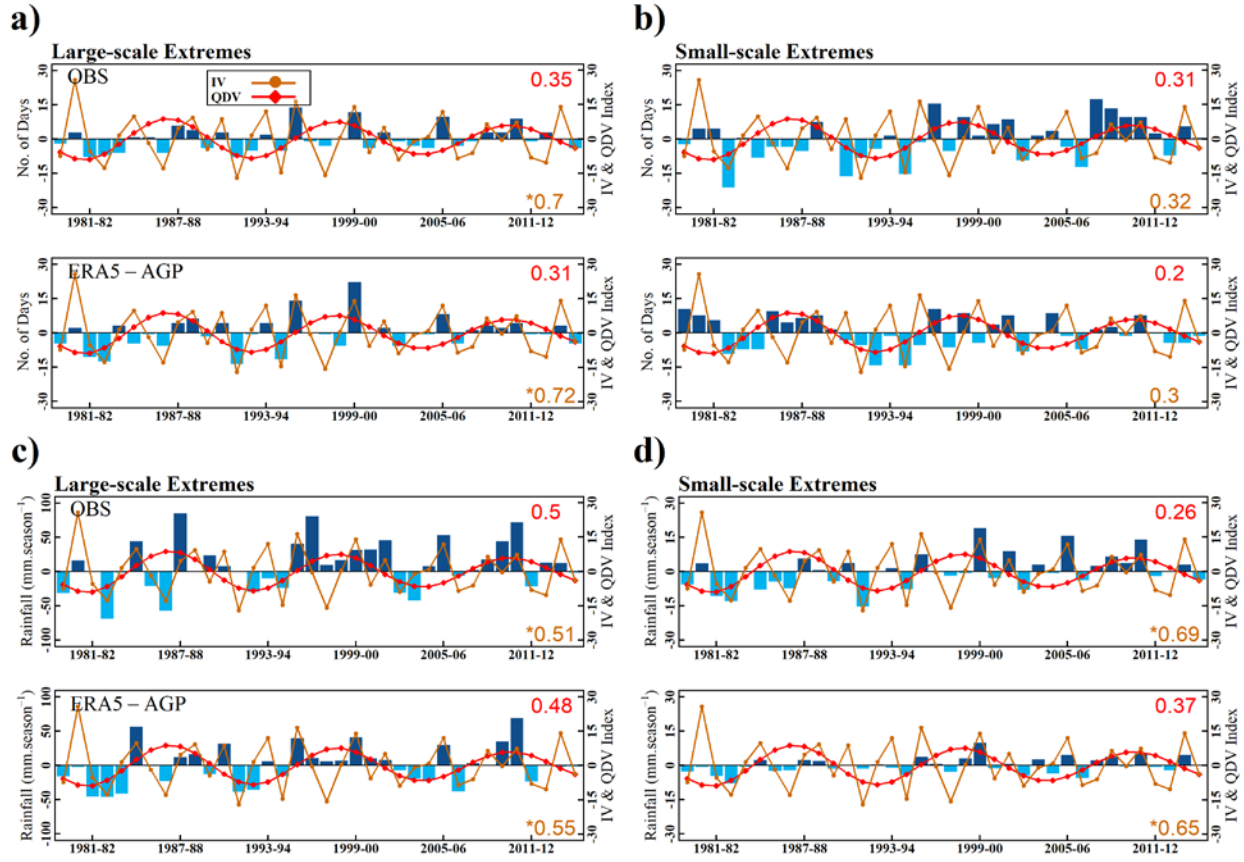


Figure. 5: Anomalies of extremes ISDs (blue bars), SRI at the IV timescale (brown line) and SRI at the QDV timescale (red line) are presented in four panels for wet days associated with large-scale extremes (a) and small-scale extremes (b), distributed row-wise from top to bottom for OBS and ERA5–AGP respectively. The same figure distribution is applied in (c) and (d) but the analysis is performed for total rainfall associated with large- and small-scale extremes. The correlation of each ISD with IV (QDV) is displayed at the bottom (top) of each panel using the same colour as used for their timeseries. The y-axis on left-hand-side in each panel is used to display the unit of ISDs while the y-axis on right-hand-side is commonly used for SRI corresponding to IV and QDV index. The correlations marked with “*” are significant at $p=0.05$ according to the Bravais–Pearson test.

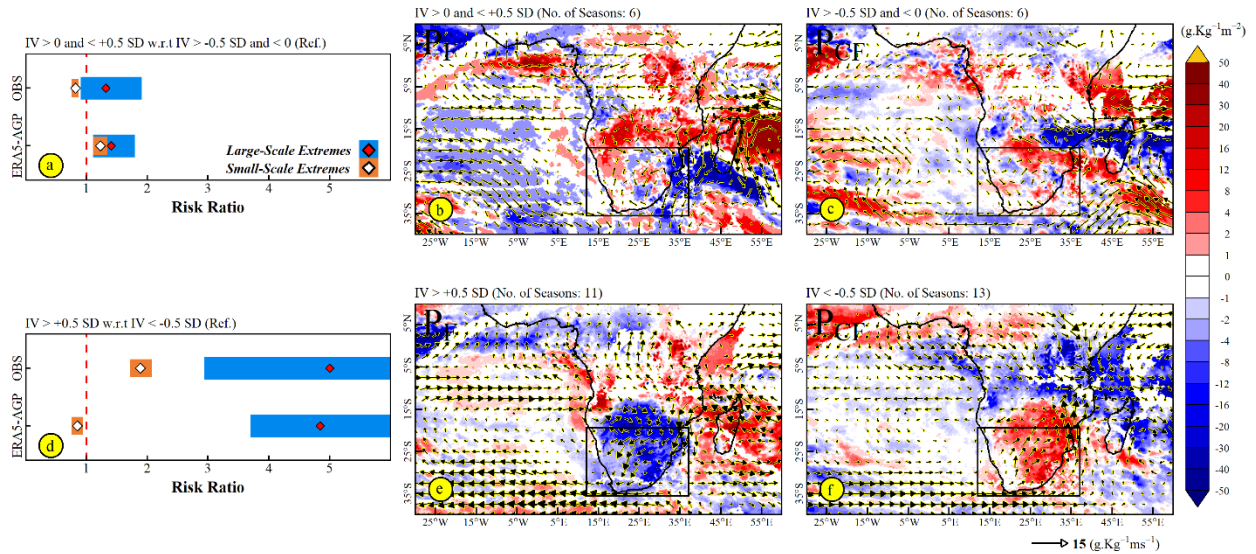


Figure 6: Estimated risk ratio computed for wet days associated with large- and small-scale extremes computed for the P_F scenario i.e., the period when $IV > 0$ and $< +0.5$ SD (weaker positive phase of IV) with respect to P_{CF} scenario i.e., the period when $IV > -0.5$ SD and < 0 (weaker negative phase of IV) (a). The red (white) symbols represent the numerical position of risk ratio for large-scale extremes (small-scale extremes) computed at $p=0.05$. The horizontal expansion of stripes (blue and brown for large- and small-scale extremes respectively) represents the minimum and maximum limits of the 95% confidence interval. $RR = 1$ corresponds to an equiprobable risk of occurrence of extremes either in P_F scenario or in P_{CF} scenario. A risk ratio above or below 1 can be interpreted with a factor, for instance, 0.2, 0.4 and 0.6 indicate a 20%, 40% and 60% higher risk of occurrence of extremes during P_F scenario as compared to the P_{CF} scenario or vice versa if below 1. The composite anomalies of vertically integrated moisture flux divergence ($\text{g. Kg}^{-1}\text{m}^{-2}$) and moisture flux ($\text{g. Kg}^{-1}\text{ms}^{-1}$) at 850 hPa for both periods which are considered to compute the risk ratio are shown in (b) and (c) where only those anomalies are shown which are significant at 95% confidence level according to the one-tailed students' t -test. The panels are distributed similarly in the second row but here the risk ratio for large- and small-scale extremes is computed for the P_F scenario i.e., the period when $IV > +0.5$ SD (strong positive phase of IV) with respect to P_{CF} scenario i.e., the period when $IV < -0.5$ SD (strong negative phase of IV) (d-f).

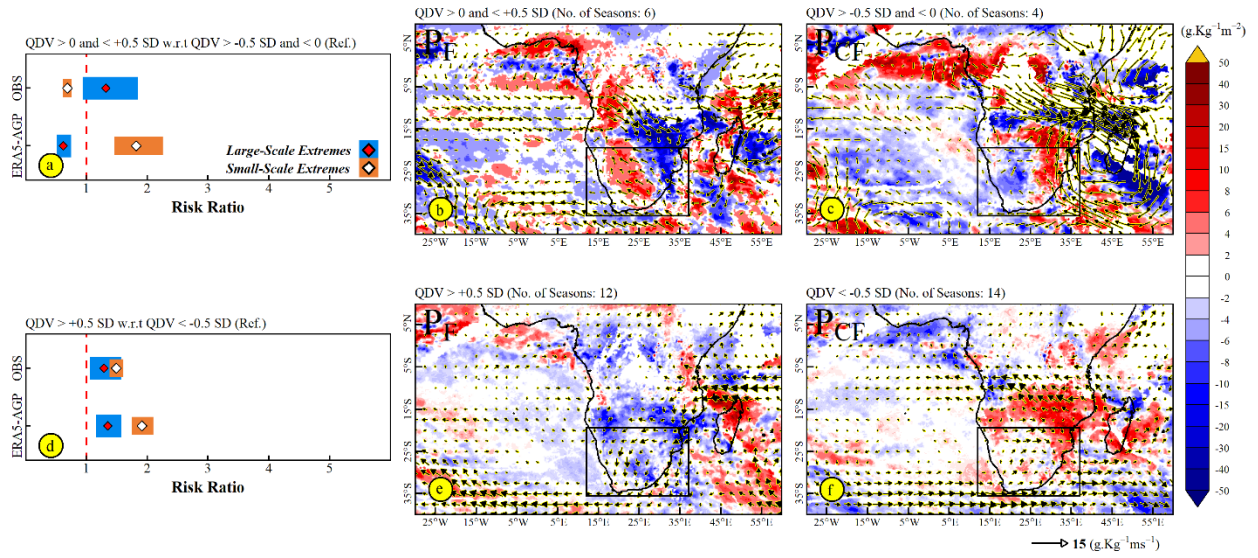
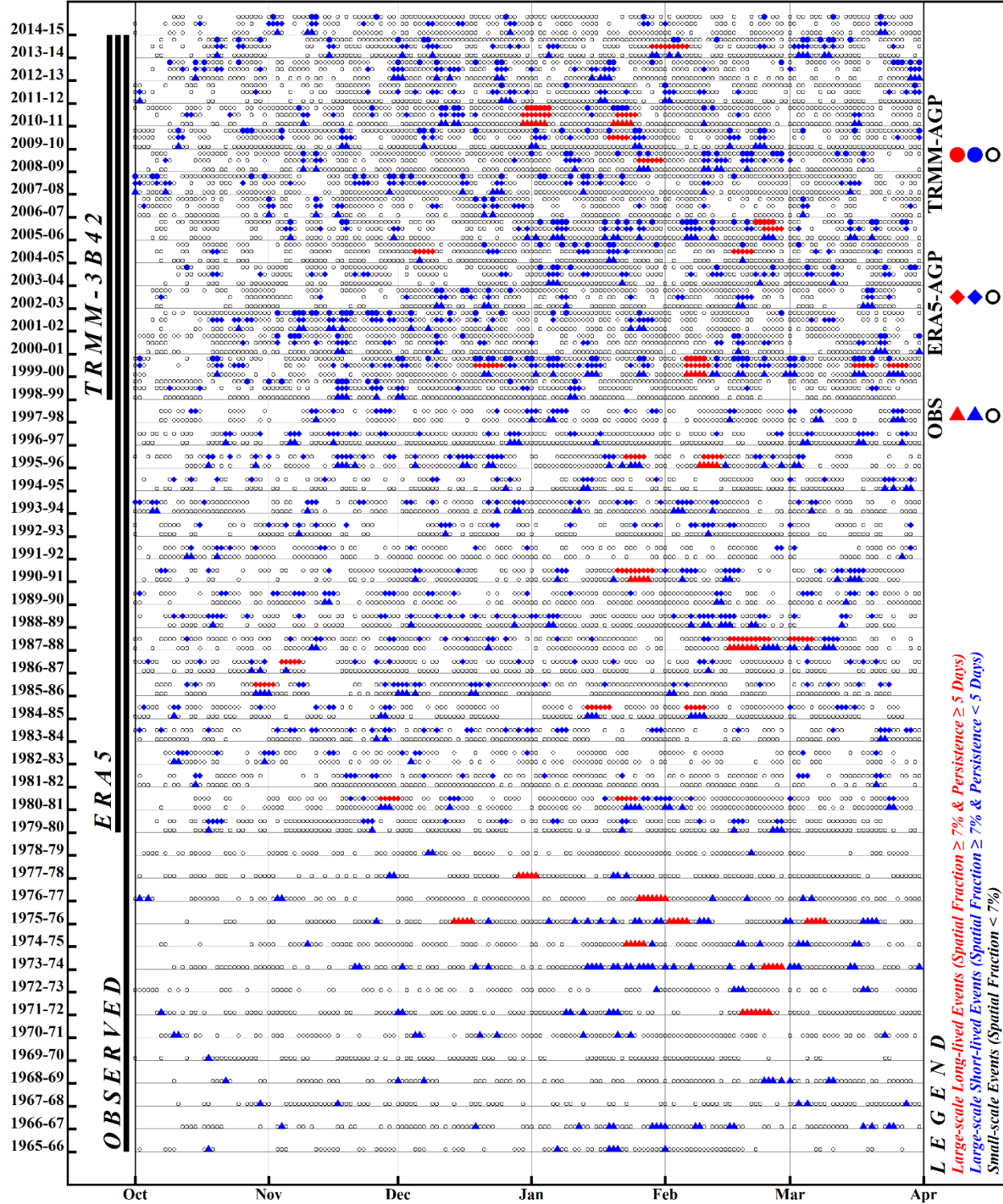


Figure. 7: Same as Figure 6 but for QDV timescale.

Intraseasonal Calendar of daily rainfall extremes using OBS, ERA5-AGP and TRMM-AGP



*** Analysis performed using all grid-points of ERA5 and TRMM lies under the masked region of South Africa

Figure. 8: Intraseasonal calendar of extreme rainfall typology for OBS (1965–2015), ERA5–AGP (1979–2015), and TRMM–AGP (1998–2015) for the extended austral summer season ONDJFM. Large-scale long-lived (large-scale short-lived) rainfall spells for OBS, ERA5–AGP and TRMM–AGP are presented in red symbols “▲”, “◆” and “●” (blue symbols “▲”, “◆” and “●”) respectively. Small-scale events are displayed in black symbols “○” regardless of the dataset. The shape of the symbol represents the dataset, and the colour represents the type of the event (i.e., large-scale long-lived or short-lived) which is based on the duration of the persistence of a spell. The intraseasonal calendar is produced for extended austral summer season (October–March) and distinct baseline periods depending on data availability (OBS: 1965–2015, ERA5: 1979–2015, and TRMM: 1998–2015). The extended season is selected here to investigate the occurrence of large-scale long-lived events during onset (October) and cessation (March) months of core rainy season.

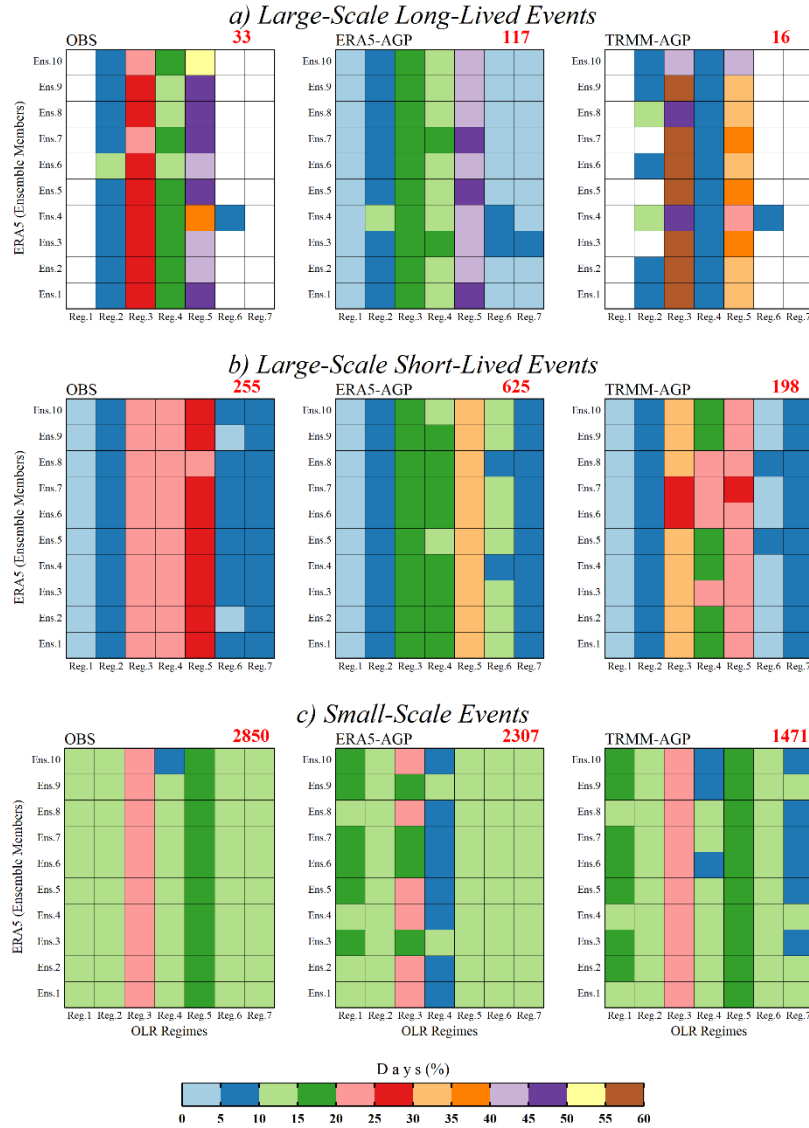


Figure. 9: The co-occurrence of different types of rainfall extremes identified by OBS, ERA5 and TRMM during NDJF over the period of 1979–2015 in seven OLR regimes produced by 10 ensemble members of ERA5. Panels are distributed row-wise from top to bottom for the days associated with large-scale long-lived events (a), large-scale short-lived events (b), and small-scale events (c). The reference values are displayed at the upper-right corner of each panel in red letters (i.e., the total number of days of associated with respective type of extreme events identified by each dataset). Colour shading displays how these reference values are distributed in terms of percentage in seven OLR regimes produced by 10 ensemble members of ERA5.

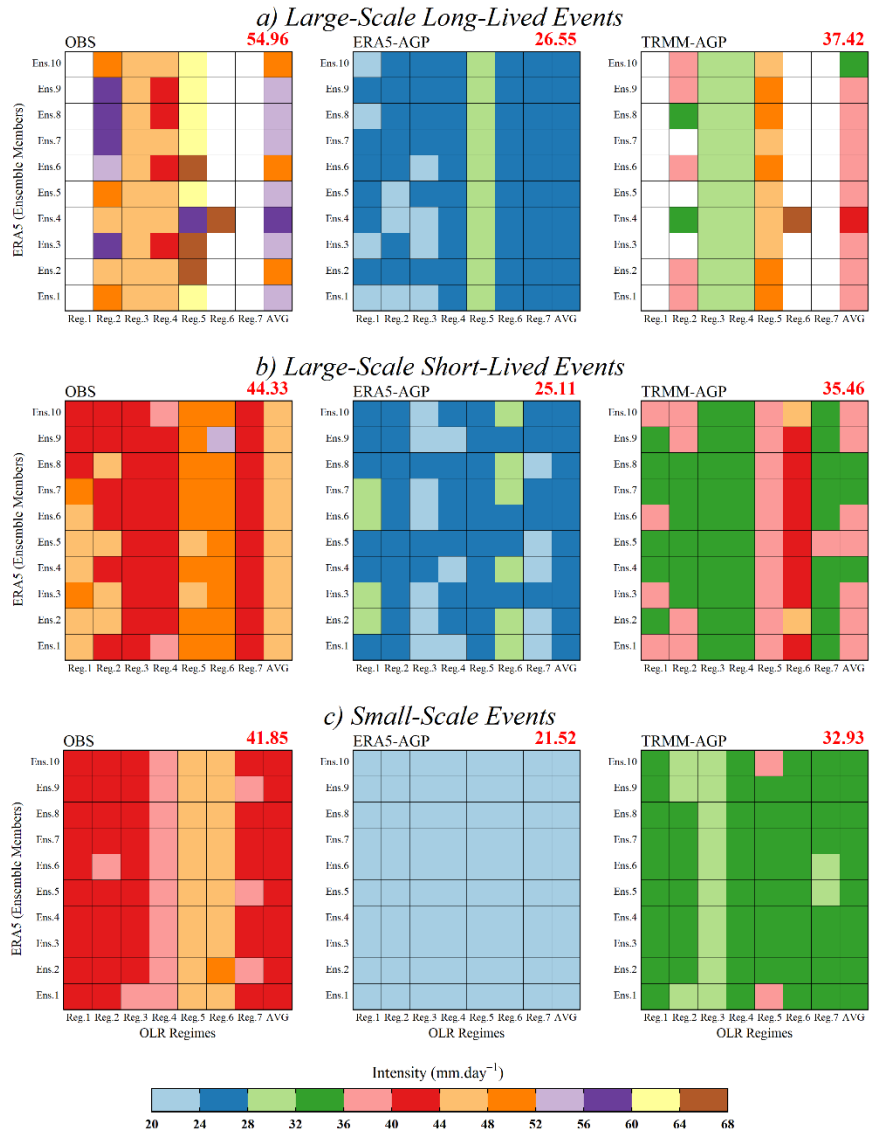


Figure. 10: Same as Figure 9 but for intensity except the reference values are displayed at the upper-right corner of each panel in red letters are the average intensity of respective type of extreme events identified by each dataset.

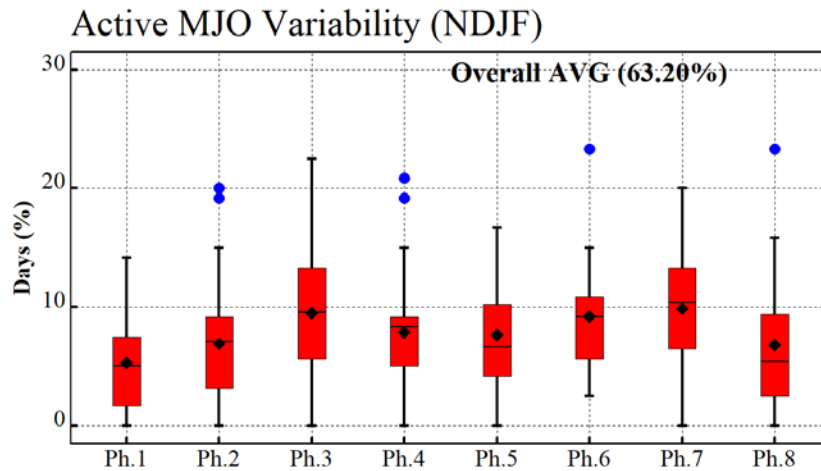
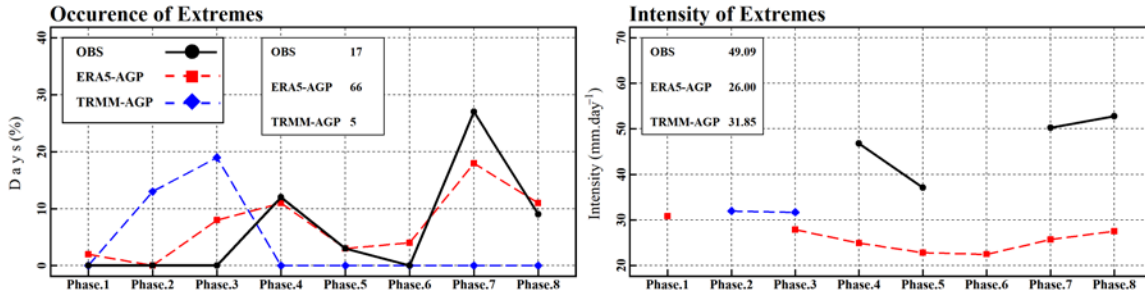
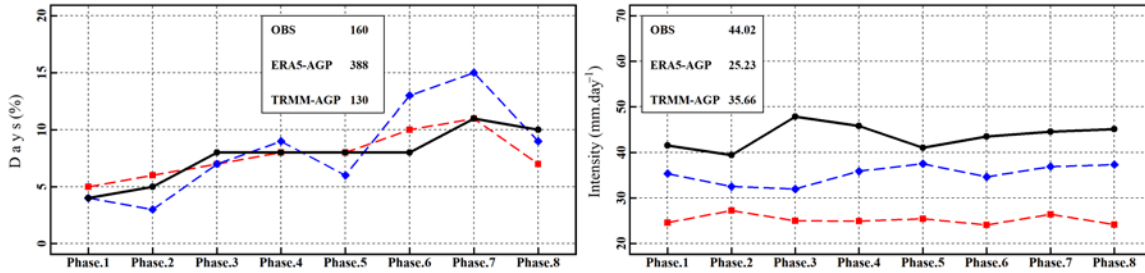


Figure. 11: The box and whisker plots display the active MJO variability during NDJF from 1979–2015 computed by considering only those days in each phase where the amplitude exceeded 1.0 RMM indices. The lower and upper end of red box show the lower and upper quartile respectively while the black line indicates the median of the distribution. The whiskers at the bottom and top indicate the lower and upper extreme of the distribution. The black “◆” and blue symbols “●” indicate mean and outliers of the distribution respectively.

a) Large-Scale Long-Lived Events



b) Large-Scale Short-Lived Events



c) Small-Scale Events

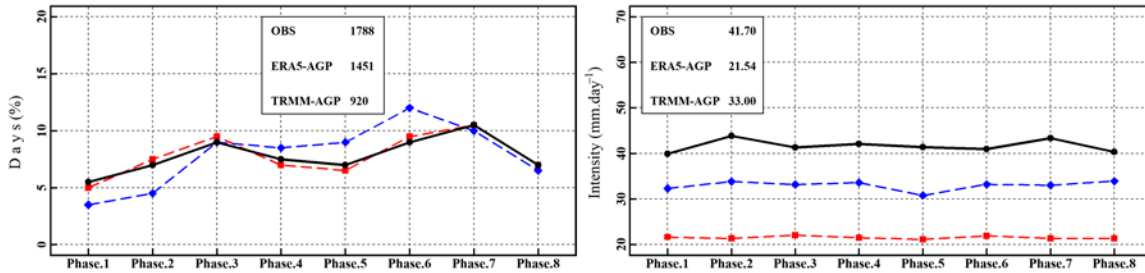


Figure 12: The occurrence and intensity of different types of rainfall extremes during NDJF in convective regimes associated with eight MJO phases during the period of 1979–2015. Panels on the left (right) refer to the occurrence (intensity) and are distributed row-wise from top to bottom for the days associated with large-scale long-lived events (a), large-scale short-lived events (b), and small-scale events (c). The reference values (i.e., the total number of days or average intensity of respective type of extreme events as identified by each dataset) are displayed inside each panel. The reference values are computed by considering only those days in each phase where the amplitude exceeded 1.0 RMM index of the MJO.

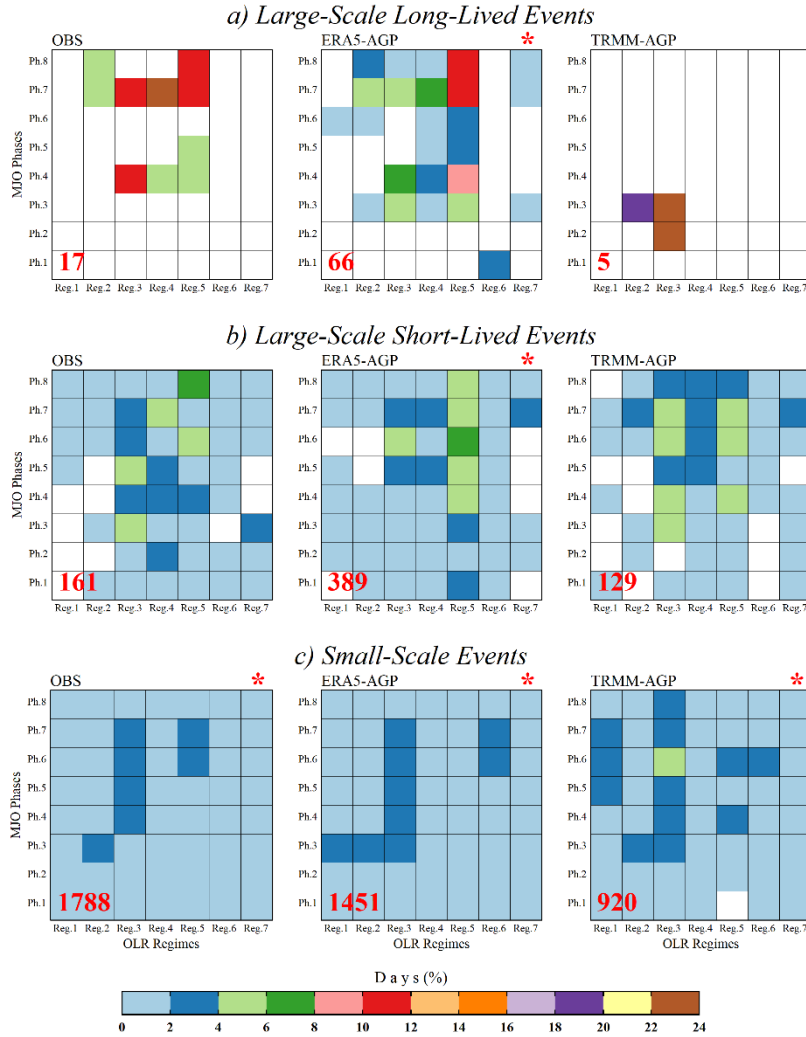


Figure. 13: Concomitance between OLR regimes and MJO phases for number of days associated with different types of extremes during NDJF over the period 1979–2015, distributed row-wise for the days associated with large-scale long-lived events (a), large-scale short-lived events (b), and small-scale events (c). For 8 phases of the MJO, only those days are considered in which the MJO amplitude exceeded 1.0 RMM. The panels indicated by “*” are significant according to the *chi-squared* test at $p=0.05$. The reference values are the total number of days of a respective type of extreme event identified by datasets and displayed at the bottom-left corner of each panel in bold red letters. Colour shading displays how these reference values are distributed in terms of percentage in 56 combinations produced by seven synoptic-scale convective regimes and eight MJO phases. For the combined influence of OLR regimes and MJO phases, the OLR field from the first ensemble member of ERA5 is used.

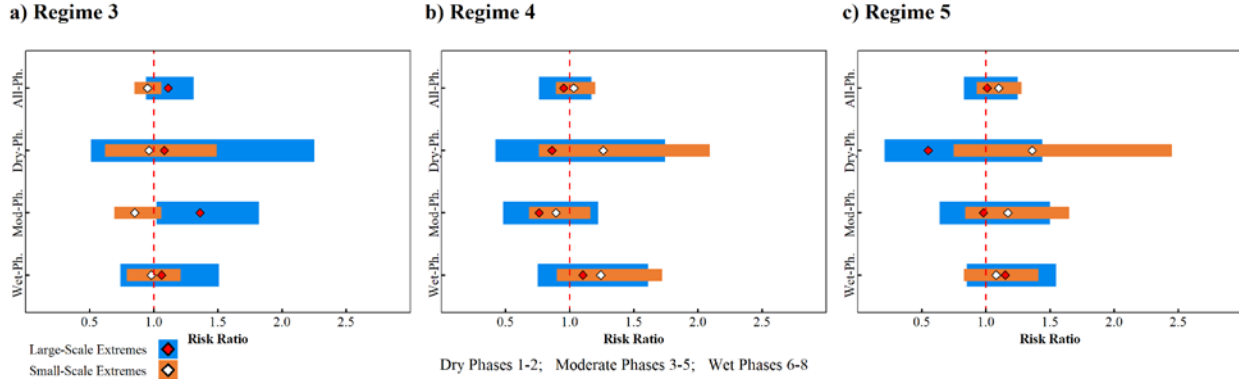


Figure 15: Estimated risk ratio for the P_F scenario i.e., the active MJO days (Amplitude > 1.0 RMM) in each regime computed with respect to the P_{CF} scenario i.e., all days when MJO does not represent any phase (Amplitude < 1.0 RMM) in respective regime provided explicitly for regime #3 (a), regime #4 (b), and regime #5 (c). For each regime, the risk ratio is computed by considering dry (i.e., phases #1–2), moderate (i.e., phases #3–5), and wet (i.e., phases #6–8), phases of the MJO. The blue stripes with red symbols in each panel represent risk ratio for large-scale extremes, whereas brown stripes with white symbols represent small-scale extremes. The horizontal expansion of stripes represents the minimum and maximum limits of the 95% confidence intervals. The symbols represent the numerical position of the risk ratio computed at $p=0.05$. $RR = 1.0$ corresponds to an equiprobable risk of occurrence of extremes during P_F scenario (with MJO influence) or during P_{CF} scenario (without MJO influence). A risk ratio above or below 1.0 can be interpreted with a factor, for instance, 0.2, 0.4 and 0.6 indicate a 20%, 40% and 60% higher risk of occurrence of extremes during P_F scenario as compared to the P_{CF} scenario or vice versa if below 1.0.

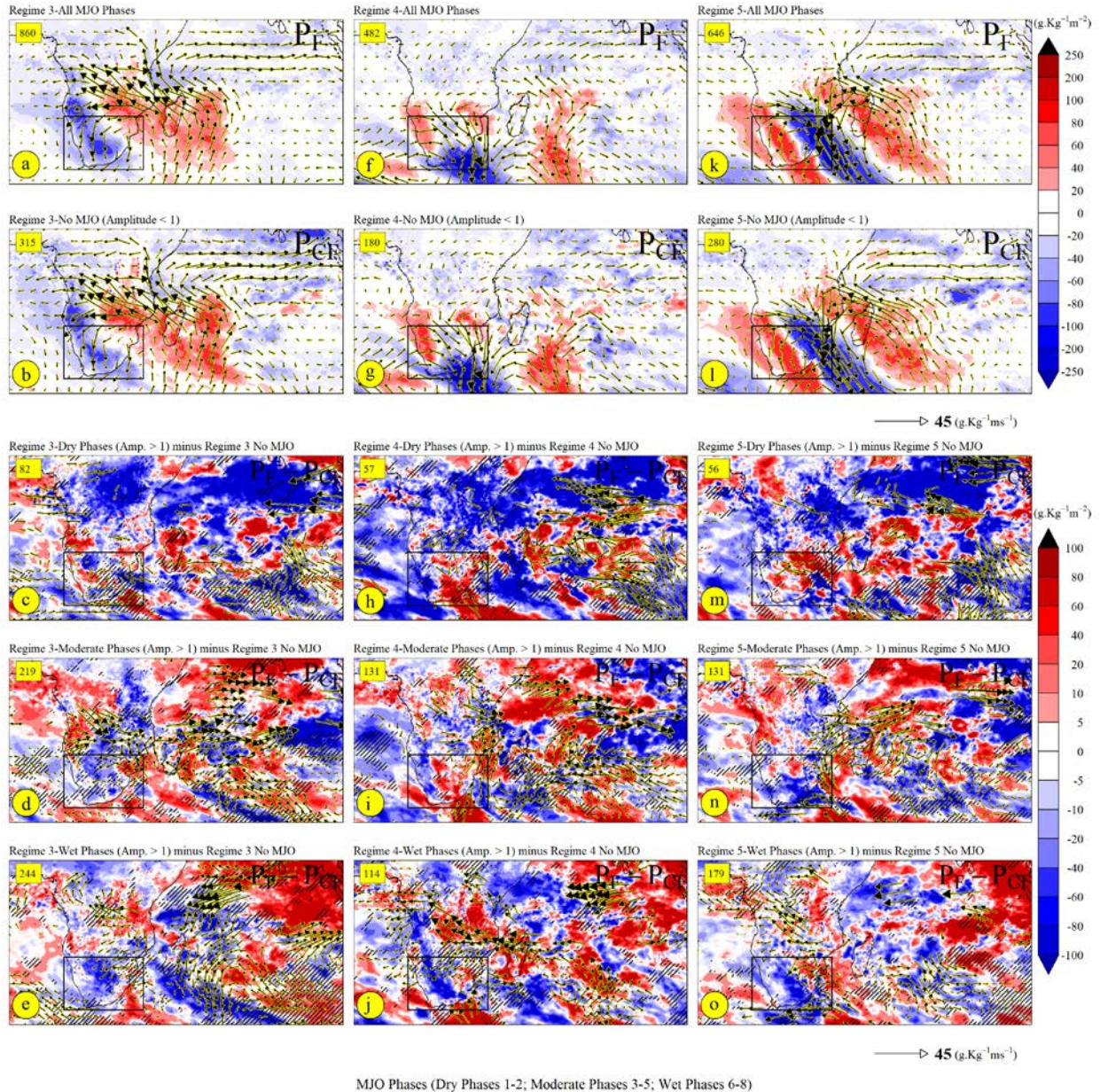


Figure. 16: Set of six panels in top display the composite anomalies of vertically integrated moisture flux divergence ($\text{g. Kg}^{-1}\text{m}^{-2}$) and moisture flux ($\text{g. Kg}^{-1}\text{ms}^{-1}$) at 850 hPa in each P_F and P_{CF} scenario during regime #3 (a-b), regime #4 (f-g) and regime #5 (k-l) respectively, where only those anomalies are shown which are significant at 95% confidence level according to the one-tailed students' t -test. Anomalies are computed with respect to the climatology of NDJF from 1979 to 2015. Set of nine panels in bottom represent the differences between composite anomalies produced by considering those days in each set of phases (dry, moderate and wet phases) when amplitude > 1.0 RMM and when MJO does not represent any phase (i.e., P_F minus P_{CF}) for regime #3 (c-e), for regime #4 (h-j) and for regime #5 (m-o). Stippling indicates the anomalies are significant according to the two-tailed students' t -test at $p < 0.1$ while only significant fluxes are shown. The reference values in the upper-right corner indicate the number

in of days in each composite while the black rectangle represents the area of interest i.e., South Africa.

Supplementary Figures: Chapter 3

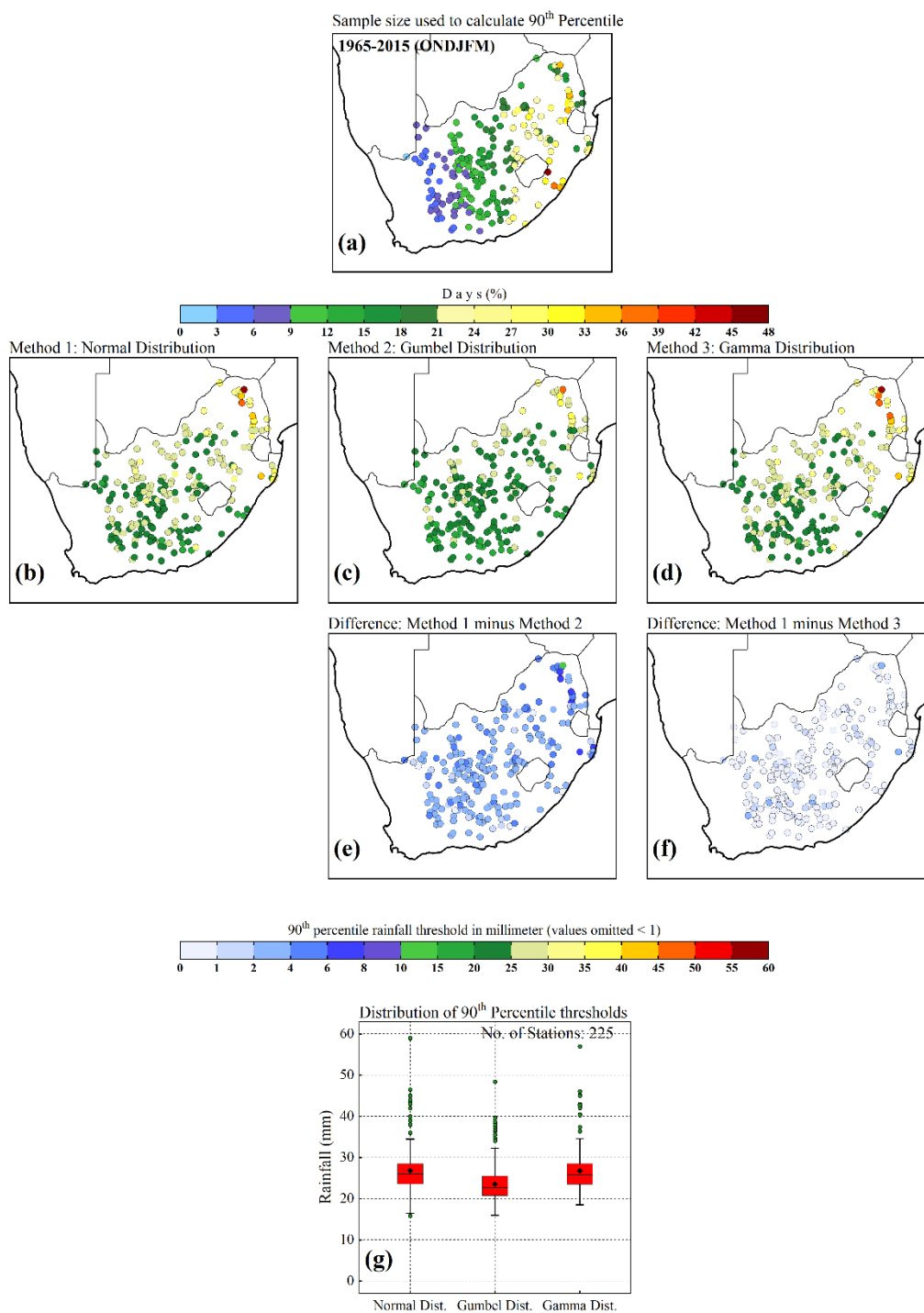


Figure. S1: Sample size used to compute 90th percentile threshold (a), while 90th percentile threshold computed by considering Normal distribution (b), theoretical extreme value computed by Gumbel and Gamma distribution (c-d) and the difference of both methods with normal distribution (e-f). The overall distribution of 90th percentile thresholds using Normal, Gumbel and Gamma distribution is presented using Box and Whisker plots (g). The lower and upper end

of red box show the lower and upper quartile respectively, while the black line indicates the median of the distribution. The whiskers at the bottom and top indicate the lower and upper extreme of the distribution. The black “◆” and green symbols “●” indicate mean and outliers of the distribution respectively.

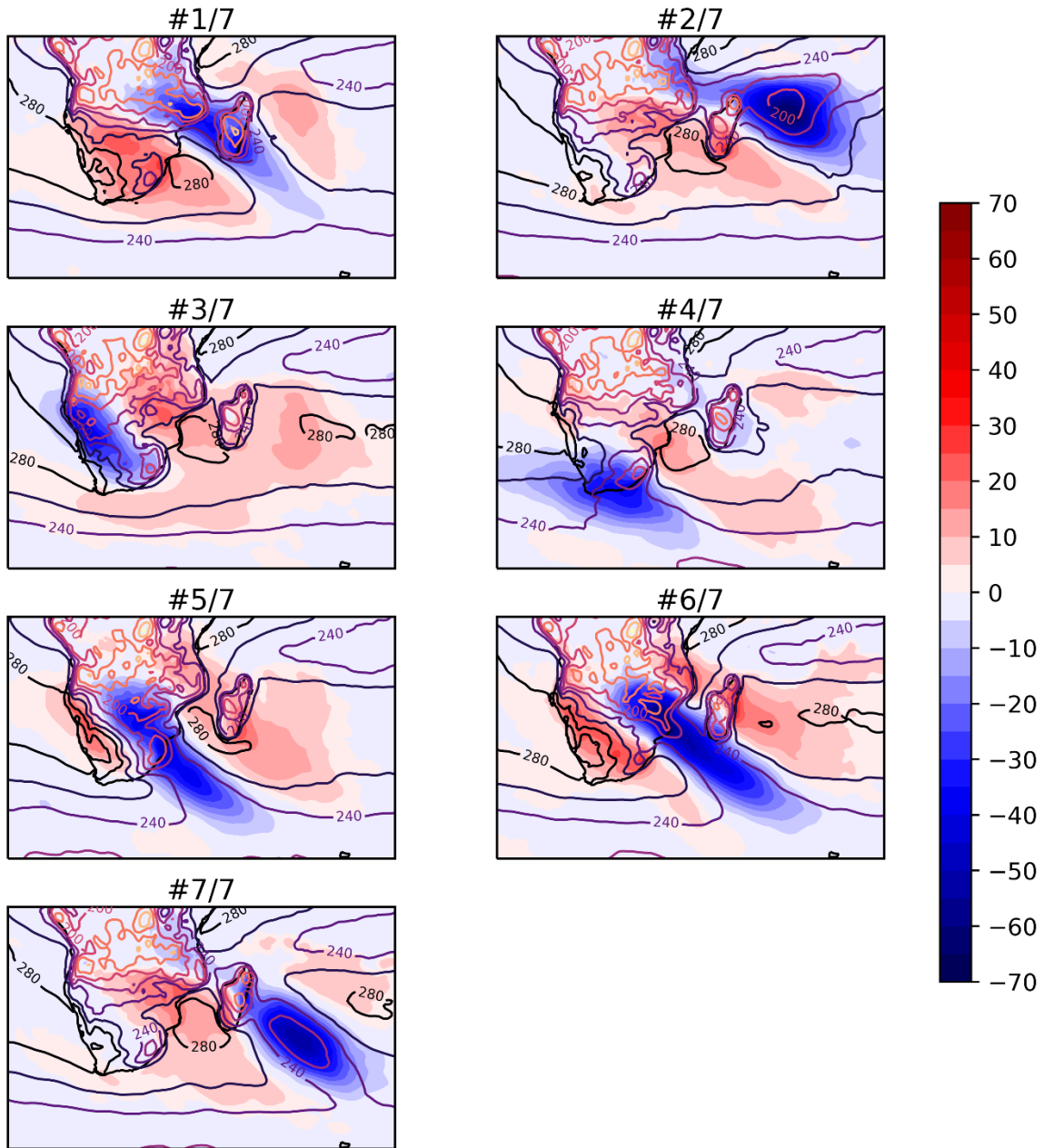


Figure. S2: Mean daily OLR anomalies illustrating seven convective regimes during the austral summer season (NDJF) over the period 1979–2015. The colour bar describes the composite anomalies (interval 5 W.m^{-2}), whereas the mean values are displayed by contours (interval 20 W.m^{-2}).

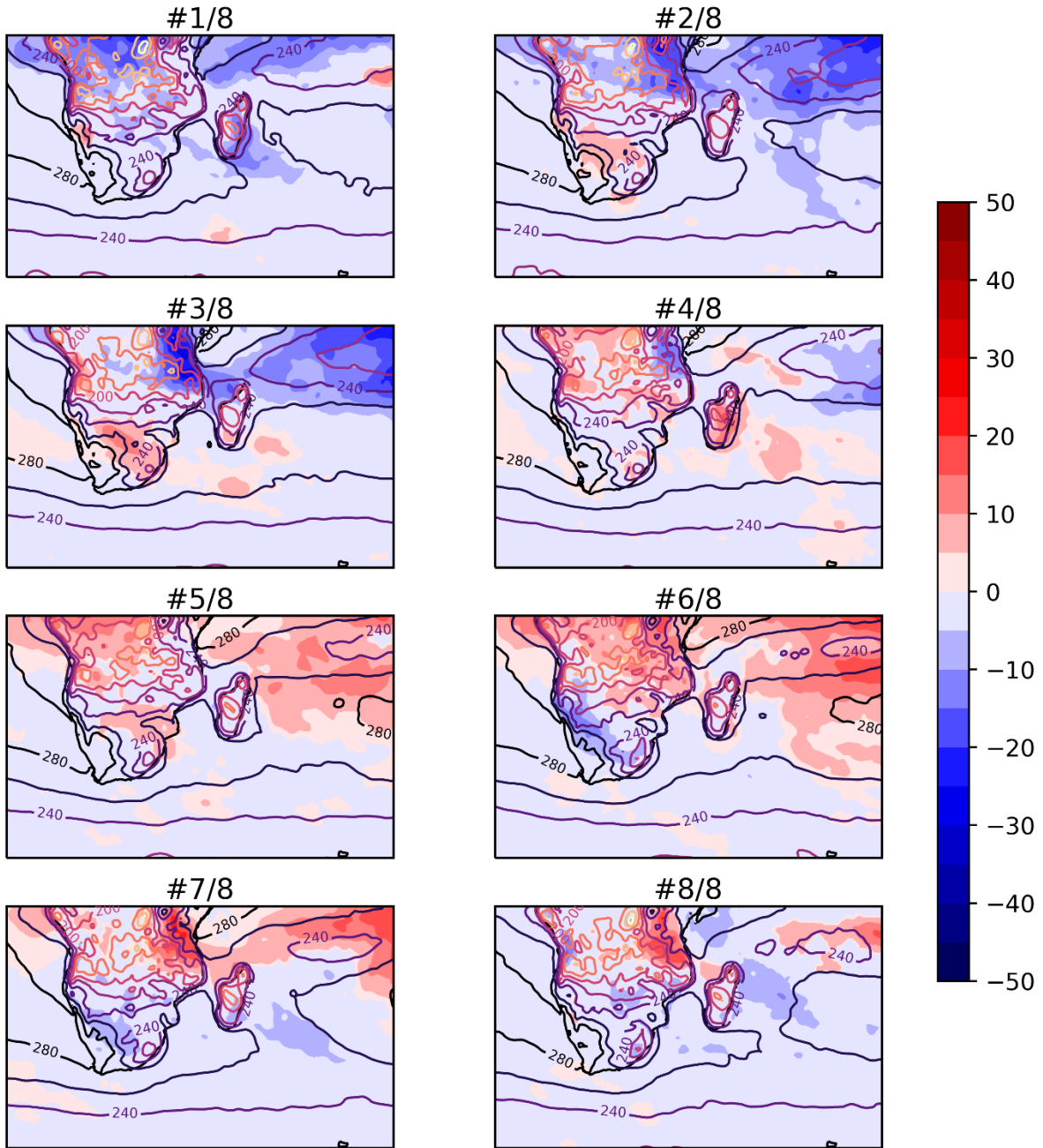


Figure. S3: Same as Figure S2, but for the eight phases of the MJO.

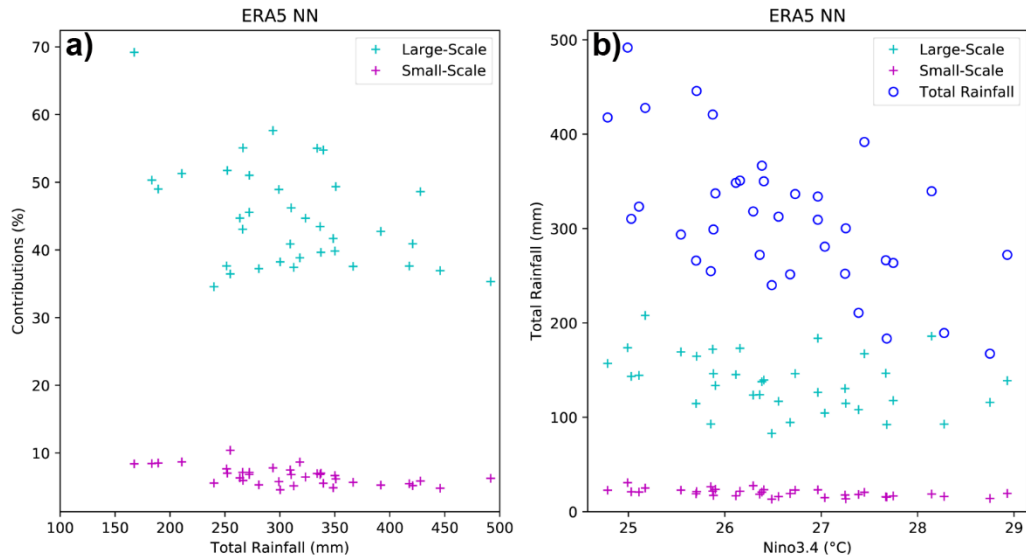


Figure. S4: Same as Figure 2, but for ERA5-NN.

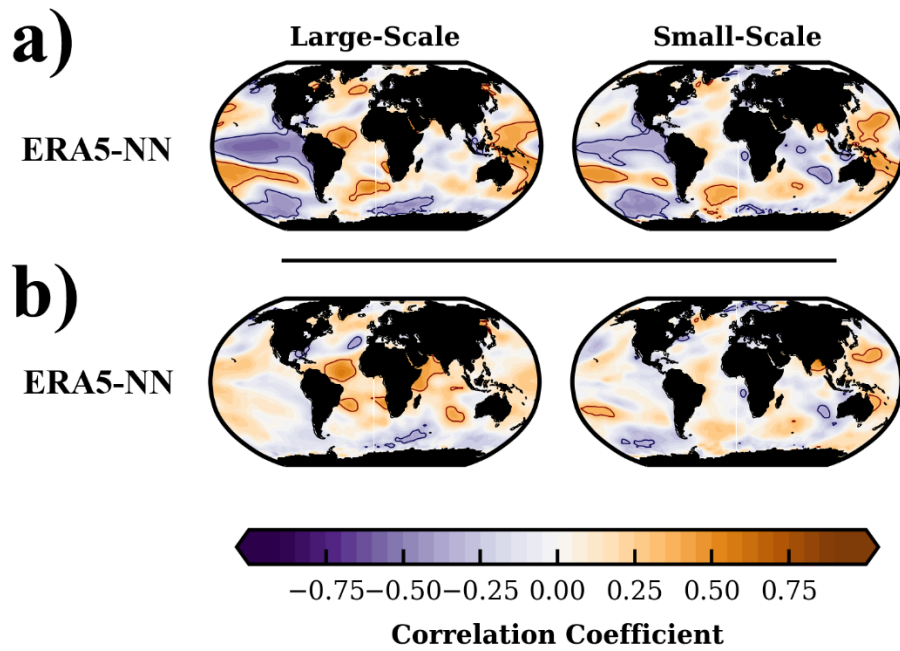


Figure. S5: Same as Figure 3, but for ERA5-NN.

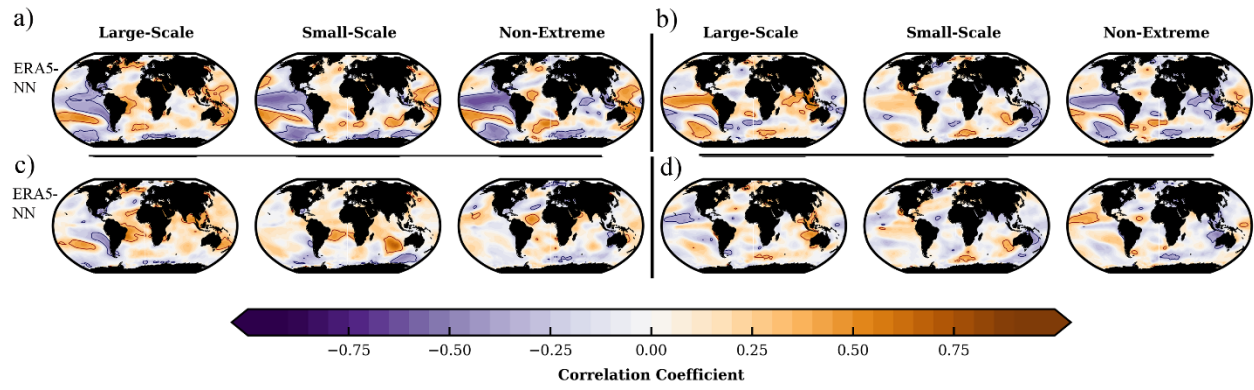


Figure. S6: Same as Figure 4, but for ERA5-NN.

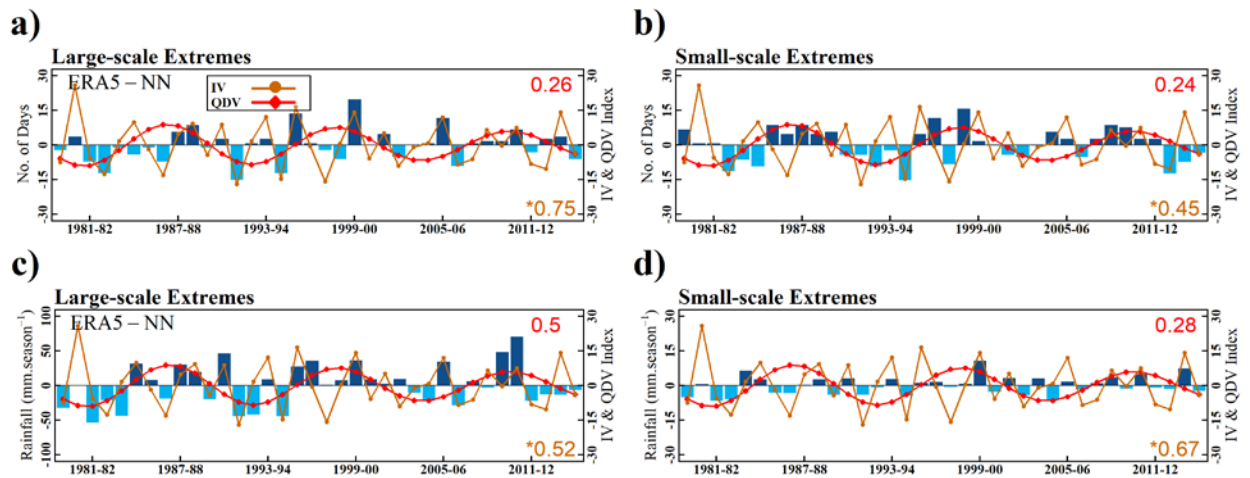
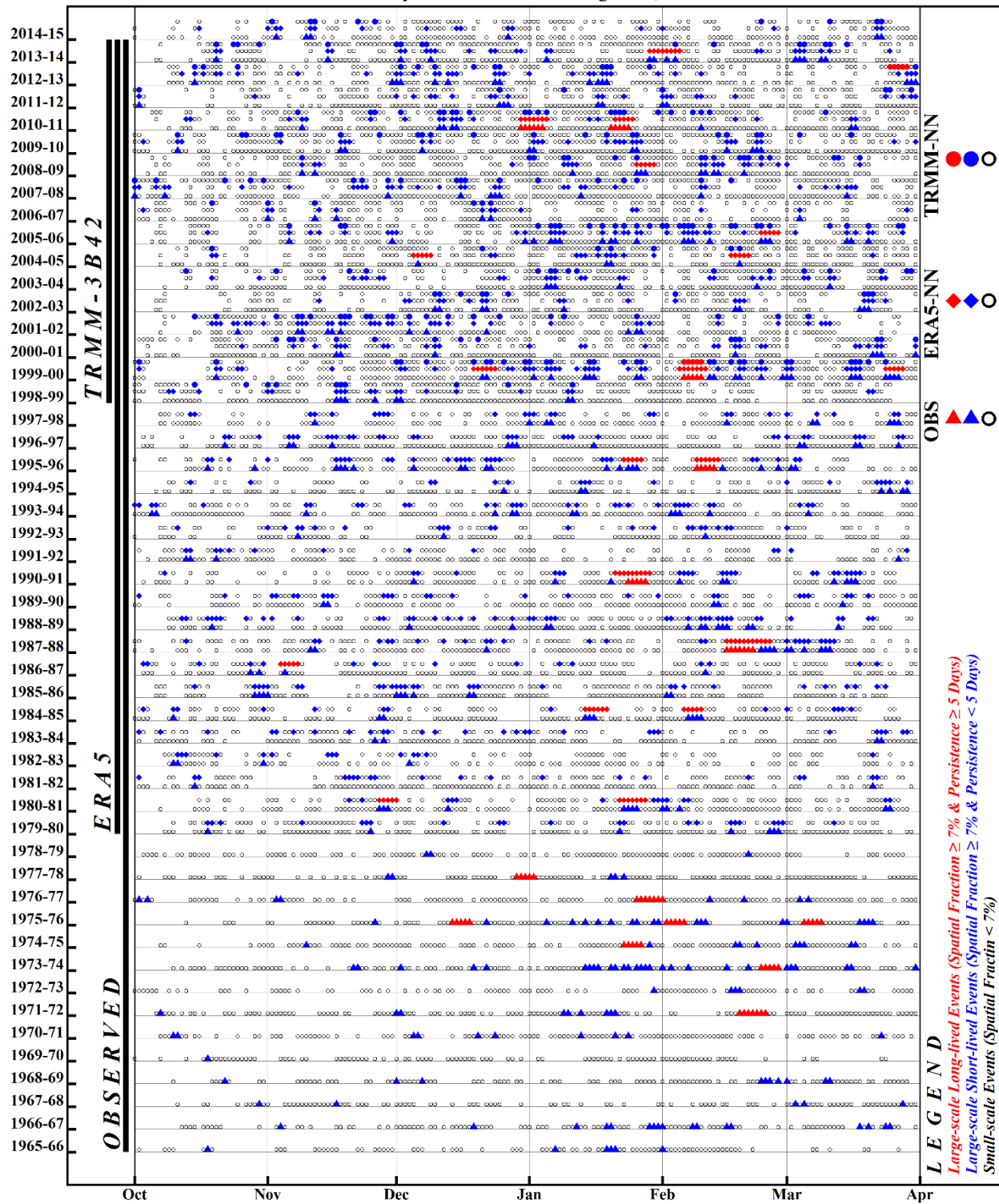


Figure. S7: Same as Figure 5, but for ERA5-NN.

Intraseasonal Calendar of daily rainfall extremes using OBS, ERA5-NN and TRMM-NN



*** Analysis performed using nearest neighbor grid-points of ERA5 and TRMM

Figure. S8: Same as Figure 8, but for nearest neighbour (NN) fields of ERA5 and TRMM.

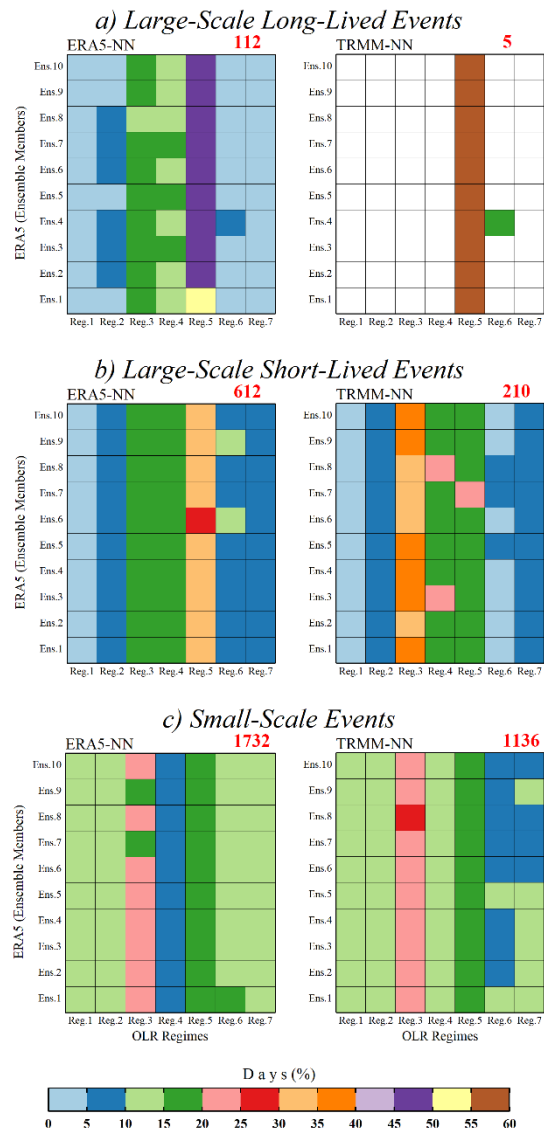
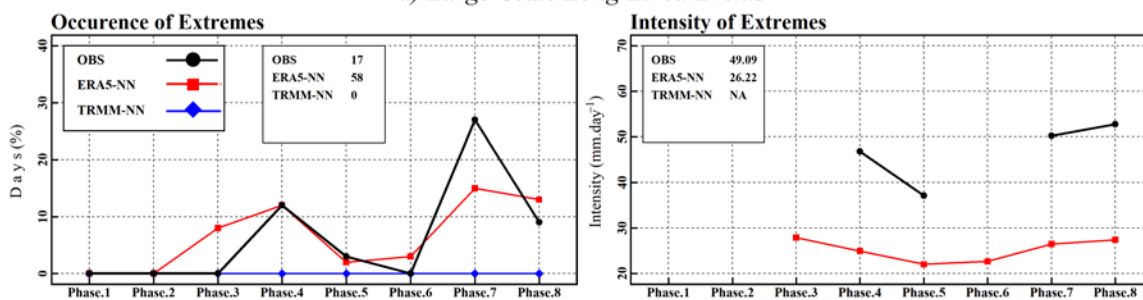


Figure. S9: Same as Figure 9, but for nearest neighbour (NN) fields of ERA5 and TRMM.

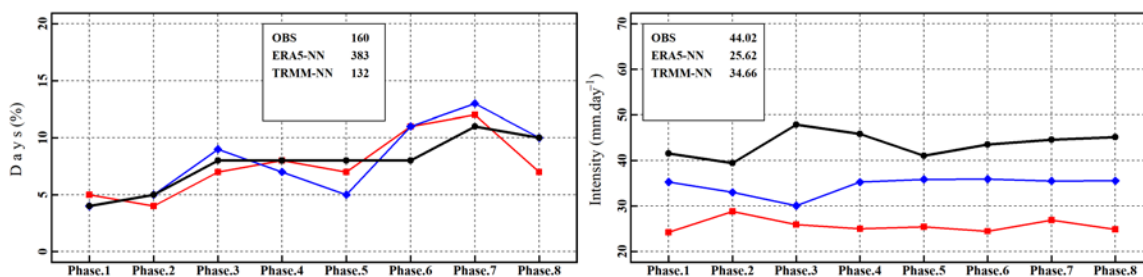


Figure. S10: Same as Figure 10, but for nearest neighbour (NN) fields of ERA5 and TRMM.

a) Large-Scale Long-Lived Events



b) Large-Scale Short-Lived Events



c) Small-Scale Events

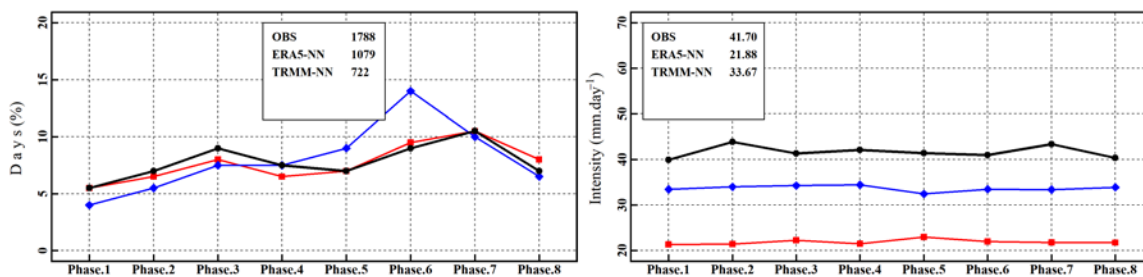


Figure. S11: Same as Figure 12, but for nearest neighbour (NN) fields of ERA5 and TRMM.

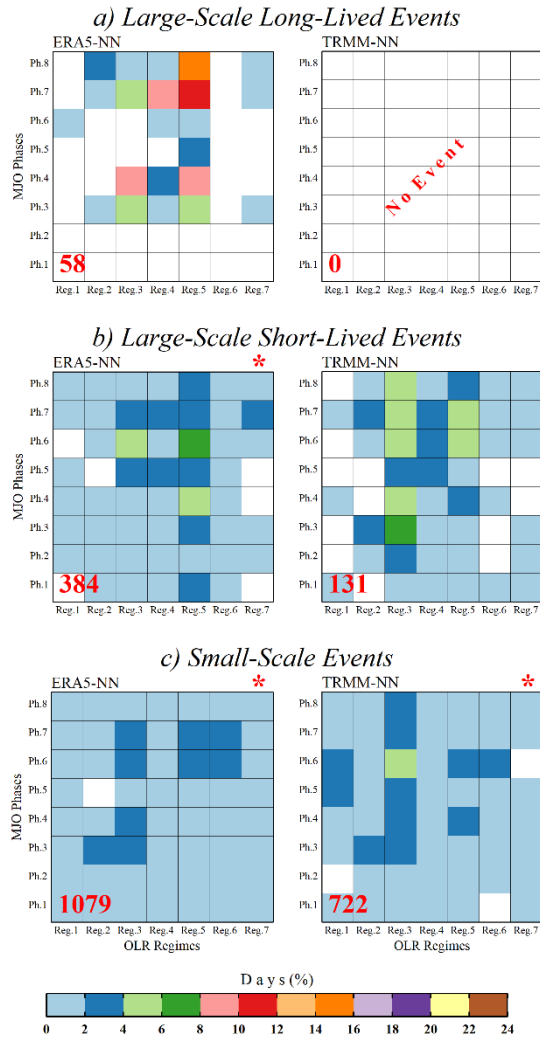


Figure. S12: Same as Figure 13, but for nearest neighbour (NN) fields of ERA5 and TRMM.

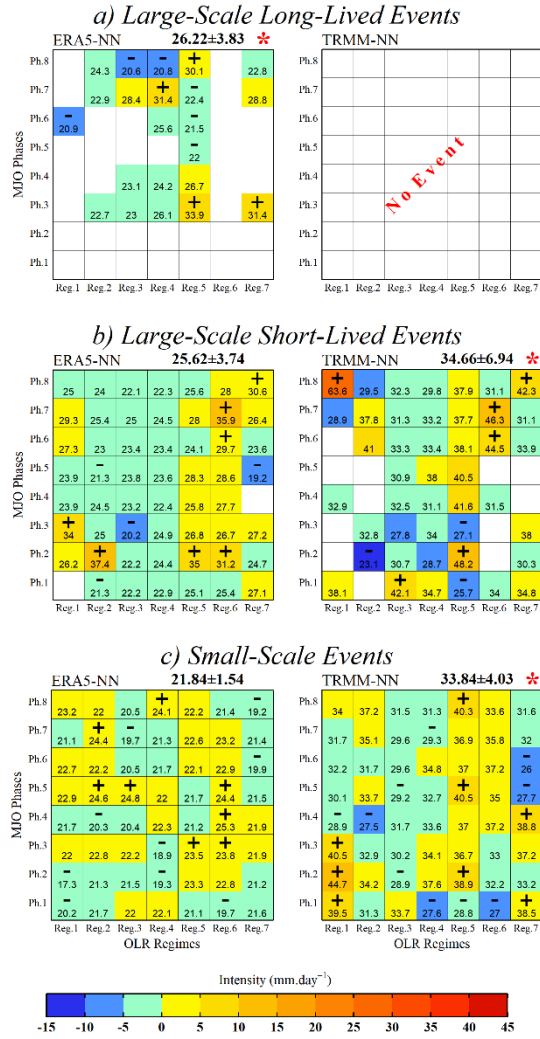
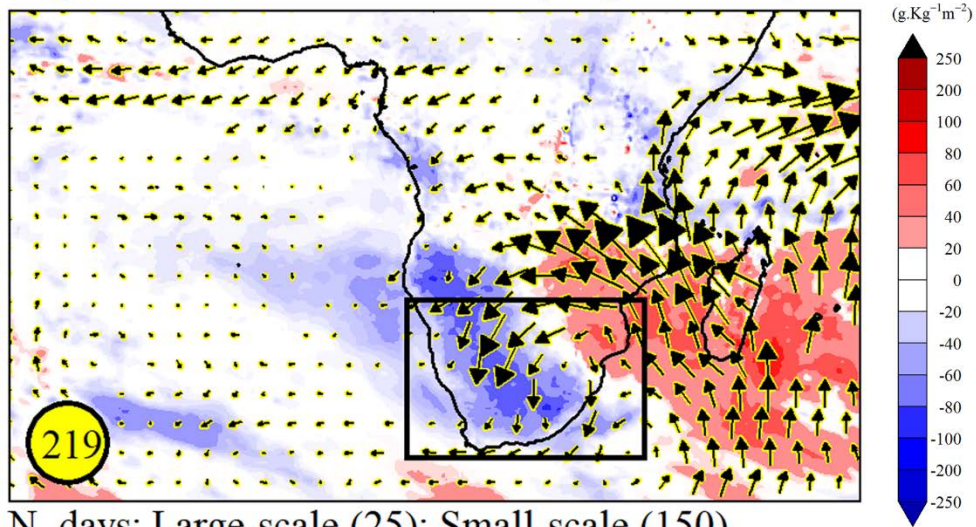


Figure. S13: Same as Figure 14, but for nearest neighbour (NN) fields of ERA5 and TRMM.

Regime 3 and Moderate Phases (Amplitude > 1)



N. days: Large-scale (25); Small-scale (150)

—▷ 45 ($\text{g.Kg}^{-1}\text{ms}^{-1}$)

Figure. S14: Composite anomalies of vertically integrated moisture flux divergence ($\text{g. Kg}^{-1}\text{m}^{-2}$) and moisture flux ($\text{g. Kg}^{-1}\text{ms}^{-1}$) at 850 hPa during regime #3 with moderate phases of the MJO i.e., phases #3, #4 and #5 computed with respect to the climatology of NDJF from 1979 to 2015. Only those anomalies are shown which are significant at 95% confidence level according to the one-tailed students' t -test. The sample size is shown in the lower left corner of the panel.

Supplementary Tables: Chapter 3

Table S1: List of large-scale long-lived rainfall events between 1979–2015 identified by OBS. First three columns represent spell number, date and season of the spell. Columns 4–6 represent OLR regime, phase and amplitude of MJO. Columns 7–11 (12–16) show average intensity (spatial fraction > 90th percentile) corresponding to each day of the event.

Spell No.	Date	Season	OLR Regime	MJO Phase	MJO Amplitude	Average Intensity (Millimeter)					Average spatial fraction > 90th Percentile (%)				
						OBS	ERA5-NN	ERA5-AGP	TRMM-NN	TRMM-AGP	OBS	ERA5-NN	ERA5-AGP	TRMM-NN	TRMM-AGP
1	2/16/1988	1987-88	4	7	1.74	42.01	22.26	21.76	NA	NA	16.89	29.78	23.38	NA	NA
	2/17/1988	1987-88	5	7	2.07	45.64	21.01	22.16	NA	NA	7.56	21.33	17.11	NA	NA
	2/18/1988	1987-88	5	7	2.23	40.47	18.97	19.93	NA	NA	15.56	17.78	14.09	NA	NA
	2/19/1988	1987-88	4	7	2.65	47.84	28.68	27.39	NA	NA	28.00	43.11	32.62	NA	NA
	2/20/1988	1987-88	4	7	3.08	68.19	53.85	46.09	NA	NA	19.56	32.89	28.31	NA	NA
	2/21/1988	1987-88	5	8	3.27	61.82	52.75	49.00	NA	NA	20.89	27.11	22.77	NA	NA
	2/22/1988	1987-88	5	8	3.10	51.83	36.89	31.15	NA	NA	15.56	28.44	20.12	NA	NA
2	1/24/1991	1990-91	3	4	1.77	52.40	28.10	24.88	NA	NA	8.44	18.22	22.28	NA	NA
	1/25/1991	1990-91	3	4	1.58	36.13	19.17	21.31	NA	NA	11.11	10.67	10.58	NA	NA
	1/26/1991	1990-91	4	4	1.29	40.77	26.57	27.32	NA	NA	18.67	53.78	44.92	NA	NA
	1/27/1991	1990-91	5	4	1.16	58.01	24.93	23.50	NA	NA	7.56	29.33	23.32	NA	NA
	1/28/1991	1990-91	5	5	1.25	37.14	22.49	22.29	NA	NA	8.44	26.22	19.02	NA	NA
3	2/9/1996	1995-96	5	NA	0.88	97.91	25.10	23.92	NA	NA	9.78	7.11	5.17	NA	NA
	2/10/1996	1995-96	5	NA	0.97	68.80	46.16	33.30	NA	NA	12.00	12.89	18.28	NA	NA
	2/11/1996	1995-96	5	NA	0.80	69.00	41.21	41.49	NA	NA	14.22	28.00	33.35	NA	NA
	2/12/1996	1995-96	5	NA	0.47	56.41	43.16	35.85	NA	NA	7.11	15.11	19.51	NA	NA
	2/13/1996	1995-96	5	NA	0.30	59.67	24.00	21.01	NA	NA	12.89	10.22	13.66	NA	NA
4	2/6/2000	1999-00	5	NA	0.79	134.72	44.99	33.27	82.04	68.34	12.00	13.33	17.91	12.44	14.13
	2/7/2000	1999-00	5	NA	0.96	65.43	41.41	37.42	62.12	51.95	13.78	18.22	19.57	21.33	16.56
	2/8/2000	1999-00	5	NA	0.96	56.31	46.05	42.42	60.58	52.96	7.56	14.22	15.51	15.11	19.65
	2/9/2000	1999-00	5	NA	0.70	48.70	48.60	48.19	33.05	34.22	11.56	16.00	15.45	15.11	14.39
	2/10/2000	1999-00	5	NA	0.56	50.44	43.05	40.32	49.04	40.85	10.67	15.11	15.75	10.22	13.86
5	12/30/2010	2010-11	3	NA	0.43	50.41	25.49	27.26	34.57	34.32	12.89	10.67	12.49	4.89	5.58
	12/31/2010	2010-11	3	NA	0.62	42.69	23.79	22.59	32.02	27.09	16.44	39.56	30.09	22.22	15.70
	1/1/2011	2010-11	4	NA	0.71	44.64	30.49	27.76	31.41	29.27	14.22	49.78	37.85	7.56	7.16
	1/2/2011	2010-11	3	NA	0.91	52.09	20.69	20.70	31.96	40.13	10.22	25.33	24.49	5.78	8.28
	1/3/2011	2010-11	3	NA	0.88	43.23	20.86	20.36	31.58	34.74	9.33	29.33	26.22	8.00	8.28
	1/4/2011	2010-11	3	NA	0.64	38.52	21.53	20.32	30.51	25.38	8.44	20.44	18.52	3.11	7.29
6	1/20/2011	2010-11	3	7	2.43	51.26	18.45	19.29	38.92	40.13	8.44	3.56	3.82	14.22	11.17
	1/21/2011	2010-11	3	7	2.59	53.78	24.50	23.02	31.43	31.46	18.22	23.11	14.58	20.00	11.43
	1/22/2011	2010-11	4	7	2.54	43.55	26.86	26.33	33.15	35.13	17.78	48.00	38.09	22.22	17.15
	1/23/2011	2010-11	2	7	2.49	59.16	22.88	24.34	41.39	38.81	10.22	23.11	27.14	12.00	14.59
	1/24/2011	2010-11	2	8	2.17	44.58	24.82	24.92	27.09	23.16	8.44	27.11	20.68	1.33	1.05

First three columns represent spell number, date and season of the spell. Columns 4–6 represent OLR regime, phase and amplitude of the MJO. Columns 7–11 (12–16) show average intensity (spatial fraction > 90th percentile) corresponding to each day of the event.

Chapter 4

Meso-scale modelling

Convection permitting downscaling of 3 large-scale longest-lived extreme rainfall events during austral summer in South Africa: reanalysis and ensemble reforecasts

Asmat Ullah^{1*} ; Benjamin Pohl¹ ; Julien Pergaud¹ ; Bastien Dieppois² ; Mathieu Rouault³

¹ Centre de Recherches de Climatologie, UMR 6282 Biogéosciences, CNRS/ Université de Bourgogne Franche-Comté, Dijon, France

² Centre for Agroecology, Water and Resilience, Coventry University, Coventry, UK

³ Nansen Tutu Center for Marine Environmental Research, Department of Oceanography, University of Cape Town, South Africa

To be submitted in Weather and Forecasting

*** Corresponding Author's Address**

Asmat Ullah: asmat-786@hotmail.com

Laboratoire Biogéosciences
Université de Bourgogne
6 Boulevard Gabriel
21000 DIJON – France

1. Introduction

Extreme rainfall events are a matter of crucial importance in the 21st century since their frequency and intensity are rapidly changing due to global warming (IPCC, 2021). This would include climate change, with expected changes in the rainfall extremes due to the Clausius-Clapeyron scaling relating air temperature to its humidity (Betts and Harshvardhan, 1987; Kharin *et al.*, 2007; Muller *et al.*, 2011; Pohl *et al.*, 2017). Hence, the losses incurred by these events are also rapidly increasing in terms of flood risk, life losses, infrastructure, crop damage, soil erosion and many more (WMO, 2021). This is also true for South African rainfall (Mason and Joubert, 1997; Mason *et al.*, 1999; Shongwe *et al.*, 2009; Engelbrecht *et al.*, 2013; Pinto *et al.*, 2016). Future scenarios include a combination of decreasing numbers of rainy days while increasing their intensity (Pohl *et al.*, 2017), which are likely to modify the intrinsic characteristics of extreme rainfall spells in the future. Accurate prediction of extreme rainfall events is critically important for effective disaster response and to help authorities to take proactive measures to mitigate the potential damages. To improve the predictability of extreme rainfall events under changing climate, the scientific community uses Numerical Weather Prediction (NWP). The Weather Research and Forecasting (WRF) model is a widely used mesoscale NWP system designed for both atmospheric research and widely used for operational forecasting applications. Several studies based on convection-permitting downscaling have recently been performed over southern Africa (Cr  tat *et al.*, 2011; Pohl *et al.*, 2011, 2014; Vigaud *et al.*, 2012; Ratnam *et al.*, 2013). However, these studies were mostly based on seasonal simulations or individual case studies of extreme rainfall events by merely using various reanalysis products. There is no study hitherto found in the literature which assessed the predictability of rainfall extremes. Thus, in this study, we for the first time attempt to provide a thorough investigations focusing on the predictability of longest-lived extreme rainfall events using NOAA’s reforecasts and the improvements in predictability of such ensemble reforecasts using convection-permitting mesoscale modelling.

The extreme rainfall spells during the austral summer (November through February) in South Africa are mainly associated with moist atmospheric convection, ranging in scale from single-cell storms to organized systems, such as Mesoscale Convective Complexes (Blamey and Reason, 2013) and tropical storms (Reason and Keibel, 2004; Reason, 2007; Malherbe *et al.*, 2012, 2014;

Fitchett and Grab, 2014). Cut-off lows (COLs) can also lead to extreme rainfall in South Africa, but they are rare during the summer season (Favre et al., 2013). In austral summer, three key regions (namely southwest Indian Ocean, tropical western Indian Ocean, and tropical southeast Atlantic Ocean) are known to inject moisture fluxes into the southern African continent (Desbiolles *et al.*, 2018; Rapolaki *et al.*, 2019, 2020). Tropical Temperate Troughs are the dominant rain-bearing systems over the region (Manhique *et al.*, 2011; Hart *et al.*, 2013; Macron *et al.*, 2014; James *et al.*, 2020). TTTs correspond to synoptic-scale cloud bands that link tropical instability over the subcontinent with an upper-tropospheric frontal system embedded in the mid-latitude westerly circulation (Todd and Washington, 1999; Todd *et al.*, 2004; Hart *et al.*, 2010). Previous studies suggest that, at the interannual timescale, rainfall variability is strongly modulated by El Niño Southern Oscillation (Nicholson and Kim, 1997; Washington and Preston, 2006; Dieppois *et al.*, 2015). Typically, El Niño conditions tend to favour dry summers while La Nina tends to be associated with above-normal rainfall in South Africa.

Ullah *et al.*, (2022) proposed a novel typology of extreme rainfall events using average spatial fraction (i.e., percentage of stations or grid-points exceeding 90th percentile on the day of the event) as a base criterion disentangling large-scale (Spatial fraction $\geq 7\%$) and small-scale (Spatial fraction $< 7\%$) extreme events. Ullah *et al.* (2023) proposed a further extension of large-scale extreme events by introducing duration metric into the definition of large-scale extreme events (Spatial fraction $\geq 7\%$ and Persistence ≥ 5 days). Large-scale long-lived events form a category of rainfall extremes that may potentially lead to high environmental and societal impacts. Thus, in this study, we attempt to downscale three events from 2000 to 2015 identified as large-scale long-lived events over South Africa (Table 1) and considered here as potential case studies. These long-lived events were first-hand identified by 225 quality-controlled in-situ observations and then correctly co-identified by nearest neighbour and all-grid-points fields of ERA5 reanalysis and TRMM satellite estimates. This suggests robustness in the methodology defined by Ullah *et al.*, (2021; 2023) to identify such highly intense and longest-lived extreme events.

The first case study corresponds to a heavy rainy event that occurred in February 2000 (from 06 to 10 February), a month which is widely known for Tropical Cyclone (TC) Eline and its unusual penetration in mainland southern Africa and its devastating impacts (Reason and Keibel, 2004).

TC Eline made landfall in Mozambique and then penetrated southern Africa around 22 February 2000 around 0600 UTC, after tracking over 7000 km west across the tropical south Indian Ocean, but a tropical depression was noticed very early in the same months (Reason and Keibel, 2004). The extreme rainfall spell persisted 5 days and was associated with widespread rainfall anomalies, contrasting with the short-lived but large-scale events observed in the same month (Fig. 8 and S8 in Ullah *et al.*, 2023). During this case study, observations and other datasets show that 7% to 20% of stations or grid-points exceed their local 90th percentile threshold (Table 1). The South African Department of Water Affairs and Forestry (DWAF) reported worth 1.3 billion Rands in damages to infrastructure as approximately 200 bridges and nearly 1000 km of road network were washed away or severely damaged. The Mozambique government estimated that at least 600 people lost their lives while thousands of people were displaced by the raging floods. The forecasts by the South African Weather Bureau showed correct prediction in terms of the location of the event but the rainfall totals were underestimated by 50 percent.

The second and third case studies were identified from 30 December 2010 to 04 January 2011 (persisted 6 days) and 20 January 2011 to 24 January 2011 (persisted 5 days), respectively. These heavy and long-lived rainfall spells were associated with record-breaking La Niña events during the 2010–11 season, one of the strongest on record, comparable in strength with the La Niña events of 1917–18, 1955–56 and 1975–76. In October 2010, the Southern Africa Regional Climate Outlook Forum (SARCOF) released its seasonal forecast, which predicts above-average precipitation for the region except for central and northern Zambia, southern Mozambique, and southwestern South Africa. This forecast took into account that the La Niña effect is expected to continue through early 2011. La Niña causes lower-than-normal temperatures in the eastern equatorial region of the Pacific Ocean, which in turn leads to above-average rainfall in southern Africa. In December 2010 and January 2011, this prediction proved accurate as above-average rainfall fell across much of the region, causing flooding in Lesotho, Mozambique, and South Africa. In mid-January 2011, the upper reaches of the Zambezi River reached levels not normally reached until early March. Historically, rainfall activity increases during the period between late January and late February (March in some countries). Therefore, the flooding at this early stage of the rainfall season, together with forecasts for continued above-average rainfall, raised concerns that the region could experience particularly severe flooding in 2011. According to United Nations Office for the Coordination of Humanitarian Affairs (OCHA), an estimated

708,000 people were affected by floods and/or storms in southern Africa during the 2010–11 rainfall season, with 314,361 either displaced or evacuated and 477 people killed.

The main objective of this chapter is to investigate to which extent these major events are predictable, how many days in advance, with which errors and uncertainties, using atmospheric reforecasts. The study also focuses on convection-permitting downscaling of reforecast global grids using WRF and assesses if downscaling can improve the properties of such highly intense long-lived events in terms of intensity, rainfall accumulation and location.

This paper is organized as follows. Section 2 presents datasets and methodology. Section 3 provides the synoptic background and the downscaling of three case studies using ERA5. Section 4 addresses the predictability of case studies in raw RF2 grids and the modelled RF2. Section 5 summarizes the results and establishes the main conclusions.

2. Data and Methods

For the downscaling of large-scale and longest-lived events, we use a state-of-the-art Weather Research and Forecasting model (WRF version 4.2.1; Skamarock *et al.*, 2021). The WRF model is a widely used state-of-the-art mesoscale Numerical Weather Prediction (NWP) system designed for both atmospheric research and widely used for operational forecasting applications.

The ERA5 reanalysis data are widely analysed in climate science to assess changes in observation systems, to scale progress in model simulations and for forecast error evaluation (Hersbach *et al.*, 2020b). ERA5 reanalysis is the 5th generation dataset available from the European Centre for Medium-Range Weather Forecasts (ECMWF) providing $0.25^\circ \times 0.25^\circ$ global resolution of hourly gridded outputs of surface and atmospheric fields at the global scale, spanning 1979 to the present. We use ERA5 in this study as forcing dataset to launch WRF simulation as well as various other atmospheric variables are also obtained from ERA5 to study the synoptic background of the case studies and to evaluate the results. These variables include, rainfall field, vertically integrated moisture divergence, u-wind, v-wind, mean sea level pressure, geopotential height, and specific humidity.

Reforecast version 2 (RF2) developed by National Oceanic and Atmospheric Administration/Physical Science Laboratory (NOAA/PSL: Hamill *et al.*, 2022) is also used to drive WRF simulations. The spatial resolution of the RF2 is 0.25° with 64 vertical hybrid levels

and is provided every 3 hours for the first 10 days of the forecast; beyond 10 days 0.50° grid spacing is used with a temporal resolution of every 6 hours. The RF2 grid proceeds from 90°N to 90°S and from 0°E to 359.75°E. Here we use the first 10 days of reforecast using five members of RF2 which includes a control run and four ensemble members where the small number of noises were added to the initial condition. The RF2 is one of several prediction systems maintained by the United States' National Weather Service (NWS) and supports medium-range weather and sub-seasonal to seasonal forecasting. The role of reforecasts has been widely recognized in validating and calibrating climate models and weather forecasts (Hamill *et al.*, 2004, 2006, 2013, 2015, 2022) diagnosing model errors (Gascón *et al.*, 2019) and predicting rare extreme events (Li *et al.*, 2019). On 23 September 2020, the finite volume-based RF2 was implemented at the NOAA (Hamill *et al.*, 2022). In the newly implemented RF2, the integration time was extended from week 1 for weather forecasts, week 2 for extended forecasts and weeks 3–5 for sub-seasonal forecasts (Guan *et al.*, 2022). RF2 provides forecasts from 1989 through 2019 in which the Climate Forecast System (CFS) reanalysis served as initial conditions for the first phase (1989–1999) of reforecasts while Global Ensemble Forecast System Version 12 (GEFSv12) reanalysis was used for the second phase (2000–2019; Guan *et al.*, 2022).

Daily rainfall field is obtained from a dense network of in-situ observations from the Water Research Commission of South Africa (<http://www.wrc.org.za>) depending on the quality of the datasets as since the number of stations varies for each case study. For cases #1, #2, and #3, data from 1832, 1073 and 1113 stations are used respectively.

In addition to rainfall field from observations and ERA5 reanalysis, we also use Tropical Rainfall Measuring Mission (TRMM v.7) 3B42 product (Huffman *et al.*, 2007) as a satellite-based estimation of extreme rainfall events. TRMM precipitation product covers an area from 50°S–50°N and 180°W–180°E, with a spatial resolution of 0.25° × 0.25°, from 1998 to the present on a 3-hourly basis. The daily accumulated precipitation (combined microwave and infrared) is used in this study for each case study. This dataset allows for a gridded estimation of rainfall, and corresponding extreme spells, thereby forming a useful complement to rain gauges and reanalysis. The datasets used in this study are summarized in Table 2.

2.1. WRF experimental design

WRF simulations over South Africa are performed using two one-way nested domains with 60 sigma levels (Fig. 1). The parent domain with 9 km horizontal resolution covers southern Africa (1.32°E–46.01°E; 44.32°S–14.22°S) with 371 grid-points in the east–west and 327 grid-points in north–south directions. The nested inner domain with a 3 km horizontal resolution covers South Africa and a few neighbouring countries (12.06°E–37.17°E; 37.96°S–19.41°S) with 1130 grid-points in the east–west and 1010 grid-points in the north–south directions.

ERA5 reanalysis is first used to derive WRF simulations for three stage sensitivity tests in order to obtain the finest WRF configuration as follows:

- Nudging and frequency of forcing
- Cumulus parameterization schemes and spin-up time
- Microphysics parameterization schemes

Nudging modifies the model's skill for capturing the spatial and temporal variability of the simulated convection. For nudging (Stauffer and Seaman, 1994) and forcing frequency testing, we run four experiments on three different case studies with 1-hour and 6-hour time steps with and without nudging at the parent domain.

For cumulus parameterization schemes and spin-up time, we consider three schemes namely Betts–Miller–Janjic scheme (BMJ: Betts and Miller, 1986; Janjic, 1994), Kain–Fritsch scheme (Kain, 2004) and KFtr as all the experiments are repeated up to 4 days spin up time. For the physical parameterization, we consider two microphysics schemes namely WSM6 and Morrison 2–moment scheme (MOR: Morrison *et al.*, 2009).

In all three evaluation stages, we consider Yonsei University (YSU) scheme for the Planetary Boundary Layer (PBL: Hong *et al.*, 2006) and the Rapid Radiative Transfer Model (RRTM) scheme for long and short waves (Iacono *et al.*, 2008). Surface Elevation Data (GMTED2010) are taken from the United States Geological Survey database, which has replaced GTOPO30 as the elevation dataset of choice for global and continental scale applications. The MODIS Combined Land Cover product is used for land use which incorporates five different land cover classification schemes, derived through a supervised decision-tree classification method. The primary land cover scheme identifies 17 classes including 11 natural vegetation classes, three

human-altered classes, and three non-vegetated classes. The sensitivity tests conducted on three case studies are summarized in supplementary Table S1.

The skill of the WRF experimental design is evaluated on three case studies using OBS, ERA5 and TRMM with various analyses (results not included). By carefully examining the results of three case studies we find that nudging with a 6-hour forcing frequency produces good results in simulating such high-intensity long-lived events. BMJ scheme for cumulus parameterization with 24h spin-up time and WSM6 for microphysics parameterization outperform other options which are also in line with previous studies over southern/South Africa (Crétat *et al.*, 2011, 2012b; Ratna *et al.*, 2014). The finest experimental setup is then used to derive WRF simulations by using ERA5 and the ensemble of RF2 as summarized in Table 3.

The finest WRF experimental setup is then used to obtain simulations by using one control run and 4 ensemble members of RF2 as forcing. The WRF model is initialized at 0600 UTC up to 9 days of lead time starting from the first day of the event. The initialization setup for each case study is summarized in Table 4.

Several model evaluation techniques are applied to evaluate the model performance and uncertainties between ensemble members by comparing it with a dense network of observations, ERA5 reanalysis and TRMM satellite estimates. For comparison purposes with the rain-gauge observational network, all grid-points (AGP) and those nearest to OBS (NN) fields of all datasets e.g., ERA5, TRMM, RF2 and WRF simulations are used in this study.

Commonly used statistical analysis techniques are employed such as the one sigma standard deviation (SD), probability density function (PDFs) and intensity-based contingency analysis to quantify and compare the performance of the WRF model against observations. The time-averaged spatial plots of rainfall, u-wind, v-wind, geopotential height, mean sea level pressure, and specific humidity are also assessed in order to study the physical mechanisms of each case.

In this study, the daily rainfall accumulation with a focus on the most intense day and the total rainfall accumulation during the entire period of the events are assessed. For the latter, only the first four- or five-day lead times were considered depending on the total duration of the respective case study. It is due to the lead time of the RF2 being 10 days. For instance, with the latest lead time (i.e., 9 days before), only the first day of the events could be retained.

The daily accumulation is computed from 0600-UTC from the previous date to 0600-UTC on the following date considering the guidelines of the World Meteorological Organization (WMO). The total event accumulation is computed by using the same approach by considering 0600-UTC of the first date of the event till 0600-UTC to the last date of the event.

3. Synoptic background and downscaling of ERA5 for three case studies

Atmospheric circulation patterns of three case studies are mapped by computing the composite anomalies of vertically integrated moisture divergence (VIMD), moisture flux and mean sea level pressure with respect to the mean climatology (Fig. 2). The mean synoptic conditions from November to February are characterized by the dominance of subtropical high-pressure system resulting in stable and clear sky conditions in the interior parts of the sub-continent (Fig 2a). Figure 3 and 4 displays the spatial distribution of total accumulated rainfall and PDFs respectively, corresponding to each case study.

a) Case #1

The strong easterly moisture flux anomalies from the Indian Ocean and the westerly anomalies from the Atlantic Ocean converge over the northeastern part of southern Africa, leading to $\sim 500 \text{ g.kg}^{-1}\text{ms}^{-2}$ moisture flux convergence anomalies over the core zone of the event (Fig. 2b). A nearly perpendicular flow of moist air was responsible for the anomalously heavy rainfall over the north-eastern parts of South Africa. From a synoptic perspective, the combined influence of tropical and mid-latitude circulations, Mascarene high-pressure system located over the South Indian Ocean and Angola Low seems responsible for heavy rainfall. In addition, a wave train pattern is also quite notable in case #1, as such patterns are also proven to be responsible for bringing extreme rainfall over the region (Crétat *et al.*, 2019).

For case #1, most of the regions received rainfall between 10 mm to 75 mm as shown by all datasets while maximum accumulation was largely concentrated over northeastern South Africa (Fig. 3a). OBS show three different high-intensity zones where rainfall exceeds 100 mm while many stations show total rainfall accumulation above 400 mm (OBS panel in Fig. 3a). The location and the intensity as shown by ERA5 is better in ERA5-WRFd1 and much better in ERA5-WRFd2 (Fig. 3a). In comparison to OBS, the three core zones seems correctly represented by TRMM dataset while ERA5-WRFd1 and ERA5-WRFd2 show similar characteristics and rainfall amounts on the correct location (Fig. 3a).

Total accumulated rainfall during case #1 is further assessed by using PDF analysis (left panel in Fig. 4). Before producing PDFs, we first obtain a relevant threshold using the average and standard deviation in OBS dataset to focus on the high-intensity zone of the event. For case #1, we note that OBS data shows an average along with a standard deviation of about 52.20 ± 89.50 mm. Using twice higher standard deviation, a threshold of 180 mm was obtained where around 167 stations (9%) out of 1832 stations show total accumulated rainfall above the 180 mm threshold. All other datasets are then analyzed using the threshold on the nearest neighbor scale. A nearly unimodal distribution is shown by all datasets where the peak of the distribution is located between 150 to 250 mm (left panel in Fig. 4). ERA5 and TRMM show approximately similar characteristics while showing large uncertainties as compared to OBS. The uncertainties shown by ERA5 are much resolved in ERA5-WRFd1 while the distribution shown by ERA5-WRFd2 is aligned nearly perfectly with the OBS including the upper tail of the distribution (>250 mm). This suggests the remarkable performance of WRF in improving the intensity of this extreme rainfall event.

b) Case #2

Case #2 on the other hand is the most spatially widespread longest-lived event (persisted 6 days) in which nearly 70% South African region received rainfall (Fig. 2c). Strong easterly flux bringing warm moisture from SWIO can be seen propagating towards southern Africa over 20°S (Fig. 2c). This easterly moisture flux diverts with nearly perpendicular southward propagation towards the mainland South Africa at 20°E (Fig. 2c). This southward propagation of moisture results in maximum convergence of moisture of about $\sim 500 \text{ g.kg}^{-1}\text{ms}^{-2}$ in the central parts of the country (Fig. 2c). The influence of blocking caused by ridging anticyclones over the southern tip of the continent is noteworthy for this particular case study (Fig. 2c). Such synoptic conditions are known to block the moisture over sub-continent causing extreme rainfall conditions and are well documented in previous studies (Xulu *et al.*, 2020; Ndarana *et al.*, 2022).

In terms of the spatial distribution of total accumulated rainfall for case #2, various stations across South Africa indicate rainfall between 75 to 350 mm (OBS panel in Fig. 3b). ERA5 dataset shows a similar representation of spatial distribution where a band of 75 to 150 mm rainfall is located over the central parts South Africa while very few grid-points of ERA5 show above 150 mm rainfall suggesting an underestimation as compared to observations (ERA5 panel

in Fig. 3b). In contrast, TRMM data shows poor performance in simulation correct location and intensity over the core zone of the event (TRMM panel in Fig. 3b). As compared to ERA5, WRF seems to improve the intensity and location of the spatial distribution of total accumulated rainfall for case #2 as the core zone of the event in both domains of WRF show the rainfall above 150 mm (ERA5-WRFd1 and d2 panels in Fig. 3b).

Following the methodology for case #1, here we once again identify the core zone of the event and produce PDFs. Using the records of 1073 stations for case #2, we note the average intensity along with standard deviation is about 59.47 ± 45.35 . PDFs for case #2 are then produced by considering a threshold of 90 mm (i.e., twice the standard deviation). Around 239 stations out of 1073 (~22%) were found exceeding the threshold of 90 mm thereby suggesting the widespread spatial extension of this particular extreme event. Almost all datasets show the peak density between 60 to 150 mm (middle panel in Fig 4). In comparison to OBS, both domains of WRF seem to underestimate the peak of the distribution while the upper tail of the distribution as shown by ERA5-WRFd2 seems to correctly reproduce the total rainfall accumulation (middle panel in Fig 4).

c) Case #3

Case #3 persisted 5 consecutive days and represents a typical TTT structure as northwest to the southeast elongated band of strong moisture convergence is quite notable (Fig. 2d). Abnormally low-pressure system over the entire southern African region especially over the preferable location of Angola Low are also seemed responsible for the penetration of the moisture from the tropical Atlantic Ocean. Previous studies show that Angola Low and Botswana High trigger austral summer precipitation over most of southern Africa while the Botswana High interlinks with the South Indian Ocean Anticyclone controlling the migration of so-called TTTs over southern Africa (Xulu *et al.*, 2020).

Figure 3c displays the spatial distribution of total rainfall accumulation in case #3. Similar to case #2, case #3 also represents an approximately similar distribution of rainfall patterns except for a narrow band of the high-intensity zone. Overall, the intensity and location shown by ERA5 seem improved in both domains of WRF (Fig. 3c).

OBS data shows an average of 47.52 mm along with a standard deviation of about 46.30 mm. A threshold of 90 mm was retrieved by considering twice the standard deviation to evaluate the model performance in simulating the high-intensity zone of the event (right panel in Fig. 4). We note that 15% of the station exceeded the threshold of 90 mm (168 stations). The distribution shown by ERA5-WRFd2 seems approximately similar to that shown by OBS while other datasets poorly represent the distribution, especially above 150 mm (right panel in Fig. 4).

4. Predictability of three cases in raw RF2 grids and the downscaled RF2

4.1. Predictability of case studies in raw RF2 grids

Figure 5a displays the spatial distribution of total accumulated rainfall for case #1 using the ensemble mean of RF2 with different lead times. For case #1, total accumulation based on 5 days (05Feb-0600-UTC to 10Feb-0600-UTC) is computed for each lead time starting from the first initialization date i.e., 05Feb-0600-UTC till the latest initialization date i.e., 01Feb-0600-UTC. In comparison to the results discussed in the previous section, the raw RF2 forecasts show a poor representation of intensity and the spatial distribution of the rainfall patterns. In almost all lead times, the RF2 shows an eastward shifted core zone of the event which is incorrect as compared to the other datasets discussed for this case study in the previous section (Fig. 5a). However, considering the forecast initialized on the 5th, 4th and 2nd February seems slightly better in terms of location as compared to the forecast of the 3rd and 1st February (Fig. 5a). In contrast, raw RF2 fields show a remarkably better forecast for case #2 for each lead time not only in terms of intensity but also in terms of location of the event (Fig. 5b). Case #3 also shows a good representation of spatial patterns of the event at least for the forecast initialized on 19th and 18th January (Fig. 5c). Here we show the ensemble mean yet the core zone of the event depending on different case studies as well as lead time yet well depicted by raw RF2 fields. This suggests the usefulness of ensemble prediction as we can anticipate better results by downscaling each ensemble member separately.

4.2. Predictability of case studies in downscaled RF2 using WRF

a) Case #1

Figure 6 shows the total rainfall accumulation from 05Feb-0600-UTC to 10Feb-0600-UTC for initialization dates beginning from 05 February to 01 February using raw RF2 fields and RF2-WRFd2 fields using a threshold of 180 mm as identified in section 3 using OBS. It is noteworthy that with all lead times, the uncertainties as shown by raw RF2 field (dashed lines) remarkably reduced in RF2-WRFd2 (solid lines: Fig. 6). With the first two lead times (initialized on 05 and 04 February), all downscaled ensemble members mimicked the observed characteristics including the peak and the tail of the distribution (first two panels from left in Fig. 6). With the latest lead times (initialized on 02 and 01 February), few downscaled ensemble members able to show the correct rainfall amounts as shown by OBS. However, the forecasts initialized on 03 February show poor performance in raw RF2 as not a single member was able to predict the rainfall. This suggest the uncertainty is low while the forecasts errors were high thereby suggesting the dependence of WRF on the quality of forcing.

The probability of ensemble members producing above threshold rainfall amounts for case #1 is further explored spatially to evaluate the intensity along with the location of the event in Figure 7. OBS data shows three core zones where the highest rainfall accumulation was recorded. The first core zone lies near the 26°S and below 30°E while the second and third zones are located at the same latitude but above 30°E (Fig. 7a). As shown by raw RF2 fields (Fig. 7b), the first core zone was not correctly predicted by any member of raw RF2 with any forecast initialization date. This deficiency can also be seen in both domains of WRF (Fig. 7c-d). However, in the other two core zones, WRF was able to improve the correct intensity as shown by almost all ensemble members and especially with the forecasts initialized on 05 February and 04 February.

5. Preliminary Conclusions

In this study, three cases of large-scale longest-lived events that are identified during the period between 2000 to 2015, were taken as case studies to investigate their predictability by downscaling reforecasts using WRF model. We first downscale ERA5 reanalysis for all three case studies. We note that WRF was able to reproduce the observed characteristics of rainfall patterns, intensity and location for all three case studies when ERA5 was used as forcing. The WRF configuration setup was also found reliable to downscale such cases of heavy rainfall events as all three cases have different rain-bearing systems yet the performance of WRF was up to the mark.

By analysing these preliminary results of downscaling of RF2 for case #1, we notice that raw RF2 forecasts have uncertainties in terms of total rainfall accumulation with different lead times as well as uncertainties between ensemble members. We note that WRF can remarkably reduce these uncertainties in simulating the total rainfall accumulation of the event. Overall, these potentially high-impact (large-scale long-lived) events are predictable in the raw RF2 grid, and their predictability can be improved by dynamical downscaling.

Currently, we provide some initial results for case #1 while the simulations for other cases e.g., cases #2 and #3 are running in the supercomputing facility of the University. Thus, these results will be extended to the other cases studies and also with other analyses which are important to further investigate the driving mechanisms of such events in terms of dynamics and probable causes of longer persistence of such events. Further, the analysis will also be devoted to the spatial variability of the events including spatial biases as well as a deeper investigation to explore the uncertainties in the ensemble members on daily and/or hourly scale.

References

- Asmat U, Athar H. 2017. Run-based multi-model interannual variability assessment of precipitation and temperature over Pakistan using two IPCC AR4-based AOGCMs. *Theoretical and Applied Climatology*, 127(1–2). <https://doi.org/10.1007/s00704-015-1616-6>.
- Asmat U, Athar H, Nabeel A, Latif M. 2018. An AOGCM based assessment of interseasonal variability in Pakistan. *Climate Dynamics*. Springer Berlin Heidelberg, 50(1–2): 349–373. <https://doi.org/10.1007/s00382-017-3614-0>.
- Betts AK, Harshvardhan. 1987. Thermodynamic constraint on the cloud liquid water feedback in climate models. *Journal of Geophysical Research: Atmospheres*. John Wiley & Sons, Ltd, 92(D7): 8483–8485. <https://doi.org/10.1029/JD092ID07P08483>.
- Betts AK, Miller MJ. 1986. A new convective adjustment scheme. Part II: Single column tests using GATE wave, BOMEX, ATEX and arctic air-mass data sets. *Quarterly Journal of the Royal Meteorological Society*. John Wiley & Sons, Ltd, 112(473): 693–709. <https://doi.org/10.1002/QJ.49711247308>.
- Blamey RC, Kolusu SR, Mahlalela P, Todd MC, Reason CJC. 2018. The role of regional circulation features in regulating El Niño climate impacts over southern Africa: A comparison of the 2015/2016 drought with previous events. *International Journal of Climatology*, 38(11): 4276–4295. <https://doi.org/10.1002/joc.5668>.
- Blamey RC, Reason CJC. 2013. The role of mesoscale convective complexes in southern Africa summer rainfall. *Journal of Climate*, 26(5): 1654–1668. <https://doi.org/10.1175/JCLI-D-12-00239.1>.
- Burls NJ, Blamey RC, Cash BA, Swenson ET, Fahad A al, Bopape MJM, Straus DM, Reason CJC. 2019. The Cape Town “Day Zero” drought and Hadley cell expansion. *npj Climate and Atmospheric Science 2019 2:1*. Nature Publishing Group, 2(1): 1–8. <https://doi.org/10.1038/s41612-019-0084-6>.
- Camberlin P, Moron V, Okoola R, Philippon N, Gitau W. 2009. Components of rainy seasons’ variability in Equatorial East Africa: Onset, cessation, rainfall frequency and intensity. *Theoretical and Applied Climatology*, 98(3–4): 237–249. <https://doi.org/10.1007/s00704-009-0113-1>.
- Conway D, Dalin C, Landman WA, Osborn TJ. 2017. Hydropower plans in eastern and southern Africa increase risk of concurrent climate-related electricity supply disruption. *Nature Energy 2017 2:12*. Nature Publishing Group, 2(12): 946–953. <https://doi.org/10.1038/s41560-017-0037-4>.
- Conway D, Van Garderen EA, Deryng D, Dorling S, Krueger T, Landman W, Lankford B, Lebek K, Osborn T, Ringler C, Thurlow J, Zhu T, Dalin C. 2015. Climate and southern Africa’s water-energy-food nexus. *Nature Climate Change*. Nature Publishing Group, 5(9): 837–846. <https://doi.org/10.1038/nclimate2735>.
- Cook C, Reason CJC, Hewitson BC. 2004. Wet and dry spells within particularly wet and dry summers in the South African summer rainfall region. *Climate Research*, 26(1): 17–31. <https://doi.org/10.3354/cr026017>.

- Cook KH. 2000. The South Indian convergence zone and interannual rainfall variability over Southern Africa. *Journal of Climate*, 13(21): 3789–3804. [https://doi.org/10.1175/1520-0442\(2000\)013<3789:TSICZA>2.0.CO;2](https://doi.org/10.1175/1520-0442(2000)013<3789:TSICZA>2.0.CO;2).
- Cook KH. 2001. A southern hemisphere wave response to ENSO with implications for Southern Africa precipitation. *Journal of the Atmospheric Sciences*, 58(15): 2146–2162. [https://doi.org/10.1175/1520-0469\(2001\)058<2146:ASHWRT>2.0.CO;2](https://doi.org/10.1175/1520-0469(2001)058<2146:ASHWRT>2.0.CO;2).
- Crétat J, Macron C, Pohl B, Richard Y. 2011. Quantifying internal variability in a regional climate model: A case study for Southern Africa. *Climate Dynamics*, 37(7–8): 1335–1356. <https://doi.org/10.1007/s00382-011-1021-5>.
- Crétat J, Pohl B, Dieppois B, Berthou S, Pergaud J. 2019. The Angola Low: relationship with southern African rainfall and ENSO. *Climate Dynamics*. Springer Berlin Heidelberg, 52(3–4): 1783–1803. <https://doi.org/10.1007/s00382-018-4222-3>.
- Crétat J, Pohl B, Richard Y, Drobinski P. 2012a. Uncertainties in simulating regional climate of Southern Africa: Sensitivity to physical parameterizations using WRF. *Climate Dynamics*, 38(3–4): 613–634. <https://doi.org/10.1007/s00382-011-1055-8>.
- Crétat J, Richard Y, Pohl B, Rouault M, Reason C, Fauchereau N. 2012b. Recurrent daily rainfall patterns over South Africa and associated dynamics during the core of the austral summer. *International Journal of Climatology*, 32(2): 261–273. <https://doi.org/10.1002/joc.2266>.
- CRI. 2021. *Global Climate Risk Index 2021: Who suffers most from extreme weather events? weather-related loss events in 2019 and 2000-2019*. .
- Desbiolles F, Blamey R, Illig S, James R, Barimalala R, Renault L, Reason C. 2018. Upscaling impact of wind/sea surface temperature mesoscale interactions on southern Africa austral summer climate. *International Journal of Climatology*, 38(12): 4651–4660. <https://doi.org/10.1002/joc.5726>.
- Desbiolles F, Howard E, Blamey RC, Barimalala R, Hart NCG, Reason CJC. 2020. Role of ocean mesoscale structures in shaping the Angola-Low pressure system and the southern Africa rainfall. *Climate Dynamics*. Springer Berlin Heidelberg, 54(7–8): 3685–3704. <https://doi.org/10.1007/s00382-020-05199-1>.
- Dieppois B, Pohl B, Crétat J, Eden J, Sidibe M, New M, Rouault M, Lawler D. 2019. Southern African summer-rainfall variability, and its teleconnections, on interannual to interdecadal timescales in CMIP5 models. *Climate Dynamics*. Springer Berlin Heidelberg, 53(5–6): 3505–3527. <https://doi.org/10.1007/s00382-019-04720-5>.
- Dieppois B, Pohl B, Rouault M, New M, Lawler D, Keenlyside N. 2016. Interannual to interdecadal variability of winter and summer southern African rainfall, and their teleconnections. *Journal of Geophysical Research*. <https://doi.org/10.1002/2015JD024576>.
- Dieppois B, Rouault M, New M. 2015. The impact of ENSO on Southern African rainfall in CMIP5 ocean atmosphere coupled climate models. *Climate Dynamics*, 45(9–10): 2425–2442. <https://doi.org/10.1007/s00382-015-2480-x>.
- Donald A, Meinke H, Power B, Maia A de HN, Wheeler MC, White N, Stone RC, Ribbe J. 2006. Near-global impact of the Madden-Julian Oscillation on rainfall. *Geophysical Research Letters*,

33(9): 6–9. <https://doi.org/10.1029/2005GL025155>.

Donat MG, Lowry AL, Alexander L V., O’Gorman PA, Maher N. 2016. More extreme precipitation in the world’s dry and wet regions. *Nature Climate Change*. <https://doi.org/10.1038/nclimate2941>.

Dosio A. 2017. Projection of temperature and heat waves for Africa with an ensemble of CORDEX Regional Climate Models. *Climate Dynamics*. Springer Verlag, 49(1–2): 493–519. <https://doi.org/10.1007/S00382-016-3355-5/FIGURES/15>.

Dyer TGJ, Tyson PD. 1977. Estimating Above and Below Normal Rainfall Periods over South Africa, 1972–2000. *Journal of Applied Meteorology*, 16(2): 145–147. [https://doi.org/10.1175/1520-0450\(1977\)016<0145:EAABNR>2.0.CO;2](https://doi.org/10.1175/1520-0450(1977)016<0145:EAABNR>2.0.CO;2).

Engelbrecht CJ, Engelbrecht FA, Dyson LL. 2013. High-resolution model-projected changes in mid-tropospheric closed-lows and extreme rainfall events over southern Africa. *International Journal of Climatology*, 33(1): 173–187. <https://doi.org/10.1002/joc.3420>.

Engelbrecht F, Adegoke J, Bopape MJ, Naidoo M, Garland R, Thatcher M, McGregor J, Katzfey J, Werner M, Ichoku C, Gatebe C. 2015. Projections of rapidly rising surface temperatures over Africa under low mitigation. *Environmental Research Letters*. IOP Publishing, 10(8): 085004. <https://doi.org/10.1088/1748-9326/10/8/085004>.

Engelbrecht FA, McGregor JL, Engelbrecht CJ. 2009. Dynamics of the Conformal-Cubic Atmospheric Model projected climate-change signal over southern Africa. *International Journal of Climatology*. John Wiley & Sons, Ltd, 29(7): 1013–1033. <https://doi.org/10.1002/JOC.1742>.

Fauchereau N, Pohl B, Reason CJC, Rouault M, Richard Y. 2009. Recurrent daily OLR patterns in the Southern Africa/Southwest Indian ocean region, implications for South African rainfall and teleconnections. *Climate Dynamics*, 32(4): 575–591. <https://doi.org/10.1007/s00382-008-0426-2>.

Favre A, Hewitson B, Lennard C, Cerezo-Mota R, Tadross M. 2013. Cut-off Lows in the South Africa region and their contribution to precipitation. *Climate Dynamics*, 41(9–10): 2331–2351. <https://doi.org/10.1007/s00382-012-1579-6>.

Favre A, Philippon N, Pohl B, Kalognomou EA, Lennard C, Hewitson B, Nikulin G, Dosio A, Panitz HJ, Cerezo-Mota R. 2016. Spatial distribution of precipitation annual cycles over South Africa in 10 CORDEX regional climate model present-day simulations. *Climate Dynamics*. Springer Berlin Heidelberg, 46(5–6): 1799–1818. <https://doi.org/10.1007/s00382-015-2677-z>.

Fitchett JM, Grab SW. 2014. A 66-year tropical cyclone record for south-east Africa: Temporal trends in a global context. *International Journal of Climatology*, 34(13): 3604–3615. <https://doi.org/10.1002/joc.3932>.

Frei C, Christensen JH, Déqué M, Jacob D, Jones RG, Vidale PL. 2003. Daily precipitation statistics in regional climate models: Evaluation and intercomparison for the European Alps. *Journal of Geophysical Research: Atmospheres*, 108(3): 1–19. <https://doi.org/10.1029/2002jd002287>.

Gascón E, Lavers D, Hamill TM, Richardson DS, Bouallègue ZB, Leutbecher M, Pappenberger F. 2019. Statistical postprocessing of dual-resolution ensemble precipitation forecasts across Europe. *Quarterly Journal of the Royal Meteorological Society*, 145(724): 3218–3235.

<https://doi.org/10.1002/qj.3615>.

Gitau W, Camberlin P, Ogallo L, Bosire E. 2018. Trends of intraseasonal descriptors of wet and dry spells over equatorial eastern africa. *International Journal of Climatology*, 38(3): 1189–1200. <https://doi.org/10.1002/joc.5234>.

Gitau W, Camberlin P, Ogallo L, Okoola R. 2015. Oceanic and atmospheric linkages with short rainfall season intraseasonal statistics over Equatorial Eastern Africa and their predictive potential. *International Journal of Climatology*, 35(9): 2382–2399. <https://doi.org/10.1002/joc.4131>.

Gitau W, Ogallo L, Camberlin P, Okoola R. 2013. Spatial coherence and potential predictability assessment of intraseasonal statistics of wet and dry spells over Equatorial Eastern Africa. *International Journal of Climatology*, 33(12): 2690–2705. <https://doi.org/10.1002/joc.3620>.

Goddard L, Baethgen WE, Bhojwani H, Robertson AW. 2014. The International Research Institute for Climate. *Earth Perspectives*, 1–14. <https://doi.org/https://doi.org/10.1186/2194-6434-1-10>.

Grimm AM. 2019. Madden–Julian Oscillation impacts on South American summer monsoon season: precipitation anomalies, extreme events, teleconnections, and role in the MJO cycle. *Climate Dynamics*. Springer Berlin Heidelberg, 53(1–2): 907–932. <https://doi.org/10.1007/s00382-019-04622-6>.

Grimm AM, Reason CJC. 2011. Does the South American Monsoon Influence African Rainfall? *Journal of Climate*. American Meteorological Society, 24(4): 1226–1238. <https://doi.org/10.1175/2010JCLI3722.1>.

Grimm AM, Reason CJC. 2015. Intraseasonal teleconnections between South America and South Africa. *Journal of Climate*, 28(23): 9489–9497. <https://doi.org/10.1175/JCLI-D-15-0116.1>.

Guan H, Zhu Y, Sinsky E, Fu B, Li W, Zhou X, Xue X, Hou D, Peng J, Nageswararao MM, Tallapragada V, Hamill TM, Whitaker JS, Bates G, Pegion P, Frederick S, Rosencrans M, Kumar A. 2022. GEFSv12 Reforecast Dataset for Supporting Subseasonal and Hydrometeorological Applications. *Monthly Weather Review*, 150(3): 647–665. <https://doi.org/10.1175/mwr-d-21-0245.1>.

Hamill TM, Bates GT, Whitaker JS, Murray DR, Fiorino M, Galarneau TJ, Zhu Y, Lapenta W. 2013. NOAA’s second-generation global medium-range ensemble reforecast dataset. *Bulletin of the American Meteorological Society*, 94(10): 1553–1565. <https://doi.org/10.1175/BAMS-D-12-00014.1>.

Hamill TM, Scheuerer M, Bates GT. 2015. Analog probabilistic precipitation forecasts using GEFS reforecasts and climatology-calibrated precipitation analyses. *Monthly Weather Review*, 143(8): 3300–3309. <https://doi.org/10.1175/MWR-D-15-0004.1>.

Hamill TM, Whitaker JS, Mullen SL. 2006. Reforecasts: An Important Dataset for Improving Weather Predictions. *Bulletin of the American Meteorological Society*. American Meteorological Society, 87(1): 33–46. <https://doi.org/10.1175/BAMS-87-1-33>.

Hamill TM, Whitaker JS, Shlyayeva A, Bates G, Fredrick S, Pegion P, Sinsky E, Zhu Y, Tallapragada V, Guan H, Zhou X, Woollen J. 2022. The Reanalysis for the Global Ensemble

Forecast System, Version 12. *Monthly Weather Review*. American Meteorological Society, 150(1): 59–79. <https://doi.org/10.1175/MWR-D-21-0023.1>.

Hamill TM, Whitaker JS, Wei X. 2004. Ensemble re-forecasting: Improving medium-range forecast skill using retrospective forecasts. *Bulletin of the American Meteorological Society*, 132(6): 1434–1447. [https://doi.org/https://doi.org/10.1175/1520-0493\(2004\)132<1434:ERIMFS>2.0.CO;2](https://doi.org/https://doi.org/10.1175/1520-0493(2004)132<1434:ERIMFS>2.0.CO;2).

Hart NCG, Reason CJC, Fauchereau N. 2010. Tropical-extratropical interactions over southern Africa: Three cases of heavy summer season rainfall. *Monthly Weather Review*, 138(7): 2608–2623. <https://doi.org/10.1175/2010MWR3070.1>.

Hart NCG, Reason CJC, Fauchereau N. 2013. Cloud bands over southern Africa: Seasonality, contribution to rainfall variability and modulation by the MJO. *Climate Dynamics*, 41(5–6): 1199–1212. <https://doi.org/10.1007/s00382-012-1589-4>.

Hersbach H, Bell B, Berrisford P, Hirahara S, Horányi A, Muñoz-Sabater J, Nicolas J, Peubey C, Radu R, Schepers D, Simmons A, Soci C, Abdalla S, Abellan X, Balsamo G, Bechtold P, Biavati G, Bidlot J, Bonavita M, De Chiara G, Dahlgren P, Dee D, Diamantakis M, Dragani R, Flemming J, Forbes R, Fuentes M, Geer A, Haimberger L, Healy S, Hogan RJ, Hólm E, Janisková M, Keeley S, Laloyaux P, Lopez P, Lupu C, Radnoti G, de Rosnay P, Rozum I, Vamborg F, Villaume S, Thépaut JN. 2020a. The ERA5 global reanalysis. *Quarterly Journal of the Royal Meteorological Society*, 146(730): 1999–2049. <https://doi.org/10.1002/qj.3803>.

Hersbach H, Bell B, Berrisford P, Hirahara S, Horányi A, Muñoz-Sabater J, Nicolas J, Peubey C, Radu R, Schepers D, Simmons A, Soci C, Abdalla S, Abellan X, Balsamo G, Bechtold P, Biavati G, Bidlot J, Bonavita M, De Chiara G, Dahlgren P, Dee D, Diamantakis M, Dragani R, Flemming J, Forbes R, Fuentes M, Geer A, Haimberger L, Healy S, Hogan RJ, Hólm E, Janisková M, Keeley S, Laloyaux P, Lopez P, Lupu C, Radnoti G, de Rosnay P, Rozum I, Vamborg F, Villaume S, Thépaut JN. 2020b. The ERA5 global reanalysis. *Quarterly Journal of the Royal Meteorological Society*. John Wiley & Sons, Ltd, 146(730): 1999–2049. <https://doi.org/10.1002/QJ.3803>.

Hoegh-Guldberg O, Jacob D, Taylor M, Bindi M, Abdul Halim S, Achlatis Australia M, Alexander L V, Allen MR, Berry P, Boyer C, Brilli L, Buckeridge M, Byers Austria E, Antonio Marengo Brazil J, Pereira J, Sherstyukov B, Jacob D, Taylor M, Bindi M, Brown S, Camilloni I, Diedhiou A, Djalante R, Ebi K, Engelbrecht F, Guiot J, Hijioka Y, Mehrotra S, Payne A, Seneviratne S, Thomas A, Warren R, Zhou G, Zhai P, Pörtner H, Roberts D, Skeea J, Shukla P, Pirani A, Moufouma-Okia W, Péan C, Pidcock R, Connors S, Matthews J, Chen Y, Zhou X, Gomis M, Lonnoy E, Maycock T, Tignor M, Waterfield T. 2018. *Impacts of 1.5°C global warming on natural and human systems*. .

Hoell A, Cheng L. 2018. Austral summer Southern Africa precipitation extremes forced by the El Niño–Southern oscillation and the subtropical Indian Ocean dipole. *Climate Dynamics*. Springer Berlin Heidelberg, 50(9–10): 3219–3236. <https://doi.org/10.1007/s00382-017-3801-z>.

Hoell A, Funk C, Magadzire T, Zinke J, Husak G. 2015. El Niño–Southern Oscillation diversity and Southern Africa teleconnections during Austral Summer. *Climate Dynamics*. Springer Berlin Heidelberg, 45(5–6): 1583–1599. <https://doi.org/10.1007/s00382-014-2414-z>.

- Hong S, Lim J. 2006. The WRF single-moment 6-class microphysics scheme (WSM6). *Journal of the Korean Meteorological Society*, 42(2): 129–151.
- Hong SY, Noh Y, Dudhia J. 2006. A New Vertical Diffusion Package with an Explicit Treatment of Entrainment Processes. *Monthly Weather Review*. American Meteorological Society, 134(9): 2318–2341. <https://doi.org/10.1175/MWR3199.1>.
- Huang B, Thorne PW, Banzon VF, Boyer T, Chepurin G, Lawrimore JH, Menne MJ, Smith TM, Vose RS, Zhang HM. 2017. Extended reconstructed Sea surface temperature, Version 5 (ERSSTv5): Upgrades, validations, and intercomparisons. *Journal of Climate*, 30(20): 8179–8205. <https://doi.org/10.1175/JCLI-D-16-0836.1>.
- Huffman GJ, Adler RF, Bolvin DT, Gu G, Nelkin EJ, Bowman KP, Hong Y, Stocker EF, Wolff DB. 2007. The TRMM Multisatellite Precipitation Analysis (TMPA): Quasi-global, multiyear, combined-sensor precipitation estimates at fine scales. *Journal of Hydrometeorology*, 8(1): 38–55. <https://doi.org/10.1175/JHM560.1>.
- Iacono MJ, Delamere JS, Mlawer EJ, Shephard MW, Clough SA, Collins WD. 2008. Radiative forcing by long-lived greenhouse gases: Calculations with the AER radiative transfer models. *Journal of Geophysical Research: Atmospheres*. John Wiley & Sons, Ltd, 113(D13): 13103. <https://doi.org/10.1029/2008JD009944>.
- IPCC. 2021. *Climate Change 2021: The Physical Science Basis. Contribution of Working Group I to the Sixth Assessment Report of the Intergovernmental Panel on Climate Change*. Cambridge University Press: Cambridge, United Kingdom and New York, NY, USA.
- Jackson LS, Finney DL, Kendon EJ, Marsham JH, Parker DJ, Stratton RA, Tomassini L, Tucker S. 2020. The effect of explicit convection on couplings between rainfall, humidity, and ascent over Africa under climate change. *Journal of Climate*, 33(19): 8315–8337. <https://doi.org/10.1175/JCLI-D-19-0322.1>.
- James R, Hart NCG, Munday C, Reason CJC, Washington R. 2020. Coupled climate model simulation of tropical–extratropical cloud bands over Southern Africa. *Journal of Climate*, 33(19): 8579–8602. <https://doi.org/10.1175/JCLI-D-19-0731.1>.
- Janjic ZI. 1994. The step-mountain eta coordinate model: further developments of the convection, viscous sublayer, and turbulence closure schemes. *Monthly Weather Review*, 122(5): 927–945. [https://doi.org/10.1175/1520-0493\(1994\)122<0927:TSMECM>2.0.CO;2](https://doi.org/10.1175/1520-0493(1994)122<0927:TSMECM>2.0.CO;2).
- Kain JS. 2004. The Kain–Fritsch Convective Parameterization: An Update. *Journal of Applied Meteorology and Climatology*, 43(1): 170–181. [https://doi.org/https://doi.org/10.1175/1520-0450\(2004\)043<0170:TKCPAU>2.0.CO;2](https://doi.org/https://doi.org/10.1175/1520-0450(2004)043<0170:TKCPAU>2.0.CO;2).
- Kalnay E, Kanamitsu M, Kistler R, Collins W, Deaven D, Gandin L, Iredell M, Saha S, White G, Woollen J, Zhu Y, Chelliah M, Ebisuzaki W, Higgins W, Janowiak J, Mo KC, Ropelewski C, Wang J, Leetmaa A, Reynolds R, Jenne R, Joseph D. 1996. The NCEP/NCAR 40-Year Reanalysis Project in: *Bulletin of the American Meteorological Society* Volume 77 Issue 3 (1996). *American Meteorological Society*, 77(3): 437–472.
- Kendall MG. 1957. *Rank Correlation Methods. 4th Edition*. Charles Griffin, London.
- Kendon EJ, Ban N, Roberts NM, Fowler HJ, Roberts MJ, Chan SC, Evans JP, Fosser G,

Wilkinson JM. 2017. Do convection-permitting regional climate models improve projections of future precipitation change? *Bulletin of the American Meteorological Society*, 98(1): 79–93. <https://doi.org/10.1175/BAMS-D-15-0004.1>.

Kendon EJ, Stratton RA, Tucker S, Marsham JH, Berthou S, Rowell DP, Senior CA. 2019. Enhanced future changes in wet and dry extremes over Africa at convection-permitting scale. *Nature Communications*. Springer US, 10(1). <https://doi.org/10.1038/s41467-019-09776-9>.

Kharin V V., Zwiers FW, Zhang X, Hegerl GC. 2007. Changes in Temperature and Precipitation Extremes in the IPCC Ensemble of Global Coupled Model Simulations. *Journal of Climate*. American Meteorological Society, 20(8): 1419–1444. <https://doi.org/10.1175/JCLI4066.1>.

Kruger AC. 2018. Africa and the Paris Agreement. *Nature Climate Change*. Springer US, 8(5): 365–366. <https://doi.org/10.1038/s41558-018-0146-5>.

Kruger AC, Nxumalo MP. 2017. Historical rainfall trends in South Africa: 1921–2015. *Water SA*, 43(2): 285–297. <https://doi.org/10.4314/wsa.v43i2.12>.

Kusangaya S, Warburton ML, Archer van Garderen E, Jewitt GPW. 2014. Impacts of climate change on water resources in southern Africa: A review. *Physics and Chemistry of the Earth, Parts A/B/C*. Pergamon, 67–69: 47–54. <https://doi.org/10.1016/J.PCE.2013.09.014>.

Lakhraj-Govender R, Grab SW. 2019. Rainfall and river flow trends for the Western Cape Province, South Africa. *South African Journal of Science*, 115(9–10): 1–6. <https://doi.org/10.17159/sajs.2019/6028>.

Lazenby MJ, Todd MC, Chadwick R, Wang Y. 2018. Future Precipitation Projections over Central and Southern Africa and the Adjacent Indian Ocean: What Causes the Changes and the Uncertainty? *Journal of Climate*. American Meteorological Society, 31(12): 4807–4826. <https://doi.org/10.1175/JCLI-D-17-0311.1>.

Li C, Zwiers F, Zhang X, Li G, Sun Y, Wehner M. 2021. Changes in Annual Extremes of Daily Temperature and Precipitation in CMIP6 Models. *Journal of Climate*. American Meteorological Society, 34(9): 3441–3460. <https://doi.org/10.1175/JCLI-D-19-1013.1>.

Li W, Zhu Y, Zhou X, Hou D, Sinsky E, Melhauser C, Peña M, Guan H, Wobus R. 2019. Evaluating the MJO prediction skill from different configurations of NCEP GEFS extended forecast. *Climate Dynamics*. Springer Verlag, 52(7–8): 4923–4936. <https://doi.org/10.1007/S00382-018-4423-9/FIGURES/12>.

Liu W, Lim WH, Sun F, Mitchell D, Wang H, Chen D, Bethke I, Shiogama H, Fischer E. 2018a. Global Freshwater Availability Below Normal Conditions and Population Impact Under 1.5 and 2 °C Stabilization Scenarios. *Geophysical Research Letters*. John Wiley & Sons, Ltd, 45(18): 9803–9813. <https://doi.org/10.1029/2018GL078789>.

Liu W, Sun F, Ho Lim W, Zhang J, Wang H, Shiogama H, Zhang Y. 2018b. Global drought and severe drought-Affected populations in 1.5 and 2 °C warmer worlds. *Earth System Dynamics*. Copernicus GmbH, 9(1): 267–283. <https://doi.org/10.5194/ESD-9-267-2018>.

Lu E, Zhao W, Zou X, Ye D, Zhao C, Zhang Q. 2017. Temporal-spatial monitoring of an extreme precipitation event: Determining simultaneously the time period it lasts and the geographic region it affects. *Journal of Climate*, 30(16): 6123–6132.

<https://doi.org/10.1175/JCLI-D-17-0105.1>.

Lyon B, Mason SJ. 2007. The 1997-98 summer rainfall season in Southern Africa. Part I: Observations. *Journal of Climate*, 20(20): 5134–5148. <https://doi.org/10.1175/JCLI4225.1>.

Ma LM, Tan ZM. 2009. Improving the behavior of the cumulus parameterization for tropical cyclone prediction: Convection trigger. *Atmospheric Research*. Elsevier B.V., 92(2): 190–211. <https://doi.org/10.1016/j.atmosres.2008.09.022>.

Macron C, Pohl B, Richard Y, Bessafi M. 2014. How do tropical temperate troughs form and develop over Southern Africa? *Journal of Climate*, 27(4): 1633–1647. <https://doi.org/10.1175/JCLI-D-13-00175.1>.

Macron C, Richard Y, Garot T, Bessafi M, Pohl B, Ratiarison A, Razafindrabe A. 2016. Intraseasonal rainfall variability over Madagascar. *Monthly Weather Review*, 144(5): 1877–1885. <https://doi.org/10.1175/MWR-D-15-0077.1>.

Madden RA, Julian PR. 1994. Observations of the 40-50-day tropical oscillation - a review. *Monthly Weather Review*. [https://doi.org/10.1175/1520-0493\(1994\)122<0814:OOTDTP>2.0.CO;2](https://doi.org/10.1175/1520-0493(1994)122<0814:OOTDTP>2.0.CO;2).

Malherbe J, Dieppois B, Maluleke P, Van Staden M, Pillay DL. 2016. South African droughts and decadal variability. *Natural Hazards*. Springer Netherlands, 80(1): 657–681. <https://doi.org/10.1007/s11069-015-1989-y>.

Malherbe J, Engelbrecht FA, Landman WA, Engelbrecht CJ. 2012. Tropical systems from the southwest Indian Ocean making landfall over the Limpopo River Basin southern Africa: A historical perspective. *International Journal of Climatology*, 32(7): 1018–1032. <https://doi.org/10.1002/joc.2320>.

Malherbe J, Landman WA, Engelbrecht FA. 2014. The bi-decadal rainfall cycle, Southern Annular Mode and tropical cyclones over the Limpopo River Basin, southern Africa. *Climate Dynamics*, 42(11–12): 3121–3138. <https://doi.org/10.1007/s00382-013-2027-y>.

Manhique AJ, Reason CJC, Rydberg L, Fauchereau N. 2011. ENSO and Indian Ocean sea surface temperatures and their relationships with tropical temperate troughs over Mozambique and the Southwest Indian Ocean. *International Journal of Climatology*, 31(1): 1–13. <https://doi.org/10.1002/joc.2050>.

Mann H. 1945. Mann Nonparametric test against trend. *Econometrica*.

Maraun D. 2016. Bias Correcting Climate Change Simulations - a Critical Review. *Current Climate Change Reports*. Current Climate Change Reports, 2(4): 211–220. <https://doi.org/10.1007/s40641-016-0050-x>.

Mason SJ, Goddard L, Graham NE, Yulaeva E, Sun L, Arkin PA. 1999. The IRI seasonal climate prediction system. *WRPMD 1999: Preparing for the 21st Century*. [https://doi.org/10.1061/40430\(1999\)4](https://doi.org/10.1061/40430(1999)4).

Mason SJ, Joubert AM. 1997. Simulated changes in extreme rainfall over southern Africa. *International Journal of Climatology*, 17(3): 291–301. [https://doi.org/10.1002/\(sici\)1097-0088\(19970315\)17:3<291::aid-joc120>3.3.co;2-t](https://doi.org/10.1002/(sici)1097-0088(19970315)17:3<291::aid-joc120>3.3.co;2-t).

- Mason SJ, Jury MR. 1997. Climatic variability and change over southern Africa: a reflection on underlying processes. *Progress in Physical Geography: Earth and Environment*, 21(1): 23–50. <https://doi.org/10.1177/030913339702100103>.
- Masupha TE, Moeletsi ME, Tsubo M. 2016. Dry spells assessment with reference to the maize crop in the Luvuvhu River catchment of South Africa. *Physics and Chemistry of the Earth*. <https://doi.org/10.1016/j.pce.2015.10.014>.
- Maure G, Pinto I, Ndebele-Murisa M, Muthige M, Lennard C, Nikulin G, Dosio A, Meque A. 2018. The southern African climate under 1.5 °C and 2 °C of global warming as simulated by CORDEX regional climate models. *Environmental Research Letters*. IOP Publishing, 13(6): 065002. <https://doi.org/10.1088/1748-9326/AAB190>.
- McKittrick R, Christy J. 2018. A Test of the Tropical 200- to 300-hPa Warming Rate in Climate Models. *Earth and Space Science*. Wiley-Blackwell Publishing Ltd, 5(9): 529–536. <https://doi.org/10.1029/2018EA000401>.
- Misra V. 2003. The influence of Pacific SST variability on the precipitation over southern Africa. *Journal of Climate*, 16(14): 2408–2418. <https://doi.org/10.1175/2785.1>.
- Moron V, Camberlin P, Robertson AW. 2013. Extracting subseasonal scenarios: An alternative method to analyze seasonal predictability of regional-scale tropical rainfall. *Journal of Climate*, 26(8): 2580–2600. <https://doi.org/10.1175/JCLI-D-12-00357.1>.
- Morrison H, Thompson G, Tatarskii V. 2009. Impact of Cloud Microphysics on the Development of Trailing Stratiform Precipitation in a Simulated Squall Line: Comparison of One- and Two-Moment Schemes. *Monthly Weather Review*. American Meteorological Society, 137(3): 991–1007. <https://doi.org/10.1175/2008MWR2556.1>.
- Mpungose N, Thoithi W, Blamey RC, Reason CJC. 2022. Extreme rainfall events in southeastern Africa during the summer. *Theoretical and Applied Climatology*. Springer Vienna, 150(1–2): 185–201. <https://doi.org/10.1007/s00704-022-04162-w>.
- Muller CJ, O’Gorman PA, Back LE. 2011. Intensification of Precipitation Extremes with Warming in a Cloud-Resolving Model. *Journal of Climate*. American Meteorological Society, 24(11): 2784–2800. <https://doi.org/10.1175/2011JCLI3876.1>.
- Nangombe S, Zhou T, Zhang W, Wu B, Hu S, Zou L, Li D. 2018. Record-breaking climate extremes in Africa under stabilized 1.5 °c and 2 °c global warming scenarios. *Nature Climate Change*, 8(5): 375–380. <https://doi.org/10.1038/s41558-018-0145-6>.
- Ndarana T, Lekoloane LE, Rammopo TS, Reason CJC, Bopape M-JM, Chikoore H, Engelbrecht FA. 2022. *Downstream development associated with two types of ridging South Atlantic Ocean anticyclones over South Africa*. *Weather and Climate Dynamics Discussions*.
- Nicholson S. 2003. Comments on “The South Indian convergence zone and interannual rainfall variability over southern Africa” and the question of ENSO’s influence on southern Africa. *Journal of Climate*, 16(3): 555–562. [https://doi.org/10.1175/1520-0442\(2003\)016<0555:COTSIC>2.0.CO;2](https://doi.org/10.1175/1520-0442(2003)016<0555:COTSIC>2.0.CO;2).
- Nicholson SE, Kim J. 1997. THE RELATIONSHIP OF THE EL NIÑO–SOUTHERN OSCILLATION TO AFRICAN RAINFALL. *International Journal of Climatology*, 17(2): 117–

135. [https://doi.org/10.1002/\(SICI\)1097-0088\(199702\)17:2<117::AID-JOC84>3.0.CO;2-O](https://doi.org/10.1002/(SICI)1097-0088(199702)17:2<117::AID-JOC84>3.0.CO;2-O).

Oettli P, Tozuka T, Izumo T, Engelbrecht FA, Yamagata T. 2014. The self-organizing map, a new approach to apprehend the Madden-Julian Oscillation influence on the intraseasonal variability of rainfall in the southern African region. *Climate Dynamics*, 43(5–6): 1557–1573. <https://doi.org/10.1007/s00382-013-1985-4>.

Otto FEL, Wolski P, Lehner F, Tebaldi C, Van Oldenborgh GJ, Hogesteegeer S, Singh R, Holden P, Fučkar NS, Odoulami RC, New M. 2018. Anthropogenic influence on the drivers of the Western Cape drought 2015-2017. *Environmental Research Letters*, 13(12). <https://doi.org/10.1088/1748-9326/aae9f9>.

Oueslati B, Pohl B, Moron V, Rome S, Janicot S. 2017. Characterization of heat waves in the Sahel and associated physical mechanisms. *Journal of Climate*, 30(9): 3095–3115. <https://doi.org/10.1175/JCLI-D-16-0432.1>.

Paciorek CJ, Stone DA, Wehner MF. 2018. Quantifying statistical uncertainty in the attribution of human influence on severe weather. *Weather and Climate Extremes*, 20(June 2017): 69–80. <https://doi.org/10.1016/j.wace.2018.01.002>.

Pascale S, Pohl B, Kapnick SB, Zhang H. 2019. On the Angola low interannual variability and its role in modulating ENSO effects in southern Africa. *Journal of Climate*, 32(15): 4783–4803. <https://doi.org/10.1175/JCLI-D-18-0745.1>.

Philippon N, Camberlin P, Moron V, Boyard-Micheau J. 2015. Anomalously wet and dry rainy seasons in Equatorial East Africa and associated differences in intra-seasonal characteristics. *Climate Dynamics*. Springer Berlin Heidelberg, 45(7–8): 2101–2121. <https://doi.org/10.1007/s00382-014-2460-6>.

Pinto I, Lennard C, Tadross M, Hewitson B, Dosio A, Nikulin G, Panitz HJ, Shongwe ME. 2016. Evaluation and projections of extreme precipitation over southern Africa from two CORDEX models. *Climatic Change*, 135(3–4): 655–668. <https://doi.org/10.1007/s10584-015-1573-1>.

Pohl B, Crétat J, Camberlin P. 2011. Testing WRF capability in simulating the atmospheric water cycle over Equatorial East Africa. *Climate Dynamics*, 37(7–8): 1357–1379. <https://doi.org/10.1007/s00382-011-1024-2>.

Pohl B, Dieppois B, Crétat J, Lawler D, Rouault M. 2018. From synoptic to interdecadal variability in southern African rainfall: Toward a unified view across time scales. *Journal of Climate*, 31(15): 5845–5872. <https://doi.org/10.1175/JCLI-D-17-0405.1>.

Pohl B, Fauchereau N. 2012. The southern annular mode seen through weather regimes. *Journal of Climate*, 25(9): 3336–3354. <https://doi.org/10.1175/JCLI-D-11-00160.1>.

Pohl B, Fauchereau N, Reason CJC, Rouault M. 2010. Relationships between the Antarctic oscillation, the Madden-Julian oscillation, and ENSO, and consequences for rainfall analysis. *Journal of Climate*, 23(2): 238–254. <https://doi.org/10.1175/2009JCLI2443.1>.

Pohl B, Fauchereau N, Richard Y, Rouault M, Reason CJC. 2009. Interactions between synoptic, intraseasonal and interannual convective variability over Southern Africa. *Climate Dynamics*, 33(7–8): 1033–1050. <https://doi.org/10.1007/s00382-008-0485-4>.

- Pohl B, MacRon C, Monerie PA. 2017. Fewer rainy days and more extreme rainfall by the end of the century in Southern Africa. *Scientific Reports*. Nature Publishing Group, 7(April): 6–12. <https://doi.org/10.1038/srep46466>.
- Pohl B, Richard Y, Fauchereau N. 2007. Influence of the Madden-Julian oscillation on southern African summer rainfall. *Journal of Climate*, 20(16): 4227–4242. <https://doi.org/10.1175/JCLI4231.1>.
- Pohl B, Rouault M, Roy S Sen. 2014. Simulation of the annual and diurnal cycles of rainfall over South Africa by a regional climate model. *Climate Dynamics*, 43(7–8): 2207–2226. <https://doi.org/10.1007/s00382-013-2046-8>.
- Pomposi C, Funk C, Shukla S, Harrison L, Magadzire T. 2018. Distinguishing southern Africa precipitation response by strength of El Niño events and implications for decision-making. *Environmental Research Letters*, 13(7). <https://doi.org/10.1088/1748-9326/aacc4c>.
- Puaud Y, Pohl B, Fauchereau N, Macron C, Beltrando G. 2017. Climate co-variability between South America and Southern Africa at interannual, intraseasonal and synoptic scales. *Climate Dynamics*. Springer Verlag, 48(11–12): 4029–4050. <https://doi.org/10.1007/S00382-016-3318-X/FIGURES/13>.
- Quagraine KA, Hewitson B, Jack C, Pinto I, Lennard C. 2019. A methodological approach to assess the co-behavior of climate processes over Southern Africa. *Journal of Climate*, 32(9): 2483–2495. <https://doi.org/10.1175/JCLI-D-18-0689.1>.
- Ranasinghe. 2021. Chapter 12: Climate change information for regional impact and for risk assessment. *Climate Change 2021: The Physical Science Basis. Contribution of Working Group I to the Sixth Assessment Report of the Intergovernmental Panel on Climate Change*, (August 2021): 351–364.
- Rapolaki RS, Blamey RC, Hermes JC, Reason CJC. 2019. A classification of synoptic weather patterns linked to extreme rainfall over the Limpopo River Basin in southern Africa. *Climate Dynamics*. Springer Berlin Heidelberg, 53(3–4): 2265–2279. <https://doi.org/10.1007/s00382-019-04829-7>.
- Rapolaki RS, Blamey RC, Hermes JC, Reason CJC. 2020. Moisture sources associated with heavy rainfall over the Limpopo River Basin, southern Africa. *Climate Dynamics*. Springer Berlin Heidelberg, 55(5–6): 1473–1487. <https://doi.org/10.1007/s00382-020-05336-w>.
- Ratan R, Venugopal V. 2013. Wet and dry spell characteristics of global tropical rainfall. *Water Resources Research*, 49(6): 3830–3841. <https://doi.org/10.1002/wrcr.20275>.
- Ratna SB, Ratnam J V., Behera SK, Rautenbach CJ d. W, Ndarana T, Takahashi K, Yamagata T. 2014. Performance assessment of three convective parameterization schemes in WRF for downscaling summer rainfall over South Africa. *Climate Dynamics*, 42(11–12): 2931–2953. <https://doi.org/10.1007/s00382-013-1918-2>.
- Ratnam J V., Behera SK, Masumoto Y, Yamagata T. 2014. Remote effects of El Niño and Modoki events on the austral summer precipitation of Southern Africa. *Journal of Climate*, 27(10): 3802–3815. <https://doi.org/10.1175/JCLI-D-13-00431.1>.
- Ratnam J V., Behera SK, Ratna SB, De Rautenbach CJW, Lennard C, Luo JJ, Masumoto Y,

Takahashi K, Yamagata T. 2013. Dynamical Downscaling of Austral Summer Climate Forecasts over Southern Africa Using a Regional Coupled Model. *Journal of Climate*, 26(16): 6015–6032. <https://doi.org/10.1175/JCLI-D-12-00645.1>.

Reason CJC. 2001. Subtropical Indian Ocean SST dipole events and southern African rainfall. *Geophysical Research Letters*. <https://doi.org/10.1029/2000GL012735>.

Reason CJC. 2007. Tropical cyclone Dera, the unusual 2000/01 tropical cyclone season in the South West Indian Ocean and associated rainfall anomalies over Southern Africa. *Meteorology and Atmospheric Physics*, 97(1–4): 181–188. <https://doi.org/10.1007/s00703-006-0251-2>.

Reason CJC, Allan RJ, Lindesay JA, Ansell TJ. 2000. Enso and climatic signals across the Indian Ocean basin in the global context: Part I, Interannual composite patterns. *International Journal of Climatology*, 20(11): 1285–1327. [https://doi.org/10.1002/1097-0088\(200009\)20:11<1285::AID-JOC536>3.0.CO;2-R](https://doi.org/10.1002/1097-0088(200009)20:11<1285::AID-JOC536>3.0.CO;2-R).

Reason CJC, Jagadheesha D. 2005. A model investigation of recent ENSO impacts over southern Africa. *Meteorology and Atmospheric Physics*, 89(1–4): 181–205. <https://doi.org/10.1007/s00703-005-0128-9>.

Reason CJC, Keibel A. 2004. Tropical Cyclone Eline and its unusual penetration and impacts over the Southern Africa mainland. *Weather and Forecasting*, 19(5): 789–805. [https://doi.org/10.1175/1520-0434\(2004\)019<0789:TCEAIU>2.0.CO;2](https://doi.org/10.1175/1520-0434(2004)019<0789:TCEAIU>2.0.CO;2).

Reason CJC, Landman W, Tennant W. 2006. Seasonal to decadal prediction of southern African climate and its links with variability of the Atlantic ocean. *Bulletin of the American Meteorological Society*, 87(7): 941–955. <https://doi.org/10.1175/BAMS-87-7-941>.

Reason CJC, Rouault M. 2002. ENSO-like decadal variability and South African rainfall. *Geophysical Research Letters*, 29(13): 1638. <https://doi.org/10.1029/2002GL014663>.

Rouault M, Florenchie P, Fauchereau N, Reason CJC. 2003. South East tropical Atlantic warm events and southern African rainfall. *Geophysical Research Letters*, 30(5): 1–4. <https://doi.org/10.1029/2002GL014840>.

Rouault M, Richard Y. 2004. Intensity and spatial extension of drought in South Africa at different time scales. *Water SA*, 29(4): 489–500. <https://doi.org/10.4314/wsa.v29i4.5057>.

Rouault M, White SA, Reason CJC, Lutjeharms JRE, Jobard I. 2002. Ocean-atmosphere interaction in the Agulhas Current region and a South African extreme weather event. *Weather and Forecasting*. [https://doi.org/10.1175/1520-0434\(2002\)017<0655:OAIITA>2.0.CO;2](https://doi.org/10.1175/1520-0434(2002)017<0655:OAIITA>2.0.CO;2).

Russo S, Marchese AF, Sillmann J, Immé G. 2016. When will unusual heat waves become normal in a warming Africa? *Environmental Research Letters*. IOP Publishing, 11(5). <https://doi.org/10.1088/1748-9326/11/5/054016>.

Scaife AA, Camp J, Comer R, Davis P, Dunstone N, Gordon M, MacLachlan C, Martin N, Nie Y, Ren HL, Roberts M, Robinson W, Smith D, Vidale PL. 2019. Does increased atmospheric resolution improve seasonal climate predictions? *Atmospheric Science Letters*, 20(8): 1–10. <https://doi.org/10.1002/asl.922>.

Senior CA, Marsham JH, Berthou S, Burgin LE, Folwell SS, Kendon EJ, Klein CM, Jones RG,

Mittal N, Rowell DP, Tomassini L, Vischel T, Becker B, Birch CE, Crook J, Dougill AJ, Finney DL, Graham RJ, Hart NCG, Jack CD, Jackson LS, James R, Koelle B, Misiani H, Mwalukanga B, Parker DJ, Stratton RA, Taylor CM, Tucker SO, Wainwright CM, Washington R, Willet MR. 2021. Convection-permitting regional climate change simulations for understanding future climate and informing decision-making in Africa. *Bulletin of the American Meteorological Society*, 102(6): E1206–E1223. <https://doi.org/10.1175/BAMS-D-20-0020.1>.

Sheshadri A, Borrus M, Yoder M, Robinson T. 2021. Midlatitude Error Growth in Atmospheric GCMs: The Role of Eddy Growth Rate. *Geophysical Research Letters*, 48(23): 1–7. <https://doi.org/10.1029/2021GL096126>.

Shongwe ME, Van Oldenborgh GJ, Van Den Hurk BJM, De Boer B, Coelho CAS, Van Aalst MK. 2009. Projected changes in mean and extreme precipitation in Africa under global warming. Part I: Southern Africa. *Journal of Climate*, 22(13): 3819–3837. <https://doi.org/10.1175/2009JCLI2317.1>.

Silvério KC, Grimm AM. 2022. Southern African monsoon: intraseasonal variability and monsoon indices. *Climate Dynamics*. Springer Berlin Heidelberg, 58(3–4): 1193–1220. <https://doi.org/10.1007/s00382-021-05954-y>.

Skamarock WC., Klemp JB, Dudhia JB, Gill DO, Barker DM, Duda MG, Huang X-Y., Wang W, Powers JG. 2021. A Description of the Advanced Research WRF Model Version 4.3. *NCAR Technical Note*, (July): 1–165. <https://doi.org/http://dx.doi.org/10.5065/1dfh-6p97>.

Spinoni J, Barbosa P, Bucchignani E, Cassano J, Cavazos T, Cescatti A, Christensen JH, Christensen OB, Coppola E, Evans JP, Forzieri G, Geyer B, Giorgi F, Jacob D, Katzfey J, Koenigk T, Laprise R, Lennard CJ, Kurnaz ML, Li D, Llopart M, McCormick N, Naumann G, Nikulin G, Ozturk T, Panitz HJ, da Rocha RP, Solman SA, Syktus J, Tangang F, Teichmann C, Vautard R, Vogt J V., Winger K, Zittis G, Dosio A. 2021. Global exposure of population and land-use to meteorological droughts under different warming levels and SSPs: A CORDEX-based study. *International Journal of Climatology*, 41(15): 6825–6853. <https://doi.org/10.1002/joc.7302>.

Spinoni J, Barbosa P, De Jager A, McCormick N, Naumann G, Vogt J V., Magni D, Masante D, Mazzeschi M. 2019. A new global database of meteorological drought events from 1951 to 2016. *Journal of Hydrology: Regional Studies*. Elsevier, 22: 100593. <https://doi.org/10.1016/J.EJRH.2019.100593>.

Stauffer DR, Seaman NL. 1994. Multiscale four-dimensional data assimilation. *Journal of Applied Meteorology*, 33(3): 416–434. [https://doi.org/10.1175/1520-0450\(1994\)033<0416:MFDDA>2.0.CO;2](https://doi.org/10.1175/1520-0450(1994)033<0416:MFDDA>2.0.CO;2).

Sun Q, Zhang X, Zwiers F, Westra S, Alexander L V. 2021. A global, continental, and regional analysis of changes in extreme precipitation. *Journal of Climate*, 34(1): 243–258. <https://doi.org/10.1175/JCLI-D-19-0892.1>.

Tennant WJ, Hewitson BC. 2002. Intra-seasonal rainfall characteristics and their importance to the seasonal prediction problem. *International Journal of Climatology*, 22(9): 1033–1048. <https://doi.org/10.1002/joc.778>.

Thoithi W, Blamey RC, Reason CJC. 2020. Dry spell frequencies, wet day counts and their

trends across southern Africa during the summer rainy season. *Geophysical Research Letters*, 48(5): 1–22. <https://doi.org/10.1029/2020GL091041>.

Todd M, Washington R. 1999. Circulation anomalies associated with tropical-temperate troughs in southern Africa and the south west Indian Ocean. *Climate Dynamics*, 15(12): 937–951. <https://doi.org/10.1007/s003820050323>.

Todd MC, Washington R, Palmer PI. 2004. Water vapour transport associated with tropical-temperate trough systems over southern Africa and the southwest Indian Ocean. *International Journal of Climatology*, 24(5): 555–568. <https://doi.org/10.1002/joc.1023>.

Tyson PD. 1981. Atmospheric circulation variations and the occurrence of extended wet and dry spells over Southern Africa. *Journal of Climatology*, 1(2): 115–130. <https://doi.org/10.1002/joc.3370010203>.

Ukkola AM, De Kauwe MG, Roderick ML, Abramowitz G, Pitman AJ. 2020. Robust Future Changes in Meteorological Drought in CMIP6 Projections Despite Uncertainty in Precipitation. *Geophysical Research Letters*. John Wiley & Sons, Ltd, 47(11): e2020GL087820. <https://doi.org/10.1029/2020GL087820>.

Ullah A, Pohl B, Pergaud J, Dieppois B, Rouault M. 2022. Intraseasonal descriptors and extremes in South African rainfall. Part I: Summer climatology and statistical characteristics. *International Journal of Climatology*. John Wiley & Sons, Ltd, 42(9): 4538–4563. <https://doi.org/10.1002/JOC.7489>.

Usman MT, Reason CJC. 2004. Dry spell frequencies and their variability over southern Africa. *Climate Research*, 26(3): 199–211. <https://doi.org/10.3354/cr026199>.

Van Heerden J, Terblanche DE, Schulze GC. 1988. The southern oscillation and South African summer rainfall. *Journal of Climatology*, 8(6): 577–597. <https://doi.org/10.1002/joc.3370080603>.

Vigaud N, Pohl B, Cr  tat J. 2012. Tropical-temperate interactions over southern Africa simulated by a regional climate model. *Climate Dynamics*, 39(12): 2895–2916. <https://doi.org/10.1007/s00382-012-1314-3>.

Washington R, Preston A. 2006. Extreme wet years over southern Africa: Role of Indian Ocean sea surface temperatures. *Journal of Geophysical Research: Atmospheres*. John Wiley & Sons, Ltd, 111(D15): 15104. <https://doi.org/10.1029/2005JD006724>.

Washington R, Todd M. 1999. Tropical-temperate links in southern African and Southwest Indian Ocean satellite-derived daily rainfall. *International Journal of Climatology*. [https://doi.org/10.1002/\(SICI\)1097-0088\(19991130\)19:14<1601::AID-JOC407>3.0.CO;2-0](https://doi.org/10.1002/(SICI)1097-0088(19991130)19:14<1601::AID-JOC407>3.0.CO;2-0).

Wheeler MC, Hendon HH. 2004. An all-season real-time multivariate MJO index: Development of an index for monitoring and prediction. *Monthly Weather Review*, 132(8): 1917–1932. [https://doi.org/10.1175/1520-0493\(2004\)132<1917:AARMMI>2.0.CO;2](https://doi.org/10.1175/1520-0493(2004)132<1917:AARMMI>2.0.CO;2).

WMO. 2021. *WMO Atlas of Mortality and Economic Losses from Weather, Climate and Water Extremes (1970–2019)* (WMO-No. 1267). WMO: Geneva.

Xulu NG, Chikoore H, Bopape MJM, Nethengwe NS. 2020. Climatology of the Mascarene High and Its Influence on Weather and Climate over Southern Africa. *Climate 2020, Vol. 8, Page 86*.

Multidisciplinary Digital Publishing Institute, 8(7): 86. <https://doi.org/10.3390/CLI8070086>.

Yuan X, Wang L, Wood EF. 2018. Anthropogenic Intensification of Southern African Flash Droughts as Exemplified by the 2015/16 Season. *Bulletin of the American Meteorological Society*. American Meteorological Society, 99(1): S86–S90. <https://doi.org/10.1175/BAMS-D-17-0077.1>.

Zhang C. 2005. Madden-Julian Oscillation. *Reviews of Geophysics*. John Wiley & Sons, Ltd, 43(2): 1–36. <https://doi.org/10.1029/2004RG000158>.

Zhang F, Qiang Sun Y, Magnusson L, Buizza R, Lin SJ, Chen JH, Emanuel K. 2019. What is the predictability limit of midlatitude weather? *Journal of the Atmospheric Sciences*, 76(4): 1077–1091. <https://doi.org/10.1175/JAS-D-18-0269.1>.

Zhao T, Dai A. 2017. Uncertainties in historical changes and future projections of drought. Part II: model-simulated historical and future drought changes. *Climatic Change*. Springer Netherlands, 144(3): 535–548. <https://doi.org/10.1007/S10584-016-1742-X/FIGURES/6>.

Figures and Tables: Chapter 4

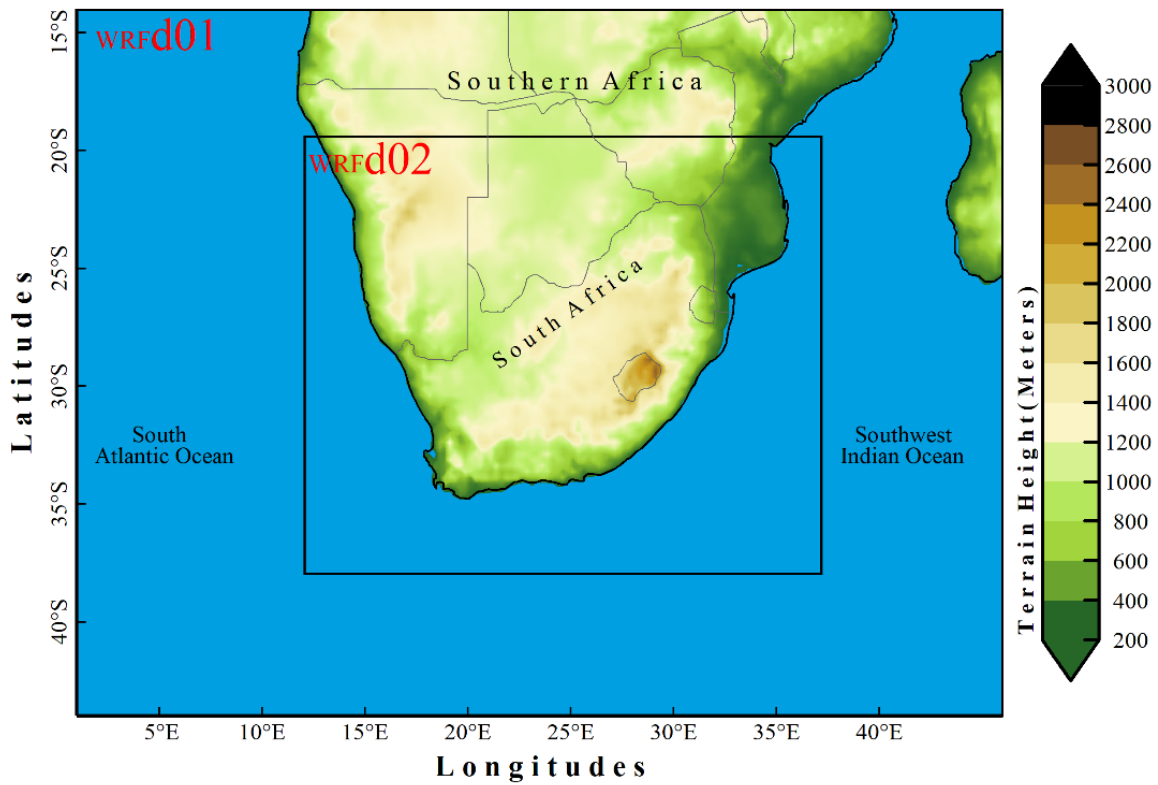


Figure 1. Model nested domains with resolutions of 9 km (d01) and 3 km (d02) in the WRF with topography in the background.

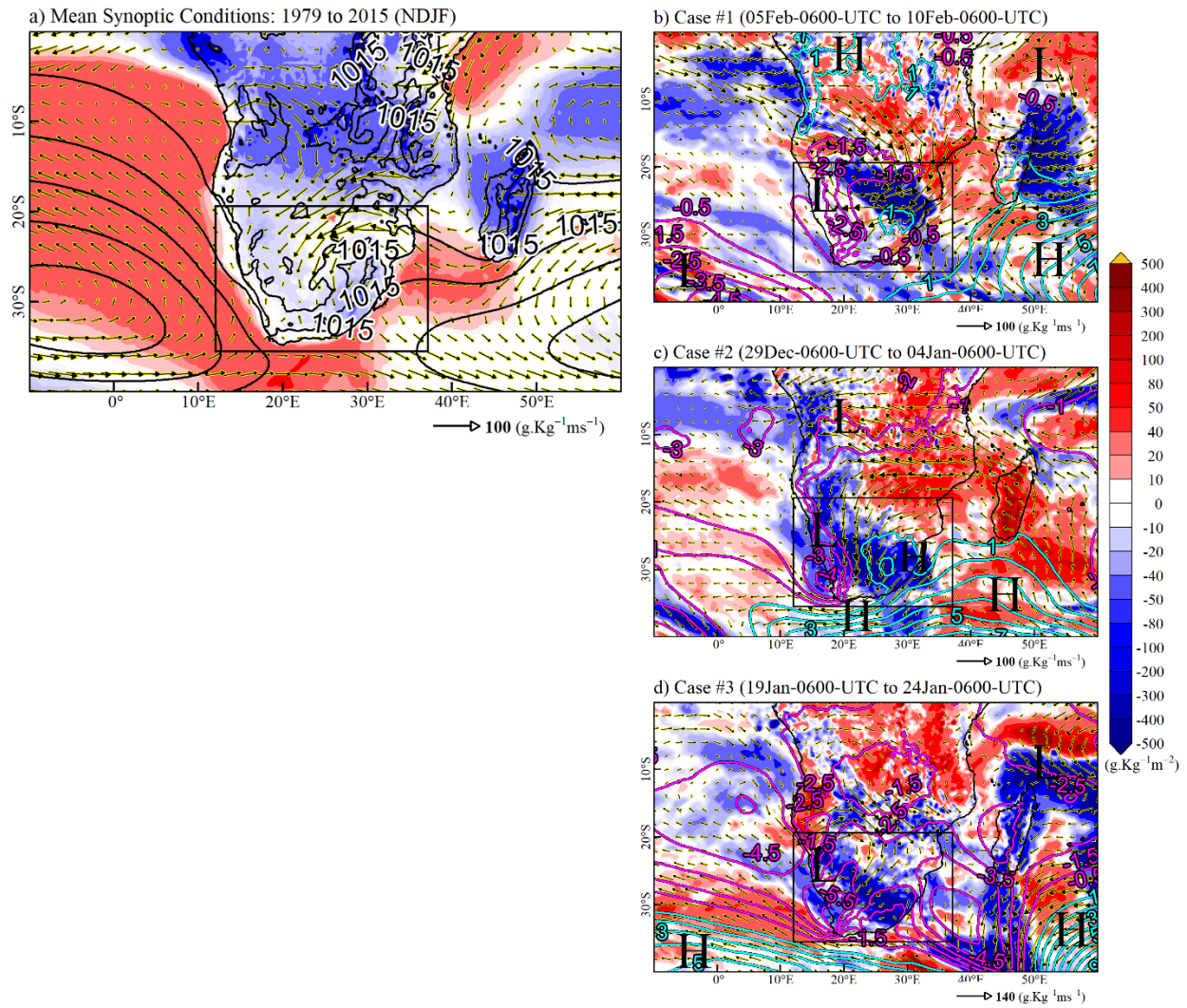


Figure 2. Mean atmospheric conditions over southern Africa with adjacent southern Atlantic Ocean and the SWIO during November through February (a), composite anomalies of vertically integrated moisture divergence (VIMD: filled contours), low-tropospheric moisture flux (850 hPa: wind barbs) and mean sea level pressure (interval 2 hpa: black contours) for cases #1 to #3 (b-d). The anomalies are calculated with respect to the climatology of NDJF from 1979 to 2015 using ERA5 reanalysis.

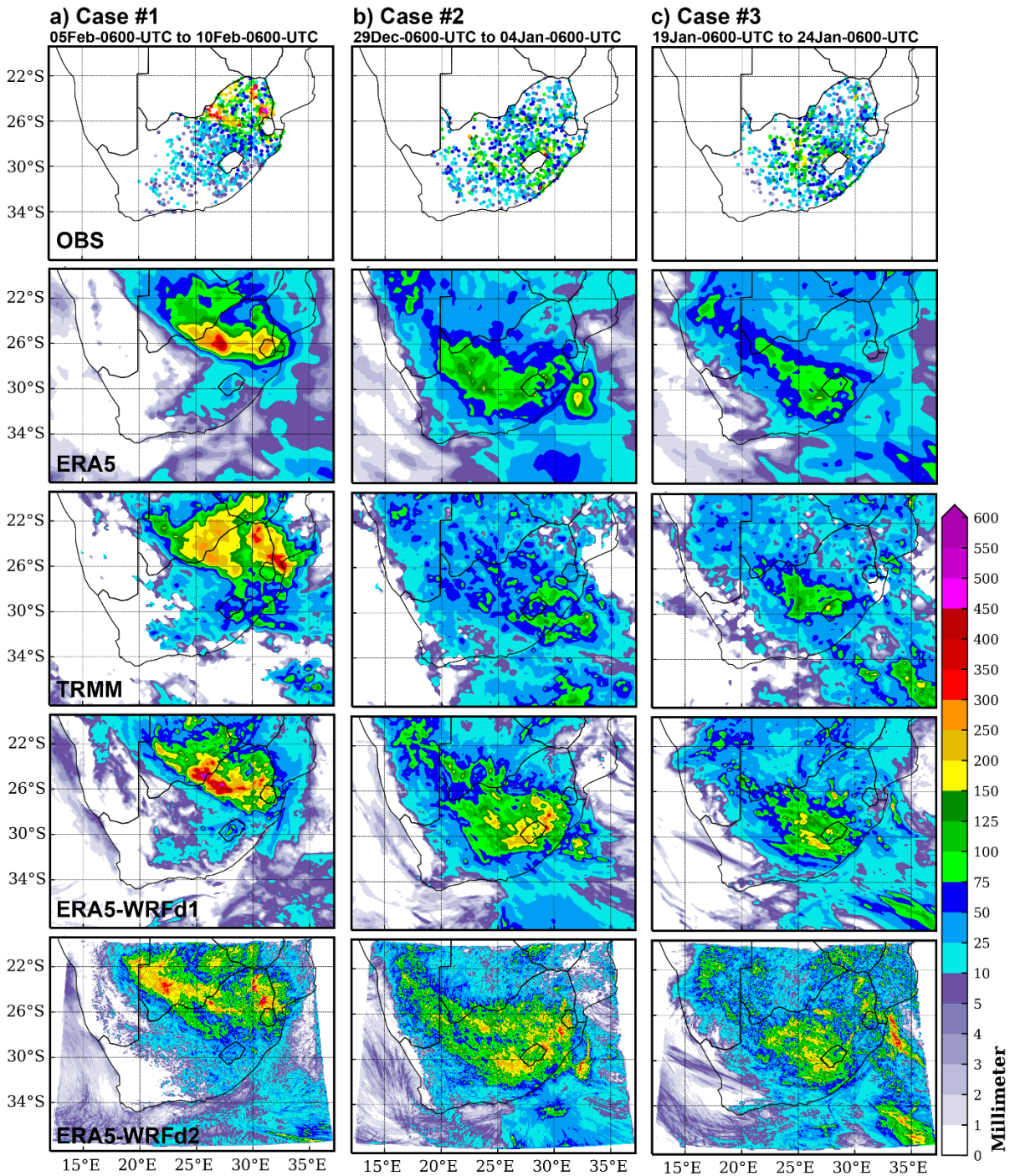


Figure 3. Total accumulated rainfall during case #1 (a), case #2 (b) and case #3 (c) as computed for OBS, ERA5, TRMM, WRFd1 and WRFd2 distributed row-wise from top to bottom respectively. For OBS, only those stations are shown that received above 1.0 millimeters of rainfall on the respective day of the event.

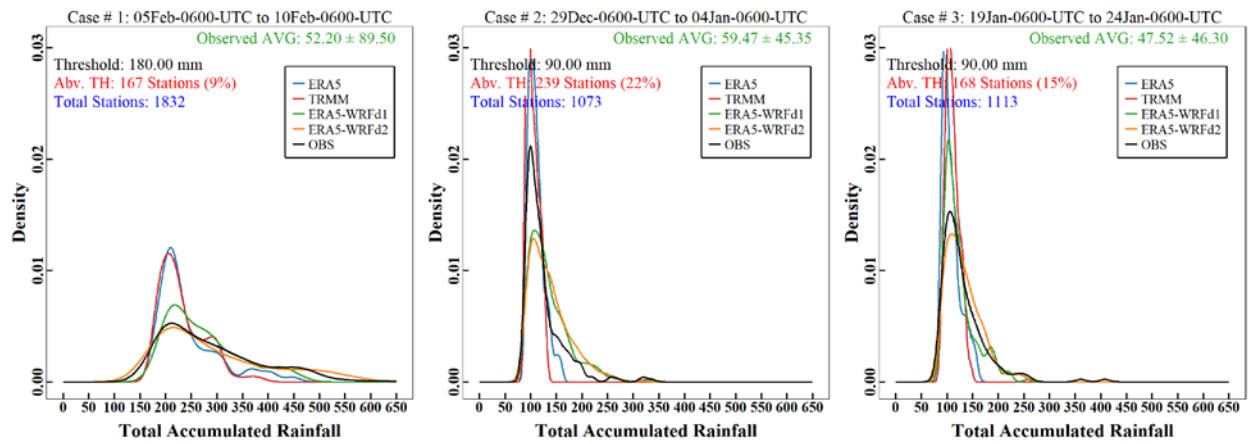


Figure 4. The normalized PDFs of total accumulated rainfall as shown by OBS, ERA5, TRMM, WRFd1 and WRFd2 for all cases #1, #2 and #2 distributed column-wise from left to right respectively.

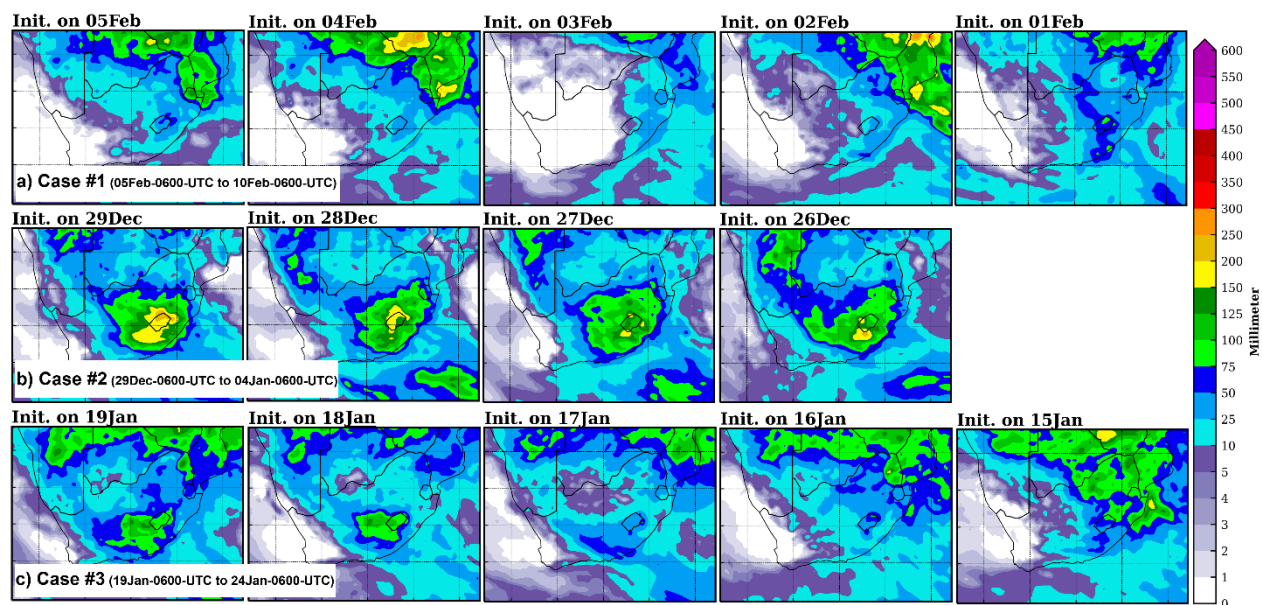


Figure 5. Total rainfall accumulation in raw RF2 grids using the ensemble mean for case #1 (a), case #2 (b) and case #3 (c) with lead times depending on the duration of the event (distributed row-wise left to right).

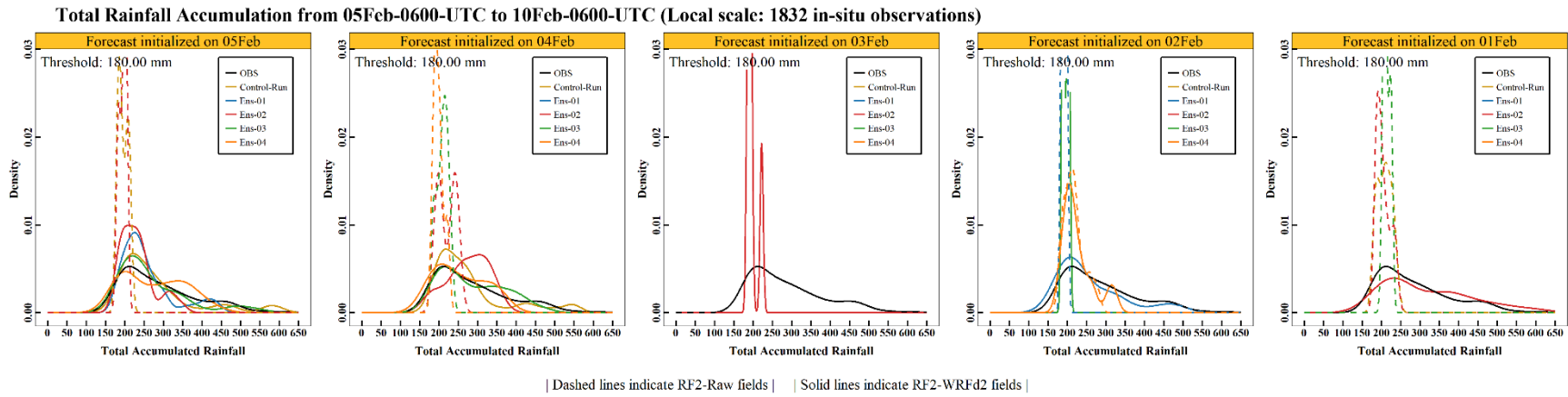


Figure 6. The normalized PDFs of total accumulated rainfall in case #1 as shown by OBS, raw RF2 and RF2-WRFd2 for one control run and four ensemble members distributed from left to right for each forecast initialization date. In each panel, dashed lines indicate raw RF2 fields while solid lines represent RF2-WRFd2.

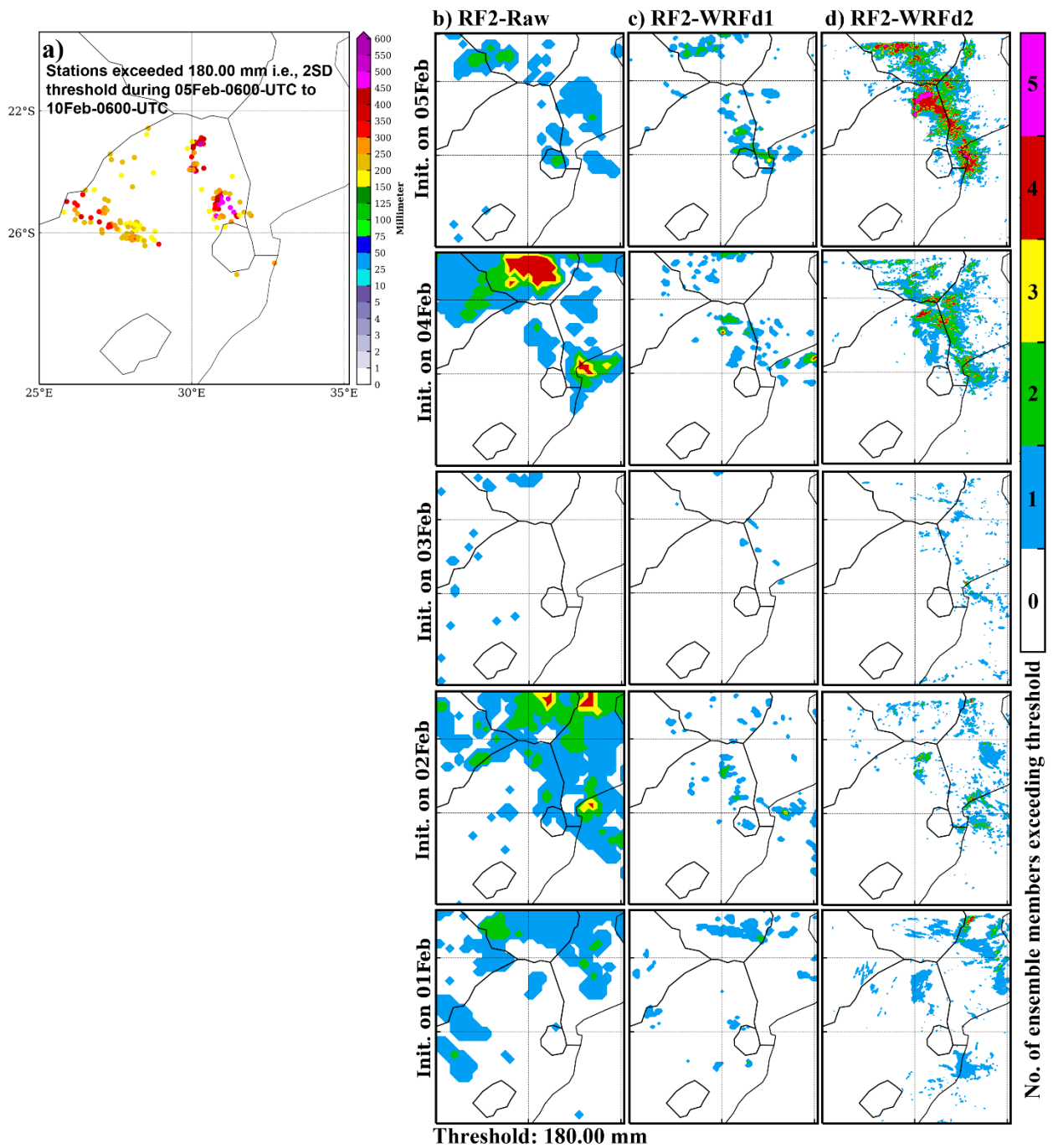


Figure 7. Spatial distribution of stations exceeded 180 mm threshold of total rainfall accumulation during case #1 (a), probability of ensemble members exceeding the threshold for raw RF2 (b), for RF2-WRFd1 (c) and RF2-WRFd2 (d) distributed row-wise from top to bottom with respect to the forecast initialization date.

Tables

Table 1. List of large-scale long-lived rainfall spells between 1999–2015 identified by 225 in-situ observations as in Ullah et al 2023.

Date	Season	OLR Regime	MJO Phase	MJO Amplitude	Average Intensity (Millimetre)					Average spatial fraction > 90th Percentile (%)				
					OBS	ERA5-NN	ERA5-AGP	TRMM-NN	TRMM-AGP	OBS	ERA5-NN	ERA5-AGP	TRMM-NN	TRMM-AGP
a) Case #1 (05Feb2000-0600-UTC to 10Feb2000-0600-UTC)														
02/06/2000	1999-00	5	NA	0.79	134.72	44.99	33.27	82.04	68.34	12.00	13.33	17.91	12.44	14.13
02/07/2000	1999-00	5	NA	0.96	65.43	41.41	37.42	62.12	51.95	13.78	18.22	19.57	21.33	16.56
02/08/2000	1999-00	5	NA	0.96	56.31	46.05	42.42	60.58	52.96	7.56	14.22	15.51	15.11	19.65
02/09/2000	1999-00	5	NA	0.70	48.70	48.60	48.19	33.05	34.22	11.56	16.00	15.45	15.11	14.39
02/10/2000	1999-00	5	NA	0.56	50.44	43.05	40.32	49.04	40.85	10.67	15.11	15.75	10.22	13.86
b) Case #2 (29Dec2010-0600-UTC to 04Jan2011-0600-UTC)														
12/30/2010	2010-11	3	NA	0.43	50.41	25.49	27.26	34.57	34.32	12.89	10.67	12.49	4.89	5.58
12/31/2010	2010-11	3	NA	0.62	42.69	23.79	22.59	32.02	27.09	16.44	39.56	30.09	22.22	15.70
01/01/2011	2010-11	4	NA	0.71	44.64	30.49	27.76	31.41	29.27	14.22	49.78	37.85	7.56	7.16
01/02/2011	2010-11	3	NA	0.91	52.09	20.69	20.70	31.96	40.13	10.22	25.33	24.49	5.78	8.28
01/03/2011	2010-11	3	NA	0.88	43.23	20.86	20.36	31.58	34.74	9.33	29.33	26.22	8.00	8.28
01/04/2011	2010-11	3	NA	0.64	38.52	21.53	20.32	30.51	25.38	8.44	20.44	18.52	3.11	7.29
c) Case #3 (19Jan2011-0600-UTC to 24Jan2011-0600-UTC)														
01/20/2011	2010-11	3	7	2.43	51.26	18.45	19.29	38.92	40.13	8.44	3.56	3.82	14.22	11.17
01/21/2011	2010-11	3	7	2.59	53.78	24.50	23.02	31.43	31.46	18.22	23.11	14.58	20.00	11.43
01/22/2011	2010-11	4	7	2.54	43.55	26.86	26.33	33.15	35.13	17.78	48.00	38.09	22.22	17.15
01/23/2011	2010-11	2	7	2.49	59.16	22.88	24.34	41.39	38.81	10.22	23.11	27.14	12.00	14.59
01/24/2011	2010-11	2	8	2.17	44.58	24.82	24.92	27.09	23.16	8.44	27.11	20.68	1.33	1.05

The first two columns represent the date (mm/dd/yyyy) and season of the spell. Columns 3–5 represent the OLR regime, phase, and amplitude of MJO. Columns 6–10 (11–15) show the average intensity (spatial fraction) corresponding to each day of the event by NN and AGP fields of OBS, ERA5 and TRMM.

Table 2. Summary of datasets used in this study.

Dataset	Description	Members	Acronym	Field	Usage	Reference
Station based observations	Quality controlled in-situ observations (1832, 1073 and 1113 for case #1, #2 and #3 respectively)		OBS		Reference dataset for model evaluation	http://www.wrc.org.za
ERA5	State-of-the-art ERA5 reanalysis	Deterministic member	ERA5	NN and AGP	Reference dataset for model evaluation and as forcing for WRF	(Hersbach <i>et al.</i> , 2020b)
TRMM-3B42	Satellite		TRMM	NN and AGP	Reference dataset for model evaluation	(Huffman <i>et al.</i> , 2007)
GEFS Reforecast	Raw forecasts from GEFS Reforecast	One control run and four ensemble members	RF2-Raw	NN and AGP	Forcing dataset for WRF	(Hamill <i>et al.</i> , 2022)
Weather Research and Forecasting Model	When WRF initialized by using ERA5 as forcings	One control run and four ensemble members	ERA5-WRFd1 and ERA5-WRFd2	NN and AGP	Model for downscaling reanalysis and reforecasts	(Skamarock <i>et al.</i> , 2021)
	When WRF initialized by using Reforecast as forcings		RF2-WRFd1 and RF2-WRFd2	NN and AGP		

NN and AGP fields correspond to the nearest to neighbour and all-grid-point fields of the respective dataset in the 3.0km domain of WRF

Table 3. Summary of major parameterization schemes use to run WRF simulations for the study.

Parameterization	Scheme	Usage	Acronym	Reference
Cumulus parameterization	Betts Miller and Janjic scheme	Domain 01	BMJ	(Betts and Miller, 1986)
Microphysics parameterization	WRF Single-moment 6-class scheme	Domain 01 and 02	WSM6	(Hong and Lim, 2006)
Radiation (Long and short wave)	Rapid Radiative Transfer Model	Domain 01 and 02	RRTM	(Iacono <i>et al.</i> , 2008)
Planetary boundary layer	Yonsei University scheme	Domain 01 and 02	YSU	(Hong <i>et al.</i> , 2006)

Table 4. WRF initialization setup for RF2.

Case #1 (05Feb-0600-UTC to 10Feb-0600-UTC)																	
Lead Time		Days of the Event															
Model Initialization Date	1st day of event									<i>Init. On</i>	05 Feb	06 Feb	07 Feb	08 Feb	09 Feb	10 Feb	
	1 day before								<i>Init. On</i>	04 Feb	05 Feb	06 Feb	07 Feb	08 Feb	09 Feb	10 Feb	
	2 days before							<i>Init. On</i>	03 Feb	04 Feb	05 Feb	06 Feb	07 Feb	08 Feb	09 Feb	10 Feb	
	3 days before						<i>Init. On</i>	02 Feb	03 Feb	04 Feb	05 Feb	06 Feb	07 Feb	08 Feb	09 Feb	10 Feb	
	4 days before					<i>Init. On</i>	01 Feb	02 Feb	03 Feb	04 Feb	05 Feb	06 Feb	07 Feb	08 Feb	09 Feb	10 Feb	
	5 days before				<i>Init. On</i>	31 Jan	01 Feb	02 Feb	03 Feb	04 Feb	05 Feb	06 Feb	07 Feb	08 Feb	09 Feb		
	6 days before			<i>Init. On</i>	30 Jan	31 Jan	01 Feb	02 Feb	03 Feb	04 Feb	05 Feb	06 Feb	07 Feb	08 Feb			
	7 days before		<i>Init. On</i>	29 Jan	30 Jan	31 Jan	01 Feb	02 Feb	03 Feb	04 Feb	05 Feb	06 Feb	07 Feb				
	8 days before	<i>Init. On</i>	28 Jan	29 Jan	30 Jan	31 Jan	01 Feb	02 Feb	03 Feb	04 Feb	05 Feb	06 Feb					
Case #2 (29Dec2010-0600-UTC to 04Jan2011-0600-UTC)																	
Model Initialization Date	1st day of event									<i>Init. On</i>	29 Dec	30 Dec	31 Dec	01 Jan	02 Jan	03 Jan	04 Jan
	1 day before								<i>Init. On</i>	28 Dec	29 Dec	30 Dec	31 Dec	01 Jan	02 Jan	03 Jan	04 Jan
	2 days before							<i>Init. On</i>	27 Dec	28 Dec	29 Dec	30 Dec	31 Dec	01 Jan	02 Jan	03 Jan	04 Jan
	3 days before						<i>Init. On</i>	26 Dec	27 Dec	28 Dec	29 Dec	30 Dec	31 Dec	01 Jan	02 Jan	03 Jan	04 Jan
	4 days before					<i>Init. On</i>	25 Dec	26 Dec	27 Dec	28 Dec	29 Dec	30 Dec	31 Dec	01 Jan	02 Jan	03 Jan	
	5 days before				<i>Init. On</i>	24 Dec	25 Dec	26 Dec	27 Dec	28 Dec	29 Dec	30 Dec	31 Dec	01 Jan	02 Jan		
	6 days before			<i>Init. On</i>	23 Dec	24 Dec	25 Dec	26 Dec	27 Dec	28 Dec	29 Dec	30 Dec	31 Dec	01 Jan			
	7 days before		<i>Init. On</i>	22 Dec	23 Dec	24 Dec	25 Dec	26 Dec	27 Dec	28 Dec	29 Dec	30 Dec	31 Dec				
	8 days before	<i>Init. On</i>	21 Dec	22 Dec	23 Dec	24 Dec	25 Dec	26 Dec	27 Dec	28 Dec	29 Dec	30 Dec					
Case #3 (18Jan2011-0600-UTC to 23Jan2011-0600-UTC)																	
Model Initialization Date	1st day of event									<i>Init. On</i>	18 Jan	19 Jan	20 Jan	21 Jan	22 Jan	23 Jan	
	1 day before								<i>Init. On</i>	19 Jan	18 Jan	19 Jan	20 Jan	21 Jan	22 Jan	23 Jan	
	2 days before							<i>Init. On</i>	18 Jan	19 Jan	18 Jan	19 Jan	20 Jan	21 Jan	22 Jan	23 Jan	
	3 days before						<i>Init. On</i>	17 Jan	18 Jan	19 Jan	18 Jan	19 Jan	20 Jan	21 Jan	22 Jan	23 Jan	
	4 days before					<i>Init. On</i>	16 Jan	17 Jan	18 Jan	19 Jan	18 Jan	19 Jan	20 Jan	21 Jan	22 Jan	23 Jan	
	5 days before				<i>Init. On</i>	15 Jan	16 Jan	17 Jan	18 Jan	19 Jan	18 Jan	19 Jan	20 Jan	21 Jan	22 Jan		
	6 days before			<i>Init. On</i>	14 Jan	15 Jan	16 Jan	17 Jan	18 Jan	19 Jan	18 Jan	19 Jan	20 Jan	21 Jan			
	7 days before		<i>Init. On</i>	13 Jan	14 Jan	15 Jan	16 Jan	17 Jan	18 Jan	19 Jan	18 Jan	19 Jan	20 Jan				
	8 days before	<i>Init. On</i>	12 Jan	13 Jan	14 Jan	15 Jan	16 Jan	17 Jan	18 Jan	19 Jan	18 Jan	19 Jan					

The model is initialized at 0600-UTC. The days of the event assessed in the study are shown in bold and italic

Supplementary Tables: Chapter 4

Table S1. Three-stage verification for WRF experimental design.

Stage 1			
<i>Nudging and time steps</i>			
Without nudging		With nudging*	
1-hour	6-hour	1-hour	6-hour*
Stage 2			
<i>Cumulus parameterization schemes and spin-up time</i>			
Betts-Miller-Janjic scheme* (BMJ)	Kain-Fritsch scheme (KF)	Kain-Fritsch scheme with trigger function (KFtr)	
1-day spin-up*	1 day spin up	1 day spin up	
2 days spin-up	2 days spin up	2 days spin up	
3 days spin-up	3 days spin up	3 days spin up	
4 days spin-up	4 days spin up	4 days spin up	
Stage 3			
<i>Microphysics parameterization schemes</i>			
WRF Single-moment 6-class scheme* (WSM6)		Morrison 2-moment scheme (MOR)	

Selected parameters in each stage are shown with bold and asterisk

General Conclusions

This dissertation is aimed to provide a better and deeper understanding of intraseasonal variability of rainfall over South Africa where focus is given to extreme rainfall spells.

Chapter 2 is devoted to examining the average characteristics of wet and dry intraseasonal descriptors in South Africa during the austral summer season from 1979 to 2015. Using observations and ERA5 reanalysis, extreme rainfall events are characterized into two types, according to their spatial fraction, disentangling large-scale and small-scale extreme events. *“The spatial fraction of an extreme event is defined as the number of stations or grid-points that simultaneously reach their local 90th percentile threshold regardless of their location on the day of the event”*. *For the first time in a region-wide study, large- and small-scales of extremes are explicitly assessed in the definition of intraseasonal descriptors*. The results demonstrate that using *a threshold of 7% network density as base criterion and as a metric for the spatial fraction produces good quality results in characterizing rainfall extremes over the region*. The 7% threshold used to differentiate large- vs small scale events is found not only relevant for the observational network, but also for nearest neighbour grid-points of ERA5. An investigation is then carried out to examine the spatial coherence of such extremes. *We find that large-scale extremes are well-organized and spatially coherent in nature*. By contrast, small-scale extreme events, which might be related to mesoscale convective complexes, are highly localized in space and prevail largely over the north-eastern parts of SA. *Summer SA rainfall is found to be primarily associated with large-scale extremes, which account for more than half of the seasonal amount in in-situ observations, and nearly half of it in ERA5*. The occurrence of large-scale extremes during summer is on average 8 ± 5 days which is comprised in 5 ± 3 spells with an average persistence of at least 2 days as confirmed by observations. This suggest that only 4 to 5 spells in a season contribute more than half of the total seasonal rainfall amount. *These statistics highlights the critical importance of such extremes for the region on one hand and the usefulness of characterizing such events on the other hand*.

Chapter 3 is dedicated to investigate the variability of two types of rainfall extremes, first at interannual (IV: 2–8 years) and quasi-decadal (QDV: 8–13 years) timescales of variability, which are associated with ENSO and IPO, respectively (Dieppo *et al.*, 2016, 2019; Pohl *et al.*, 2018). To that end, large- and small-scale extremes are assessed first by establishing their

teleconnections with global Sea Surface Temperature (SSTs). *We find that La Niña conditions favour overall wet conditions in South Africa, including an increased occurrence of rainfall extremes while the number of days associated with large-scale extremes and contribution of total rainfall is related to warmer SSTs in the North Atlantic.* The relationship with warmer Indian Ocean and tropical South Atlantic appears as statistically independent of the state of ENSO. *The contribution of large- and small-scale extremes to total rainfall is greater during El Niño, in spite of generally drier conditions during these seasons.* These results are consistent with previous studies that identified significant associations between Southern African rainfall and SST changes in the Pacific (Dieppois *et al.*, 2016, 2019) the southern Indian Ocean (Hoell and Cheng, 2018) and the Atlantic Ocean (Pomposi *et al.*, 2018; Rapolaki *et al.*, 2019, 2020). We complement these studies by assessing how these teleconnections also modify the occurrence of rainfall extremes, with a distinction made between small-scale and large-scale events. Such analyses are meant to better identify their large-scale drivers. In chapter 3 we also attempt to quantify the changes in the occurrence of extremes through risk ratio assessment. At low frequencies (IV and QDV), a risk ratio assessment suggests that the probability of extremes varies with the varying magnitude of IV and QDV timescales, primarily associated with ENSO and IPO respectively. *At the IV timescale, the number of large-scale extremes and the total rainfall associated with small-scale extremes are much more frequent when this timescale lies in a strong positive phase. During these strong positive IV seasons, we note a 400% rise in the probability of large-scale extremes as compared to the strong negative IV seasons.* This is consistent with the strong La Niña episodes in the Pacific SSTs, where interannual variations play a primary role in shaping rainfall variability in South Africa. No substantial increment in the risk ratio is noted when computed for the strong positive phase of the QDV timescale with respect to its strong negative phase. *The results suggest that that the whole statistical distribution of daily rainfall extremes is strongly related to rainfall variations at the IV timescale and weak but significant with QDV timescale.*

Chapter 3 is further dedicated to the assessment of large- and small-scale extremes at sub-seasonal (synoptic and intraseasonal) timescales. Before the assessment of extremes at sub-seasonal timescales, *we attempt to complement the typology of with the duration statistics to provide a more comprehensive and novel framework to identify potentially high-impact*

extreme rainfall events using spatial fraction of such events, as literature provides no clear definition for such events. Like in most of the studies, extremes were assessed by considering overall rainfall field. At sub-seasonal timescales the rainfall variability is related to short-lived disturbances either related to tropical convection, mid-latitude dynamics or interactions between both (Fauchereau *et al.*, 2009; Hart *et al.*, 2013; Macron *et al.*, 2014, 2016) and to the regional influence of the Madden-Julien Oscillation (Pohl *et al.*, 2007; Oettli *et al.*, 2014). *At the sub-seasonal timescales, days associated with large-scale events occur largely during the synoptic regimes describing the precursors and then the mature phases of continental TTT systems.* Small-scale extremes are nearly equiprobable during all regimes. *In terms of intraseasonal variability, dry, moderate and wet MJO are three coherent and homogeneous groups which are respectively associated with weak, moderate and high numbers of both types of extremes for South African rainfall.* Previous studies suggested that the intensity of TTT events (that is, their corresponding rainfall amounts) is increased during phase #6 and decreased in phase #1, even though TTT occurrence is not statistically modified by MJO phases (Hart *et al.*, 2013). *Our results related to continental TTTs corroborate the results found in the literature and extend them to rainfall extremes.*

Chapter 4 focused on the meso-scale modelling of large-scale long-lived event. *In such type of events large-scale extreme conditions prevail over a larger region and persist longer thereby responsible to produce high impact to the society.* Extreme rainfall spell during February 2000 is then selected as a case study for further investigation in terms of predictability where WRF is used at 9km and 3km horizontal resolution to drive simulations by using NOAA's Reforecast version 2 (RF2) as lateral forcing with a forecasting lead time up to 9 days. The major objective was to assess if large-scale long-lived events (like the cases under consideration) are predictable in raw RF2 and if WRF can improve the predictability of such events few days in advance. RF2 raw field reproduced skilfully the rainfall pattern, thereby suggesting a considerable performance to use it as a forcing to downscale it using WRF. The maximum rainfall during the highest intensity day of the event is well simulated by WRF at the 3km domain as compared to raw RF2 grids up to 7 to 8 days lead time however with some uncertainties between ensemble members. Further analysis is yet to be conducted to evaluate the biases, uncertainties, and associated dynamics. *Preliminary results of downscaling of three case studies first by using ERA5 as*

forcing and then by using RF2 suggest that: 1) convection permitting downscaling can improve the quality of the forcing and the experimental setup of WRF is reliable for such type of event; 2) such major events are predictable using raw RF2 forecasts, and the predictability of such event can be substantially improved by downscaling using WRF in terms of intensity, timing, location and total event rainfall accumulation.

Future Perspectives

Hydrometeorological extremes (i.e., droughts and heavy rainfall events) are a matter of crucial importance for human systems. The scope of this study was to investigate rainfall extremes; however, similar methodology can be used to identify and then investigate long dry spells. In this study, we characterize the extremes based on daily extremes spatial fraction thus an index is produced which can be termed as **“Extreme Spatial Fraction Index (ESFI)”**. This index can be used in further studies. For instance, in chapter 3 we left some open questions concerning combined influence of synoptic-scale and intraseasonal variability of the MJO. The extreme spatial fraction index can be used to identify the extremes and conveniently assess the dynamics of the extremes either with or without the MJO influence. Although, localized extreme events have a less contribution in total seasonal amount of rainfall but these extreme events are highly localized in space but possess the ability to bring devastating impacts on human life and infrastructure. These localized events or other types of events are now conveniently identifiable by using the methodology defined in chapter 3 or by simply using the **“Intraseasonal Calendar of Rainfall Extremes”**.

This study investigates the intraseasonal variability of rainfall extremes separately at low-frequency and sub-seasonal timescales. However, these timescales can be considered together in further studies in order to analyse climate variability according to a real continuum of scales. This would include climate change, with expected changes in the rainfall extremes due to the Clausius-Clapeyron scaling relating air temperature to its humidity (Betts and Harshvardhan, 1987; Kharin *et al.*, 2007; Muller *et al.*, 2011; Pohl *et al.*, 2017). The interdecadal timescale could also modify the changes in the intensity and occurrence of rainfall extremes, from one decade to another, thereby influencing the changes that region will experience in the coming decades. Observational datasets may be too short to perform such analyses of slowly changing

modes of variability or mechanisms, hence the need for long model simulations. However, current climate models are mostly based on parameterized atmospheric convection, and convection-permitting simulations may be needed to better ascertain the influence of interdecadal variability on rainfall extremes (Kendon *et al.*, 2017, 2019; Jackson *et al.*, 2020; Senior *et al.*, 2021). The question of their seamless predictability is also important because these events may be considered as those more likely to lead to strong impacts (Goddard *et al.*, 2014). Hence the need to develop a seamless prediction tool for rainfall extremes, and more generally, high impact events over Southern Africa and even Africa as a whole.

According to the global Climate Risk Index (CRI, 2021) developed by Germanwatch, South Africa lies among the top 30 countries which are highly vulnerable to climate change and extreme weather events. There is a growing demand from policymakers for more robust climate information of several interrelated aspects of extremes to aid in decision making for adaptation. The climate varies across a range of temporal and spatial scales from local daily weather to global climate change in a manner that appears seamless; even specific climate phenomena or certain processes may act on specific time and spatial scales. The concept of “*seamless forecast*” came from a report of the World Climate Research Programme, where the weather-climate prediction problem was considered as seamless because the atmosphere knows no barriers in time scales. This suggest that the decision and policy makers have responsibilities at multiple space and/or time scales thereby they also need up-to-date climate information at all timescales, from weather, to interannual and decadal (Mason *et al.*, 1999; Goddard *et al.*, 2014).

This study provides a profound knowledge of rainfall extremes in various dimensions as well as at various timescales, for instance: **Chapter 2** provides the first presentation of a detailed mapping of rainfall variability over South Africa, including large- and small-scale extreme events, as well as non-extreme rainfall contribution thereby have an immediate and considerable implications for theoretical and applied climate variability-based studies. The regional climate information provided here is supportive for the local agencies to have a better understanding of different types of rainfall extremes and how much rainfall they bring.

The extensive characterization of rainfall extremes carried out in **Chapter 3** at low-frequency (interannual and decadal) and sub-seasonal timescales (synoptic and intraseasonal) are crucial in promoting long-term multi-year seamless forecasts for the region on one hand, and sub-seasonal

forecasts on the other hand. For instance, it is well understood that El Niño Southern Oscillation (ENSO) have substantial influence on climate variability in southern Africa where El Niño found to be associated with below normal rainfall whereas La Niña is associated with above average rainfall. During the past decades, the prediction of El Niño has made great progress and skilful forecasts thus, if the state of the ocean is known we can predict and/or estimate the number of extremes in a season using the quantifications provided in this study. At sub-seasonal timescales, the Madden-Julian Oscillation, which is the dominant component of the intraseasonal variability in the tropical atmosphere, has been found to have a predictive limit of about 2 weeks, but now can be predicted up to 3 weeks ahead using coupled ocean-atmosphere models. Thus, by embedding the information provided in this study with the forecast of such leading modes, the policy makers may plan a better framework for adaptation.

Chapter 4 focus on the weather phenomena by providing the dynamical downscaling perspective of high-impact rainfall spells in the region. Reforecasting of such high-impact events may help scientific community to improve current numerical weather prediction models and operational forecast which will eventually help the policy makers and regional agencies in decision making. The findings of this study as a whole are also crucial for other sector of the society, for instance, societal sectors related to environment and energy, hydrology modelling and water resource management, and more specifically to agriculture. In this study, we only focus on the large-scale longest-lived events and attempt to downscale in order to investigate the predictability. We find that, even with preliminary results, that downscaling of GEFS reforecasts will have determinantal benefits in terms of improving the predictability of such events. Large-scale short-lived events are also equally devastating events while having a persistence less than 5 days. In order to promote seasonal to sub-seasonal (S2S) predictability (Mason *et al.*, 1999; Goddard *et al.*, 2014), it is crucial to perform a similar downscaling practice of reforecasts for such events (Scaife *et al.*, 2019). However, it requires a dedicated budget considering the major cost of this practice belongs to the computational resources.

Bibliography

- Asmat U, Athar H. 2017. Run-based multi-model interannual variability assessment of precipitation and temperature over Pakistan using two IPCC AR4-based AOGCMs. *Theoretical and Applied Climatology*, 127(1–2). <https://doi.org/10.1007/s00704-015-1616-6>.
- Asmat U, Athar H, Nabeel A, Latif M. 2018. An AOGCM based assessment of interseasonal variability in Pakistan. *Climate Dynamics*. Springer Berlin Heidelberg, 50(1–2): 349–373. <https://doi.org/10.1007/s00382-017-3614-0>.
- Betts AK, Harshvardhan. 1987. Thermodynamic constraint on the cloud liquid water feedback in climate models. *Journal of Geophysical Research: Atmospheres*. John Wiley & Sons, Ltd, 92(D7): 8483–8485. <https://doi.org/10.1029/JD092ID07P08483>.
- Betts AK, Miller MJ. 1986. A new convective adjustment scheme. Part II: Single column tests using GATE wave, BOMEX, ATEX and arctic air-mass data sets. *Quarterly Journal of the Royal Meteorological Society*. John Wiley & Sons, Ltd, 112(473): 693–709. <https://doi.org/10.1002/QJ.49711247308>.
- Blamey RC, Kolusu SR, Mahlalela P, Todd MC, Reason CJC. 2018. The role of regional circulation features in regulating El Niño climate impacts over southern Africa: A comparison of the 2015/2016 drought with previous events. *International Journal of Climatology*, 38(11): 4276–4295. <https://doi.org/10.1002/joc.5668>.
- Blamey RC, Reason CJC. 2013. The role of mesoscale convective complexes in southern Africa summer rainfall. *Journal of Climate*, 26(5): 1654–1668. <https://doi.org/10.1175/JCLI-D-12-00239.1>.
- Burls NJ, Blamey RC, Cash BA, Swenson ET, Fahad A al, Bopape MJM, Straus DM, Reason CJC. 2019. The Cape Town “Day Zero” drought and Hadley cell expansion. *npj Climate and Atmospheric Science 2019 2:1*. Nature Publishing Group, 2(1): 1–8. <https://doi.org/10.1038/s41612-019-0084-6>.
- Camberlin P, Moron V, Okoola R, Philippon N, Gitau W. 2009. Components of rainy seasons’ variability in Equatorial East Africa: Onset, cessation, rainfall frequency and intensity. *Theoretical and Applied Climatology*, 98(3–4): 237–249. <https://doi.org/10.1007/s00704-009-0113-1>.
- Conway D, Dalin C, Landman WA, Osborn TJ. 2017. Hydropower plans in eastern and southern Africa increase risk of concurrent climate-related electricity supply disruption. *Nature Energy 2017 2:12*. Nature Publishing Group, 2(12): 946–953. <https://doi.org/10.1038/s41560-017-0037-4>.
- Conway D, Van Garderen EA, Deryng D, Dorling S, Krueger T, Landman W, Lankford B, Lebek K, Osborn T, Ringler C, Thurlow J, Zhu T, Dalin C. 2015. Climate and southern Africa’s water-energy-food nexus. *Nature Climate Change*. Nature Publishing Group, 5(9): 837–846. <https://doi.org/10.1038/nclimate2735>.
- Cook C, Reason CJC, Hewitson BC. 2004. Wet and dry spells within particularly wet and dry summers in the South African summer rainfall region. *Climate Research*, 26(1): 17–31. <https://doi.org/10.3354/cr026017>.

Cook KH. 2000. The South Indian convergence zone and interannual rainfall variability over Southern Africa. *Journal of Climate*, 13(21): 3789–3804. [https://doi.org/10.1175/1520-0442\(2000\)013<3789:TSICZA>2.0.CO;2](https://doi.org/10.1175/1520-0442(2000)013<3789:TSICZA>2.0.CO;2).

Cook KH. 2001. A southern hemisphere wave response to ENSO with implications for Southern Africa precipitation. *Journal of the Atmospheric Sciences*, 58(15): 2146–2162. [https://doi.org/10.1175/1520-0469\(2001\)058<2146:ASHWRT>2.0.CO;2](https://doi.org/10.1175/1520-0469(2001)058<2146:ASHWRT>2.0.CO;2).

Crétat J, Macron C, Pohl B, Richard Y. 2011. Quantifying internal variability in a regional climate model: A case study for Southern Africa. *Climate Dynamics*, 37(7–8): 1335–1356. <https://doi.org/10.1007/s00382-011-1021-5>.

Crétat J, Pohl B, Dieppois B, Berthou S, Pergaud J. 2019. The Angola Low: relationship with southern African rainfall and ENSO. *Climate Dynamics*. Springer Berlin Heidelberg, 52(3–4): 1783–1803. <https://doi.org/10.1007/s00382-018-4222-3>.

Crétat J, Pohl B, Richard Y, Drobinski P. 2012a. Uncertainties in simulating regional climate of Southern Africa: Sensitivity to physical parameterizations using WRF. *Climate Dynamics*, 38(3–4): 613–634. <https://doi.org/10.1007/s00382-011-1055-8>.

Crétat J, Richard Y, Pohl B, Rouault M, Reason C, Fauchereau N. 2012b. Recurrent daily rainfall patterns over South Africa and associated dynamics during the core of the austral summer. *International Journal of Climatology*, 32(2): 261–273. <https://doi.org/10.1002/joc.2266>.

CRI. 2021. *Global Climate Risk Index 2021: Who suffers most from extreme weather events? weather-related loss events in 2019 and 2000-2019*. .

Desbiolles F, Blamey R, Illig S, James R, Barimalala R, Renault L, Reason C. 2018. Upscaling impact of wind/sea surface temperature mesoscale interactions on southern Africa austral summer climate. *International Journal of Climatology*, 38(12): 4651–4660. <https://doi.org/10.1002/joc.5726>.

Desbiolles F, Howard E, Blamey RC, Barimalala R, Hart NCG, Reason CJC. 2020. Role of ocean mesoscale structures in shaping the Angola-Low pressure system and the southern Africa rainfall. *Climate Dynamics*. Springer Berlin Heidelberg, 54(7–8): 3685–3704. <https://doi.org/10.1007/s00382-020-05199-1>.

Dieppois B, Pohl B, Crétat J, Eden J, Sidibe M, New M, Rouault M, Lawler D. 2019. Southern African summer-rainfall variability, and its teleconnections, on interannual to interdecadal timescales in CMIP5 models. *Climate Dynamics*. Springer Berlin Heidelberg, 53(5–6): 3505–3527. <https://doi.org/10.1007/s00382-019-04720-5>.

Dieppois B, Pohl B, Rouault M, New M, Lawler D, Keenlyside N. 2016. Interannual to interdecadal variability of winter and summer southern African rainfall, and their teleconnections. *Journal of Geophysical Research*. <https://doi.org/10.1002/2015JD024576>.

Dieppois B, Rouault M, New M. 2015. The impact of ENSO on Southern African rainfall in CMIP5 ocean atmosphere coupled climate models. *Climate Dynamics*, 45(9–10): 2425–2442. <https://doi.org/10.1007/s00382-015-2480-x>.

Donald A, Meinke H, Power B, Maia A de HN, Wheeler MC, White N, Stone RC, Ribbe J. 2006. Near-global impact of the Madden-Julian Oscillation on rainfall. *Geophysical Research*

Letters, 33(9): 6–9. <https://doi.org/10.1029/2005GL025155>.

Donat MG, Lowry AL, Alexander L V., O’Gorman PA, Maher N. 2016. More extreme precipitation in the world’s dry and wet regions. *Nature Climate Change*. <https://doi.org/10.1038/nclimate2941>.

Dosio A. 2017. Projection of temperature and heat waves for Africa with an ensemble of CORDEX Regional Climate Models. *Climate Dynamics*. Springer Verlag, 49(1–2): 493–519. <https://doi.org/10.1007/S00382-016-3355-5/FIGURES/15>.

Dyer TGJ, Tyson PD. 1977. Estimating Above and Below Normal Rainfall Periods over South Africa, 1972–2000. *Journal of Applied Meteorology*, 16(2): 145–147. [https://doi.org/10.1175/1520-0450\(1977\)016<0145:EAABNR>2.0.CO;2](https://doi.org/10.1175/1520-0450(1977)016<0145:EAABNR>2.0.CO;2).

Engelbrecht CJ, Engelbrecht FA, Dyson LL. 2013. High-resolution model-projected changes in mid-tropospheric closed-lows and extreme rainfall events over southern Africa. *International Journal of Climatology*, 33(1): 173–187. <https://doi.org/10.1002/joc.3420>.

Engelbrecht F, Adegoke J, Bopape MJ, Naidoo M, Garland R, Thatcher M, McGregor J, Katzfey J, Werner M, Ichoku C, Gatebe C. 2015. Projections of rapidly rising surface temperatures over Africa under low mitigation. *Environmental Research Letters*. IOP Publishing, 10(8): 085004. <https://doi.org/10.1088/1748-9326/10/8/085004>.

Engelbrecht FA, McGregor JL, Engelbrecht CJ. 2009. Dynamics of the Conformal-Cubic Atmospheric Model projected climate-change signal over southern Africa. *International Journal of Climatology*. John Wiley & Sons, Ltd, 29(7): 1013–1033. <https://doi.org/10.1002/JOC.1742>.

Fauchereau N, Pohl B, Reason CJC, Rouault M, Richard Y. 2009. Recurrent daily OLR patterns in the Southern Africa/Southwest Indian ocean region, implications for South African rainfall and teleconnections. *Climate Dynamics*, 32(4): 575–591. <https://doi.org/10.1007/s00382-008-0426-2>.

Favre A, Hewitson B, Lennard C, Cerezo-Mota R, Tadross M. 2013. Cut-off Lows in the South Africa region and their contribution to precipitation. *Climate Dynamics*, 41(9–10): 2331–2351. <https://doi.org/10.1007/s00382-012-1579-6>.

Favre A, Philippon N, Pohl B, Kalognomou EA, Lennard C, Hewitson B, Nikulin G, Dosio A, Panitz HJ, Cerezo-Mota R. 2016. Spatial distribution of precipitation annual cycles over South Africa in 10 CORDEX regional climate model present-day simulations. *Climate Dynamics*. Springer Berlin Heidelberg, 46(5–6): 1799–1818. <https://doi.org/10.1007/s00382-015-2677-z>.

Fitchett JM, Grab SW. 2014. A 66-year tropical cyclone record for south-east Africa: Temporal trends in a global context. *International Journal of Climatology*, 34(13): 3604–3615. <https://doi.org/10.1002/joc.3932>.

Frei C, Christensen JH, Déqué M, Jacob D, Jones RG, Vidale PL. 2003. Daily precipitation statistics in regional climate models: Evaluation and intercomparison for the European Alps. *Journal of Geophysical Research: Atmospheres*, 108(3): 1–19. <https://doi.org/10.1029/2002jd002287>.

Gascón E, Lavers D, Hamill TM, Richardson DS, Bouallègue ZB, Leutbecher M, Pappenberger F. 2019. Statistical postprocessing of dual-resolution ensemble precipitation forecasts across

- Europe. *Quarterly Journal of the Royal Meteorological Society*, 145(724): 3218–3235. <https://doi.org/10.1002/qj.3615>.
- Gitau W, Camberlin P, Ogallo L, Bosire E. 2018. Trends of intraseasonal descriptors of wet and dry spells over equatorial eastern africa. *International Journal of Climatology*, 38(3): 1189–1200. <https://doi.org/10.1002/joc.5234>.
- Gitau W, Camberlin P, Ogallo L, Okoola R. 2015. Oceanic and atmospheric linkages with short rainfall season intraseasonal statistics over Equatorial Eastern Africa and their predictive potential. *International Journal of Climatology*, 35(9): 2382–2399. <https://doi.org/10.1002/joc.4131>.
- Gitau W, Ogallo L, Camberlin P, Okoola R. 2013. Spatial coherence and potential predictability assessment of intraseasonal statistics of wet and dry spells over Equatorial Eastern Africa. *International Journal of Climatology*, 33(12): 2690–2705. <https://doi.org/10.1002/joc.3620>.
- Goddard L, Baethgen WE, Bhojwani H, Robertson AW. 2014. The International Research Institute for Climate. *Earth Perspectives*, 1–14. <https://doi.org/https://doi.org/10.1186/2194-6434-1-10>.
- Grimm AM. 2019. Madden–Julian Oscillation impacts on South American summer monsoon season: precipitation anomalies, extreme events, teleconnections, and role in the MJO cycle. *Climate Dynamics*. Springer Berlin Heidelberg, 53(1–2): 907–932. <https://doi.org/10.1007/s00382-019-04622-6>.
- Grimm AM, Reason CJC. 2011. Does the South American Monsoon Influence African Rainfall? *Journal of Climate*. American Meteorological Society, 24(4): 1226–1238. <https://doi.org/10.1175/2010JCLI3722.1>.
- Grimm AM, Reason CJC. 2015. Intraseasonal teleconnections between South America and South Africa. *Journal of Climate*, 28(23): 9489–9497. <https://doi.org/10.1175/JCLI-D-15-0116.1>.
- Guan H, Zhu Y, Sinsky E, Fu B, Li W, Zhou X, Xue X, Hou D, Peng J, Nageswararao MM, Tallapragada V, Hamill TM, Whitaker JS, Bates G, Pegion P, Frederick S, Rosencrans M, Kumar A. 2022. GEFSv12 Reforecast Dataset for Supporting Subseasonal and Hydrometeorological Applications. *Monthly Weather Review*, 150(3): 647–665. <https://doi.org/10.1175/mwr-d-21-0245.1>.
- Hamill TM, Bates GT, Whitaker JS, Murray DR, Fiorino M, Galarneau TJ, Zhu Y, Lapenta W. 2013. NOAA’s second-generation global medium-range ensemble reforecast dataset. *Bulletin of the American Meteorological Society*, 94(10): 1553–1565. <https://doi.org/10.1175/BAMS-D-12-00014.1>.
- Hamill TM, Scheuerer M, Bates GT. 2015. Analog probabilistic precipitation forecasts using GEFS reforecasts and climatology-calibrated precipitation analyses. *Monthly Weather Review*, 143(8): 3300–3309. <https://doi.org/10.1175/MWR-D-15-0004.1>.
- Hamill TM, Whitaker JS, Mullen SL. 2006. Reforecasts: An Important Dataset for Improving Weather Predictions. *Bulletin of the American Meteorological Society*. American Meteorological Society, 87(1): 33–46. <https://doi.org/10.1175/BAMS-87-1-33>.

Hamill TM, Whitaker JS, Shlyayeva A, Bates G, Fredrick S, Pegion P, Sinsky E, Zhu Y, Tallapragada V, Guan H, Zhou X, Woollen J. 2022. The Reanalysis for the Global Ensemble Forecast System, Version 12. *Monthly Weather Review*. American Meteorological Society, 150(1): 59–79. <https://doi.org/10.1175/MWR-D-21-0023.1>.

Hamill TM, Whitaker JS, Wei X. 2004. Ensemble re-forecasting: Improving medium-range forecast skill using retrospective forecasts. *Bulletin of the American Meteorological Society*, 132(6): 1434–1447. [https://doi.org/https://doi.org/10.1175/1520-0493\(2004\)132<1434:ERIMFS>2.0.CO;2](https://doi.org/https://doi.org/10.1175/1520-0493(2004)132<1434:ERIMFS>2.0.CO;2).

Hart NCG, Reason CJC, Fauchereau N. 2010. Tropical-extratropical interactions over southern Africa: Three cases of heavy summer season rainfall. *Monthly Weather Review*, 138(7): 2608–2623. <https://doi.org/10.1175/2010MWR3070.1>.

Hart NCG, Reason CJC, Fauchereau N. 2013. Cloud bands over southern Africa: Seasonality, contribution to rainfall variability and modulation by the MJO. *Climate Dynamics*, 41(5–6): 1199–1212. <https://doi.org/10.1007/s00382-012-1589-4>.

Hersbach H, Bell B, Berrisford P, Hirahara S, Horányi A, Muñoz-Sabater J, Nicolas J, Peubey C, Radu R, Schepers D, Simmons A, Soci C, Abdalla S, Abellan X, Balsamo G, Bechtold P, Biavati G, Bidlot J, Bonavita M, De Chiara G, Dahlgren P, Dee D, Diamantakis M, Dragani R, Flemming J, Forbes R, Fuentes M, Geer A, Haimberger L, Healy S, Hogan RJ, Hólm E, Janisková M, Keeley S, Laloyaux P, Lopez P, Lupu C, Radnoti G, de Rosnay P, Rozum I, Vamborg F, Villaume S, Thépaut JN. 2020a. The ERA5 global reanalysis. *Quarterly Journal of the Royal Meteorological Society*, 146(730): 1999–2049. <https://doi.org/10.1002/qj.3803>.

Hersbach H, Bell B, Berrisford P, Hirahara S, Horányi A, Muñoz-Sabater J, Nicolas J, Peubey C, Radu R, Schepers D, Simmons A, Soci C, Abdalla S, Abellan X, Balsamo G, Bechtold P, Biavati G, Bidlot J, Bonavita M, De Chiara G, Dahlgren P, Dee D, Diamantakis M, Dragani R, Flemming J, Forbes R, Fuentes M, Geer A, Haimberger L, Healy S, Hogan RJ, Hólm E, Janisková M, Keeley S, Laloyaux P, Lopez P, Lupu C, Radnoti G, de Rosnay P, Rozum I, Vamborg F, Villaume S, Thépaut JN. 2020b. The ERA5 global reanalysis. *Quarterly Journal of the Royal Meteorological Society*. John Wiley & Sons, Ltd, 146(730): 1999–2049. <https://doi.org/10.1002/QJ.3803>.

Hoegh-Guldberg O, Jacob D, Taylor M, Bindi M, Abdul Halim S, Achlatis Australia M, Alexander L V, Allen MR, Berry P, Boyer C, Brilli L, Buckeridge M, Byers Austria E, Antonio Marengo Brazil J, Pereira J, Sherstyukov B, Jacob D, Taylor M, Bindi M, Brown S, Camilloni I, Diedhiou A, Djalante R, Ebi K, Engelbrecht F, Guiot J, Hijioka Y, Mehrotra S, Payne A, Seneviratne S, Thomas A, Warren R, Zhou G, Zhai P, Pörtner H, Roberts D, Skea J, Shukla P, Pirani A, Moufouma-Okia W, Péan C, Pidcock R, Connors S, Matthews J, Chen Y, Zhou X, Gomis M, Lonnoy E, Maycock T, Tignor M, Waterfield T. 2018. *Impacts of 1.5°C global warming on natural and human systems*. .

Hoell A, Cheng L. 2018. Austral summer Southern Africa precipitation extremes forced by the El Niño–Southern oscillation and the subtropical Indian Ocean dipole. *Climate Dynamics*. Springer Berlin Heidelberg, 50(9–10): 3219–3236. <https://doi.org/10.1007/s00382-017-3801-z>.

Hoell A, Funk C, Magadzire T, Zinke J, Husak G. 2015. El Niño–Southern Oscillation diversity and Southern Africa teleconnections during Austral Summer. *Climate Dynamics*. Springer Berlin

Heidelberg, 45(5–6): 1583–1599. <https://doi.org/10.1007/s00382-014-2414-z>.

Hong S, Lim J. 2006. The WRF single-moment 6-class microphysics scheme (WSM6). *Journal of the Korean Meteorological Society*, 42(2): 129–151.

Hong SY, Noh Y, Dudhia J. 2006. A New Vertical Diffusion Package with an Explicit Treatment of Entrainment Processes. *Monthly Weather Review*. American Meteorological Society, 134(9): 2318–2341. <https://doi.org/10.1175/MWR3199.1>.

Huang B, Thorne PW, Banzon VF, Boyer T, Chepurin G, Lawrimore JH, Menne MJ, Smith TM, Vose RS, Zhang HM. 2017. Extended reconstructed Sea surface temperature, Version 5 (ERSSTv5): Upgrades, validations, and intercomparisons. *Journal of Climate*, 30(20): 8179–8205. <https://doi.org/10.1175/JCLI-D-16-0836.1>.

Huffman GJ, Adler RF, Bolvin DT, Gu G, Nelkin EJ, Bowman KP, Hong Y, Stocker EF, Wolff DB. 2007. The TRMM Multisatellite Precipitation Analysis (TMPA): Quasi-global, multiyear, combined-sensor precipitation estimates at fine scales. *Journal of Hydrometeorology*, 8(1): 38–55. <https://doi.org/10.1175/JHM560.1>.

Iacono MJ, Delamere JS, Mlawer EJ, Shephard MW, Clough SA, Collins WD. 2008. Radiative forcing by long-lived greenhouse gases: Calculations with the AER radiative transfer models. *Journal of Geophysical Research: Atmospheres*. John Wiley & Sons, Ltd, 113(D13): 13103. <https://doi.org/10.1029/2008JD009944>.

IPCC. 2021. *Climate Change 2021: The Physical Science Basis. Contribution of Working Group I to the Sixth Assessment Report of the Intergovernmental Panel on Climate Change*. Cambridge University Press: Cambridge, United Kingdom and New York, NY, USA.

Jackson LS, Finney DL, Kendon EJ, Marsham JH, Parker DJ, Stratton RA, Tomassini L, Tucker S. 2020. The effect of explicit convection on couplings between rainfall, humidity, and ascent over Africa under climate change. *Journal of Climate*, 33(19): 8315–8337. <https://doi.org/10.1175/JCLI-D-19-0322.1>.

James R, Hart NCG, Munday C, Reason CJC, Washington R. 2020. Coupled climate model simulation of tropical–extratropical cloud bands over Southern Africa. *Journal of Climate*, 33(19): 8579–8602. <https://doi.org/10.1175/JCLI-D-19-0731.1>.

Janjic ZI. 1994. The step-mountain eta coordinate model: further developments of the convection, viscous sublayer, and turbulence closure schemes. *Monthly Weather Review*, 122(5): 927–945. [https://doi.org/10.1175/1520-0493\(1994\)122<0927:TSMECM>2.0.CO;2](https://doi.org/10.1175/1520-0493(1994)122<0927:TSMECM>2.0.CO;2).

Kain JS. 2004. The Kain–Fritsch Convective Parameterization: An Update. *Journal of Applied Meteorology and Climatology*, 43(1): 170–181. [https://doi.org/https://doi.org/10.1175/1520-0450\(2004\)043<0170:TKCPAU>2.0.CO;2](https://doi.org/https://doi.org/10.1175/1520-0450(2004)043<0170:TKCPAU>2.0.CO;2).

Kalnay E, Kanamitsu M, Kistler R, Collins W, Deaven D, Gandin L, Iredell M, Saha S, White G, Woollen J, Zhu Y, Chelliah M, Ebisuzaki W, Higgins W, Janowiak J, Mo KC, Ropelewski C, Wang J, Leetmaa A, Reynolds R, Jenne R, Joseph D. 1996. The NCEP/NCAR 40-Year Reanalysis Project in: *Bulletin of the American Meteorological Society* Volume 77 Issue 3 (1996). *American Meteorological Society*, 77(3): 437–472.

Kendall MG. 1957. *Rank Correlation Methods. 4th Edition. Charles Griffin, London*.

- Kendon EJ, Ban N, Roberts NM, Fowler HJ, Roberts MJ, Chan SC, Evans JP, Fosser G, Wilkinson JM. 2017. Do convection-permitting regional climate models improve projections of future precipitation change? *Bulletin of the American Meteorological Society*, 98(1): 79–93. <https://doi.org/10.1175/BAMS-D-15-0004.1>.
- Kendon EJ, Stratton RA, Tucker S, Marsham JH, Berthou S, Rowell DP, Senior CA. 2019. Enhanced future changes in wet and dry extremes over Africa at convection-permitting scale. *Nature Communications*. Springer US, 10(1). <https://doi.org/10.1038/s41467-019-09776-9>.
- Kharin V V., Zwiers FW, Zhang X, Hegerl GC. 2007. Changes in Temperature and Precipitation Extremes in the IPCC Ensemble of Global Coupled Model Simulations. *Journal of Climate*. American Meteorological Society, 20(8): 1419–1444. <https://doi.org/10.1175/JCLI4066.1>.
- Kruger AC. 2018. Africa and the Paris Agreement. *Nature Climate Change*. Springer US, 8(5): 365–366. <https://doi.org/10.1038/s41558-018-0146-5>.
- Kruger AC, Nxumalo MP. 2017. Historical rainfall trends in South Africa: 1921–2015. *Water SA*, 43(2): 285–297. <https://doi.org/10.4314/wsa.v43i2.12>.
- Kusangaya S, Warburton ML, Archer van Garderen E, Jewitt GPW. 2014. Impacts of climate change on water resources in southern Africa: A review. *Physics and Chemistry of the Earth, Parts A/B/C*. Pergamon, 67–69: 47–54. <https://doi.org/10.1016/J.PCE.2013.09.014>.
- Lakhraj-Govender R, Grab SW. 2019. Rainfall and river flow trends for the Western Cape Province, South Africa. *South African Journal of Science*, 115(9–10): 1–6. <https://doi.org/10.17159/sajs.2019/6028>.
- Lazenby MJ, Todd MC, Chadwick R, Wang Y. 2018. Future Precipitation Projections over Central and Southern Africa and the Adjacent Indian Ocean: What Causes the Changes and the Uncertainty? *Journal of Climate*. American Meteorological Society, 31(12): 4807–4826. <https://doi.org/10.1175/JCLI-D-17-0311.1>.
- Li C, Zwiers F, Zhang X, Li G, Sun Y, Wehner M. 2021. Changes in Annual Extremes of Daily Temperature and Precipitation in CMIP6 Models. *Journal of Climate*. American Meteorological Society, 34(9): 3441–3460. <https://doi.org/10.1175/JCLI-D-19-1013.1>.
- Li W, Zhu Y, Zhou X, Hou D, Sinsky E, Melhauser C, Peña M, Guan H, Wobus R. 2019. Evaluating the MJO prediction skill from different configurations of NCEP GEFS extended forecast. *Climate Dynamics*. Springer Verlag, 52(7–8): 4923–4936. <https://doi.org/10.1007/S00382-018-4423-9/FIGURES/12>.
- Liu W, Lim WH, Sun F, Mitchell D, Wang H, Chen D, Bethke I, Shiogama H, Fischer E. 2018a. Global Freshwater Availability Below Normal Conditions and Population Impact Under 1.5 and 2 °C Stabilization Scenarios. *Geophysical Research Letters*. John Wiley & Sons, Ltd, 45(18): 9803–9813. <https://doi.org/10.1029/2018GL078789>.
- Liu W, Sun F, Ho Lim W, Zhang J, Wang H, Shiogama H, Zhang Y. 2018b. Global drought and severe drought-Affected populations in 1.5 and 2 °C warmer worlds. *Earth System Dynamics*. Copernicus GmbH, 9(1): 267–283. <https://doi.org/10.5194/ESD-9-267-2018>.
- Lu E, Zhao W, Zou X, Ye D, Zhao C, Zhang Q. 2017. Temporal-spatial monitoring of an extreme precipitation event: Determining simultaneously the time period it lasts and the

geographic region it affects. *Journal of Climate*, 30(16): 6123–6132.
<https://doi.org/10.1175/JCLI-D-17-0105.1>.

Lyon B, Mason SJ. 2007. The 1997-98 summer rainfall season in Southern Africa. Part I: Observations. *Journal of Climate*, 20(20): 5134–5148. <https://doi.org/10.1175/JCLI4225.1>.

Ma LM, Tan ZM. 2009. Improving the behavior of the cumulus parameterization for tropical cyclone prediction: Convection trigger. *Atmospheric Research*. Elsevier B.V., 92(2): 190–211. <https://doi.org/10.1016/j.atmosres.2008.09.022>.

Macron C, Pohl B, Richard Y, Bessafi M. 2014. How do tropical temperate troughs form and develop over Southern Africa? *Journal of Climate*, 27(4): 1633–1647. <https://doi.org/10.1175/JCLI-D-13-00175.1>.

Macron C, Richard Y, Garot T, Bessafi M, Pohl B, Ratiarison A, Razafindrabe A. 2016. Intraseasonal rainfall variability over Madagascar. *Monthly Weather Review*, 144(5): 1877–1885. <https://doi.org/10.1175/MWR-D-15-0077.1>.

Madden RA, Julian PR. 1994. Observations of the 40-50-day tropical oscillation - a review. *Monthly Weather Review*. [https://doi.org/10.1175/1520-0493\(1994\)122<0814:OOTDTP>2.0.CO;2](https://doi.org/10.1175/1520-0493(1994)122<0814:OOTDTP>2.0.CO;2).

Malherbe J, Dieppois B, Maluleke P, Van Staden M, Pillay DL. 2016. South African droughts and decadal variability. *Natural Hazards*. Springer Netherlands, 80(1): 657–681. <https://doi.org/10.1007/s11069-015-1989-y>.

Malherbe J, Engelbrecht FA, Landman WA, Engelbrecht CJ. 2012. Tropical systems from the southwest Indian Ocean making landfall over the Limpopo River Basin southern Africa: A historical perspective. *International Journal of Climatology*, 32(7): 1018–1032. <https://doi.org/10.1002/joc.2320>.

Malherbe J, Landman WA, Engelbrecht FA. 2014. The bi-decadal rainfall cycle, Southern Annular Mode and tropical cyclones over the Limpopo River Basin, southern Africa. *Climate Dynamics*, 42(11–12): 3121–3138. <https://doi.org/10.1007/s00382-013-2027-y>.

Manhique AJ, Reason CJC, Rydberg L, Fauchereau N. 2011. ENSO and Indian Ocean sea surface temperatures and their relationships with tropical temperate troughs over Mozambique and the Southwest Indian Ocean. *International Journal of Climatology*, 31(1): 1–13. <https://doi.org/10.1002/joc.2050>.

Mann H. 1945. Mann Nonparametric test against trend. *Econometrica*.

Maraun D. 2016. Bias Correcting Climate Change Simulations - a Critical Review. *Current Climate Change Reports*. Current Climate Change Reports, 2(4): 211–220. <https://doi.org/10.1007/s40641-016-0050-x>.

Mason SJ, Goddard L, Graham NE, Yulaeva E, Sun L, Arkin PA. 1999. The IRI seasonal climate prediction system. *WRPMD 1999: Preparing for the 21st Century*. [https://doi.org/10.1061/40430\(1999\)4](https://doi.org/10.1061/40430(1999)4).

Mason SJ, Joubert AM. 1997. Simulated changes in extreme rainfall over southern Africa. *International Journal of Climatology*, 17(3): 291–301. [https://doi.org/10.1002/\(sici\)1097-](https://doi.org/10.1002/(sici)1097-)

0088(19970315)17:3<291::aid-joc120>3.3.co;2-t.

Mason SJ, Jury MR. 1997. Climatic variability and change over southern Africa: a reflection on underlying processes. *Progress in Physical Geography: Earth and Environment*, 21(1): 23–50. <https://doi.org/10.1177/030913339702100103>.

Masupha TE, Moeletsi ME, Tsubo M. 2016. Dry spells assessment with reference to the maize crop in the Luvuvhu River catchment of South Africa. *Physics and Chemistry of the Earth*. <https://doi.org/10.1016/j.pce.2015.10.014>.

Maure G, Pinto I, Ndebele-Murisa M, Muthige M, Lennard C, Nikulin G, Dosio A, Meque A. 2018. The southern African climate under 1.5 °C and 2 °C of global warming as simulated by CORDEX regional climate models. *Environmental Research Letters*. IOP Publishing, 13(6): 065002. <https://doi.org/10.1088/1748-9326/AAB190>.

McKittrick R, Christy J. 2018. A Test of the Tropical 200- to 300-hPa Warming Rate in Climate Models. *Earth and Space Science*. Wiley-Blackwell Publishing Ltd, 5(9): 529–536. <https://doi.org/10.1029/2018EA000401>.

Misra V. 2003. The influence of Pacific SST variability on the precipitation over southern Africa. *Journal of Climate*, 16(14): 2408–2418. <https://doi.org/10.1175/2785.1>.

Moron V, Camberlin P, Robertson AW. 2013. Extracting subseasonal scenarios: An alternative method to analyze seasonal predictability of regional-scale tropical rainfall. *Journal of Climate*, 26(8): 2580–2600. <https://doi.org/10.1175/JCLI-D-12-00357.1>.

Morrison H, Thompson G, Tatarskii V. 2009. Impact of Cloud Microphysics on the Development of Trailing Stratiform Precipitation in a Simulated Squall Line: Comparison of One- and Two-Moment Schemes. *Monthly Weather Review*. American Meteorological Society, 137(3): 991–1007. <https://doi.org/10.1175/2008MWR2556.1>.

Mpungose N, Thoithi W, Blamey RC, Reason CJC. 2022. Extreme rainfall events in southeastern Africa during the summer. *Theoretical and Applied Climatology*. Springer Vienna, 150(1–2): 185–201. <https://doi.org/10.1007/s00704-022-04162-w>.

Muller CJ, O’Gorman PA, Back LE. 2011. Intensification of Precipitation Extremes with Warming in a Cloud-Resolving Model. *Journal of Climate*. American Meteorological Society, 24(11): 2784–2800. <https://doi.org/10.1175/2011JCLI3876.1>.

Nangombe S, Zhou T, Zhang W, Wu B, Hu S, Zou L, Li D. 2018. Record-breaking climate extremes in Africa under stabilized 1.5 °C and 2 °C global warming scenarios. *Nature Climate Change*, 8(5): 375–380. <https://doi.org/10.1038/s41558-018-0145-6>.

Ndarana T, Lekoloane LE, Rammopo TS, Reason CJC, Bopape M-JM, Chikoore H, Engelbrecht FA. 2022. Downstream development associated with two types of ridging South Atlantic Ocean anticyclones over South Africa. *Weather and Climate Dynamics Discussions*.

Nicholson S. 2003. Comments on “The South Indian convergence zone and interannual rainfall variability over southern Africa” and the question of ENSO’s influence on southern Africa. *Journal of Climate*, 16(3): 555–562. [https://doi.org/10.1175/1520-0442\(2003\)016<0555:COTSIC>2.0.CO;2](https://doi.org/10.1175/1520-0442(2003)016<0555:COTSIC>2.0.CO;2).

- Nicholson SE, Kim J. 1997. THE RELATIONSHIP OF THE EL NIÑO–SOUTHERN OSCILLATION TO AFRICAN RAINFALL. *International Journal of Climatology*, 17(2): 117–135. [https://doi.org/10.1002/\(SICI\)1097-0088\(199702\)17:2<117::AID-JOC84>3.0.CO;2-O](https://doi.org/10.1002/(SICI)1097-0088(199702)17:2<117::AID-JOC84>3.0.CO;2-O).
- Oettli P, Tozuka T, Izumo T, Engelbrecht FA, Yamagata T. 2014. The self-organizing map, a new approach to apprehend the Madden-Julian Oscillation influence on the intraseasonal variability of rainfall in the southern African region. *Climate Dynamics*, 43(5–6): 1557–1573. <https://doi.org/10.1007/s00382-013-1985-4>.
- Otto FEL, Wolski P, Lehner F, Tebaldi C, Van Oldenborgh GJ, Hogesteegeer S, Singh R, Holden P, Fučkar NS, Odoulami RC, New M. 2018. Anthropogenic influence on the drivers of the Western Cape drought 2015-2017. *Environmental Research Letters*, 13(12). <https://doi.org/10.1088/1748-9326/aae9f9>.
- Oueslati B, Pohl B, Moron V, Rome S, Janicot S. 2017. Characterization of heat waves in the Sahel and associated physical mechanisms. *Journal of Climate*, 30(9): 3095–3115. <https://doi.org/10.1175/JCLI-D-16-0432.1>.
- Paciorek CJ, Stone DA, Wehner MF. 2018. Quantifying statistical uncertainty in the attribution of human influence on severe weather. *Weather and Climate Extremes*, 20(June 2017): 69–80. <https://doi.org/10.1016/j.wace.2018.01.002>.
- Pascale S, Pohl B, Kapnick SB, Zhang H. 2019. On the Angola low interannual variability and its role in modulating ENSO effects in southern Africa. *Journal of Climate*, 32(15): 4783–4803. <https://doi.org/10.1175/JCLI-D-18-0745.1>.
- Philippon N, Camberlin P, Moron V, Boyard-Micheau J. 2015. Anomalously wet and dry rainy seasons in Equatorial East Africa and associated differences in intra-seasonal characteristics. *Climate Dynamics*. Springer Berlin Heidelberg, 45(7–8): 2101–2121. <https://doi.org/10.1007/s00382-014-2460-6>.
- Pinto I, Lennard C, Tadross M, Hewitson B, Dosio A, Nikulin G, Panitz HJ, Shongwe ME. 2016. Evaluation and projections of extreme precipitation over southern Africa from two CORDEX models. *Climatic Change*, 135(3–4): 655–668. <https://doi.org/10.1007/s10584-015-1573-1>.
- Pohl B, Crétat J, Camberlin P. 2011. Testing WRF capability in simulating the atmospheric water cycle over Equatorial East Africa. *Climate Dynamics*, 37(7–8): 1357–1379. <https://doi.org/10.1007/s00382-011-1024-2>.
- Pohl B, Dieppois B, Crétat J, Lawler D, Rouault M. 2018. From synoptic to interdecadal variability in southern African rainfall: Toward a unified view across time scales. *Journal of Climate*, 31(15): 5845–5872. <https://doi.org/10.1175/JCLI-D-17-0405.1>.
- Pohl B, Fauchereau N. 2012. The southern annular mode seen through weather regimes. *Journal of Climate*, 25(9): 3336–3354. <https://doi.org/10.1175/JCLI-D-11-00160.1>.
- Pohl B, Fauchereau N, Reason CJC, Rouault M. 2010. Relationships between the Antarctic oscillation, the Madden-Julian oscillation, and ENSO, and consequences for rainfall analysis. *Journal of Climate*, 23(2): 238–254. <https://doi.org/10.1175/2009JCLI2443.1>.
- Pohl B, Fauchereau N, Richard Y, Rouault M, Reason CJC. 2009. Interactions between synoptic, intraseasonal and interannual convective variability over Southern Africa. *Climate Dynamics*,

33(7–8): 1033–1050. <https://doi.org/10.1007/s00382-008-0485-4>.

Pohl B, MacRon C, Monerie PA. 2017. Fewer rainy days and more extreme rainfall by the end of the century in Southern Africa. *Scientific Reports*. Nature Publishing Group, 7(April): 6–12. <https://doi.org/10.1038/srep46466>.

Pohl B, Richard Y, Fauchereau N. 2007. Influence of the Madden-Julian oscillation on southern African summer rainfall. *Journal of Climate*, 20(16): 4227–4242. <https://doi.org/10.1175/JCLI4231.1>.

Pohl B, Rouault M, Roy S Sen. 2014. Simulation of the annual and diurnal cycles of rainfall over South Africa by a regional climate model. *Climate Dynamics*, 43(7–8): 2207–2226. <https://doi.org/10.1007/s00382-013-2046-8>.

Pomposi C, Funk C, Shukla S, Harrison L, Magadzire T. 2018. Distinguishing southern Africa precipitation response by strength of El Niño events and implications for decision-making. *Environmental Research Letters*, 13(7). <https://doi.org/10.1088/1748-9326/aacc4c>.

Puaud Y, Pohl B, Fauchereau N, Macron C, Beltrando G. 2017. Climate co-variability between South America and Southern Africa at interannual, intraseasonal and synoptic scales. *Climate Dynamics*. Springer Verlag, 48(11–12): 4029–4050. <https://doi.org/10.1007/S00382-016-3318-X/FIGURES/13>.

Quagraine KA, Hewitson B, Jack C, Pinto I, Lennard C. 2019. A methodological approach to assess the co-behavior of climate processes over Southern Africa. *Journal of Climate*, 32(9): 2483–2495. <https://doi.org/10.1175/JCLI-D-18-0689.1>.

Ranasinghe. 2021. Chapter 12: Climate change information for regional impact and for risk assessment. *Climate Change 2021: The Physical Science Basis. Contribution of Working Group I to the Sixth Assessment Report of the Intergovernmental Panel on Climate Change*, (August 2021): 351–364.

Rapolaki RS, Blamey RC, Hermes JC, Reason CJC. 2019. A classification of synoptic weather patterns linked to extreme rainfall over the Limpopo River Basin in southern Africa. *Climate Dynamics*. Springer Berlin Heidelberg, 53(3–4): 2265–2279. <https://doi.org/10.1007/s00382-019-04829-7>.

Rapolaki RS, Blamey RC, Hermes JC, Reason CJC. 2020. Moisture sources associated with heavy rainfall over the Limpopo River Basin, southern Africa. *Climate Dynamics*. Springer Berlin Heidelberg, 55(5–6): 1473–1487. <https://doi.org/10.1007/s00382-020-05336-w>.

Ratan R, Venugopal V. 2013. Wet and dry spell characteristics of global tropical rainfall. *Water Resources Research*, 49(6): 3830–3841. <https://doi.org/10.1002/wrcr.20275>.

Ratna SB, Ratnam J V., Behera SK, Rautenbach CJ d. W, Ndarana T, Takahashi K, Yamagata T. 2014. Performance assessment of three convective parameterization schemes in WRF for downscaling summer rainfall over South Africa. *Climate Dynamics*, 42(11–12): 2931–2953. <https://doi.org/10.1007/s00382-013-1918-2>.

Ratnam J V., Behera SK, Masumoto Y, Yamagata T. 2014. Remote effects of El Niño and Modoki events on the austral summer precipitation of Southern Africa. *Journal of Climate*, 27(10): 3802–3815. <https://doi.org/10.1175/JCLI-D-13-00431.1>.

- Ratnam J V., Behera SK, Ratna SB, De Rautenbach CJW, Lennard C, Luo JJ, Masumoto Y, Takahashi K, Yamagata T. 2013. Dynamical Downscaling of Austral Summer Climate Forecasts over Southern Africa Using a Regional Coupled Model. *Journal of Climate*, 26(16): 6015–6032. <https://doi.org/10.1175/JCLI-D-12-00645.1>.
- Reason CJC. 2001. Subtropical Indian Ocean SST dipole events and southern African rainfall. *Geophysical Research Letters*. <https://doi.org/10.1029/2000GL012735>.
- Reason CJC. 2007. Tropical cyclone Dera, the unusual 2000/01 tropical cyclone season in the South West Indian Ocean and associated rainfall anomalies over Southern Africa. *Meteorology and Atmospheric Physics*, 97(1–4): 181–188. <https://doi.org/10.1007/s00703-006-0251-2>.
- Reason CJC, Allan RJ, Lindesay JA, Ansell TJ. 2000. Enso and climatic signals across the Indian Ocean basin in the global context: Part I, Interannual composite patterns. *International Journal of Climatology*, 20(11): 1285–1327. [https://doi.org/10.1002/1097-0088\(200009\)20:11<1285::AID-JOC536>3.0.CO;2-R](https://doi.org/10.1002/1097-0088(200009)20:11<1285::AID-JOC536>3.0.CO;2-R).
- Reason CJC, Jagadheesha D. 2005. A model investigation of recent ENSO impacts over southern Africa. *Meteorology and Atmospheric Physics*, 89(1–4): 181–205. <https://doi.org/10.1007/s00703-005-0128-9>.
- Reason CJC, Keibel A. 2004. Tropical Cyclone Eline and its unusual penetration and impacts over the Southern Africa mainland. *Weather and Forecasting*, 19(5): 789–805. [https://doi.org/10.1175/1520-0434\(2004\)019<0789:TCEAIU>2.0.CO;2](https://doi.org/10.1175/1520-0434(2004)019<0789:TCEAIU>2.0.CO;2).
- Reason CJC, Landman W, Tennant W. 2006. Seasonal to decadal prediction of southern African climate and its links with variability of the Atlantic ocean. *Bulletin of the American Meteorological Society*, 87(7): 941–955. <https://doi.org/10.1175/BAMS-87-7-941>.
- Reason CJC, Rouault M. 2002. ENSO-like decadal variability and South African rainfall. *Geophysical Research Letters*, 29(13): 1638. <https://doi.org/10.1029/2002GL014663>.
- Rouault M, Florenchie P, Fauchereau N, Reason CJC. 2003. South East tropical Atlantic warm events and southern African rainfall. *Geophysical Research Letters*, 30(5): 1–4. <https://doi.org/10.1029/2002GL014840>.
- Rouault M, Richard Y. 2004. Intensity and spatial extension of drought in South Africa at different time scales. *Water SA*, 29(4): 489–500. <https://doi.org/10.4314/wsa.v29i4.5057>.
- Rouault M, White SA, Reason CJC, Lutjeharms JRE, Jobard I. 2002. Ocean-atmosphere interaction in the Agulhas Current region and a South African extreme weather event. *Weather and Forecasting*. [https://doi.org/10.1175/1520-0434\(2002\)017<0655:OAIITA>2.0.CO;2](https://doi.org/10.1175/1520-0434(2002)017<0655:OAIITA>2.0.CO;2).
- Russo S, Marchese AF, Sillmann J, Immé G. 2016. When will unusual heat waves become normal in a warming Africa? *Environmental Research Letters*. IOP Publishing, 11(5). <https://doi.org/10.1088/1748-9326/11/5/054016>.
- Scaife AA, Camp J, Comer R, Davis P, Dunstone N, Gordon M, MacLachlan C, Martin N, Nie Y, Ren HL, Roberts M, Robinson W, Smith D, Vidale PL. 2019. Does increased atmospheric resolution improve seasonal climate predictions? *Atmospheric Science Letters*, 20(8): 1–10. <https://doi.org/10.1002/asl.922>.

Senior CA, Marsham JH, Berthou S, Burgin LE, Folwell SS, Kendon EJ, Klein CM, Jones RG, Mittal N, Rowell DP, Tomassini L, Vischel T, Becker B, Birch CE, Crook J, Dougill AJ, Finney DL, Graham RJ, Hart NCG, Jack CD, Jackson LS, James R, Koelle B, Misiani H, Mwalukanga B, Parker DJ, Stratton RA, Taylor CM, Tucker SO, Wainwright CM, Washington R, Willet MR. 2021. Convection-permitting regional climate change simulations for understanding future climate and informing decision-making in Africa. *Bulletin of the American Meteorological Society*, 102(6): E1206–E1223. <https://doi.org/10.1175/BAMS-D-20-0020.1>.

Sheshadri A, Borrus M, Yoder M, Robinson T. 2021. Midlatitude Error Growth in Atmospheric GCMs: The Role of Eddy Growth Rate. *Geophysical Research Letters*, 48(23): 1–7. <https://doi.org/10.1029/2021GL096126>.

Shongwe ME, Van Oldenborgh GJ, Van Den Hurk BJM, De Boer B, Coelho CAS, Van Aalst MK. 2009. Projected changes in mean and extreme precipitation in Africa under global warming. Part I: Southern Africa. *Journal of Climate*, 22(13): 3819–3837. <https://doi.org/10.1175/2009JCLI2317.1>.

Silvério KC, Grimm AM. 2022. Southern African monsoon: intraseasonal variability and monsoon indices. *Climate Dynamics*. Springer Berlin Heidelberg, 58(3–4): 1193–1220. <https://doi.org/10.1007/s00382-021-05954-y>.

Skamarock WC., Klemp JB, Dudhia JB, Gill DO, Barker DM, Duda MG, Huang X-Y., Wang W, Powers JG. 2021. A Description of the Advanced Research WRF Model Version 4.3. *NCAR Technical Note*, (July): 1–165. <https://doi.org/http://dx.doi.org/10.5065/1dfh-6p97>.

Spinoni J, Barbosa P, Buchignani E, Cassano J, Cavazos T, Cescatti A, Christensen JH, Christensen OB, Coppola E, Evans JP, Forzieri G, Geyer B, Giorgi F, Jacob D, Katzfey J, Koenigk T, Laprise R, Lennard CJ, Kurnaz ML, Li D, Llopart M, McCormick N, Naumann G, Nikulin G, Ozturk T, Panitz HJ, da Rocha RP, Solman SA, Syktus J, Tangang F, Teichmann C, Vautard R, Vogt J V., Winger K, Zittis G, Dosio A. 2021. Global exposure of population and land-use to meteorological droughts under different warming levels and SSPs: A CORDEX-based study. *International Journal of Climatology*, 41(15): 6825–6853. <https://doi.org/10.1002/joc.7302>.

Spinoni J, Barbosa P, De Jager A, McCormick N, Naumann G, Vogt J V., Magni D, Masante D, Mazzeschi M. 2019. A new global database of meteorological drought events from 1951 to 2016. *Journal of Hydrology: Regional Studies*. Elsevier, 22: 100593. <https://doi.org/10.1016/J.EJRH.2019.100593>.

Stauffer DR, Seaman NL. 1994. Multiscale four-dimensional data assimilation. *Journal of Applied Meteorology*, 33(3): 416–434. [https://doi.org/10.1175/1520-0450\(1994\)033<0416:MFDDA>2.0.CO;2](https://doi.org/10.1175/1520-0450(1994)033<0416:MFDDA>2.0.CO;2).

Sun Q, Zhang X, Zwiers F, Westra S, Alexander L V. 2021. A global, continental, and regional analysis of changes in extreme precipitation. *Journal of Climate*, 34(1): 243–258. <https://doi.org/10.1175/JCLI-D-19-0892.1>.

Tennant WJ, Hewitson BC. 2002. Intra-seasonal rainfall characteristics and their importance to the seasonal prediction problem. *International Journal of Climatology*, 22(9): 1033–1048. <https://doi.org/10.1002/joc.778>.

- Thoithi W, Blamey RC, Reason CJC. 2020. Dry spell frequencies, wet day counts and their trends across southern Africa during the summer rainy season. *Geophysical Research Letters*, 48(5): 1–22. <https://doi.org/10.1029/2020GL091041>.
- Todd M, Washington R. 1999. Circulation anomalies associated with tropical-temperate troughs in southern Africa and the south west Indian Ocean. *Climate Dynamics*, 15(12): 937–951. <https://doi.org/10.1007/s003820050323>.
- Todd MC, Washington R, Palmer PI. 2004. Water vapour transport associated with tropical-temperate trough systems over southern Africa and the southwest Indian Ocean. *International Journal of Climatology*, 24(5): 555–568. <https://doi.org/10.1002/joc.1023>.
- Tyson PD. 1981. Atmospheric circulation variations and the occurrence of extended wet and dry spells over Southern Africa. *Journal of Climatology*, 1(2): 115–130. <https://doi.org/10.1002/joc.3370010203>.
- Ukkola AM, De Kauwe MG, Roderick ML, Abramowitz G, Pitman AJ. 2020. Robust Future Changes in Meteorological Drought in CMIP6 Projections Despite Uncertainty in Precipitation. *Geophysical Research Letters*. John Wiley & Sons, Ltd, 47(11): e2020GL087820. <https://doi.org/10.1029/2020GL087820>.
- Ullah A, Pohl B, Pergaud J, Dieppois B, Rouault M. 2022. Intraseasonal descriptors and extremes in South African rainfall. Part I: Summer climatology and statistical characteristics. *International Journal of Climatology*. John Wiley & Sons, Ltd, 42(9): 4538–4563. <https://doi.org/10.1002/JOC.7489>.
- Usman MT, Reason CJC. 2004. Dry spell frequencies and their variability over southern Africa. *Climate Research*, 26(3): 199–211. <https://doi.org/10.3354/cr026199>.
- Van Heerden J, Terblanche DE, Schulze GC. 1988. The southern oscillation and South African summer rainfall. *Journal of Climatology*, 8(6): 577–597. <https://doi.org/10.1002/joc.3370080603>.
- Vigaud N, Pohl B, Crétaf J. 2012. Tropical-temperate interactions over southern Africa simulated by a regional climate model. *Climate Dynamics*, 39(12): 2895–2916. <https://doi.org/10.1007/s00382-012-1314-3>.
- Washington R, Preston A. 2006. Extreme wet years over southern Africa: Role of Indian Ocean sea surface temperatures. *Journal of Geophysical Research: Atmospheres*. John Wiley & Sons, Ltd, 111(D15): 15104. <https://doi.org/10.1029/2005JD006724>.
- Washington R, Todd M. 1999. Tropical-temperate links in southern African and Southwest Indian Ocean satellite-derived daily rainfall. *International Journal of Climatology*. [https://doi.org/10.1002/\(SICI\)1097-0088\(19991130\)19:14<1601::AID-JOC407>3.0.CO;2-0](https://doi.org/10.1002/(SICI)1097-0088(19991130)19:14<1601::AID-JOC407>3.0.CO;2-0).
- Wheeler MC, Hendon HH. 2004. An all-season real-time multivariate MJO index: Development of an index for monitoring and prediction. *Monthly Weather Review*, 132(8): 1917–1932. [https://doi.org/10.1175/1520-0493\(2004\)132<1917:AARMMI>2.0.CO;2](https://doi.org/10.1175/1520-0493(2004)132<1917:AARMMI>2.0.CO;2).
- WMO. 2021. *WMO Atlas of Mortality and Economic Losses from Weather, Climate and Water Extremes (1970–2019) (WMO-No. 1267)*. WMO: Geneva.

Xulu NG, Chikoore H, Bopape MJM, Nethengwe NS. 2020. Climatology of the Mascarene High and Its Influence on Weather and Climate over Southern Africa. *Climate 2020, Vol. 8, Page 86*. Multidisciplinary Digital Publishing Institute, 8(7): 86. <https://doi.org/10.3390/CLI8070086>.

Yuan X, Wang L, Wood EF. 2018. Anthropogenic Intensification of Southern African Flash Droughts as Exemplified by the 2015/16 Season. *Bulletin of the American Meteorological Society*. American Meteorological Society, 99(1): S86–S90. <https://doi.org/10.1175/BAMS-D-17-0077.1>.

Zhang C. 2005. Madden-Julian Oscillation. *Reviews of Geophysics*. John Wiley & Sons, Ltd, 43(2): 1–36. <https://doi.org/10.1029/2004RG000158>.

Zhang F, Qiang Sun Y, Magnusson L, Buizza R, Lin SJ, Chen JH, Emanuel K. 2019. What is the predictability limit of midlatitude weather? *Journal of the Atmospheric Sciences*, 76(4): 1077–1091. <https://doi.org/10.1175/JAS-D-18-0269.1>.

Zhao T, Dai A. 2017. Uncertainties in historical changes and future projections of drought. Part II: model-simulated historical and future drought changes. *Climatic Change*. Springer Netherlands, 144(3): 535–548. <https://doi.org/10.1007/S10584-016-1742-X/FIGURES/6>.